

# University of St Andrews



Full metadata for this thesis is available in  
St Andrews Research Repository  
at:

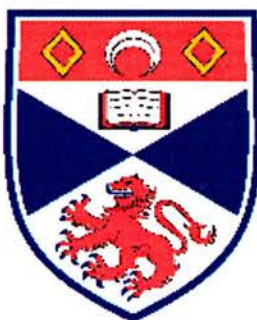
<http://research-repository.st-andrews.ac.uk/>

This thesis is protected by original copyright

DISPERSION ENGINEERING IN  
PLANAR PHOTONIC CRYSTAL WAVEGUIDES

By

Timothy James Karle



University  
of  
St Andrews

Thesis submitted for the degree of

Doctor of Philosophy

On

6<sup>th</sup> January 2005



Th  
F301

To my parents

## **Acknowledgements**

I would like to thank the large number of people involved in this work, perhaps most importantly my supervisor Thomas Krauss, who has supported me enormously and provided a challenging research topic. The mixture of collaborative interactions that he has fostered with groups in the UK, Europe and wider world, coupled with the opportunity and encouragement for his staff and students to travel to meetings and conferences at home and abroad has made the Photonic Crystals group at St Andrews a stimulating place to work.

My office mates of the past few years, Donald Brown, Maria Kotlyar and George Robb have been brilliant. George has simultaneously kept the cleanroom running and the music playing. Donald taught me my micro-fabrication skills. The group has grown quickly from those who started in St Andrews five years ago, Lijun Wu, Rab Wilson, and Abbes Tahraoui, and began to develop the many fabrication processes and simulation techniques that we use. My own studies and the help of those mentioned here has taught me characterisation expertise, fabrication competence, modelling methods and taken me around the world and up volcanoes.

I must thank Amr Helmy and Judith Hankey previously of Agilent Technologies for their support via a CASE award and for the advice, SOAs, InP material and ELEDs that they supplied. My examiners Professor Skolnick and Dr Korolkova were very thorough and I thank them for their patience.

Matt Bell, Steve White and Alvaro Gomez Iglesias have worked hard trying to couple optical pulses through my devices, in spite of the losses. Surprisingly they did not even lose (ping) that many. John Livesey has provided five years of friendship which has brightened up St Andrews. Honourable mentions also go to Dave Malins, Mikey Settle, Steve Neale, William Whelan-Curtin, Simon Cran-McGeehin, Andreas Vasdekis, Stephen Moore, Mike Flynn, Klaus Metzger, Graham Milne, Lynn Paterson, Jon Markham, Justin Lawrence, Andy Lewis and Mark Goossens among many others. Thanks to all the other members of our rapidly expanding group past and present.

Within the UPC, Martin Cryan helped me to understand the modelling tools that we use and has always been a friendly face. Many thanks to the guys from the Rankine Building in Glasgow, Iraklis, Aju, Harold, Pierre, and Marco as well as Sascha, Pierre and Paul from Imperial College. Thanks are also due to Michael Mazilu whose comprehension of his subject and whose constructive criticism made me think that little bit harder. The enthusiasm and advice from Chris Morgan and YewJun Chai was really appreciated, especially their thorough characterisation of the coupled cavity devices. Chris Leburn kindly allowed us to study the interaction of high power high rep-rate short pulses with the waveguide samples.

Without a doubt Henkjan Gersen's, Kobus Kuipers' and Rob Engelen's outstanding measurement results have added a sparkle to this report. An enjoyable week spent in the Netherlands with Henkjan and Eliane Flück really helped our mutual understanding of what we were trying to achieve. Their success at making spatially and temporally resolved measurements on waveguide samples with a highly sensitive and fragile apparatus and a pulsed OPO, spread over three optical benches, on the ninth floor of a tower block, with an adjoining fire escape is testament to the dedication of these guys.

Stefano Boscolo's and Michele Midrio's work helped to make the modelling more accessible. The assistance of the support guys at RSoft and Photon Design has been very valuable.

I should also thank Cameron Rae, Bruce Sinclair, Derek Bayne, Les Kirk and Aly Gillies for the equipment and expertise which they have offered over the course of the project. Niara Elejade, Paul Cruickshank, Daniel Rhodes, and Julia Fenn (among others) all trusted me with their precious equipment at various stages.

I really must thank my parents, my sister and Niall for their love and support. To my wonderful girlfriend Melanie who makes a lovely cup of tea and who also carefully proof read the manuscript, a big thankyou.

I, Timothy James Karle, hereby certify that this thesis, which is approximately 40,000 words in length, has been written by me, that it is the record of work carried out by me and that it has not been submitted in any previous application for a higher degree.

Date : 6th January 2005

Signature of Candidate

I was admitted as a research student in January, 2001 and as a candidate for the degree of Doctor of Philosophy in January, 2001; the higher study for which this is a record was carried out in the University of St Andrews between 2001 and 2004.

Date : 6th January 2005

Signature of Candidate

I hereby certify that the candidate has fulfilled the conditions of the Resolution and Regulations appropriate for the degree of Doctor of Philosophy in the University of St Andrews and that the candidate is qualified to submit this thesis in application for that degree.

Date : 6th January 2005

Signature of Supervisor

In submitting this thesis to the University of St Andrews I understand that I am giving permission for it to be made available for use in accordance with the regulations of the University Library for the time being in force, subject to any copyright vested in the work not being affected thereby. I also understand that the title and abstract will be published, and that a copy of the work may be made and supplied to any *bona fide* library or research worker.

Date : 6th January 2005

Signature of Candidate

## **Publications and Conference Reports where this work has been presented**

T.J. Karle, D.H. Brown, R. Wilson, M. Steer and T.F. Krauss, "Planar Photonic Crystal Cavity Waveguides", [Invited Paper], J. Sel. Top. Quantum Electron. **8**, pp909 (2002)

T.J.Karle, Y.J.Chai, C.N.Morgan, I.H.White and T.F.Krauss, "Observation of Pulse Compression in Photonic Crystal Coupled Cavity Waveguides", J. Lightwave. Technol., **22**, pp 514-9, (2004)

Y.J. Chai, C.N. Morgan, R.V.Penty I.H. White, T.J. Karle and T.F. Krauss, "Propagation of optical pulses in photonic crystal waveguides", IEE Proc.- Optoelectronics, **151**, pp109-13, (2004)

L. Wu, M. Mazilu, T. Karle, T.F.Krauss, "Superprism Phenomena in Planar Photonic Crystals", IEEE J. Quantum Elect., **38**, pp915-8 (2002)

R. Wilson, T.J. Karle, I. Moerman, T.F.Krauss "Efficient photonic crystal-Y junctions", J. Opt. A: Pure Appl. Opt. **5** pp76-80, (2003)

T.J. Karle, H. Gersen, R.J.P. Engelen, W. Bogaerts, J.P. Korterik, N.F. van Hulst, T.F. Krauss, and L. Kuipers, "Modal dispersion and mini stop bands in photonic crystal waveguides: experiment and modelling", To be submitted

H. Gersen, T.J. Karle, R.J.P. Engelen, W. Bogaerts, J.P. Korterik, N.F. van Hulst, T.F. Krauss, and L. Kuipers, "Direct observation of Bloch harmonics and negative phase velocity in photonic crystal waveguides", Phys. Rev. Lett (2004)

H. Gersen, T.J. Karle, R.J.P. Engelen, W. Bogaerts, J.P. Korterik, N.F. van Hulst, T.F. Krauss, and L. Kuipers, "Real space observation of ultraslow light in photonic crystal waveguides", Phys. Rev. Lett (2004)

R.J.P. Engelen, H. Gersen, J.P. Korterik, T.J. Karle, T.F. Krauss, L. Kuipers and N.F. van Hulst "Direct probing of Bloch mode dispersion in photonic crystal waveguides", accepted for publication Optics Express.

M. Ayre, T.J. Karle, L.Wu, T. Davies, T.F. Krauss, "Experimental Verification of Numerically Optimised Photonic Crystal Y-Splitter and Bend", IEEE Selected Areas in Communications, accepted for publication July 2005

M. V. Kotlyar, T. Karle, M. D. Settle, L. O'Faolain, and T. F. Krauss., "Low-loss photonic crystal defect waveguides in InP", Appl. Phys. Lett. **84**, pp3588 (2004)

T. J. Karle, D. H. Brown, R. Wilson, M. Steer and T. F. Krauss "Transmission through Photonic Crystal Coupled Cavity Waveguides with varying degrees of isolation" [Post deadline Conference Paper], QEP 15, Glasgow

T. J. Karle, D. H. Brown, R. Wilson, M. Steer and T. F. Krauss, [Invited Conference Paper], Progress In Electromagnetics Research Symposium, Cambridge, Mass, USA, July 2002.

T.J.Karle, Y.J. Chai,C.N Morgan, I.H. White and T.F. Krauss, 'Propagation of picosecond pulses through photonic crystal waveguides at C-band region.' [Conference Paper] Technical Digest, Summaries of paper presented at the IEEE Laser and Electro Optics Society Annual Meeting, pg. ThBB 2, November 2002.

T.J.Karle, Y.J. Chai, C.N Morgan, I.H. White and T.F. Krauss, 'Comparison of Simulation and Experimental Pulse Compression in Photonic Crystal Coupled Cavity Waveguides', [Invited Conference Paper], Progress in Electromagnetics Research Symposium, Hawaii, USA, October 2003.

T.J. Karle, M.R. Bell, S. White, C. Leburn, C.T.A. Brown, W. Sibbett, A. Miller, T.F. Krauss, H. Gersen, L. Kuipers, W. Bogaerts, Y.J. Chai, C.N. Morgan, I.H. White, M.J.Cryan, "Autocorrelation of pulses dispersed by photonic crystals", [Conference Paper] PECSV Kyoto, Japan, March 2004,

T. J. Karle, "Planar Photonic Crystal Cavity Waveguides", [Conference Presentation], International Conference of Physics Students, Denmark, July 2003

T. J. Karle, D. H. Brown, R. Wilson, M. Steer and T. F. Krauss, "Planar Photonic Crystal Cavity Waveguides", [Poster Presentation], Workshop and European Optical Society topical meeting on Two Dimensional Photonic Crystals, Ascona, Switzerland, August 2002

T. J. Karle, "Pulse Compression in Planar Photonic Crystal Cavity Waveguides", [Poster Presentation], International Conference of Physics Students, Odense, Denmark, August 2003

T.J. Karle, Y.J. Chai, C.N. Morgan, M Cryan, P.Pottier, R.V.Penty I.H. White, and T.F. Krauss, "Pulse Compression in Planar Photonic Crystal Cavity Waveguides", [Poster Presentation], UPC review meeting, July 2003

M. Settle, T.J. Karle, T.F. Krauss "Fourier Analysis of Photonic Crystal Waveguide Losses", [Poster Presentation], Tu-P36, PECSV Kyoto, Japan, March 2004,

M. Ayre, T.J. Karle, L.Wu, T.Davies, T.F. Krauss "Experimental measurement of 3D-optimised design Photonic Crystal Bends and Y-Splitters", [Poster Presentation], Tu-P36, PECSV Kyoto, Japan, (2004)

## Table of commonly used symbols

$\epsilon_0$	Dielectric permittivity of free space
$\mu_0$	Magnetic permeability of free space
c	Speed of light in vacuum
$\omega$	Angular frequency
$\lambda_0$	Free space wavelength
h	Planck's constant
$\hbar$	Planck's constant/ $2\pi$
D	Electric Displacement
E	Electric field
B	Magnetic Induction
H	Magnetic field
r	Position vector
t	Time

## **Abstract**

The strong spatial and temporal dispersion of Planar Photonic Crystal waveguides promises compact dispersion compensation of optical pulses. In this Thesis we report on the design, fabrication, characterisation and modelling of various Photonic Crystal waveguide configurations. Measurements with pulsed sources at telecommunications relevant wavelengths and Continuous Wave experiments allow us to map the dispersion of these components. The design and simulation of dispersive elements with 1D, 2D and 3D modelling tools allows accurate confirmation of the experimental measurements. The compression of picosecond pulses transmitted by a Planar Photonic Crystal device is demonstrated. The device exhibits a dispersion  $10^7$  times greater than that of standard single mode fibre. The direct visualisation of 100fs pulses propagating in a Photonic Crystal waveguide is achieved by time resolved heterodyne interference NSOM measurement. The Fourier analysis of the spatial data allows us to map the photonic bandstructure of the waveguides. We resolve the Bloch harmonics of the Planar Photonic Crystals both above and below the light line as a result of this phase sensitive technique. Analysis of the data reveals waves travelling with positive and negative phase velocities (both forwards and backwards) whilst the pulse can be seen to move with positive group velocity. Over the range of frequencies studied pulse-breakup is observed due to the strong multimoded dispersion of the Photonic Crystal waveguide. Where the group velocity tends to zero, a standing wave is observed, which does not diminish over a timescale of  $> 5\text{ps}$ . This standing wave is formed in an open structure, rather than in a cavity, due to the flat dispersion at the band edge.

# Contents

<i>Publications and Conference Reports where this work has been presented .....</i>	<i>iv</i>
<i>Table of commonly used symbols .....</i>	<i>vii</i>
<i>Abstract.....</i>	<i>viii</i>
<i>Contents.....</i>	<i>vii</i>
<b>Chapter 1 .....</b>	<b>1</b>
1.1    Introduction .....	1
1.2    Chromatic Dispersion .....	4
1.3    Analogy.....	9
1.4    State of The Art Dispersion Compensation.....	10
1.5    Photonic Crystals.....	17
1.5.1    Photonic Crystal Fibres .....	22
1.6    Outline .....	23
<b>Chapter 2 .....</b>	<b>27</b>
2.1    1D periodic structures.....	27
2.2    Maxwell's Equations .....	27
2.3    Bragg Stack .....	28
2.4    Transfer Matrix Method (TMM).....	30
2.5    Semi-Analytical Equations for 1D structures .....	36
2.6    Plane Wave Expansion Method .....	39
2.6.1    Calculation of 1D Bragg grating.....	41
2.6.2    Discussion of numerical computation: truncation errors and dielectric representation ..	43
2.7    FDTD .....	44
2.7.1    Convergence Testing .....	49
2.8    Coupled Cavity Waveguides in 1D .....	51
2.9    Pulse Compression/Dilation.....	58
2.10    Conclusion.....	62
<b>Chapter 3 .....</b>	<b>66</b>
3.1    2D Coupled Cavity Waveguides.....	66
3.2    2D Slab Waveguides – Out of plane dispersion .....	69
3.2.1    Symmetries .....	72
3.3    Mode Solvers.....	73
3.3.1    Mode profiles for GaAs heterostructure .....	73
3.3.2    Mode dispersion .....	74
3.3.3    Out-of-Plane confinement .....	76
3.3.4    Coupling Ridge Waveguides .....	78

<b>3.4</b>	<b>Bandstructure in 2D – In plane dispersion for a square of free space.....</b>	<b>79</b>
3.4.1	Pillars in Air – square lattice .....	82
3.4.2	Air Holes in Dielectric – triangular lattice.....	83
<b>3.5</b>	<b>Coupled Cavity Waveguides.....</b>	<b>84</b>
3.5.1	H1in1 CCWs .....	86
<b>3.6</b>	<b>Fabrication.....</b>	<b>90</b>
3.6.1	Results .....	94
3.6.2	H1in1 Transmission and Reflection .....	97
3.6.3	Coupled Cavity Waveguides – summary.....	102
<b>3.7</b>	<b>EigenMode Expansion Modelling .....</b>	<b>108</b>
3.7.1	Device dispersion using 2D EME.....	108
3.7.2	Phase Retrieval from 2D FDTD .....	115
<b>3.8</b>	<b>Pulse Measurement on L2in1 waveguides.....</b>	<b>118</b>
3.8.1	Introduction .....	118
3.8.2	Device properties.....	119
3.8.3	Measurements.....	123
<b>3.9</b>	<b>3D Bandstructure Calculations Using FDTD .....</b>	<b>129</b>
<b>3.10</b>	<b>Pulse Compression.....</b>	<b>135</b>
3.10.1	Fourier Transform propagation method .....	135
3.10.2	Fibre & CCW Dispersion.....	136
3.10.3	Comparison between Experiment and Model .....	139
<b>3.11</b>	<b>Conclusions .....</b>	<b>141</b>
	Appendix B – Field Components.....	142
<b>Chapter 4</b>	.....	<b>146</b>
<b>4.1</b>	<b>Line defect waveguides.....</b>	<b>146</b>
<b>4.2</b>	<b>Line defect waveguides –W1.....</b>	<b>148</b>
4.2.1	W1 Silicon Membrane – modelling benchmark .....	149
4.2.2	W1 Silicon Nitride Membrane – model and experiment .....	151
4.2.3	W1 AlGaAs heterostructures – Transmission measurements .....	155
4.2.4	W1 SOI.....	164
4.2.5	W1 Summary .....	165
<b>4.3</b>	<b>Line defect waveguides –W3.....</b>	<b>167</b>
4.3.1	St Andrews W3 AlGaAs heterostructure .....	168
4.3.2	Non-linearities .....	168
4.3.3	Wafer design .....	169
4.3.4	W3 Dispersion .....	170
4.3.5	W3 AlGaAs transmission spectra .....	171
<b>4.4</b>	<b>Time resolved heterodyne interference Scanning Near Field Microscopy....</b>	<b>176</b>
4.4.1	Sample preparation - W3 SOI.....	178
4.4.2	Far field imaging .....	185
4.4.3	Near field imaging .....	188
4.4.4	Fourier mode profiles .....	193
<b>4.5</b>	<b>Conclusions .....</b>	<b>199</b>
<b>Chapter 5</b>	.....	<b>202</b>
<b>5.1</b>	<b>Spatial dispersion and Routing in Planar Photonic Crystals .....</b>	<b>202</b>
<b>5.2</b>	<b>Superprism.....</b>	<b>202</b>
<b>5.3</b>	<b>Waveguide junctions and bends.....</b>	<b>207</b>
<b>5.4</b>	<b>Conclusions .....</b>	<b>207</b>

<i>Chapter 6</i> .....	209
<b>Conclusion</b> .....	<b>209</b>

# **Chapter 1**

## **1.1 Introduction**

This thesis summarises my contribution to a number of collaborative projects researching the dispersive properties of planar photonic crystals. The main focus of the work is aligned to the Ultrafast Photonics Collaboration, a consortium of seven Universities and seven Industrial companies researching novel technologies for future telecommunications networks. Photonic crystals rely on the same principles of Bragg reflection as exploited in DFB lasers, Fibre Bragg Gratings and Thin Film Filters. Photonic Crystals are expected to offer enhanced control over the propagation of light, irrespective of frequency, polarisation and propagation direction.

Photonic Crystals are wavelength scale dielectric microstructures, which by their periodic patterning insulate photons in a manner similar to electrons in a semiconductor crystal. The periodicity couples forwards and backwards travelling waves inside the Photonic Crystal, causing a net cancellation of the optical field. The scale of these structures is, however, typically a factor 1000 larger than semiconductor crystals, permitting current fabrication technology precise control over the design. In this way defects can be deliberately positioned within the pattern allowing only the desired waves to propagate. This affords great control over the optical properties of the Photonic Crystals.

Optical technologies are becoming ubiquitous within modern life, from the diode laser based barcode scanners at supermarket Points Of Sale, to photodetectors controlling cleansing in restrooms, from display technologies conveying statistics at sporting events to the correction of myopia by focussing laser light. The application relevant to this work is rapid optical data communications, driven by the emergence of the Internet [1]. The data traffic on networks is growing at an exponential rate which far outstrips voice traffic. Such technology is dependent on passive dielectrics such as Silica and Silicon and active III-V semiconductors such as GaAs and InP. Increasingly the boundaries between conventionally passive and active materials is blurring as they are engineered to integrate various functionalities together within a smaller package.

The size of optical components is a critical factor in the development of these devices. The development of WDM technology for volume manufacturing (e.g. for devices such as Arrayed Waveguide Gratings (AWG) and Mach Zehnder Interferometers (MZI)) has witnessed the advent of optical Large Scale Integration [2]. Wafer scale integration leads eventually to increased profits for component manufacturers as the cost per device plummets as devices become commodities. Photonics manufacturers wish to emulate the model of the electronics industry and at least initially follow the famous Moore's Law. In turn it is hoped that the science and technology will benefit from increased investment. Photonic Crystals appear to offer a dramatic and desirable scale reduction, which they achieve by increasing the refractive index contrast and therefore reducing the interaction length required for common optical processes.

In their brief history Photonic Crystals have already made substantial waves in the field of light matter interactions. Photonic Crystal lasers have been fabricated with the smallest demonstrated modal volumes, relying on the feedback from surrounding mirror layers. Cavities have been characterised with the highest Q/V ratios ever, storing more energy, for longer in the tiniest volume. This bodes well for cavity QED experiments and quantum information processing, where single photon sources are desired.

Microstructured Optical Fibres (which include Photonic Crystal Fibres) have opened up a revolutionary new field of low energy nonlinear optics. The high optical confinement allows observation of non-linear effects over centimetre length scales and using femtosecond pulses with only nanoJoule power levels. Such fibres can possess either a solid silica or hollow core. The former are used with increasing frequency in supercontinuum generation. In the latter case the combination of spatially multimode propagation, strong waveguide dispersion, and massive cumulative interaction length have enabled efficient frequency conversion in gases filling the hollow fibre core [3]. These special fibres also have a prospective role in telecommunications. Low transmission losses through novel types of fibre have recently been reported and are now (1dB/km) only one order of magnitude above the lowest loss ever achieved (0.1dB/km).

Superprisms combine the refractive properties of conventional prisms with the diffractive properties of gratings. These devices exploit the spatial dispersion contours that result from a two dimensional grating. Experimentally, they have been shown to possess wavelength sensitivity, more than two orders of magnitude greater than diffraction gratings and prisms.

Photonic Crystal waveguides have been proposed which are capable of routing light with theoretically zero loss. The Photonic Crystal cladding insulates the waveguide, preventing the existence of radiation modes. More recently the interest in Photonic Crystal waveguides has focussed on their distinctive waveguide dispersion. In practical demonstrations compact delay lines have been proven to be readily achievable. These entail waveguide modes in which the light travels slowly. This slow propagation is a result of the forward and backward travelling waves which comprise the mode, almost cancelling one another, producing a slow forwards wave. The ability to vary the delay between different spectral components of our signal is highly desirable. This temporal dispersion is prevalent in Photonic Crystals across large spectral bandwidths due to the high refractive index contrast.

It is this dispersive functionality that we wish to study in our work. Control over the dispersion of an optical circuit is sought after in order to manage the propagation of optical pulses. The shorter the pulse the more likely it is to exhibit chirp, which refers to the change in instantaneous frequency of the pulse with time. These could be pulses chirped as the light from a laser source is modulated or pulses dispersed by transmission through an optical network. We need to take into account practical device lengths in order to make realistic estimates of the impact of Photonic Crystal dispersion. Ideally this would be configurable, allowing devices to adapt to changing network conditions. Such devices need not though be particularly quick to configure, as the changes may occur over a time scale of hours. These properties will be particularly dependent on the materials that we choose to employ.

## 1.2 Chromatic Dispersion

A beautiful illustration of chromatic dispersion can be seen in a rainbow. The white light of the sun's rays is refracted by tiny water droplets in the atmosphere, resulting in a colourful arc. The light is separated into its different spectral components as the light rays belonging to each colour travel at a different speeds inside the water. The refractive index of the water for a particular colour is the ratio of the speed of light in vacuum to the speed of light in the water. In the air the different colours travel with the same speed. At the surface of the water droplet the change in speed causes the light rays to bend, or refract. Rays belonging to different colours are refracted through a range of angles, hence forming a rainbow. This exemplifies material dispersion; whereas in this work we also consider waveguide dispersion.

The refractive index of a waveguide varies typically with wavelength for two reasons; firstly the dielectric materials from which it is fabricated have absorption resonances in the UV or visible regions of the spectrum. Far from these resonances the refractive index varies less dramatically and can be approximated by a sum over each of the individual resonances. Secondly the power travelling in the waveguide is distributed amongst the discrete modes of the structure. The modes conserve the wavevector at the interfaces to the structure and are therefore strongly dependent upon the physical extent of the structure, and hence the wavelength.

A pulse travelling in free space, in the z direction contains a narrow band of frequencies centred around  $\omega_0$ . At each frequency, the Electric field,  $\mathbf{E}$ , can be written as

$$E(\omega, z) = E(\omega) e^{-jk(\omega)z} \quad \{1.1\}$$

The time dependence of the field is given by

$$E(t, z) = \int_{-\infty}^{+\infty} E(\omega) e^{j(\omega - k(\omega)z)} d\omega \quad \{1.2\}$$

The propagation constant,  $k$  can be expanded as a Taylor series to first order as

$$\Delta\omega = (\omega - \omega_0), \text{ to give } k(\omega) = k(\omega_0) + \frac{dk}{d\omega} \Big|_{\omega_0} \Delta\omega \quad \{1.3\}$$

Substituting {1.3} into {1.2}, and changing variables to  $\Delta\omega$  gives,

$$E(t, z) = e^{j(\omega - k(\omega_0)z)} \int_{-\infty}^{+\infty} E_+(\Delta\omega) e^{j\Delta\omega(t - \frac{dk}{d\omega}z)} d\Delta\omega \quad \{1.4\}$$

$$= e^{j\omega\left(t - \frac{z}{v_p}\right)} \int_{-\infty}^{+\infty} E_+(\Delta\omega) e^{j\Delta\omega\left(t - \frac{z}{v_g}\right)} d\Delta\omega$$

The pulse can be seen to be the product of a rapidly varying carrier wave, propagating at the phase velocity  $v_p = \frac{\omega}{k(\omega_0)}$  and a slowly varying envelope propagating at the group velocity,  $v_g = \frac{d\omega}{dk}$ .

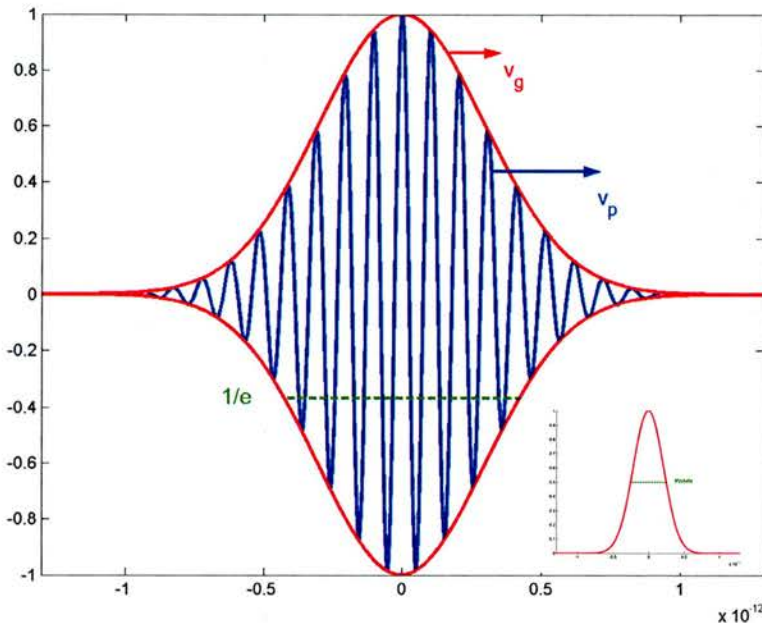


**Figure 1.1 The Electric field of a pulse (blue), showing the Gaussian envelope modulation of the sinusoidal carrier wave. The pulse propagates at the group velocity,  $v_g$  whereas the carrier propagates with a phase velocity,  $v_p$ . The corresponding pulse intensity (inset) has a FWHM of 500fs. The carrier wavelength is scaled by a factor 20 to simplify the picture.**

For the same pulse travelling through a dispersive material or waveguide, each spectral (Fourier) component experiences a different phase shift. This can dilate, compress or otherwise distort the shape of the pulse. The effects of dispersion are then treated as an extended Taylor expansion about the pulse centre frequency, including as many higher order terms as necessary. Conventionally when dealing with waveguides the propagation constant is denoted by  $\beta$  rather than by  $k$ .

$$\beta(\omega) = n(\omega) \frac{\omega}{c} = \beta_0 + \beta_1(\omega - \omega_0) + \frac{1}{2} \beta_2(\omega - \omega_0)^2 + \dots, \quad \{1.5\}$$

where expansion coefficients are given by  $\beta_m = \left( \frac{d^m \beta_m}{d\omega^m} \right)_{\omega=\omega_0}$ , for positive integer m.

The velocity of a pulse propagating in the dispersive medium is then determined from the first coefficient by,

$$\beta_1 = \frac{1}{v_g} = \frac{N_{group}}{c} = \frac{1}{c} \left( n - \omega \frac{dn}{d\omega} \right), \quad \{1.6\}$$

where we have defined a group index  $N_{group} = n - \omega \frac{dn}{d\omega} = n - \lambda \frac{\partial n}{\partial \lambda}$  (see equation 3.17). In travelling a distance, L, the pulse is retarded by a time delay,  $L\beta_1$ .

The second coefficient in the expansion determines broadening of the pulse,

$$\beta_2 = \frac{d}{d\omega} \left( \frac{1}{v_g} \right) = \frac{d\beta_1}{d\omega} = \frac{1}{c} \left( 2 \frac{dn}{d\omega} + \omega \frac{d^2n}{d\omega^2} \right) \quad \{1.7\}$$

and it is known as the Group Velocity Dispersion (GVD) parameter (it has units  $s^2/m$ , typically  $ps^2/km$ ). Higher order coefficients are responsible for distorting the envelope of the pulse and can lead to pulse break-up. Ideally we would like a waveguide with a well behaved, broadband GVD.

In practice the wavelength dependence of the first coefficient, commonly known as the Dispersion,  $D = \frac{d\beta_1}{d\lambda}$ , is used to describe the properties of optical fibres (it typically has units of  $ps/nm \cdot km$ ). In other terms,

$$D = \frac{d\beta_1}{d\lambda} = \frac{d}{d\lambda} \left( \frac{N_{group}}{c} \right) = \frac{1}{c} \frac{\partial}{\partial \lambda} \left( n - \lambda \frac{dn}{d\lambda} \right) = -\frac{\lambda}{c} \frac{d^2n}{d\lambda^2}. \quad \{1.8\}$$

The dispersion and GVD are related, by  $D = \frac{d\omega}{d\lambda} \beta_2 = -\frac{2\pi c}{\lambda^2} \beta_2$ .  $\{1.9\}$

\*  $\beta_2$  is strictly the Group Delay Dispersion (GDD) coefficient as we differentiate the Group Delay,  $L\beta_1$ , with respect to frequency to obtain the GDD,  $\beta_2 = \frac{1}{L} \frac{d(L\beta_1)}{d\omega}$ . The Group Velocity Dispersion (GVD) is given as  $\frac{dv_g}{d\omega} = \frac{d}{d\omega} \left( \frac{1}{d\beta/d\omega} \right) = \frac{d^2\beta/d\omega^2}{(\beta_1)^2} = -\beta_2 v_g^2$ .

In fibre optics, once low loss waveguiding was established and low cost in-line amplifiers became available, systems evolved rapidly to utilise the available bandwidth [4]. The two dominant techniques for maximising the capacity are Time Division Multiplexing (TDM) and Wavelength Division Multiplexing (WDM). Current deployed technologies consist of 2.5Gbps transceivers for TDM. As the data rate increases to the 10 and 40Gbps rates, which are beginning to enter the marketplace the spread of wavelengths in the pulses reaches the  $\Delta f=50\text{GHz}$  ( $\Delta\lambda=0.4\text{nm}$ ) mark. The chromatic dispersion prevalent in the fibre network is then becoming the pressing concern to the system designers.

Despite the recent downturn in the fortunes of the telecommunications sector [5], R&D is looking way beyond these data rates, to systems using ever shorter pulses. The existing fibre-in-the-ground, is on the other hand, here to stay. The manufacture of silica waveguides and indeed the silica itself costs next to nothing, but the expense and disruption involved in laying the cables precludes replacement. Novel devices for controlling the transmission of ultrashort pulses through links of sometimes unknown<sup>\*</sup> dispersions are in high demand. Chromatic dispersion can be compensated for by replacing lengths of the transmission line with devices designed to give zero net dispersion. Such devices work either in transmission or reflection geometries. Working in reflection brings the additional complexity of requiring an expensive circulator or isolator. We have therefore attempted to use transmission geometries. Our choice of material leaves open the option of actively tuning our devices via a number of mechanisms, including thermal heating and carrier injection. In this work however we will concentrate on passive devices only.

Potential economies of scale due to small device footprint are certainly a motivating factor in Photonic Crystal research. This small scale introduces its own challenges, however, as coupling from the large  $6\mu\text{m}$  mode diameter of Single Mode Fibre to the typical  $<0.5\mu\text{m}$  mode diameter of Photonic Crystal waveguides is clearly difficult.

---

\* At the time of installation the dispersion did not feature in the thoughts of the engineers, pulses were long and essentially “single frequency”. To utilise these links will require rigorous characterisation or very robust design. Cables on under sea links are easier to update. There is an estimated  $1.5\times 10^7\text{km}$  of fibre in the ground, which was manufactured prior to 1995 when newer fibres became available.

Polarisation mode dispersion (PMD) is increasingly a concern for fibre engineers, where the propagating cylindrically symmetric mode has two identical solutions with perpendicular polarisations. Small changes in the fibre profile cause waves propagating in the two states to drift apart in time. Polarisation transparency is therefore a useful feature for optical networks. Photonic Crystals, on the other hand, exhibit a strong polarisation response, making them difficult to employ where polarisation insensitivity is required, for instance as part of the receiver. Photonic Crystals are however suited to monitoring the polarisation state.

The semiconductor laser sources and modulators typically employed in telecommunications networks have a well defined polarisation, especially where quantum well devices are employed. The polarisation response of the Photonic Crystals in this report is designed to match this.

In addition to polarisation, high optical confinement, small scale, material dispersion and system geometry; when dealing with pulses in a transmission system, care must be taken with non-linear processes. Propagating signal pulses can be distorted by Self Phase Modulation (SPM), cross Phase Modulation (XPM) and Four Wave Mixing (FWM) processes [7]. SPM and XPM are third order ( $\chi^3$ ) non-linear processes. In SPM the refractive index of the medium has an intensity dependent term. This gives rise to a phase shift after a given propagation distance, additionally for a pulse it leads to a time dependent frequency deviation and hence spectral broadening. The resulting frequency chirp may interact with the waveguide dispersion (GVD) causing dilation or compression. This alters the peak intensity and hence dynamically affects the signal level, creating amplitude distortion. Similar spectral broadening occurs as a result of XPM, due to the interaction between two distinct signal pulses, at two carrier frequencies,  $\omega_1$  and  $\omega_2$ , in a WDM system. FWM relies on phase matching between different spectral components, which occurs in a system with zero dispersion. This gives rise to new frequencies,  $\omega_{mn} = m\omega_1 \pm n\omega_2$ , for integer m and n. In each case the overall behaviour is dependent upon both the nonlinearities and the dispersion. Two Photon Absorption (TPA) is a further nonlinear hazard particularly for semiconductor waveguides (Si, GaAs and InP), for wavelengths above the half bandgap,

$\lambda_{\frac{1}{2}gap} = \frac{2E_{gap}}{hc}$ . Briefly, a pair of photons with energies,  $E_1$  and  $E_2$  where  $E_1 + E_2 > E_{gap}$  can be absorbed, if both coincide within a temporal interval of  $\Delta t = \frac{\hbar}{2\Delta E}$ . The high optical confinement increases the optical intensity and hence the absorption constitutes an optical loss. The free carriers generated by the optical absorption can give rise to additional effects.

Dispersion compensation is the term given to the field of optical engineering which attempts to deal with chromatic dispersion. In relation to the Ultrafast Photonics Collaboration the development of dispersion compensating elements will allow us to achieve a number of goals, targeting applications such as;

- i) Compensation of modulator chirp, when the carrier frequency of a directly or externally modulated laser is modified by changes to the carrier and photon populations.
- ii) Dilation, amplification and then re-compression of a pulse. This allows a Semiconductor Optical Amplifier (SOA) to be operated in a linear gain regime.
- iii) Nonlinear filtering of pulses in an integrated dispersion imbalanced loop.

### **1.3 Analogy**

Pulse dispersion compensation is very much like traffic management. Take for example the M25, London's orbital motorway. At peak times of the day the traffic joins the network at a junction, when the traffic signals allow, and small groups of vehicles form. These groups are our pulses, and we want to get all the cars in them home safely and to the correct destination. The pulses unfortunately disperse, the individual elements, the drivers, prefer to drive at different speeds. Some break the mandatory limit whilst others prefer to idle in the slow lane. As the slower drivers are left behind they are gradually caught by the faster drivers from the previous junction. This is known as bunching [6], and cannot be controlled by the system management. It has been proposed, that if everyone was to travel at 50mph (20mph under the speed limit), everyone would get home, on average, in a lot less time. The bunching leads to traffic jams, delays and in the worst case accidents (in a fibre network the same

overloading causes non-linear effects!). What concerns us more is that the pulses overlap and we lose the ability to distinguish between them. Were it not for the fact that the individual drivers are able to find their own way home (intelligent data header) we would lose them. Dispersion in a fibre network similarly causes loss of data by smearing out well defined -managed- pulses, but we cannot unfortunately just ask all of the spectral components to travel at the same speed.

#### **1.4 State of The Art Dispersion Compensation**

The simplest solution to the problem of dispersion is to insert a length of Dispersion Compensating Fibre (DCF) to compensate 1:1 for the  $D_{SMF}=17\text{ps/nm/km}$  of the SMF with a  $D_{DCF}=-17\text{ps/nm/km}$ . These are already deployed in networks. They utilise a unique fibre structure with a mode which travels mainly in the lower index cladding. This mode exhibits strong dispersion [4], as it is close to cut-off. Originally DCF was narrowband and could not compensate for a wide range of optical frequencies. Newer wideband DCFs have removed this problem and a system optimised for the C-band (1550nm) can provide acceptable dispersion control for the L band, and wavelengths beyond 1600nm [7]. The DCF can be positioned to give pre-, post- or hybrid (both) compensation to the pulses before or after transmission through the lengths of SMF. In a combined system the dispersion, nonlinearities and amplifier noise all must be accounted for to optimise performance. The Bit Error Rate (BER) is the figure of merit applied to indicate successful transmission. Values of the order of  $BER=10^7$  are acceptable. The choice of either Return to Zero (RZ) or Non-RZ data formats affects the spectral content of the system and hence RZ pulses (for the same bitrate) are more susceptible to dispersion. This can actually aid the system as the resultant broadening can lower the influence of nonlinear effects such as Self Phase Modulation (SPM) and allow higher input powers to be used, with better signal to noise performance. Reverse or Inverse (R or I)DCFs have been designed with lower attenuation and more favourable non-linear properties than conventional DCF, compensating from 1:1 to 1:6 with values of  $D$  up to  $-100\text{ps/nm/km}$ . Many researchers deem it unnecessary to quote the dispersion in terms of the length of their device, e.g. where a single etalon or thin film filter is used. If the dispersive property is waveguide based, however, it appears more suitable to include the length. We have hence chosen to include the lengths in our work.

In a similar manner Higher Order Mode (HOM) fibres are utilised to provide strong dispersion. A suitable coupler may be required to couple power out of the fundamental mode of the SMF into this HOM. Integrated versions of this HOM technique utilise supermodes, a combination of two modes in parallel slab waveguides to achieve high dispersion (see for example Figure 1.2). A practical demonstration in a coupled pair of InGaAsP waveguides demonstrated 10% compression of a 5ps pulse [8]. A similar structure proposed by Peschel [9] should be capable of dispersions  $10^3$ - $10^6$  times greater than the GVD of SMF, dependent upon the waveguide separation,  $w$ , and the refractive index contrast,  $\Delta n$ . A TiO<sub>2</sub>/Si HOM waveguide device has been shown to exhibit better performance than the InGaAsP system if we include the bandwidth,  $\Delta\lambda$ , in our figure of merit,  $D \cdot \Delta\lambda \propto \Delta n$ . Lee has demonstrated [10] a pulse compression of 37%, for an incident 2.8ps pulse.

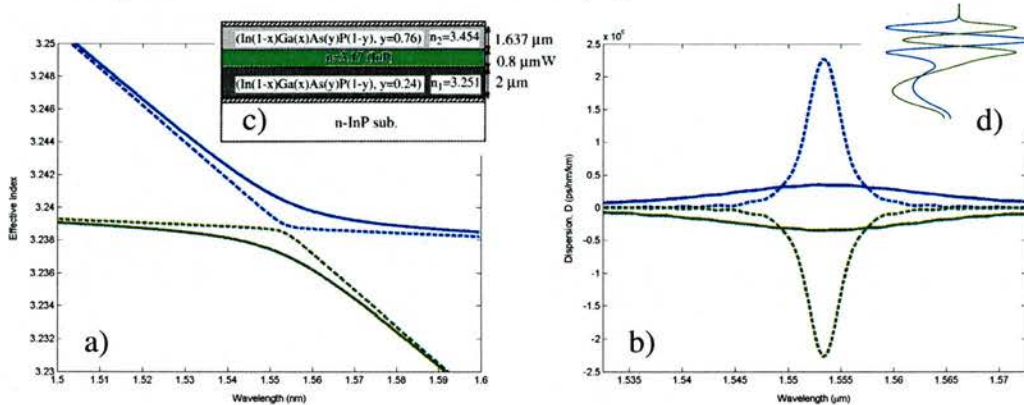


**Figure 1.2** The a) effective indices and corresponding b) Dispersion of the coupled modes of the c) inset dual InGaAsP core waveguides. The spacer layer (light green) is  $w=0.8\mu\text{m}$  for the solid lines and  $w=1.5\mu\text{m}$  for the dashed lines d) Symmetric (blue) and anti-symmetric (green) supermode profiles. (calculated using Fimmwave, after [8])

The FESTA research organisation have demonstrated a Twin Chirped FBG system based upon a pair of linearly chirped gratings (chirp=56pm/nm) of different lengths and with a ~200ps delay across a 3nm bandwidth. Applying a set of three heaters along the length of the FBGs allows the slope of the dispersion to be altered. Their best result is a 42% compression of a 4.3ps input pulse [11]. As mentioned above a circulator is required in order to use these reflection mode devices, adding complexity and cost.

Fibre Bragg Gratings (FBGs) are being exploited in non-linear regimes to compress pulses. A high intensity pump with a centre frequency away from the stop band can

be used to alter the frequency chirp seen by a weaker probe beam tuned to the band edge. The high GVD of the structure contributes strongly to the observed affect [12]. More conventionally a pulse chirped by Self Phase Modulation (SPM) in the gain material of the source laser (here a mode locked Q-switched YLF laser) can be compressed (by 20%) purely by the linear dispersion of a FBG [13].

AWGs integrated with an equaliser array, on Silica-on-Silicon has been used to compensate  $16 \times 20\text{Gb/s}$  or  $8 \times 40\text{Gb/s}$  data streams, with dispersions up to  $D = \pm 250\text{ps/nm}$  over a  $\sim 40\text{GHz}$  bandwidth [14]. Ring resonators integrated, on a Silica-on-Silicon platform, into the arms of an asymmetric Mach Zehnder interferometer [15] have provided thermally tunable dispersion of  $\pm 2000\text{ps/nm}$  across a  $16\text{GHz}$  bandwidth and can be readily deployed in series. The devices exhibited PMD which had to be compensated for. SiON waveguides with a 5% index contrast have been utilised for a ring resonator system with a  $22.5\text{GHz}$  bandwidth and a tunable dispersion of  $\pm 500\text{ps/nm}$ . This system has a 1.5 by  $0.25\text{cm}$  footprint [16].

Programmable pulse shapers have also been developed based upon time to space conversion schemes. A Liquid Crystal (LC) array (a Spatial Light Modulator(SLM)) can be used to impart near exact phase correction, in conjunction with DCF, for a  $400\text{fs}$  pulse which has been transmitted through a  $10\text{km}$  link[17].

Gires Tournois [15] interferometers (GTIs) are a special case of Fabry Pérot (F-P) cavity, where the second of the two mirrors is  $\sim 100\%$  reflecting. As such it is an example of an all-pass amplitude filter, in reflection. The cavity exhibits periodic resonances in its phase response, with an associated group delay (see Figure 1.3) which was measured in [18], by observing the duration of  $115\text{fs}$  pulse after four bounces off the GTI. The variation of this delay with frequency, the group velocity dispersion is plotted in Figure 1.3c). GTIs have been investigated to provide broadband order dispersion compensation, due to their quadratic group delay [19], which is relevant to the generation of much shorter pulses ( $\sim 10\text{fs}$ ). A Fabry Pérot cavity (with equally reflecting mirrors) has qualitatively comparable, although quantitatively weaker dispersive properties to the GTI; (the GTI has higher finesse because of the 100% reflecting rear mirror). The F-P cavity has the distinct

disadvantage that the transmission and reflection amplitude responses are also resonantly peaked.

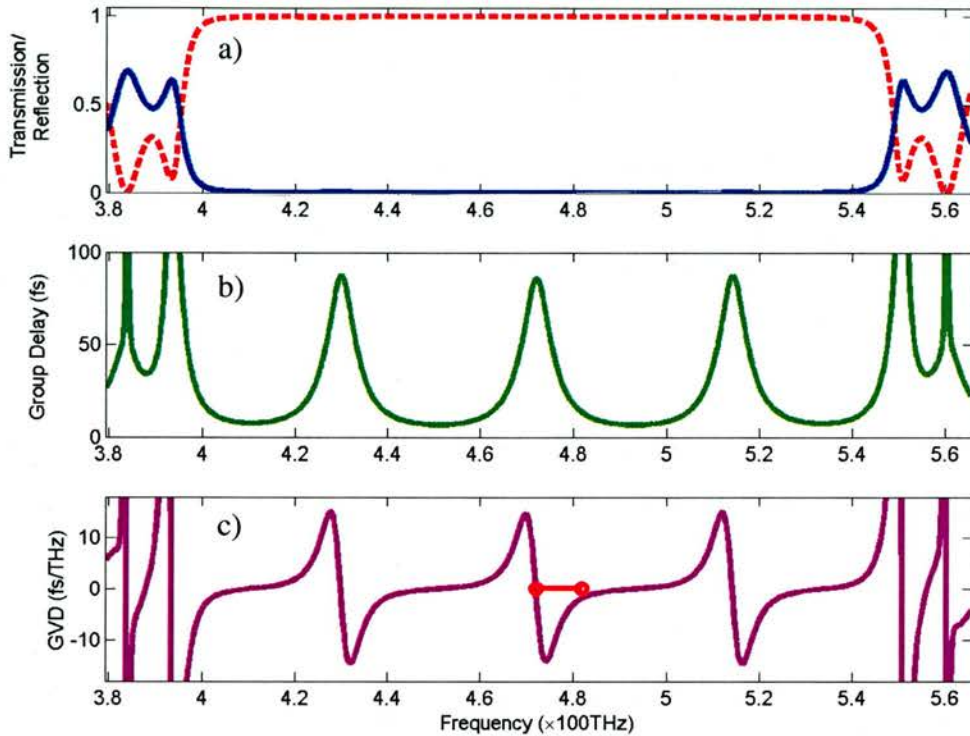


**Figure 1.3** a) The unity Reflection (red-dashed) and zero Transmission (blue solid) spectra of a Gires Tournois interferometer, after reference [18]. The high reflection rear mirror is provided by a 1D Photonic Crystal (or Bragg grating). b) The group delay peaks when light is resonant in the cavity. c) The Group Velocity Dispersion ( $2\pi dT/d\omega$ ) is zero on resonance, but varies smoothly between high positive and negative dispersion, at each resonance. The experimental pulse bandwidth FWHM (~13nm) is marked by the red bar. Calculated using CAMFR.

Micro Electro Mechanical (MEMS) devices can be used to form (Gires-Tournois type) etalons with electrostatically tuned membranes, which adjust the reflectivity of the front mirror, this changes the cavity Finesse, a measure of the sharpness of the peaks. Additionally thermo electric coolers are used to thermo optically tune the substrate to modify the cavity thickness, and with it the Free Spectral Range ( $FSR = c / 2N_g L = 100\text{GHz} = 0.8\text{nm}$ ). A linear net dispersion results, when a pair of devices is configured as a two stage filter. Detuning the relative centre wavelengths and adjusting the reflectivity of the etalon gives tunable dispersion compensation [15]. These GTIs have demonstrated  $\pm 100\text{ps/nm}$  with 50GHz bandwidth and low residual

delay ripple, though these devices are particularly tricky to cascade.

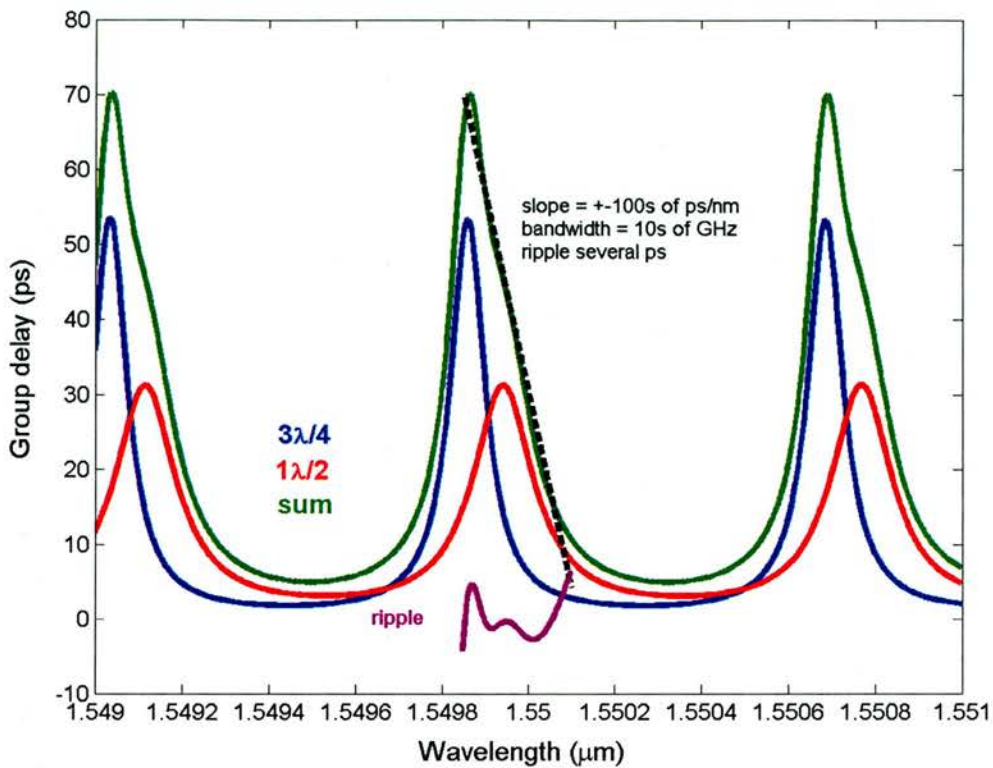


**Figure 1.4** The net group delay (green) of a two stage MEMS GTI. The application of a voltage to the device causes the membrane to deflect, changing the thickness of the air cavity from ( $3\lambda/4$ ) to ( $\lambda/2$ ) thus adjusting the front mirror reflectivity. The centre wavelength of either device is thermally tunable resulting in versatile dispersion compensation. The residual delay ripple (3-4ps) is shown in magenta, beneath the plot. Calculated using CAMFR.

Integrated AlGaAs Photonic Crystal waveguides demonstrated the spectral properties that are associated with 20% pulse compression [20]. Measurements required high repetition rate, low peak power sources and a high resolution spectrum analyser.

An enhancement of the phase modulation in a Mach-Zehnder waveguide modulator was demonstrated by Shaw et al. [21]. A series of gratings were etched across an optical waveguide and the coupling between one resonant cavity and the next causes a delay reducing the group velocity in the waveguide. The efficiency of the M-Z device was improved by a factor 2.9 at resonance (1543nm). Increasing the delay does however reduce the bandwidth (~20GHz). The principle applied here is very similar to the coupled cavity waveguides that we will discuss in later Chapters.

At current bit rates, electronic methods of dispersion compensation at the receiver have been vigorously pursued by some vendors. The technology can be installed almost as an afterthought. Either a pulse can be deliberately chirped at launch to correct the dispersion (Optical Phase Equaliser/Phase conjugate approach). The alternative is to enhance the receiver electronics.

We summarise the discussion above in the following table and compare and contrast the conventional device properties with those of the Photonic Crystals that we will encounter in the next section.

<b>Technology</b>	<b>Dispersion (figure of merit)</b>	<b>Advantages</b>	<b>Disadvantages</b>
<b>Conventional devices</b>			
DCF	-100 ps/nm/km[22]	Incumbent solution (cheap!) Low losses Low PMD, athermal Scalable Free Spectral Range (FSR) with substrate thickness	Non-linear problems
Etalon (Gires Tournois)	$\pm 100\text{ps/nm}$ [15]	Thermal+electrical tunability High power handling [23]	Cascading difficult Reflection geometry High insertion loss
Chirped Fibre Bragg Grating	-800 to -200ps/nm [24] Pair gives $\pm 1000$ ps/nm tunability	No nonlinear effects, Single grating low insertion loss, medium size, thermal tunability. Can compensate entire C or L band.	Expensive Phase Masks [25] Works typically in reflection, requiring circulator. Long device for bandwidth and dispersion
Ring Resonators	$\pm 500\text{ps/nm}$	Tunable	Waveguide birefringence $\rightarrow$ PMD
AWG	$\pm 250\text{ps/nm}$	Many channels	
MZI	500-1000ps/nm $\pm 2000\text{ps/nm}$	Thermooptic tunability	10dB insertion narrowband

Technology	Dispersion (figure of merit)	Advantages	Disadvantages
Electronic	+Forward Error Correction [26] Receiver correction Used with another element (DCF)	Cheap Launch pulse which will compensate itself Complete correction	Only up to 10Gb/s Require DCF Bulky
Pulse shapers (SLM)		Big effective area – low loss –low nonlinearities	Multipath Interference possible need to be below -40dB
HOM fibres	$\pm 378 \times \text{ps/nm/km}$ [27]		
HOM waveguides	$\pm 1.7 \times 10^4 \times 10^7 \text{ ps/nm/km}$ [9]	Monolithic Integration	Excitation of both parts of supermode with correct ratio difficult

## Free Space optics

(used to dispersion compensate laser cavities)

Prism Pair	-5 ps <sup>2</sup> double pass SF10[28]	Tuneable	Bulky
Grating stretcher	-0.5 ps <sup>2</sup> [29]		Narrowband
Double - chirped mirrors		Custom designed for laser system	

## Photonic Crystals

(FOM is scaled for comparison- assuming unrealistic device lengths)

Microcavity	6ps cavity ring down Noda (ring down) [53]		
Line defect	IBM Standing wave ring down over >5ps , pulse propagating at c/1000	Losses [IBM]	
	Gersen [32] simulation		
	$v_g < c/350$ [33]		
Superprism	Kawakami [64]	Interfaces	
	Possibility of MZI and	Bandwidth	
Bends	AWG at small scale		
	[46]		
PC Fibre	-2000ps/nm/km	Mode mismatch to SMF	

Technology	Dispersion (figure of merit)	Advantages	Disadvantages
Extractors	Noda, Chutinan Gratings [34] Wavelength/temporally chirped radiation	Out of plane emission into fibre (micro cavity or lattice) can be wavelength delayed	Difficult to hit designed resonance
CCW	$\pm 8 \times 10^7$ ps/nm/km [35] $10^7$ ps/nm/km [36]		Long lengths require E-beam field stitching
3D Polystyrene	$40\text{ps}^2\text{m}$	Fabricate from a suspension	Disorder of each particle directly affect next lattice site
1D ZnS/SrF <sub>2</sub> multilayer	550fs delay	Angle tuning to shift spectral delay	Disorder of each layer directly affect next “lattice” site
Omniguide	$\pm 5 \times 10^5$ ps/nm/km [37]	Low Loss, No PMD Multiply independent methods of tuning structural hence optical response	Small Bandwidth at each operating point

**Table 1-1 The conventional elements used in dispersion compensation, along with the temporal/spatial dispersion properties of PhCs**

## 1.5 Photonic Crystals

So where have Photonic Crystals made their mark and what can they be expected to yield for dispersion compensation? Following the discussion regarding integration above, the demonstration in 1996 of 2D Planar Photonic Crystals (PhC) etched into an AlGaAs heterostructure waveguide [38] has opened up a wealth of opportunities for controlling the dispersion of light. A full characterisation of these 2D hexagonal lattices of air holes, using an internal light source technique [39], exhibits the properties of the PhC lattices, point defects and line defects. The behaviour of these 2D PhCs is strongly dependent upon the waveguide into which they are etched. The allowed states in which light can propagate through the PhC lattice can be classified as either guided modes [40] or guided resonances [41]. The guided modes are Bloch waves that are truly lossless within the periodic lattice. The guided resonances are akin to leaky modes in waveguides, but it is the periodicity of the PhC which folds a

component of the mode above the cladding light line and hence these modes decay as they propagate.

Conventional interest in DFB structures is for the narrowband filtering effect, observed when waves propagate perpendicular to the grating. The effects of off-axis propagation and stronger refractive index contrast (which couples more waves more strongly) in 1D and 2D gratings had tended to be ignored. The rather beautiful patterns of light scattered from such guided resonances in a weakly periodic system were first studied by Russell [42] and Zengerle [43]. They observed beam steering effects, beam focussing effects and interference between the Bloch modes. Real interest in the rich physics of these structures was not sparked until 1987 when both Yablonovitch [44] and John [45] proposed the concept of an omni-directional bandgap.

Much stronger refractive index contrast and modern e-beam patterning systems allow tight control over the structure of the PhCs and very intricate passive circuits are being constructed which rely on a number of PhC effects [46]; namely point defect cavities, line defect waveguides [47] and tight waveguide bends. The properties of these structures are keenly dependent upon the loss from the structure [48], [49], and measurements of loss have become a vital issue for the community. In brief the multiple reflections that waves undergo in such highly scattering PhCs mean that any loss has a detrimental affect upon the desired constructive or destructive interference of forwards and backwards travelling waves.

Conventional dispersion compensation works on one of two principles:

- i) propagation in a waveguide exhibiting chromatic dispersion (DCF, HOM, FBG)
- ii) spectrally resolving the separate frequency components and allowing them to propagate along different path lengths before recombining (prism, grating, AWG, MMI, etalon)

The first approach is exclusively waveguide based, and requires a length of dispersive waveguide in which to propagate. The advantage of the periodic structure is that the different spectral components can be made to transit the waveguide at vastly different  $v_{gs}$ , and with both positive and negative sign. PhCs which exhibit strong waveguide

dispersion have been demonstrated by Notomi [50]. This strong dispersion has been verified in both the frequency and time domain. In the spectral measurement the facets of the device reflect and the group index,  $N_g$ , is calculated from the fringe spacing of the resulting Fabry-Perot cavity [51]. For the length=88a devices measured, a value of  $N_g \approx 90$  was determined. Using a 3GHz modulated temporal signal, waveguides of length 0.76mm (W0.65) and 1mm (W1) were measured, and group delays in the range 20-200ps were recovered corresponding to  $N_g = 10-60$ . W refers to the width of a waveguide, where W1 is one missing row of holes. Lengths of straight PhC waveguides which transmit >3dB of inserted light have since reached 4mm (a loss of 0.67dB/mm) [52], this has been a significant lithographic challenge.

The temporal properties of PhC waveguides and microcavities have been studied in [53]. A passive mode-locked fibre laser producing 0.6-3ps pulses at a 50kHz repetition rate was used to make time of flight measurements of W1 waveguides. Again the multiple round trips due to reflections from the PhC facets cause multiple pulses to exit from the sample. By extending the autocorrelation delay the time (e.g.  $t=17\text{ps}$ ,  $L=250\mu\text{m}$ ) between these multiple pulses can be found and a group index calculated,  $N_g = c\Delta t/2L = 10$ . This technique is limited by the dispersive broadening of the pulses, which serves to reduce the intensity of the sub-pulses beneath the non-linear signal level required for autocorrelation. Similar measurements were reported by Chai for PhC + coupling waveguides [54]. Hybrid combinations of line defects and microcavities allow extremely dispersive waveguides to be formed. Combined with the routing properties of these systems which allow the 2D plane of the wafer to be utilised, very compact systems can be conceived. As in FBGs, by chirping the period of the structure, one can operate at constant delay over a wide bandwidth. The principle is reversed, however, as FBGs work in reflection whereas the proposal, by Baba [33], works in transmission, in a 2D FDTD model. Two waveguides with opposite dispersion are used form a composite device, to obtain a pulse which is delayed at  $N_g=350$ , over a 1mm sample amounting to a 1ns delay.

The first measurements of pulse compression in 3D photonic crystals were made in 1999 by Imhof [55]. Samples of length 0.4mm were fabricated from a suspension of polystyrene spheres, of diameter 222nm. At the edges of the transmission bands

group indices as high as  $N_g=1.25$  are reported. The group velocity dispersion was measured from the pulse duration and found to be of the order  $\pm 40\text{ps}^2/\text{m}$ . In 1D multilayer samples [56], consisting 15 pairs of ZnS/SrF<sub>2</sub> layers ( $n=2.29/1.46$ ) the duration of chirped pulses were measured. As the incident angle is increased the pulse duration compressed by 20% for positively chirped input pulses and dilated for negatively chirped pulses by approximately 15%.

Pulse propagation measurements in 2D PhCs have often been limited to time-of-flight studies due to the low coupling efficiency and poor transmission properties. Time-of-flight measurements were made in the visible and near infrared (450-900nm) for  $\sim 10\mu\text{m}$  PhC lattices etched into 1cm long Si<sub>3</sub>N<sub>4</sub>/ SiO<sub>2</sub> waveguides, by using a femtosecond white light continuum and a SFL6 glass Kerr shutter (resolution 250fs) [57]. The group velocities of the fundamental and higher modes were measured across this large wavelength range. The fundamental TE and TM modes both exhibited a band gap, but no evidence of strong dispersion was apparent at the band edges. Higher index contrast PhC structures were studied by Rahn et al. [58] using 120fs pulses, the spectra of pulses propagating at the upper band edge were recorded. Spectral narrowing was observed due to a combination of linear and Two Photon Absorption and self phase modulation in the access waveguides and the filtering effect of the PhC. This highlights the need to be wary of higher powers and low repetition rate sources in exciting non-linearities. The losses of similar samples were characterised using 200fs pulses by observing the relative intensities of the multiple reflections caused by the waveguide facets and the waveguide-PhC interface [59]. The delay of pulses propagating inside and out with the band gap was measured using a cross-correlation geometry and an (Second Harmonic Generation) frequency up-conversion technique. The experiment was extended [60] to include both heterostructure based PhCs and membranes. Group velocities ranging from 0.17c in the middle of a transmission band to only 0.03c at the band edge were observed. Pulse broadening occurred due to spectral filtering by the PhC.

Microcavities can be used to delay pulses exactly analogously to their larger cousins, etalons. In many of the perceived applications of microcavities the ratio of Quality factor to volume is important, for the interaction with active materials. Values of

$Q=45,000$  and  $V=7\times10^{-14}\text{cm}^3=0.8(\lambda/n)^3$  are reported in [61]. Larger Qs in similar volumes are becoming more frequent as cavity design is better understood [62], and presently an experimental record of 600,000 has been reported [63]. These high Qs also have applications in integrated add-drop multiplexing. For dispersion applications controlling the cavity Q and having a tunable centre wavelength leads to the ability to synthesise a desired dispersion curve. With the small scale of PhCs one could envisage a collection of many cavities being used to control higher orders of dispersion.

Spatially dispersive PhCs have been reported which have strong spectral resolving power [64]. In the second approach following the spatial dispersion of the components a free propagation region is utilised to yield a path length delay. This region does not lend itself to large scale integration, as ideally it would be a large as possible. The application of a temporally dispersive waveguide in this region could dramatically increase the achievable group length in a short length. Again hybrid devices may prove to yield the most elegant solutions.

Remarkably structures with higher order symmetries such as Penrose lattices have been demonstrated to exhibit a bandgap [65]. The picture below (see Figure 1.5) shows the optical diffraction pattern from such a quasicrystal structure. Nonlinear materials such as Lithium Niobate can be poled with a hexagonal lattice pattern and quasi-phase matched non-linear processes result in a beautiful spatially dependent, high efficiency multiple wavelength output [66].

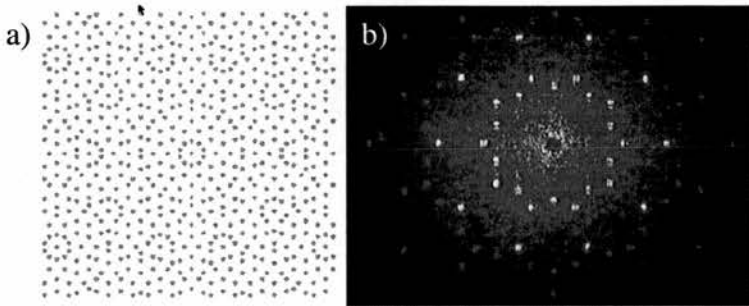


**Figure 1.5 a)** Photonic crystal quasicrystal designed as a Diffractive Optic Element. **b)** The quasicrystal illuminated with a HeNe laser and imaged in a 4f system to filter the central non-diffracting spot. Multiple spatial diffraction orders can be observed. Samples fabricated by Abbes Tahraoui.

Outwith the optics community Photonic Crystals are being brought to market in areas such as gas sensing [67]. The emissivity of a surface can be controlled by wavelength scale structures etched into its surface.

Photonic crystals have the advantage of size, allowing very high density integration of optical components. They are naturally suited to high dielectric contrast (semiconductor) materials allowing access to a wide range of fast switching mechanisms, for tunability. Although they exhibit strong polarisation response, applications for integrated dispersion compensators often require a device positioned at the output of a polarised source. The long temporal delays and the low losses achieved indicate a bright future for application of dispersive elements if fabrication can be controlled adequately. The strong contrast and small scale do present challenges for manufacture, as the tolerance to small imperfections is not well understood.

### 1.5.1 Photonic Crystal Fibres

For completeness we should also mention the excellent work on photonic crystal fibres, pioneered at the University of Bath by Russell and co-workers. The dispersion compensating properties of photonic crystal fibres are also very favourable. Values of  $D=-2000\text{ps/nm/km}$  are readily achieved [68]. These fibres suffer from mode mismatch to conventional Single Mode Fibre, but it is anticipated that this will not limit their application for long. The application of these fibres to nonlinear applications such as supercontinuum and soliton generation is very promising [69]. Endlessly single mode fibres have also been developed which allow very broadband use of waveguides.

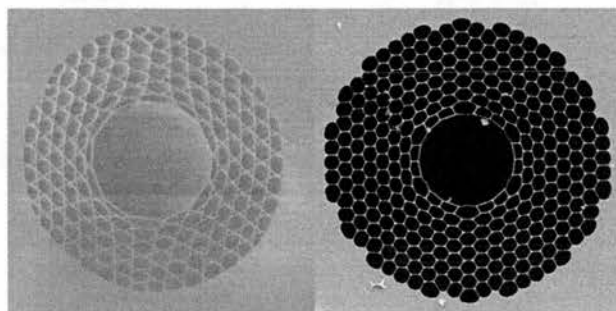


Figure 1.6 Photonic Crystal fibres with a hollow core

## **1.6 Outline**

We now give a brief overview of the structure of the Thesis. In Chapter 2 we will look at temporally dispersive 1D structures. We will take advantage of the scalar nature of the problem to introduce the basic concepts and the modelling tools that we will use to design and verify the properties of PhCs. We will investigate some simple 1D Coupled Cavity Waveguides and use this to test our models. In Chapter 3 we will look at the optical properties of 2D PhC Coupled Cavity Waveguides, these consist of chains of microresonators. We will introduce the basic fabrication techniques which we use to etch these 2D PhCs into GaAs heterostructure waveguides. In order to model the dispersion of the waveguides we will make a 2D approximation. We will then outline a pulse propagation experiment, which we will use to verify the high dispersion at the band edge of these PhC waveguides. The pulse lengths considered here are much longer than the dispersive structure, so we can treat the interaction as a scattering event. We find that it is then necessary to consider the full 3D system to account for the waveguide losses. In Chapter 4 we will concentrate on line defect waveguides and attempt to minimise the optical loss from the structures. We will study two different techniques used to characterise the dispersion with similar high quality pulsed laser sources. In the first technique we find that by avoiding non-linear materials it is possible to autocorrelate the pulses transmitted through AlGaAs PhC waveguides. The second technique allows us direct access to the fields of optical pulses travelling inside the Silicon-On-Insulator PhC waveguides. We show a number of beautiful and interesting effects such as; the folding of the Bloch harmonics excited within the waveguide, components of the pulse which move backwards although the pulse propagates forwards in space, a standing wave pattern excited in an open waveguide which dwells for longer than 5ps. Combined with 2D and 3D modelling and CW measurements we show how the modal dispersion of the waveguides evolves. The pulses here are of similar length to the dispersive structures. In the final experimental section, Chapter 5, we report on some of the spatially dispersive structures that we have analysed. We report on a PhC superprism with a strong angular beam deflection for a small change in incident wavelength. The properties of waveguide bends and splitters are then briefly reviewed. In Chapter 6 we summarise the main results and draw some conclusions from this work.

- 
- 1 R.E. Slusher, Lucent, "Photonic Bandgaps Who Needs Em?", presentation at "Two Dimensional Photonic Crystals" workshop, Monte Verita Ascona, Switzerland, (2002)
- 2 R. März, Infineon Technologies Corporate Research, "Integrated Optics: Status and Trends", presentation at "Two Dimensional Photonic Crystals" workshop, Monte Verita Ascona, Switzerland, (2002)
- 3 A.M. Zheltikov presentation at "Two Dimensional Photonic Crystals" workshop, Monte Verita Ascona, Switzerland, (2002); A.M. Zheltikov, "Propagation of short light pulses in photonic bandgap structures", in "Ultrafast Photonics", proceedings of SUSSP 56, IOP Publishing, (2004);
- 4 G.P. Agrawal, "Nonlinear Fibre Optics", 3<sup>rd</sup> edition, Academic Press, (2001)
- 5 W. Stewart "Photonic Bandgaps And How They Can Help", presentation at "Two Dimensional Photonic Crystals" workshop, Monte Verita Ascona, Switzerland, (2002)
- 6 Also known as the ripple effect or queuing theory see  
[http://www.highways.gov.uk/news/press\\_releases/m25/2003\\_02\\_28.htm](http://www.highways.gov.uk/news/press_releases/m25/2003_02_28.htm) or  
<http://www.trafficmaster.co.uk/shownews.cfm?num=158>
- 7 "Management of Dispersion and Non-linearities", Dispersion management research at COM, available [http://www.com.dtu.dk/research/systems/research\\_areas/dispersion\\_management.html](http://www.com.dtu.dk/research/systems/research_areas/dispersion_management.html)
- 8 Y. Lee, Appl. Phys. Lett. **73**, pp2715, (1998); Y. Lee, A. Herbele, "Observation of Enhanced Group Velocity Dispersion in Coupled Waveguide Structures", J. Lightwave Technol., **17**, pp1049, (1999)
- 9 U. Peschel, Appl. Phys. Lett., **67**, pp2111, (1995)
- 10 Y. Lee, IEICE Trans. Electron, **E85-C**, pp190, (2002)
- 11 O. Wada, "Femtosecond All-Optical Devices for Ultrafast Communications", talk at Ultrafast Summer School, St Andrews August 2002.
- 12 N.G.R. Broderick, D. Taverner, D.J. Richardson, M. Ibsen, R.I. Laming, "Optical pulse Compression in Fiber Bragg Gratings", Phys. Rev. Lett., **79**, pp4566-9, (1997)
- 13 B.J. Eggleton, G.L. Lenz, R.E. Slusher, N.M. Litchinitser, "Compression of Optical Pulses Spectrally Broadened by Self Phase Modulation with a Fiber Bragg Grating in Transmission", Appl. Opt., **37**, pp7055-61, (1998)
- 14 K. Takiguchi, K. Okamoto, T. Goh, M. Itoh, "Integrated-Optic Dispersion Slope Equalizer for NxSeveral Tens of Gb/s WDM Transmission", J. Lightwave. Technol., **21**, pp2463, (2003)
- 15 C.K. Madsen, "Tunable Dispersion Compensators Based On Optical All Pass Filters", available <http://www.ieee.org/organizations/pubs/newsletters/leos/oct01/madsen.htm>; C.K.Madsen, J.A.Walker, J.E. Ford, K.W. Goosen, T.N. Nielson, G. Lenz, "A Tunable Dispersion Compensating MEMS All pass Filter", IEEE Photonics Technol. Lett. **12**, pp651-3(2000); F-Gires, P. Tournois, C.R. Acad Sci. Paris, **258**, pp6112, (1964)
- 16 K. Suzuki, I. Nakamatsu, T. Shimoda, S. Takaesu, H. Katou, H. Yamazaki, "High performance tunable dispersion compensator module with PLC ring resonators", Networking Research Laboratories, NEC
- 17 S. Shen, A.M. Weiner, Complete Dispersion Compensation for 400fs Pulse Transmission over 100km Fiber Link Using Dispersion Compensating Fiber and Spectral Phase Equalizer", IEEE Photon. Technol. Lett. **11**, pp827-9, (1999)
- 18 J. Kuhl, J. Heppner, "Compression of Femtosecond Optical Pulses with Dielectric Multilayer Interferometers", IEEE J. Quantum Electron., **22**, pp182, (1986)
- 19 K.D. Li, W.H. Knox, N.M. Pearson, "Broadband cubic-phase compensation with resonant Gires-Tournois interferometers", Optics Letters, **14**, pp450, (1989)
- 20 N.G.R. Broderick, P. Millar, D.J. Richardson, J.S. Aitchison, R. De La Rue, T. Krauss, "Spectral features associated with nonlinear pulse compression in Bragg gratings", Opt. Lett., **25**, pp740-2, (2000)
- 21 N. Shaw, W.J. Stewart, J. Heaton, D.R. Wight, "Optical slow-wave resonant modulation in electro-optic GaAs/AlGaAs modulators", Electron. Lett., **35**, pp1557-8, (1999)
- 22 Oplink Communications, Inc, "Tunable 100GHz Channel Spacing Chromatic Dispersion Compensation Module(CDCM)"
- 23 "Power Shaper Fixed Dispersion Etalon Simulator", Product Specification, Avanex 2, [www.avanex.com](http://www.avanex.com)
- 24 M. Guy, Y. Painchaud, "Fibre Bragg Gratings: A versatile approach to Dispersion Compensation", TeraXion Inc, Photonics Spectra, Laurin, pp.96-101 (August 2004)
- 25 Personal visit to COM, DTU, Denmark
- 26 DispersionXX , Applied Micro Circuits Corporation (AMCC)

- 
- 27 S. Ramachandran, "Higher-Order-Mode dispersion Compensation for Broadband Dispersion and Non-linearity Management in Transmission Systems", Bell Labs, OSA; S. Ramachandran, S. Ghalmi, S. Chandrasekhar, I. Ryazansky, M.F. Yan, Dimarcello, W.A. Reed, "Tunable Dispersion Compensators Utilizing Higher Order Mode Fibers IEEE Photon. Technol. Lett., **15**, 727-9, (2003)
- 28 R.L. Fork, O.E. Martinez, J.P. Gordon, "Negative dispersion using pairs of prisms", Opt. Lett., **9**, 150, (1984)
- 29 E.B. Treacy, "Optical Pulse Compression With Diffraction Gratings", IEEE J. Quant. Electron. **QE-5**, pp 454-8, (1969)
- 30 R. Szipöcs, K. Ferencz, C. Spielmann, F. Krausz, "Chirped multilayer coatings for broadband dispersion compensation control in femtosecond lasers", Opt. Lett., **19**, pp201-3, (1994)
- 31 F.X. Kärtner, N. Matuschek, T. Schibli, U. Keller, H.A. Haus, C. Heine, R. Morf, V. Scheuer, m.Tilsch, T. Tschudi, "Design and Fabrication of Double Chirped Mirrors", Opt. Lett., **22**, pp831-3, (1997)
- 32 H. Gersen, T.J. Karle, R.J.P. Engelen, W. Bogaerts, J.P. Korterik, N.F. van Hulst, T.F. Krauss, and L. Kuipers, "Real space observation of ultraslow light in photonic crystal waveguides", Submitted to PRL (2004)
- 33 D. Mori, T. Baba, "Dispersion-controlled optical group delay device by chirped photonic crystal waveguides", Appl. Phys. Lett., **85**, pp 1101-3, (2004)
- 34 D. Taillaert, W. Bogaerts, P. Bienstman, T.F. Krauss, P. Van Daele, I. Moerman, S. Verstuyft, K. De Mesel, R. Baets, "An Out of Plane Grating Coupler for Efficient Butt-Coupling Between Compact Planar Waveguides and Single Mode Fibres", IEEE J. Quant. Electron., **38**, pp949-55, (2002)
- 35 K. Hosomi, T. Katsuyama, "A Dispersion Compensator Using Coupled Defects In A Photonic Crystal", IEEE J. Quant. Electron., **38**, pp825-29, (2002)
- 36 T.J. Karle, Y.J. Chai, C.N. Morgan, I.H. White, T.F. Krauss, "Observation of Pulse Compression in Photonic Crystal Coupled Cavity Waveguides", J. Lightwave. Technol., **22**, pp 514-9, (2004)
- 37 T.D. Engeness, M. Ibenescu, S.G. Johnson, O. Weisberg, M. Skorobogatiy, S. Jacobs, Y. Fink, "Dispersion tailoring and compensation by modal interactions in OmnidGuide fibers", Opt. Express, **11**, pp1175-96, (2003)
- 38 T.F. Krauss, R.M. De La Rue, "Two-Dimensional Photonic Bandgap Structures Operating at Near Infra Red Wavelengths", Nature, **383**, pp699-702, (1996)
- 39 H. Benisty, C. Weisbuch, D. Labillois, M. Rattier, C.J.M. Smith, T.F. Krauss, R.N. De La Rue, R. Houdre, U. Oesterle, C. Jouanin, D. Cassagne, "Optical and Confinement Properties of Two-Dimensional Photonic Crystals", J. Lightwave. Technol., **17**, pp2063-77,(1999)
- 40 S.G. Johnson, S. Fan, P.R.Villeneuve, J.D. Joannopoulos, L.A. Kolodziejski, "Guided modes in photonic crystal slabs", Phys. Rev. B, **60**, pp 5751-8, (1999)s
- 41 S. Fan, J.D. Joannopoulos, "Analysis of Guided Resonances in photonic crystal slabs", Phys. Rev. B, **65**, pp 235112, (2002)
- 42 P.St J. Russell, R. Ulrich, "Elementary and coupled waves in periodic planar waveguides", IEE conf. publ. **227**, pp88-91, (1983)
- 43 R. Zengerle, "Light Propagation in singly and doubly periodic planar waveguides", J. Mod. Opt. **34**, 1589-1617, (1987)
- 44 E. Yablonovitch, "Inhibited Spontaneous Emission in Solid State Physics and Electronics", PRL, **58**, pp2059-62, (1987)
- 45 S. John, "Strong localization of photons in certain disordered dielectric superlattices "Phys. Rev. Lett., **58**, 2486-9 (1987)
- 46 Y. Sugimoto, Y. Tanaka, N. Ikeda, T. Yang, H. Nakamura, K. Asakawa, K. Inoue, T. Maruyama, K. Miyashita, K. Ishida, Y. Watanabe, "Design, fabrication and characterisation of coupling strength controlled directional coupler based on two dimensional photonic crystal slab waveguides", Appl. Phys. Lett., **83**, pp3236-8, (2003)
- 47 S.G. Johnson, P.R.Villeneuve, S. Fan, J.D. Joannopoulos, "Linear waveguides in photonic crystal slabs", Phys. Rev. B., **62**, pp8212-22, (2000)
- 48 L.C.Andreani, M.Agio, "Photonic Mode Dispersion and Intrinsic Diffraction Losses in Photonic Crystal Slabs", presentation at "Two Dimensional Photonic Crystals" workshop, Monte Verita Ascona, Switzerland, (2002)
- 49 W. Kuang, C. Kim, A. Stapleton, W.J. Kim, J.D. O'Brien, "Calculated out-of-plane transmission loss for photonic crystal slab waveguides", Opt. Lett., pp1781-3, **28**,(2003)
- 50 M. Notomi, A. Shinya, S. Mitsugi, E. Kuramochi, and H. -. Ryu, "Waveguides, resonators and their coupled elements in photonic crystal slabs," Opt. Express **12**, 1551-1561 (2004)

- 
- 51 M. Notomi, K. Yamada, A. Shinya, J. Takahashi, C. Takahashi , I. Yokohama, "Extremely large group velocity dispersion of line defect waveguides in PhC slabs", Phys. Rev. Lett., **87**, 253902, (2001)
- 52 Y. Sugimoto, et al, presentation at PECS V, Kyoto Japan, (2004)
- 53 T. Asano, K. Kiyota, D. Kumamoto, B-S. Song, S. Noda "Time domain measurement of picosecond light pulse propagation in a two-dimensional photonic crystal slab waveguide", Appl. Phys. Lett., **84**, 4690-2, (2004)
- 54 T.J. Karle, Y.J. Chai, C.N. Morgan, I.H. White and T.F. Krauss, 'Propagation of picosecond pulses through photonic crystal waveguides at C-band region.' [Conference Paper] Technical Digest, Summaries of paper presented at the IEEE Laser and Electro Optics Society Annual Meeting, ThBB (2002)
- 55 A. Imhof, W. Vos, R. Sprik, A. Lagendijk, "Large dispersive effects near the band edge of photonic crystals", Phys. Rev. Lett., **15**, (1999)
- 56 A.V. Andreev, A.V. Balakin, I.A. Ozdardov, A.I. Shkurinov, P. Massdin, G. Mouret, D. Brucher, Phys. Rev. E., **63**, 016602, (2002)
- 57 M.C. Netti, C.E. Finlayson, J.J. Baumberg, M.D.B. Charlton, M.E. Zoorob, J.S. Wilkinson, G.J. Parker, "Separation of photonic crystal waveguides modes using femtosecond time-of-flight", Appl. Phys. Lett., **81**, pp3927-9, (2002)
- 58 M.D. Rahn, A.M. Fox, M.S. Skolnick, T.F. Krauss, "Propagation of ultrashort nonlinear pulses through two-dimensional AlGaAs high-contrast photonic crystal waveguides", J. Opt. Soc. Am. B, **19**, pp 716-21, (2002)
- 59 N. Kawai, K. Inoue, N. Ikeda, N. Carlsson, Y. Sugimoto, K. Asakawa, S. Yamada, Y. Katayama, "Transmittance and time-of-flight study of  $\text{Al}_x\text{Ga}_{1-x}\text{As}$ -based photonic crystal waveguides", Phys. Rev. Lett., **63**, 153313, (2001)
- 60 K. Inoue, N. Kawai, Y. Sugimoto, N. Carlsson, N. Ikeda, K. Asakawa, "Observation of small group velocity in two-dimensional AlGaAs-based photonic crystal slabs", Phys. Rev. B, **65**, 121308, (2002)
- 61 Y. Akahane, T. Asano, B-S. Song, S. Noda, "High Q photonic nanocavity in a 2D photonic crystal", Nature, **425**, pp944, (2003)
- 62 O. Painter, presentation at "Two Dimensional Photonic Crystals" workshop, Monte Verita Ascona, Switzerland, (2002),  $Q_{\text{vert}}=1.5\times 10^5$ ,  $Q_{\parallel}=3\times 10^5$ ,  $V=0.28(\lambda/n)^3$ ; S.G. Johnson, S. Fan, A. Mekis, J.D. Joannopoulos, "Multipole cancellation mechanism for high Q cavities in absence of a complete photonic band gap", Appl. Phys. Lett., **78**, (2001)
- 63 S. Noda, presentation at University of St Andrews, (2005)
- 64 H. Kosaka, T. Kawashima, A. Tomita, M. Notomi, T. Tamamura, T. Sato, S. Kawakami, "Superprism phenomena in photonic crystals", Phys Rev B, R10096, (1998)
- 65 M.A. Kaliteevski, S. Brand, R.A. Abram, T.F. Krauss, P. Millar, R.M. De La Rue, "Diffraction and transmission of light in low-refractive index Penrose-tiled photonic quasicrystals", J. Phys. Condens. Matter, **13**, 10459-70, (2001)
- 66 N.G.R. Broderick, G.W. Ross, H.L. Offerhaus, D.J. Richardson, D.C. Hanna, "Hexagonally Poled Lithium Niobate: A Two Dimensional Nonlinear Photonic Crystal", Phys. Rev. Lett., **84**, pp4344-8, (2000)
- 67 J.T. Daly, E.A. Johnson, W.A. Stevenson, A.C. Greenwald, J.A. Wollam, "Tuned Infrared Emission From Lithographically defined Silicon Surface Structures", Ion Optics Inc., Mater. Res. Soc. Symp. OO4.7, (1999)
- 68 T.A. Birks, D. Mogilevtsev, J.C. Knight, P.St.J. Russell, "Dispersion Compensation Using Single Material Fibers", IEEE Photonics. Technol. Lett., **11**, pp 674-6, (1999); D. Mogilevtsev, T.A. Birks, P.St.J. Russell "Group velocity dispersion in photonic crystal fibers", Opt. Lett, **23**, 1662-4, (1998)
- 69 J.C. Knight, J. Arriaga, T.A. Birks, A. Ortigosa-Blanch, W.J. Wadsworth, P.St.J. Russell, "Anomalous Dispersion in Photonic Crystal Fiber", IEEE Photonics. Technol. Lett., **12**, pp 807-9, (2000)

## Chapter 2

### 2.1 1D periodic structures

We begin with one-dimensional structures, as a means of introducing the basic concepts, the terminology and the variety of computational methods at our disposal. Initially we look at the basic optical properties of periodic dielectric structures. This leads us to consider infinitely periodic dielectric lattices and to compute and demonstrate the photonic properties of these systems. We will then introduce defects into these periodic lattices to create systems of coupled cavities. To understand the practicalities of interfacing with periodicity, we then look at structures of finite length, which are locally periodic. Three different calculation techniques are discussed in this section, allowing us to take advantage of a simple scalar geometry to explain the strengths and weaknesses of each. We will then give some examples to show how these structures can be used to disperse ultrashort optical pulses.

### 2.2 Maxwell's Equations

The basis for the electromagnetic wave analysis in this report is Maxwell's four equations, relating the time dependent Electric,  $\mathbf{E}$ , and Magnetic,  $\mathbf{H}$ , fields;

$$\nabla \cdot \mathbf{D}(\mathbf{r}, t) = \rho(\mathbf{r}, t) = 0$$

$$\nabla \cdot \mathbf{B}(\mathbf{r}, t) = 0$$

$$\nabla \times \mathbf{H}(\mathbf{r}, t) = \frac{d\mathbf{D}(\mathbf{r}, t)}{dt} + \mathbf{J}(\mathbf{r}, t) = \frac{d\mathbf{D}(\mathbf{r}, t)}{dt}, \quad \{2.1\}$$

$$\nabla \times \mathbf{E}(\mathbf{r}, t) = \frac{d\mathbf{B}(\mathbf{r}, t)}{dt}$$

which reduce to the form on the RHS under the assumptions that;

- 1) we have a source free space, so that free charges,  $\rho$ , and the electric current,  $\mathbf{J}$ , are absent,  $\rho(\mathbf{r}, t) = \mathbf{J}(\mathbf{r}, t) = 0$
- 2) the materials are lossless,  $\epsilon(\mathbf{r})$  is real
- 3) the material response is linear and time invariant
- 4) we do not deal with magnetic materials so the magnetic permeability  $\mu(\mathbf{r})$  is constant  $\sim 1$ ,  $\mu = \mu_0$ .

We may represent  $\mathbf{E}$  and  $\mathbf{H}$  as complex valued fields (this representation is very well explained by Haus [1]), taking only the real part as that with physical significance. These are then written,

$$\begin{aligned}\mathbf{E}(\mathbf{r}, t) &= \mathbf{E}(\mathbf{r})e^{j\omega t} \\ \mathbf{H}(\mathbf{r}, t) &= \mathbf{H}(\mathbf{r})e^{j\omega t},\end{aligned}\quad \{2.2\}$$

factoring out the time dependence {2.1} become,

$$\begin{aligned}\nabla \cdot \epsilon_0 \epsilon(\mathbf{r}) \mathbf{E}(\mathbf{r}) &= 0 \\ \nabla \cdot \mathbf{H}(\mathbf{r}) &= 0 \\ \nabla \times \mathbf{H}(\mathbf{r}) &= j\omega \epsilon_0 \epsilon(\mathbf{r}) \mathbf{E}(\mathbf{r}) \\ \nabla \times \mathbf{E}(\mathbf{r}) &= -j\omega \mu_0 \mathbf{H}(\mathbf{r})\end{aligned}\quad \{2.3\}$$

where we have used the definition of the electric displacement  $\mathbf{D}(\mathbf{r}) = \nabla \cdot \epsilon_0 \epsilon(\mathbf{r}) \mathbf{E}(\mathbf{r})$  and magnetic induction,  $\mathbf{B}(\mathbf{r}) = \mu_0 \mathbf{H}(\mathbf{r})$ .

By substitution of the last two equations of {2.3}, we arrive at the Helmholtz equation [2],

$$\nabla \times \frac{1}{\epsilon(\mathbf{r})} \nabla \times \mathbf{H}(\mathbf{r}) = \left( \frac{\omega}{c} \right)^2 \mathbf{H}(\mathbf{r}), \quad \{2.4\}$$

remembering that,  $c = \frac{1}{\sqrt{\epsilon_0 \mu_0}}$ . Similar equations exist for the other fields,  $\mathbf{E}$  and  $\mathbf{D}$ .

### 2.3 Bragg Stack

A multilayer stack comprising two materials with refractive indices,  $n_1$  and  $n_2$  respectively can form a simple 1D photonic crystal. The special case in which each alternate layer is a quarter wavelength thick is commonly known as a Bragg stack, i.e.

$h_i = \lambda_0 / 4n_i$ , where  $\lambda_0$  is the vacuum wavelength and  $n_i$  is the refractive index of each

layer  $i=1,2$ . The repeat period of the structure is  $a=h_1+h_2$ . Such a structure provides a good starting point for a discussion of dispersion within photonic crystals, as the underlying physics is not shrouded in geometry. In this following study we will choose air ( $n_1=1$ ) and a typical semiconductor ( $n_2=3$ , for near infrared (NIR) and telecommunications wavelengths) as our pair of materials, and restrict the analysis to normal incidence. Over certain frequency ranges the Electromagnetic (EM) field cannot simultaneously satisfy the continuity conditions at the boundaries and

propagate forwards as a travelling wave. The incident field becomes evanescent (suffers an exponential decay) and therefore the transmission tends to zero over a significant spectral range which we refer to as a 1D photonic band gap. An example of a band gap for an N=5 period structure with this layer sequence is plotted in Figure 2.1a. The bandgap deepens for increasing number of periods. Greater complexity arises as we tilt the angle of incidence away from the normal to the layers, as the composite material will then exhibit birefringence due to the boundary conditions imposed at each dielectric interface.

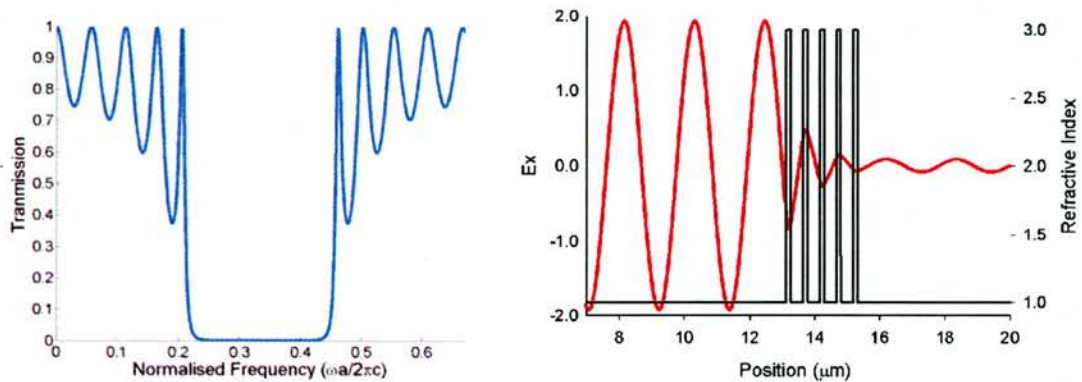


**Figure 2.1 a)** The transmission spectrum of a 5 period Bragg stack, **b)** the electric field tunnelling through the edge of the photonic band gap at ( $u=0.22$ ). Refractive index profile shown inset.

The Electric field,  $E_x$ , is plotted in Figure 2.1b for a normalised frequency ( $u=0.22^\dagger$ ) corresponding to the lower frequency edge of the band gap. Note that the field is incident from the left, the total field to the left of the grating is the sum of incident and reflected fields. The layer structure is plotted inset into the figure.

Such band gaps (or stop bands) have been studied for many years in a wide variety of guises, for example Distributed Feedback Lasers, Thin Film Filters and Fibre Bragg Gratings. Each of these displays a stop band albeit with lower index contrast and consequently narrower bandwidth. The novelty, and hence the renaissance observed, in Photonic Crystals recent years is attributable to i) the fabrication technology maturing to a level permitting the manufacture of high contrast gratings ( $\Delta n > 2$ ) and ii) the concept of a full three dimensional photonic band gap with which radiation over a wide range of frequencies, angles of incidence and polarisations can be controlled.

<sup>†</sup> Normalised Frequency units,  $u=a/\lambda=\omega a/2\pi c$  are used throughout this report as the Helmholtz equation is linearly scalable and so the properties of 1D and 2D structures can be normalised to their periodic length. We will qualify this statement later for 3D structures.

Both Yablonovitch [3] and John [4] proposed an omni-directional bandgap independently in 1987. The term Photonic Crystal (PhC) reflects the periodic nature of many of the candidate materials, which have exhibited such a photonic bandgap (PBG). None of the structures dealt with in this report possess a true PBG, but their geometry reduces the density of other states and the experiments attempt to limit the likelihood of excitation of states not strongly affected by the periodic patterning.

Many analogies can be drawn between the electronic band structure of semiconductor crystals such as Si and GaAs ( $a\sim 5\text{-}6\text{\AA}$ ) and their larger cousins, that are the artificial dielectric structures ( $a\sim 1\mu\text{m}$ ) with their photonic band structure. The similarities (and the dissimilarities) will be highlighted below, indeed the starting point of our analysis will utilise a well-established computation technique from electronic band theory, the plane wave expansion method. Much of the physics of these PhCs is prevalent in the 1D (scalar case) and it makes a great deal of sense to begin in this simple system. The fundamental properties of these gratings can be inferred from an infinitely periodic system, but in practice we will be dealing with PhCs of finite length and we must ensure that our analysis bridges the gap between the two.

Deeply etched 1D structures have been fabricated, but their properties have been far from ideal [5,6], due to significant real world problems such as diffraction and scattering loss, which serve to reduce the transmission and dispersion. For the time being we will forgo the restrictions that these considerations pose.

For an infinite structure the optical properties of these gratings can be formulated as an eigenvalue problem. The field components of an incident wave are bound to a restricted set of eigenvectors corresponding to the eigenvalues, the allowed states. Within a photonic band gap there is an absence of allowed states and hence the propagation of the wave is forbidden.

## **2.4 Transfer Matrix Method (TMM)**

An exact analysis of the Bragg grating above can be performed using a multilayer matrix technique which accounts for the electric,  $\mathbf{E}$ , and magnetic,  $\mathbf{H}$ , fields incident on each of the boundaries of the structure. A very accessible account is given in [7,8] and so we will only deal with the main points here. The mathematics are identical for

solving the 2D ridge waveguides that we deal with later on. Across a single layer the transfer matrix,

$$M_{AB} = \begin{bmatrix} \cos k_0 h & (i \sin k_0 h) / Y_{AB} \\ Y_{AB} i \sin k_0 h & \cos k_0 h \end{bmatrix}, \quad \{2.5\}$$

relates the fields at boundary BC to those at boundary AB.

$$\begin{bmatrix} E_{AB} \\ H_{AB} \end{bmatrix} = M_{AB} \begin{bmatrix} E_{BC} \\ H_{BC} \end{bmatrix}. \quad \{2.6\}$$

$k_0$  is the free space wavevector ( $k_0=2\pi/\lambda$ ) and  $h$  is again the layer thickness. The characteristic admittance  $Y_{AB}$  is defined as,

$$Y_{AB} = \begin{cases} \sqrt{\frac{\epsilon_0}{\mu_0}} n_1 \cos \theta_{iBC} & \text{out of the plane} \\ \sqrt{\frac{\epsilon_0}{\mu_0}} n_1 & \text{respectively} \\ \cos \theta_{iBC} & \text{in the plane of incidence} \end{cases}, \quad \text{for } \mathbf{E} \quad \{2.7\}$$

$\theta$  is the angle of incidence, and while not used in this section, it provides for a novel 2D use of 1D gratings. Propagation of a beam through a 1D stack at off-normal incidence, has been used to demultiplex two wavelengths (separated by  $\lambda_2-\lambda_1=4\text{nm}$ ) of light incident within a beam of  $10\mu\text{m}$  diameter [9].

The behaviour of multiple layers is simply given by the product of their individual transfer matrices.  $M = M_{AB} M_{BC} \dots M_N = \begin{bmatrix} m_{11} & m_{12} \\ m_{21} & m_{22} \end{bmatrix}$ . The reader is directed to

Figure 3.1 in Chapter 3 for the details of the fields. The transmission and reflection coefficients of the multilayer stack of films are then calculated from the matrix elements as,

$$t = |t| e^{i\phi_t} = \frac{2Y_0}{Y_0 m_{11} + Y_0 Y_s m_{12} + m_{21} + Y_s m_{22}} \quad \{2.8\}$$

$$r = |r| e^{i\phi_r} = \frac{Y_0 m_{11} + Y_0 Y_s m_{12} - m_{21} - Y_s m_{22}}{Y_0 m_{11} + Y_0 Y_s m_{12} + m_{21} + Y_s m_{22}}$$

The transmittance,  $T$ , and reflectance,  $R$ , of the film are then calculated by multiplying  $t$  and  $r$  by their respective complex conjugates. Also available to us are

the phases of the transmitted and reflected fields [10,11]; these are calculated from the ratio of the real and imaginary parts of the transmission coefficients

$$\phi_t = \arctan\left(\frac{\text{imag}(t)}{\text{real}(t)}\right), \text{ and similarly for } \phi_r. \quad \{2.9\}$$

The incident (*i*) wave is a cosinusoidal electric field with  $\phi_i = 0$  at the input interface. Plotting T, R,  $\phi_t$ , and  $\phi_r$  for our initial structure over the same spectral range we observe that between each transmission maxima the phase cycles through  $2\pi$ . In the centre of the passbands, the phase increases monotonously with frequency, but at the band edges the phase increases much more rapidly. This effect is mirrored at the opposite band edge, where the initially rapidly varying phase slows with increasing frequency. For comparison a dispersionless material would exhibit a linear increase in phase with frequency in this model.

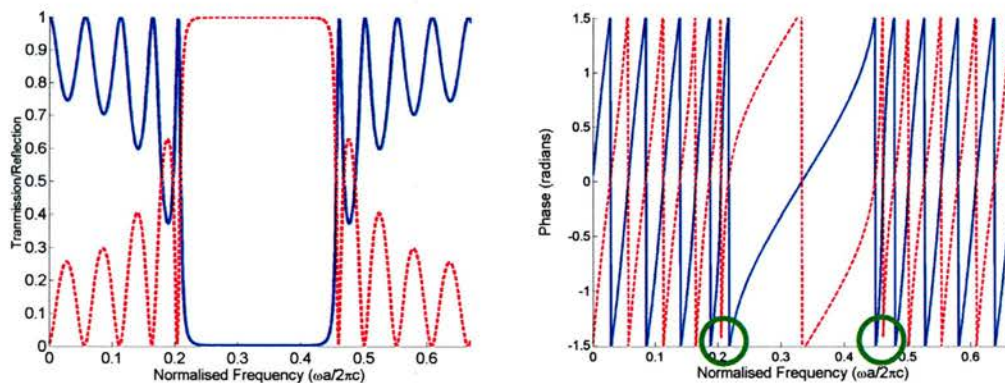


**Figure 2.2 a)** The transmission (solid line) and reflection spectra (dotted line) of the  $N=5$  period Bragg stack, **b)** the transmitted and reflected phases

The additional phase shifts observed at the band edge are analogous to the pulse propagating through an optically longer material. Since the grating is of fixed length, we can only assume that by layering the two materials together we have created a meta-material with an effective index,  $n_{\text{eff}} = n(u)$ .

The optical path length in the grating can be written as

$$\text{path length} = n_{\text{eff}} L, \quad \{2.10\}$$

where  $L = Na$ .

The total phase shift crossing a material with an effective index  $n_{\text{eff}}$  is,

$$\phi_{TOTAL} = \frac{2\pi n_{eff} L}{\lambda} = 2\pi n_{eff} Nu, \quad \{2.11\}$$

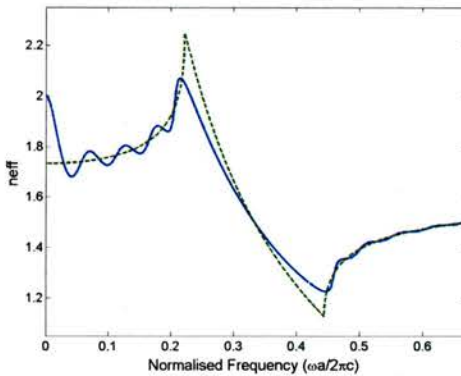
where  $\lambda$  is the free space wavelength, and recalling that  $u = \frac{a}{\lambda}$ . The phase, plotted in

Figure 2.2b, as recovered from equation {2.5} is modulo  $\pi$ . In order to obtain the total phase we must unwrap it. For systems exhibiting high dispersion, high frequency resolution is required to enable this unwrapping. An example of this in the reflected phase curve of Figure 2.2b), where phase excursions below  $-\pi/2$  at either side of the band gap (as marked) are not fully resolved. This is a disadvantage of working in the frequency domain, using frequency as the independent variable; we have limited resolution of fast phase changes.

By differentiating the phase with respect to  $u$ , we can calculate this effective index as,

$$n_{eff} = \frac{1}{2\pi N} \frac{d\phi_{TOTAL}}{du}, \quad \{2.12\}$$

this is plotted in figure 2.3.



**Figure 2.3 Effective index (solid line) calculated from {2.12} and from the Bloch phase (dashed line). This compares a finite periodic structure to an infinitely periodic structure.**

This is the first chance for us to catch our breath and think about the consequences of the dispersion of the periodic structure. Referring back to the discussion, in the previous chapter, on the dispersion required to reshape optical pulses; at the lower band edge, the phase dispersion is anomalous (or normal), whereas at  $u \sim 0.2$  the higher frequency components are slowed with respect to lower frequencies, this causes transform limited pulses to dilate in time. At the upper band edge the situation is reversed and the higher frequencies propagate faster than the lower frequencies.

Pulses having propagated through a fibre or gain medium are often positively chirped (the leading edge is red shifted with respect to the centre frequency). Such a pulse propagating through the above grating at a centre frequency of  $\omega \sim 0.45$  would compress in length by a small amount. As the high transmission ( $T > 0.5$ ) window is spectrally narrow at the edge of the band (see Figure 2.2) in the case above we could only rely on successful compression of a narrowband (long temporal) pulse or only anticipate partial transmission of a compressed pulse and have a large reflected component. Optimising the grating to enhance both transmission bandwidth and increasing the total dispersion for a specific pulse is the key challenge.

If we consider longer and longer grating structures the heuristic limit is of a structure with infinite extent. A wave propagating in this near infinite grating sees an almost negligible effect from the ends of the structure, and to all intents and purposes one period appears exactly the same as the next. Behind the effective index curve, in Figure 2.3, the (unfolded) Bloch index is plotted, and the reader can ascertain that the former follows the trend of the latter. We find that if we increase  $N$  then the effective index curve will tend to the Bloch index curve (the case of  $N = \infty$ ). These terms will be qualified later in the text. To study a system with infinite extent we actually need only look at a single period of the grating (a unit cell). The dielectric profile in one period is equal to that in the neighbouring period, or mathematically

$$\varepsilon(r) = \varepsilon(r + a). \quad \{2.13\}$$

The fields in one period should mimic those in the next, albeit for a phase term,

$$\begin{bmatrix} E_I \\ H_I \end{bmatrix} = e^{iK_a} \begin{bmatrix} E_{II} \\ H_{II} \end{bmatrix} \quad \{2.14\}$$

We have conveniently retained the matrix notation as this applies equally to **E** and **H** fields. Referring to equation {2.6} this forms an eigenvalue equation,

$$M \begin{bmatrix} E_I \\ H_I \end{bmatrix} = e^{-iK_a} \begin{bmatrix} E_I \\ H_I \end{bmatrix}, \quad \{2.15\}$$

relating the fields at the entrance side of the unit cell to those at the exit side [12,13].

This is convenient because, having set the previous calculation up with judicious forethought, utilising this unit cell, we have already calculated this matrix **M**. It follows that the Bloch wavevector **K** (where the Bloch phase is  $Ka$ ), is given by,

$$K(u) = \frac{1}{a} \cos^{-1} \left[ \frac{1}{2} (m_{11} + m_{22}) \right] \quad \{2.16\}$$

or in normalised units

$$K(u) = \frac{1}{2\pi} \cos^{-1} \left[ \frac{1}{2} (m_{11} + m_{22}) \right] \quad \{2.17\}.$$

The real and imaginary parts of this function are displayed (again for the N=5 period grating) in Figure 2.4. The real part is seen to curve distinctly at the band edges and the wavevector becomes purely evanescent in the band gap. The complex wavevector amplifies the reflected wave at the expense of the transmitted wave which is attenuated. The sum of transmittance and reflectance, T+R=1, maintains conservation of energy.

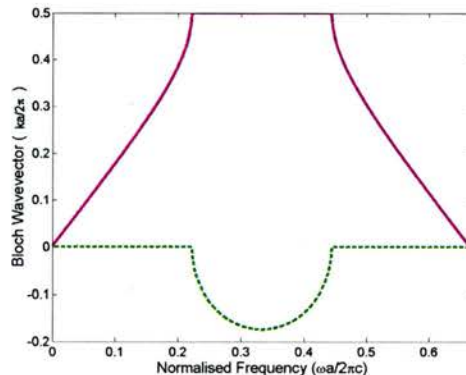


**Figure 2.4** Bloch wavevector calculated from {2.12} where the real part denotes allowed states (solid line) and the imaginary part denotes evanescent, decaying states (dashed line)

The above bandstructure (or wavevector) diagram is rotated through 90° from the conventional  $\omega$ - $k$  plot. This is simply to allow the reader to compare the agreement between the positions of the bands and the transmission curves used above (we will adopt the conventional orientation for the rest of the report). The abscissa is frequency (albeit normalised), which is constant in all media. The ordinate, the wavevector  $k$  is the inverse spatial length of the wave ( $\times 2\pi$ ), i.e.  $k = \frac{2\pi}{\lambda} = \frac{2\pi n}{\lambda_0}$ ,

which is scaled by the refractive index,  $n$ , of the material in which the wave is propagating. Again we normalise to a convenient length scale. The  $\omega$ - $k$  diagram does require a little thought, but is nothing more than a plot of the frequency versus the inverse length of the wave.

As an interesting, but highly relevant aside; regarding active devices, this technique has the ability to treat problems where the wavevector is complex. Other band-solving techniques where  $k$  is the independent variable and  $\omega$  is the dependent variable often struggle to cope.

At the end of this section we will use the results of a transfer matrix calculation to simulate the propagation of pulses through various 1D grating structures. We will return to a matrix formulation (although a scattering matrix) in Chapter 3, in the form of an eigenmode expansion calculation, where we adopt a similar approach to calculate the optical properties of the 2D photonic crystal waveguides.

## 2.5 Semi-Analytical Equations for 1D structures

The TMM can be used to study the entire multilayer structure or simply a single unit cell of arbitrary profile. In the latter case a complicated profile can be constructed as a stack of many small elements, of differing thickness and index profile. The resurgence in recent years of periodic structures has led to the (re)discovery of a semi-analytic method for determining the transmission features of the photonic crystal entire from the Bloch phase and the transmission coefficient of the unit cell. The derivation is fairly straightforward, making use of time-reverse symmetry, parity and energy conservation [14,15]. In essence we re-derive the straightforward result from above but the consequence is an expression which we can use to quickly and efficiently search for structures with the properties that we desired above. In this instance we begin with the Helmholtz equation {2.4} for a field,  $a$ ,

$$\frac{d^2a_k(x)}{dx^2} + \left(\frac{\omega}{c}\right)^2 n^2(x)a_k(x) = 0 \quad \{2.18\}$$

The solutions to this equation are forward and backward travelling waves,

$$\begin{pmatrix} u^+(x) \\ u^-(x) \end{pmatrix} = \begin{pmatrix} f^+(x)e^{+ikx} \\ f^-(x)e^{-ikx} \end{pmatrix} \quad \{2.19\}$$

We have the boundary condition,

$$\begin{pmatrix} 1 \\ r \end{pmatrix} = \begin{pmatrix} A & B \\ C & D \end{pmatrix} \begin{pmatrix} t \\ 0 \end{pmatrix} = M \begin{pmatrix} t \\ 0 \end{pmatrix} \quad \{2.20\}$$

and imposing the restriction of time reversal,  $\hat{\tau}$ , which is simply complex conjugation  $\hat{\tau}(E) = E^*$ , we obtain the (reflected wave)<sup>\*</sup> as the new incident wave.

$$\begin{pmatrix} r^* \\ 1 \end{pmatrix} = \begin{pmatrix} A & B \\ C & D \end{pmatrix} \begin{pmatrix} 0 \\ t^* \end{pmatrix} \quad \{2.21\}$$

so for the linear, real system the matrix is in general,

$$M = \begin{pmatrix} 1/t & r^*/t^* \\ r/t & 1/t^* \end{pmatrix} \quad \{2.22\}$$

Energy conservation can be checked very simply for these matrices, as

$$T + R = |t|^2 + |r|^2 = 1. \quad \{2.23\}$$

The matrix is unimodular as its determinant,  $\det|M| = 1$ .

The eigenvalue problem from above {2.15} is recast as

$$\mu^2 - 2\mu \operatorname{Re}\{1/t\} + 1 = 0, \quad \{2.24\}$$

and the eigenvector equation as,

$$\mu^\pm_B u_B = e^{\pm i K a} u_B \quad \{2.25\}$$

If we substitute the eigenvalues from {2.25} into {2.24} and equate real and imaginary parts, the Bloch phase can now be found from,

$$\operatorname{Re}\{1/t\} = \cos K a, \quad \{2.26\}$$

which is equivalent to {2.16}.

Inserting the matrix M into {2.24},

$$\hat{M}^2 - 2\hat{M} \cos K a + \hat{I} = 0 \quad \{2.27\}$$

and by induction it can be shown that,

$$\hat{M}^N - \hat{M} \frac{\sin N K a}{\sin K a} + \hat{I} \frac{\sin(N-1) K a}{\sin K a} = 0. \quad \{2.28\}$$

Using a modified equation {2.22}

$$M = \begin{pmatrix} 1/t_N & r_N^*/t_N^* \\ r_N/t_N & 1/t_N^* \end{pmatrix},$$

the transmission of an N layer system, can be determined from the single layer transmission spectrum T(u),

$$\frac{1}{T^N} = 1 + \frac{\sin^2 N K a}{\sin^2 K a} \left[ \frac{1}{T} - 1 \right]. \quad \{2.29\}$$

Moreover, highly relevant for this work, the group velocity,  $v_g = \frac{d\omega}{dk}$ , can also be

determined as

$$v_g = Na \frac{\cos^2 NKa + \eta^2 \frac{\sin^2 NKa}{\sin^2 Ka}}{\frac{1}{2} \frac{\sin 2 NKa}{\sin Ka} \left[ \eta' + \frac{\eta \xi \xi'}{(1 - \xi^2)} \right] - \frac{N \eta \xi'}{(1 - \xi^2)}} \quad \{2.30\}$$

The coefficients  $\xi = x/T$  and  $\eta = y/T$  are the real and imaginary parts of  $T$  as a fraction of the unit cell transmittance,  $T$ , along with their derivatives  $\eta'$  and  $\xi'$ .

The details of the derivation can be found in [14]. Essentially we can replace the loops in our matrix code which multiply successive matrices together with this pair of equations {2.29 and 2.30}. To calculate the group velocity in this one dimensional periodic system we need only obtain the transmission and Bloch phase spectra of the unit cell. These useful results can be applied to the physics of many other periodic media, in mechanics, acoustics and electromagnetics [16].

We have taken a brief journey through the basic properties of 1D grating structures. As we move into 2D in later chapters we will struggle to make use of simple techniques to calculate the properties of these more complex gratings. Transfer matrices have been applied very successfully, but the formulation of the problem increases vastly in complexity. The computational overheads of the TMM remain however more manageable than the Plane Wave Expansion method discussed below. The reader is encouraged to consult [17, 18, 19, 20] for more insight.

Realising that the fundamental behaviour of a grating is governed by the physics of a single unit cell provides a real motivation to examine other methods which deal exclusively with infinite cases. A successful approach, adopted from electronic band-structure calculations involves consideration of the interaction between the structure and a discrete spectrum of geometrically relevant plane waves. This is best achieved if we work in inverse space, or  $k$ -space. The periodic boundary condition is now contained in the vector  $\mathbf{k}$ . We remain in frequency space, but now take  $k$  as the independent variable rather than  $\omega$ .

## 2.6 Plane Wave Expansion Method

The basic principles of the plane wave expansion (PWE) method are outlined below. PWE is based upon the Fourier expansion of the electromagnetic field and the dielectric function. The mathematical description is augmented with a guide to computation as the method is relatively straightforward, though the notation disguises this. The extension of this method to study two and three dimensional structures is also simple if computationally expensive. The convergence of the method is investigated and discussed relative to other methods. Two dimensional structures are evaluated in the following chapters using a highly optimised algorithm which has been made freely available on the internet [21]. This has been shown to demonstrate superior convergence performance to the codes discussed here, which are based on the work of Guo[22].

The significance of the "plane-wave" is that the fields  $\mathbf{H}$  and  $\mathbf{D}$  are now constructed as a sum of transverse plane waves, defined such that each plane wave is perpendicular to its k-vector i.e.  $\mathbf{k} \cdot \mathbf{H} = 0$ ,  $\mathbf{k} \cdot \mathbf{D} = 0$ . Enforcing these divergence equations, i.e. a requirement for transversality allows us to consider only the two curl equations. Decoupling the fields  $\mathbf{E}$  and  $\mathbf{H}$  yields the Helmholtz equation {2.4}. Equation {2.4} is a standard eigenvalue problem, however, had we attempted to formulate the problem in terms of  $\mathbf{E}$  and not  $\mathbf{H}$ , we would obtain either a generalised eigenvalue problem or break the transversality requirement [23]. Once  $\mathbf{H}$  is known the  $\mathbf{E}$  field can be found using {2.3}.

We mentioned the scaling properties of the Helmholtz equation {2.4} at the start of the chapter. Here it is possible to see that if we were to scale the length,  $\mathbf{r}$ , by a factor  $x$ , to give  $\mathbf{r}' = x\mathbf{r}$  and  $\nabla' = \frac{\nabla}{x}$  the result would be,

$$\nabla' \times \frac{1}{\epsilon'(\mathbf{r}')} \nabla' \times \mathbf{H}(\mathbf{r}'/x) = \left( \frac{\omega}{cx} \right)^2 \mathbf{H}(\mathbf{r}'/x) \quad \{2.31\}$$

the mode profiles and frequencies are linearly scaled.

We continue to use the magnetic field here. The spatial dependence of the magnetic field is now considered to be periodic. In accordance with Bloch's Theorem (see Appendix A), a plane wave in a periodic structure acquires a modulation,

$$\mathbf{H}(\mathbf{r}) = e^{j\mathbf{k}\cdot\mathbf{r}} h(\mathbf{r}) \hat{\mathbf{e}}_{\mathbf{k}} \quad \{2.32\}$$

where  $h(\mathbf{r}) = h(\mathbf{r} + \mathbf{a})$ .

The components differ between successive lattice periods by only a phase term. For the present we will keep the full 3D representation.  $\mathbf{a}_l = l_1 \mathbf{a}_1 + l_2 \mathbf{a}_2 + l_3 \mathbf{a}_3$  is an arbitrary lattice vector,  $\mathbf{G}_h = h_1 \mathbf{b}_1 + h_2 \mathbf{b}_2 + h_3 \mathbf{b}_3$  is an arbitrary reciprocal lattice vector ( $l$  and  $h$  are integers),  $\hat{\mathbf{e}}_{\mathbf{k}}$  is a unit vector perpendicular to  $\mathbf{k}$  and parallel to  $\mathbf{H}$ . The reciprocal lattice vectors are orthogonal to the primitive lattice vectors, which is expressed mathematically as,  $\mathbf{a}_i \cdot \mathbf{b}_j = 2\pi \delta_{ij}$ . Where  $\delta_{ij}$  is the Kronecker delta function. The reciprocal lattice vectors are given by  $\mathbf{b}_1 = \frac{2\pi}{V} (\mathbf{a}_2 \times \mathbf{a}_3)$ ,  $\mathbf{b}_2 = \frac{2\pi}{V} (\mathbf{a}_3 \times \mathbf{a}_1)$ , and  $\mathbf{b}_3 = \frac{2\pi}{V} (\mathbf{a}_1 \times \mathbf{a}_2)$ , where  $V = \mathbf{a}_1 \cdot (\mathbf{a}_2 \times \mathbf{a}_3)$ , the volume of the unit cell (alternatively length or area in 1D and 2D). Note the cyclic permutations.

In the present analysis the dielectric is real, isotropic, perfectly periodic and independent of frequency,  $\omega$ . In reality the dielectric is complex, suffers from roughness and is dispersive, but we will not let that spoil the simplification. Across the telecommunications window of the IR spectrum many of the materials that we will deal with do satisfy this approximately. This allows us to expand the dielectric function as a Fourier series,

$$\varepsilon^{-1}(\mathbf{r}) = \frac{1}{\varepsilon(\mathbf{r})} = \sum_{G_i} \varepsilon(G_i) e^{jG_i \cdot \mathbf{r}} \quad \{2.33\}$$

and then also the magnetic field,

$$\mathbf{H}(\mathbf{r}) = \hat{\mathbf{e}}_{\mathbf{k}} e^{j\mathbf{k} \cdot \mathbf{r}} \sum_{G_i} \mathbf{H}(G_i) e^{jG_i \cdot \mathbf{r}} = \sum_{G_i} \mathbf{H}(G_i, \lambda) e^{j(\mathbf{k} + \mathbf{G}_i) \cdot \mathbf{r}} \hat{\mathbf{e}}_{\lambda, \mathbf{k} + \mathbf{G}_i} \quad \{2.34\}$$

This method only includes those unit vectors  $\perp$  to  $\mathbf{k} + \mathbf{G}_i$  and thus enforces the transversality requirement for the magnetic field,  $\nabla \cdot \mathbf{H}(\mathbf{r}) = 0$  {2.3}.

The magnetic field operator  $\nabla \times \frac{1}{\epsilon(\mathbf{r})} \nabla \times$  is linear and so  $\mathbf{H}(G)$  can be constructed by a

linear combination of two orthogonal vectors,  $\hat{\mathbf{e}}_1$  and  $\hat{\mathbf{e}}_2$ . The Hermitian property of the operator provides us with real eigenvalues and orthogonal eigenvectors.

Substituting equations {2.20} and {2.21} into {2.17} we obtain,

$$\sum_G |k+G| |k+G| \epsilon^{-1}(G-G') \begin{bmatrix} \hat{\mathbf{e}}_2 \hat{\mathbf{e}}_2' & -\hat{\mathbf{e}}_2 \hat{\mathbf{e}}_1' \\ -\hat{\mathbf{e}}_1 \hat{\mathbf{e}}_2' & \hat{\mathbf{e}}_1 \hat{\mathbf{e}}_1' \end{bmatrix} \begin{bmatrix} h_1' \\ h_2' \end{bmatrix} = \left( \frac{\omega}{c} \right)^2 \begin{bmatrix} h_1 \\ h_2 \end{bmatrix} \quad \{2.35\}$$

this is a standard eigenvalue problem which we can solve numerically. The terms in the sum represent an Hermitian matrix. We can make life a little simpler for ourselves, if we treat structures with inversion symmetry and real index, thereby we will only need to search for real eigenvalues. Symmetry operators commute with the magnetic field operator, making modes which undergo symmetry transforms degenerate.

### 2.6.1 Calculation of 1D Bragg grating

To compute the eigenvalues, which correspond to the allowed frequencies within the periodic structure for a given wavevector, we need to construct the inverse of our periodic lattice. This involves calculating the Fourier components ( $\epsilon^{-1}$ ) of the dielectric profile and the reciprocal lattice vectors once the real space lattice has been determined. The periodic boundary condition is then expressed through the addition of  $\mathbf{k}$  to  $\mathbf{G}$ , the reciprocal lattice vector.

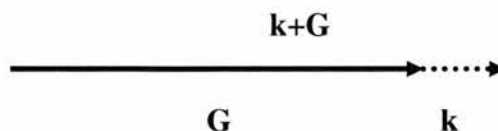


**Figure 2.5 Addition of wavevectors to include periodic boundary condition in 1D**

We only need calculate those  $\mathbf{k}$ -points lying within the 1st Brillouin Zone (1BZ). This is further reduced by symmetry considerations to the Irreducible Brillouin Zone (IBZ). In 1D this corresponds to  $k=0 \rightarrow \pi$ . For higher dimensions, calculation of the values on the edges of the IBZ is enough, in many cases, though states may lie just inside the IBZ.

To compute the PWE bandstructure for our original Bragg stack the real space lattice vector,  $\mathbf{a}$ , becomes,  $\mathbf{b}=2\pi/a$  in reciprocal space. We include a large enough range of  $\mathbf{G}$  (number of plane waves) to ensure convergence, as the truncation of the matrix gives rise to problems which are discussed below. As we work exclusively in reciprocal space it is convenient to directly express the Fourier Transform of the dielectric profile with analytic functions. As we will see the FFT of real space functions adds a certain degree of noise, to the  $\epsilon^{-1}$  profile.

To determine the dielectric profile (for two materials c and d) for use in the PWE in 1D we express the permittivity as

$$\begin{aligned}\epsilon(\mathbf{r}) &= \sum_{\mathbf{G}_r} \epsilon(\mathbf{G}_r) e^{i\mathbf{G}_r \cdot \mathbf{r}} \\ \epsilon(\mathbf{G}_r) &= \frac{1}{\Omega} \int_{\Omega} \epsilon(\mathbf{r}) e^{-i\mathbf{G}_r \cdot \mathbf{r}} d\mathbf{r}\end{aligned}\quad \{2.36\}$$

We wish to have a function of the form, DC + Modulation so writing,

$$\epsilon(\mathbf{r}) = \epsilon_d + (\epsilon_c - \epsilon_d) \sum_{R_p} S(R - |\mathbf{r} - \mathbf{a}|), \quad \{2.37\}$$

and substituting in above gives

$$\epsilon(\mathbf{G}_r) = \frac{1}{\Omega} \int_{\Omega} \epsilon_d e^{-i\mathbf{G}_r \cdot \mathbf{r}} d\mathbf{r} + \frac{1}{\Omega} \int_{\Omega} (\epsilon_c - \epsilon_d) \sum_{R_p} S(R - |\mathbf{r} - \mathbf{a}|) e^{-i\mathbf{G}_r \cdot \mathbf{r}} d\mathbf{r} \quad \{2.38\}$$

The first term in the integral is everywhere zero apart from at  $\mathbf{G}_r=0$

$$\frac{1}{\Omega} \int_{\Omega} \epsilon_d e^{-iG_r r} = \begin{cases} \epsilon_b & \text{if } G_r = 0 \\ 0 & \text{elsewhere} \end{cases} \quad \{2.39\}$$

For the second term in the integral we make a change of variable  $r'=r-a$  and evaluating for a one-dimensional binary grating for  $G_r=0$  is simply ,

$$\frac{1}{\Omega} \int_{\Omega} (\epsilon_c - \epsilon_d) \sum_{R_p} S(R - r') e^{-iG_r r'} dr' = \frac{(\epsilon_c - \epsilon_d)}{\Omega} \int_{-R}^R dr' = ff(\epsilon_c - \epsilon_d) \quad \{2.40\}$$

The sum over a single period has been replaced with an integral over the whole space.

The fillfactor, ff, is the ratio of the length of material c to the Period, a,  $ff = \frac{2R}{a}$ .

For the case  $G_r \neq 0$ ,

$$\frac{(\epsilon_c - \epsilon_d)}{\Omega} \int_R^R e^{-iG_r \cdot r'} dr' = ff(\epsilon_c - \epsilon_d) \text{sinc}(G \cdot r), \quad \{2.41\}$$

where  $\text{sinc } x = \frac{\sin x}{x}$

For all other structures analysed with the PWE in 1D we rely on well gridded real space dielectric profiles which are FFTed into reciprocal space. In 2D for a cylinder, the most common inclusion, the sinc function above is replaced by a Bessel function of the first kind.

This provides the dielectric profile for matrix {2.20}, we then take the product of the inverse of this matrix with the  $(k+G)$  matrices, and solve for the eigenvalues. The periodic boundary condition is introduced by  $k$ , and as its value is swept from  $=-\pi/a$  to  $\pi/a$ , it cycles the reciprocal lattice vector,  $(k+G)$ , through  $2\pi/a$ .

### **2.6.2 Discussion of numerical computation: truncation errors and dielectric representation**

The truncation of any of our computational problems to fit the constraints of processing time and memory requirements, for solution on a modern Personal Computer, introduces numerical error. The size of the matrix increases as the number of terms retained in the expansion to the power of the number of dimensions in the structure. Complete convergence analysis could not be carried out even on a supercomputer [24] (an estimated requirement of 100Gb of working memory is suggested for 35 plane waves in a 3D structure).

The formulation of the problem is therefore critical to the rapid convergence with retention of the minimum number of terms.

The two preferred methods are

- 1) to take the inverse the Fourier Transform of the dielectric function  $\epsilon(r)$
- 2) to Fourier Transform the dielectric function  $\epsilon(r)$  and then invert the matrix [6] (known as Ho's method)

Problems with method (1) are attributed to the slow convergence of the Fourier expansion of the dielectric function [25]. Calculation of  $\epsilon(G)$  analytically rather than

numerically is preferred [25], especially as the sharp step like index profiles of the PhC often involve singularities in the fields. The discrete Fourier Transform can cause rounding errors and requires a fine grid to retain high accuracy. This is known as the Gibb's phenomenon, which often manifests itself as an oscillation in the converging series. This arises via truncation of the higher terms of the Fourier Transform of the step discontinuity (a Bessel function).

Alternatively the dielectric function may be represented by a super-Gaussian function [24] which is a continuous function of  $\mathbf{r}$ . This avoids the singularity and can be considered relatively realistic as many materials exhibit a barrier layer (e.g. an oxide skin on GaAs or Si) so that the desired step function is actually somewhat blurred in practice. Even the best shutter on an evaporator exhibits some degree of lag.

Ho et al. [26] provided an alternative formulation of this problem by substituting the Toeplitz matrix  $[[1/\epsilon]]$  with  $[[\epsilon]]^{-1}$ . This improves the convergence of the technique, but can further be improved upon by a hybrid technique [27], which shows promisingly rapid convergence for a 1D structure.

For completeness in this discussion it is worth noting that for certain 2D/3D geometries with say cylinders or spheres, a spherical wave (or KKR (Koringa-Kohn-Roster)) expansion is more appropriate and exhibits much enhanced convergence. This has been applied to the very uniform spherical atoms of electronic crystals.

## 2.7 FDTD

The Finite Difference Time Domain (FDTD) method solves Maxwell's curl equations rigorously without approximation. There are no restrictions on the materials: dielectric or magnetic that can be included. Maxwell's equations are discretised onto the Yee mesh (see Chapter 3) using central differences in time and space and are solved numerically using an iterative leapfrog algorithm to advance the simulation in time. In addition to inputting the spatial refractive index distribution and the field excitation; the computational domain must be bounded, to fit the simulation into the memory of a computer. The boundary conditions can be perfect conductors,

absorbing or periodic. The mesh's grid size, allows resolution of the smallest features of the field (dependent upon the wavelength in the material). To ensure stability the time step is kept small enough, via a stability condition.

Working in the time domain allows the system response over a wide range of frequencies to be determined simultaneously. The time per frequency point is comparable to that of a frequency domain method, as we move to higher dimensions. Use of sophisticated techniques can compensate for dispersion in FDTD, which eventually limits the high frequency response of the standard algorithm.  $\chi^3$  nonlinearities can be modelled by updating the refractive index distribution in addition to the fields at each time step.

In 1D the benefits of FDTD are not so apparent. The main drawbacks are low speed, high memory consumption and lack of accuracy. In reality the technique will come into its own in 2D where the ability to seamlessly deal with guided, leaky and radiation modes is almost unsurpassed. Its real space and time domain nature give it a very intuitive character. Symmetry boundaries help reduce computation time and can also aid mode classification. Post-processing using numerous Fourier analyses reveals much of the same information as is gained from many of the other techniques. A section on 1D FDTD is included here to familiarise ourselves with the algorithm, develop gridding routines for the dielectric profiles and understand absorbing boundary conditions.

We have from equation {2.1}, reduced to 1D in free space,

$$\begin{aligned}\frac{\partial E}{\partial t} &= -\frac{1}{\epsilon_0} \nabla \times H_y \\ \frac{\partial H}{\partial t} &= \frac{1}{\mu_0} \nabla \times E_x\end{aligned}\quad \{2.42\}$$

The finite central difference approximations to these derivatives are [28,29],

$$\begin{aligned}\frac{E_x^{n+1/2}(p) - E_x^{n-1/2}(p)}{\Delta t} &= -\frac{1}{\epsilon_0} \frac{H_y^n(p+1/2) - H_y^n(p-1/2)}{\Delta z} \text{ and} \\ \frac{H_y^{n+1}(p+1/2) - H_y^n(p+1/2)}{\Delta t} &= -\frac{1}{\mu_0} \frac{E_x^{n+1/2}(p+1) - E_x^{n+1/2}(p)}{\Delta z}\end{aligned}\quad \{2.43\}$$

The p values represent the spatial positions in the grid ( $p\Delta z$ ) and the n values denote the time ( $n\Delta t$ ). The two sets of field components are interleaved on a spatial grid as shown in Figure 2.6, where the distance between neighbouring Ex components is  $\Delta z$ .

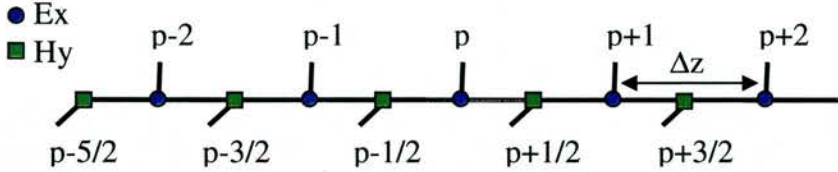


**Figure 2.6 1D FDTD grid showing interleaved Ex and Hy components**

We structure the updating algorithm to be as flexible as possible, including terms representing the local dielectric constant,  $\epsilon$ , magnetic permeability  $\mu$ , conductivity  $\sigma$  and magnetic resistivity  $\rho$ . These are properties specific to the field components that are local to each spatial position allowing us to deal with multiple refractive indices and also utilise advanced absorbing boundary conditions. We then need to retain these terms in the initial equations.

$$\begin{aligned}\frac{\partial E}{\partial t} &= -\frac{1}{\epsilon_r \epsilon_0} \nabla \times H_y - \frac{\sigma}{\epsilon_r} E_x \\ \frac{\partial H}{\partial t} &= \frac{1}{\mu_r \mu_0} \nabla \times E_x - \frac{\rho}{\mu_r} H_y\end{aligned}\quad \{2.44\}$$

$$\text{The } C_c = \begin{pmatrix} 1 - \frac{\sigma \Delta t}{2\epsilon} \\ \frac{\Delta t}{1 + \frac{\sigma \Delta t}{2\epsilon}} \end{pmatrix}, \quad C_d = \begin{pmatrix} \frac{\Delta t}{\epsilon \Delta z} \\ 1 + \frac{\sigma \Delta t}{2\epsilon} \end{pmatrix}, \quad D_c = \begin{pmatrix} 1 - \frac{\rho \Delta t}{2\mu} \\ \frac{\Delta t}{1 + \frac{\rho \Delta t}{2\mu}} \end{pmatrix}, \quad D_d = \begin{pmatrix} \frac{\Delta t}{\mu \Delta z} \\ 1 + \frac{\rho \Delta t}{2\mu} \end{pmatrix}, \quad \{2.45\}$$

Given an initial **E** field condition (at  $E=0$ ,  $t=0$ ), the **H** field is updated (at time  $t=1/2\Delta t$ ) using,

$$H_y^{n+1}(p+1/2) = D_c H_y^n(p+1/2) - D_d (E_x^{n+1/2}(p+1) - E_x^{n+1/2}(p)) \quad \{2.46\}$$

The **E** field (at  $t=\Delta t$ ), is then calculated by the difference of the **H** field,

$$E_x^{n+1/2}(p) = C_c E_x^{n-1/2}(p) - C_d (H_y^n(p+1/2) - H_y^n(p-1/2)) \quad \{2.47\}$$

In the vectorised notation of a higher level programming program such as Matlab, coding the spatial derivative is no more difficult than writing this directly as

```
ex(1:N) = caex(1:N) .* ex(1:N) + ...  
cbex(1:N) .* (hy(2:N+1) - hy(1:N));
```

Otherwise this requires a *for* loop in a lower level language. The reason for preferring Matlab is that even for FDTD in higher dimensions the code just contains this single line (and a single line for the associated **H** field). The time stepping is also accomplished by enclosing these in a *for* loop.

The problem is usually gridded to cater for the centre wavelength of interest, the commonly suggested grid size is  $\Delta z = \lambda/10$ . We use the Courant stability limit, S, to determine the upper stable limit for time step,

$$\Delta t = \frac{1}{c\sqrt{\left(\frac{1}{\Delta x}\right)^2 + \left(\frac{1}{\Delta y}\right)^2 + \left(\frac{1}{\Delta z}\right)^2}}, \text{ (defined here for 3D simulations) } \{2.48\}$$

$$S = \frac{c\Delta t}{\Delta x} \text{ in 1D.}$$

The algorithm is exact in the limit  $\Delta z \rightarrow 0$ ,  $\Delta t \rightarrow 0$  and for  $S=1$  in free space as the phase velocity is equal to c. At other values the grid exhibits worsening dispersion for higher frequencies.

Gridding of rapid index changes is very tricky. In the TMM exact lengths are entered into the matrices, but in FDTD the step profile may not lie neatly on a grid point. Phase errors accumulating from poor gridding can adversely affect the accuracy of the code. There are a number of ways to address this problem, including non-uniform, conformal grids which mould themselves around the structure. In higher dimensions great care needs to be taken to represent the structure. For this 1D analysis a local submesh technique was adopted. The coefficients were calculated over a  $10\times$  finer mesh and then averaged to give better resolution of the structure. The convergence is discussed in a later section.

Very important to this study is the creation of a periodic boundary condition (PBC) in this real space, time domain model. The PBC is simple to implement in the frequency domain, however translating this into a stable algorithm in the time domain is not trivial. We can very simply create a loop, by linking the beginning to the end of the spatial grid, (for instance the  $H(p+N/2)$  component can be updated with the value at  $H(p-N/2)$ ), but this only corresponds to a phase shift of  $\mathbf{k}a=0$ . A stable implementation of

the periodic phase boundary condition involves two fields which are  $\pi/2$  out of phase, which are obtained by calculating [30].

$$\begin{aligned} H_x^{n+1}(p + N/2) &= [H_x^{n+1}(p - N/2) - H_x^{n+1}(p - N/2)] e^{-jka} \\ H_x^{n+1}(p - N/2) &= [H_x^{n+1}(p + N/2) - H_x^{n+1}(p + N/2)] e^{jka}, \end{aligned} \quad \{2.49\}$$

where the period,  $a = N\Delta z$ . These two equations correspond to waves propagating in forward and backward directions. Continuing the formulation in Matlab we can, for convenience, take advantage of the *complex* variable type. Care then needs to be taken to split the PBC into cos and (-)sin terms in this case to avoid confusing the complex terms. This PBC formulation has the disadvantage of needing to calculate the fields twice, which doubles the computational overheads. The **E** field could easily be used as alternative PBC, or a pair of **E** and **H** points.

The periodic structure is analysed by exciting it with a pulse. The field is monitored at several random positions in order to avoid field nodes. At the end of the simulation the temporal response is Fourier Transformed to reveal the resonant frequencies,  $\omega$ .

This is repeated for  $\mathbf{k}$  in the range,  $0 < k < \frac{\pi}{a}$  and the results displayed in an  $\omega$ - $\mathbf{k}$  diagram.

In order to keep the algorithm stable in all cases we build the fields up from zero over a few cycles of the field. This naturally then introduces a wider band spectrum than we perhaps desire if a Continuous Wave (CW) analysis is required. If CW analysis is required the time domain model must be left to ring down to remove the transients. If we concentrate on Gaussian pulses we mitigate this effect. It is important to use a soft source, adding the field to the existing field in a particular cell, as a hard source (imposing the field on the cell) will interact with the back reflections from the grating. To terminate the propagation model it is necessary to implement absorbing boundary conditions (ABC). The most widely used absorber in 1D is the Mur ABC [29]. This requires modification when we deal with a configuration with a dielectric material at the boundary.

It is also possible to implement more advanced boundary conditions to counter the moderate reflections from the Mur conditions. These are Perfectly Matched Layers

(PML), first introduced by Berenger[31], and take advantage of the lack of Fresnel reflection from an interface between two materials when the wave impedances are matched, i.e.

$$R = \frac{Z_A - Z_B}{Z_A + Z_B} = 0, \quad Z_A = Z_B, \quad \{2.50\}$$

where  $Z_i = \sqrt{\frac{\mu}{\epsilon}}$  and  $Z_0 = \sqrt{\frac{\mu_0}{\epsilon_0}}$  is the impedance of free space.

This only prevents a back reflection from the interface, what we also require is for the material to attenuate the forward travelling wave. This is obtained by gradually increasing the conductivity of the material away from the boundary. To maintain the  $R=0$  condition this requires that the magnetic resistivity also be increased according to  $\rho = Z_0^n \sigma$ , where  $n$  is the order of the PML. Finite gridding effects naturally give rise to some small back reflections. Note that in this 1D formulation we do not require a split field approach as is often the case in 3D. These PML layers will come into their own in 2D, where they demonstrate the lowest reported back reflections over a wide range of angles.

These 1D models contain the basic principles behind the models which we will use in later Chapters to study more complicated geometries.

### 2.7.1 Convergence Testing

It is now pertinent to compare the convergence of the two (non-exact) band solvers; the PWE and FDTD. We take the lower and upper band edges, and also the folded point at  $u \sim 0.67$  (see Figure 2.4). The first two lie at the K point ( $k=0.5$ ) and the second at the Gamma point ( $k=0$ ). The FDTD is intrinsically dispersive so we would expect the performance to deteriorate as we increase the frequency. For the PWE we have included the behaviour of both the analytic dielectric profile and the FFT of the profile used in the FDTD.

The results are shown in Figure 2.7. The PWE would seem to be the obvious choice for bandsolving. For an analytically defined dielectric profile the convergence is very rapid for a limited number of plane waves. Inset into graph (d) is the expanded plot over the first 25  $\frac{1}{2}^*$ Plane waves of the analytic model. Here we can still observe a tiny ripple in the eigenfrequencies, these are due to the Gibbs phenomenon. The

flexibility of the real space representation is a major bonus, but nevertheless, it would take some effort to design a supercell technique to adapt to the wide range of structures we may wish to use. As the FFT does seem to converge relatively rapidly, it appears that this could be useful in limited circumstances. The dispersion of the FDTD grid is certainly very evident as graphs (c)-(d) show the line failing to converge, with decreasing  $\Delta z$ . We will, fortunately, not need to stretch the capabilities of the FDTD this much and in the mid gap regime the performance is modestly acceptable.

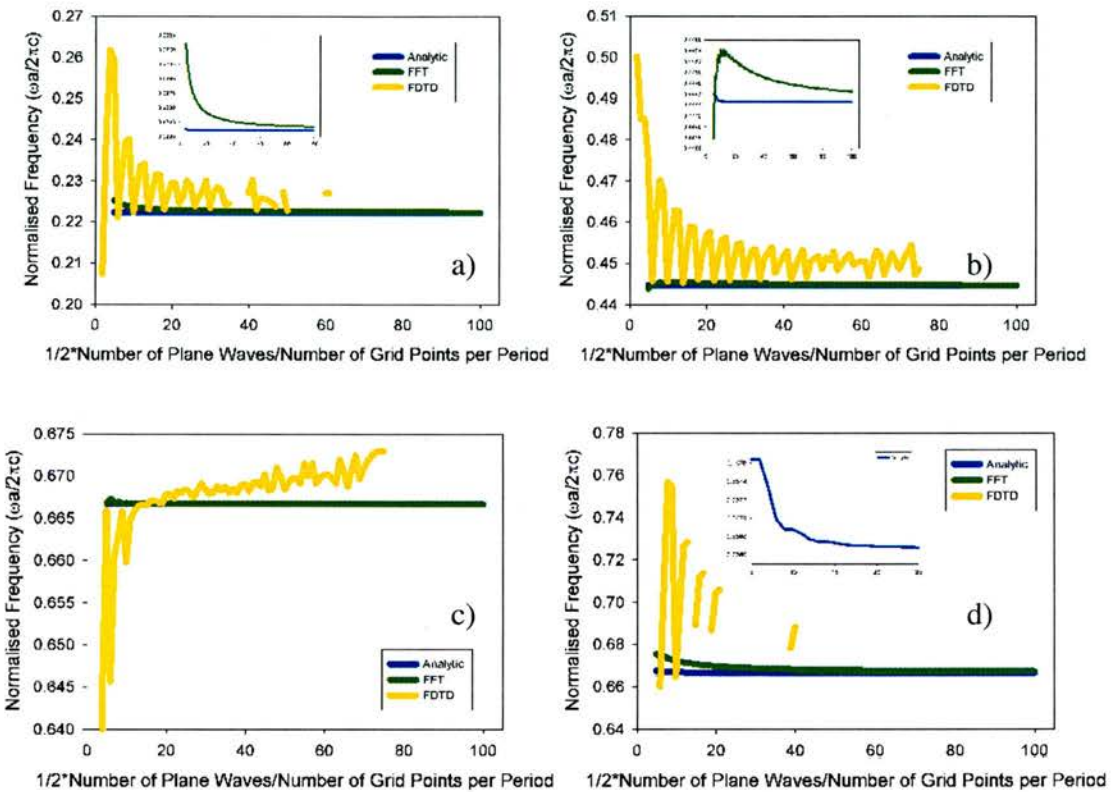


**Figure 2.7** The convergence of the PWE and FDTD codes. The analytic dielectric profile outperforms both methods consistently and rapidly tends to a steady value as the number of plane wave increases. The FFT of the real space profile is far slower to converge. The FDTD is relatively stable but exhibits oscillations as the number of grid points per period increases. At the upper  $\Gamma$  point the FDTD starts to fail to converge.

## 2.8 Coupled Cavity Waveguides in 1D

By increasing the size of one of the layers in a Bragg stack we create a defect cavity in the photonic crystal. The defect causes localisation of the field around the defect site and is characterised by a resonance peak in the transmission spectrum. The greatest degree of localisation, and hence the narrowest spectral bandwidths are observed when the defect layer is a multiple of  $\lambda/2$ , double the width of a mirror layer [32]. We are equally free to choose either material to obtain the resonance. By varying the defect thickness we can tune the resonance across the PBG. By repeating the defect layer-sequence, periodically throughout the PhC, a chain of coupled cavities is formed. Increasing the number of mirror pairs on each side of the defect causes the bandwidth to narrow due to increasing isolation. Optical coupled cavity waveguides have been demonstrated in a  $\text{Si}_3\text{N}_4/\text{SiO}_2$  system [33]. The single resonance peak of single cavity is split by each successive cavity, to give N peaks for N cavities. In the limit  $N \rightarrow \infty$  the structure forms an impurity band. This is almost the same mechanism as for the photonic pass band that we investigated in the first section, however on the band edges we observe  $N-1$  peaks per N repeat structures. The difference can be seen in the poles of equation {2.29}, the resonances occur for  $\frac{\sin^2 N K a}{\sin^2 K a} \rightarrow 0$ , i.e.  $N-1$  times.

For an additional resonance peak where  $T \rightarrow 1, \left[ \frac{1}{T} - 1 \right] \rightarrow 0$ , gives  $N-1+1=N$  peaks.

The defect peak occurs mid band, whereas the band edge transmission maxima occur between bands.

The effect of adding additional layers to the structure is now investigated using the TMM. Starting with the initial Bragg stack we increase the thickness of the higher index layer and then add one extra layer of each material. The periodic repeat structure is inset into each figure, and is constructed symmetrically. Figure 2.8a) shows our original Bragg band structure with a band gap between  $u=0.22-0.45$ . Figure 2.8b) shows that, even in the absence of a band gap, the defect layer nonetheless forms an impurity band. For (c)-(e) the band gap is very evident and the  $\lambda/2$  defect band sits in the centre. The bandwidths for these impurity bands are  $\Delta u=0.107, 0.032, 0.011, 0.004$  respectively. The bands each have alternately opposite

slopes, this is more apparent if we plot their group velocities,  $v_g = \frac{du}{dk}$ , which are shown in Figure 2.9. The four bands share a common zero dispersion point at  $u=0.333$  and alternate in sign.

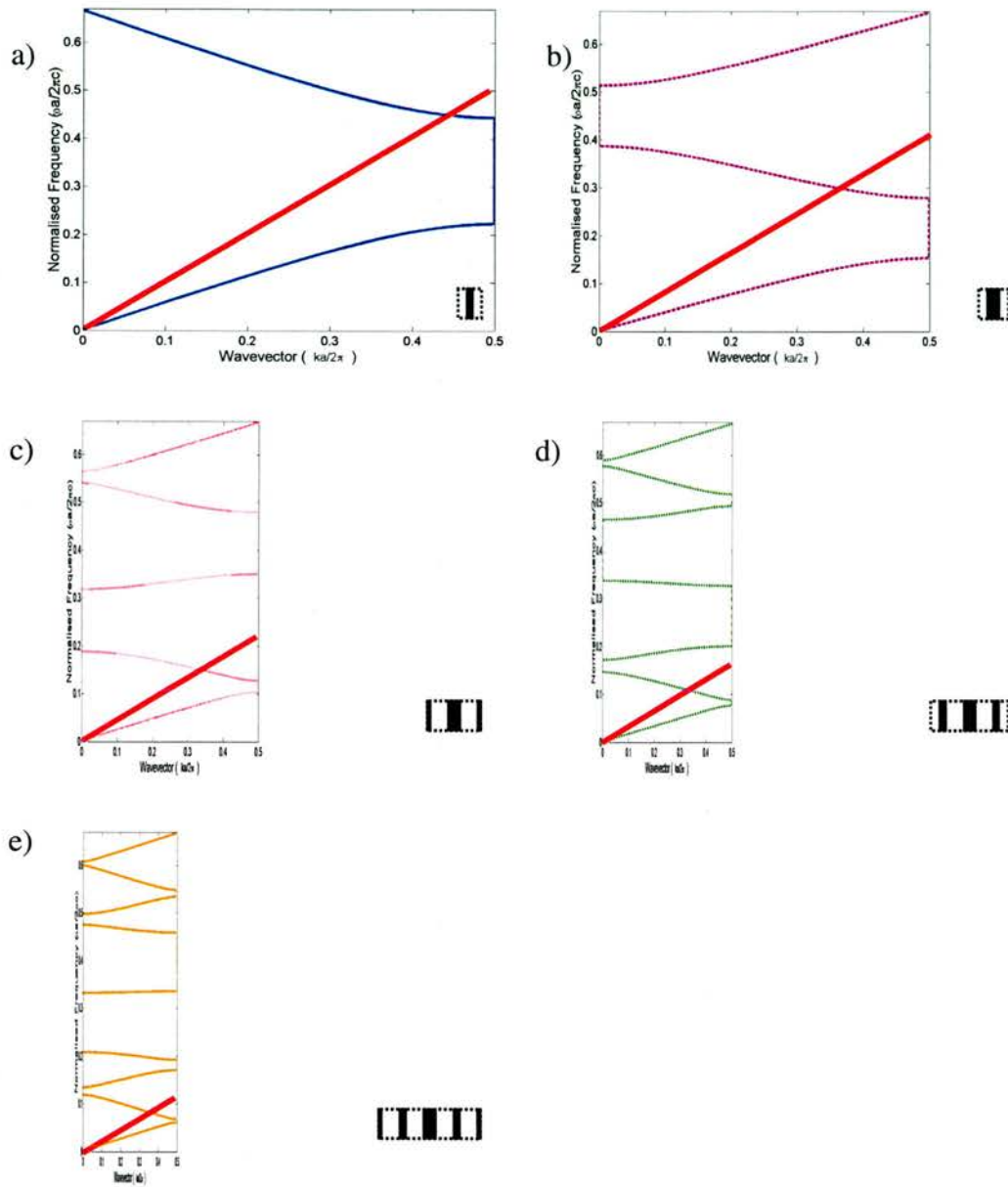


**Figure 2.8 Evolution of defect bandstructure increasing the number of layers between coupled cavities ( $n_1=1, n_2=3$ ). The quarter wave Bragg stack exhibits a band gap between  $u=0.22-0.45$ .**

The defect band is centered on  $u=0.333$  for each of the cases (b)-(e). The bandwidths are  $\Delta u=0.107, 0.032, 0.011, 0.004$  respectively. As the unit cell period,  $a$ , increases in length the  $k$  vector shrinks, decreasing the extent of the Brillouin Zone. The dispersion of free space is included as a red line in each diagram.

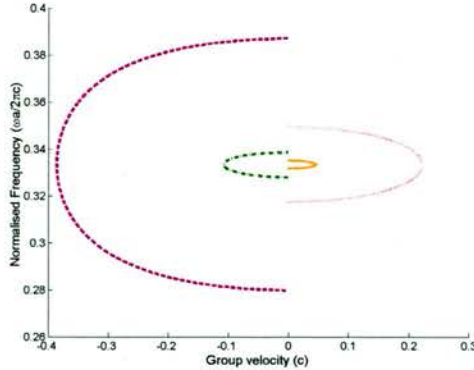


**Figure 2.9 Group velocities for the four defect bands (b)-(e), in units of  $c$ , speed of light. Each exhibits an alternate sign and all are centred on the same zero dispersion point of  $u=0.333$ . For the first case the group velocity is almost equal to that of a wave propagating in a uniform material of refractive index,  $n=3$ , the average index across this structure is  $n_{av}=1.8$ , indicating the magnitude of field localisation. For the fourth case the maximum group velocity is  $<1/20^{\text{th}}$  of the speed of light. At the band edges of each defect band the group velocity tends to zero.**

It is necessary for us to bridge the gap between the infinite lattices shown above and the finite length structures that we will consider in later sections. To this end we pick cases Figure 2.8 (c) and (d) for further investigation. The defect bands in c) and d) have opposite dispersions, but with wide enough band width to support transmission of short pulses.

Recall that in order to plot Figure 2.3 we unwrapped the phase before taking the spectral derivative,  $\frac{d\phi_{i,TOTAL}}{du}$ , equation {2.12}. This was necessary due to multiple repeats of our basic period creating a longer combined dispersion, (a sample of  $n=1$ , of length  $N=1$  repeat units would cause the phase to cycle once, whereas a sample of length  $N=5$  repeat units would cause the phase to cycle 5 times, across the same spectral bandwidth). In order to fit the infinite bandstructure of the second band to the effective index, it was necessary to unfold it into the 2<sup>nd</sup> Brillouin zone. This is essentially mirroring it around the plane  $k=0.5$ , the Brillouin zone boundary. The new curve takes the form  $\mathbf{k}_{\text{unfolded}} = 0.5 + (0.5 - \mathbf{k}_{\text{folded}}) = 1 - \mathbf{k}_{\text{folded}}$ . As the wavevector  $\mathbf{k}$  is the inverse spatial length of the wave ( $\times 2\pi$ ) as mentioned above, can we gain any insight from plotting the spatial fields?

The spatial fields are output using a modified TMM code, which separately accounts for the interfaces and the propagation sections of the structure. This allows us to output the fields by evaluating them as forwards and backwards travelling waves in each propagation section of the grating, but is otherwise equivalent to our original TMM [17,34,35].

The transmission spectrum of case (c) is plotted in Figure 2.10, for air as the external medium. The spatial Electric and Magnetic fields are plotted for the positions marked with dots, in Figure 2.11. The spectrum has a distinctive triangular distribution, with fringes that decrease in *Visibility* =  $\frac{T_{\max} - T_{\min}}{T_{\max} + T_{\min}}$ , with increasing frequency. From the symmetry of the group velocity curve (see Figure 2.9), around the centre frequency one would expect a symmetric transmission spectrum. It is the interface between the CCW and the surrounding medium which dominates the spectrum. Inset into Figure 2.8c) is the air light line, i.e. the dispersion of the impinging wave before and after the grating. The termination of the structure by a  $\lambda/8n_2$  layer appears to yield a good match between the propagation velocities (wave impedance, remembering the behaviour of the PML from the FDTD) between the surrounding medium and the CCW and consequently a broad region of high transmission around  $u=0.346$ . At lower frequencies a large mismatch is evident, and the resulting reflectivity of the interface causes the onset of Fabry-Pérot etalon-like behaviour [32].

We will now examine the two fields at these high transmission frequencies and compare these to the spatial frequencies we expect from the bandstructure. For each case in Figure 2.11 we see an envelope modulating a higher frequency wave. The field is enhanced substantially at the resonance peaks, spectrally we observe a proportionally narrower band width (and resultant high quality factor  $Q = \frac{\omega}{\Delta\omega}$ ). Note that for i), ii), iii), v) and vi) the input field is equal in amplitude to the output field, we have unity Transmission. For the first three cases i)  $u=0.317461$ , ii)  $u=0.318070$  and iii)  $u=0.319064$  we see the envelope resonate with the CCW. The wave is propagating purely in the forward direction outwith the CCW, but we see a standing wave pattern inside. At iv)  $u=0.3197375$  the envelope is out of phase by  $\pi$ , and hence

we observe low transmission. The Fabry-Pérot behaviour that we have anticipated from the transmission spectrum appears to be equivalent to the resonance of the Bloch wave envelope within the length of the periodic grating. Close to the centre of the band v)  $u=0.333333$  the field is only moderately enhanced, we can still discern an envelope with 10 waves. At the high frequency vi)  $u=0.348597$  we have a puzzling situation, the standing wave appears to a convolution of the 19<sup>th</sup> peak field and something behaving similar to the field of the 2<sup>nd</sup> peak. Also we have made no mention of the high spatial frequency of the “carrier” wave.

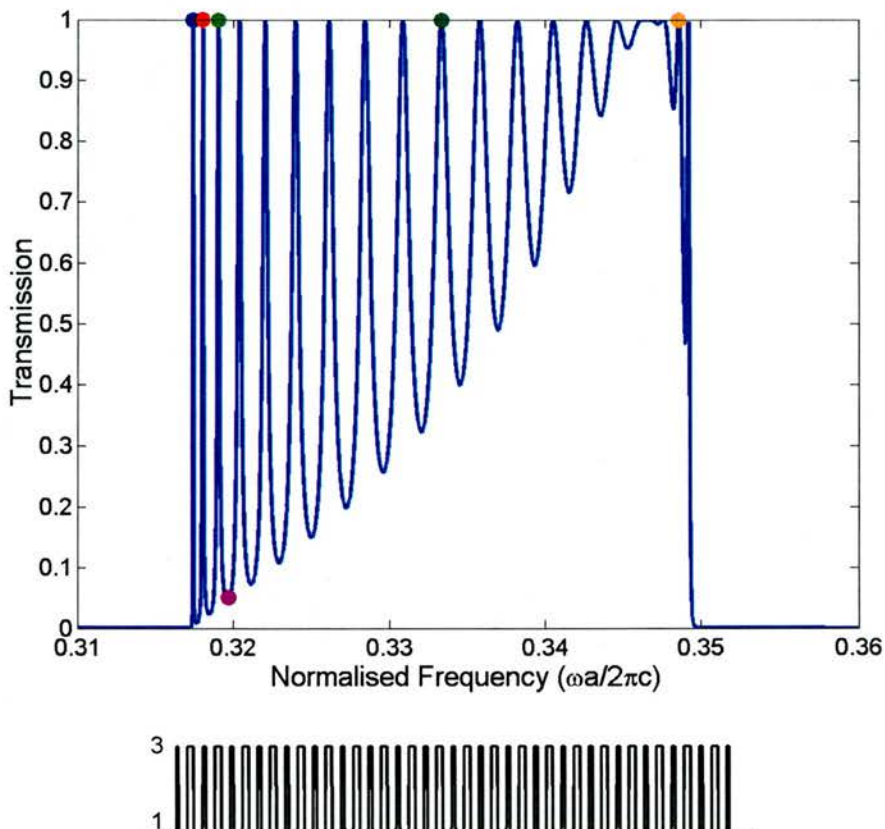


**Figure 2.10 a)**Transmission spectrum of 20 period CCW (case (c)) . Dots mark the positions at which the fields are plotted in Figure 2.11. **b)** Index profile of 20 period grating

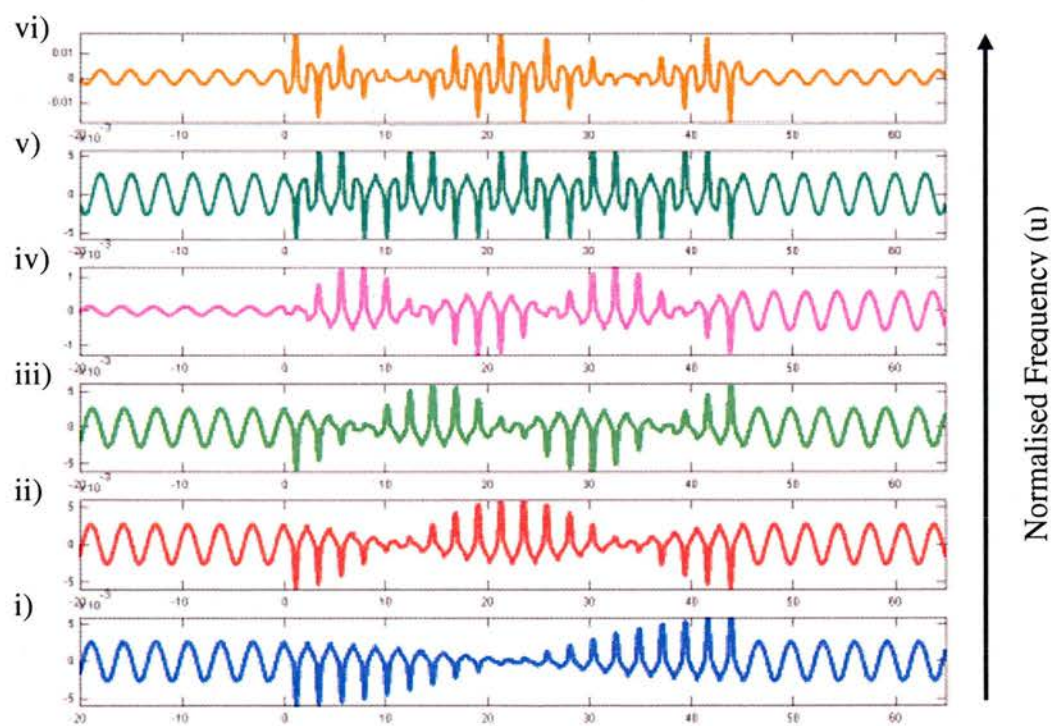
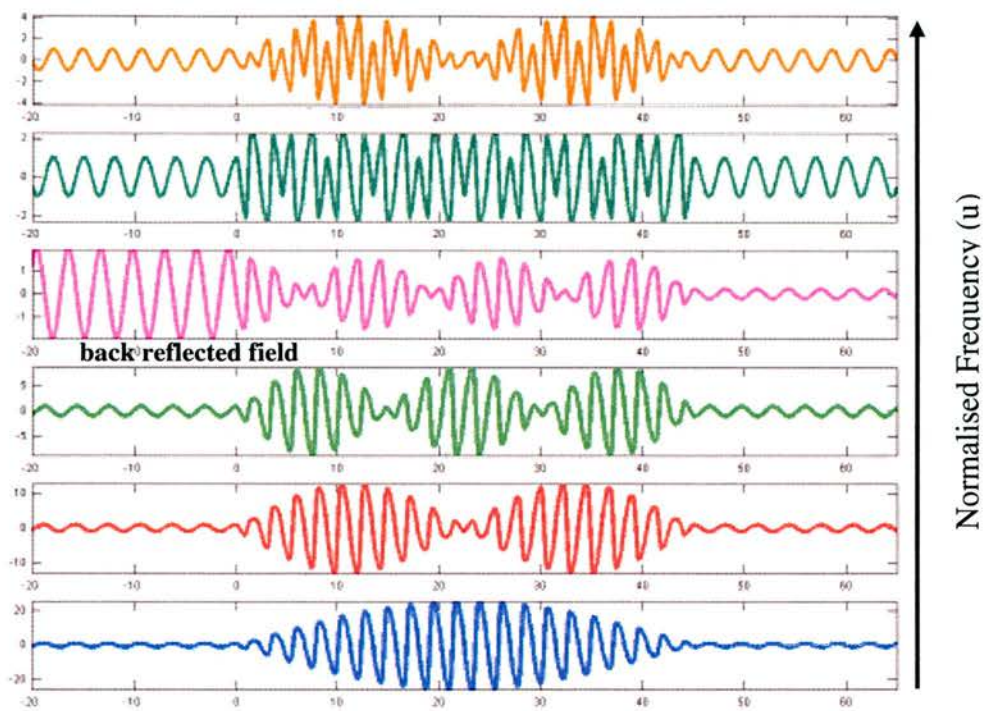
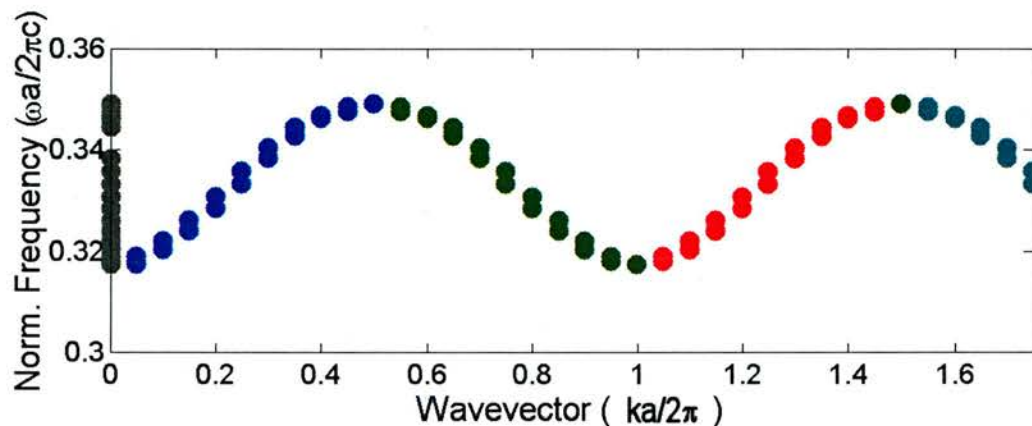


Figure 2.11 a) Electric and b) Magnetic fields plotted for a 20 period long CCW (case (c))

The envelopes of the two fields can be seen to be  $\pi$  out of phase. The frequencies increase from the bottom of the graph upwards, values were chosen at the peaks of transmission for plots i)  $u=0.317461$ , ii)  $u=0.318070$ , iii)  $u=0.319064$ , v)  $u=0.333333$  and vi)  $u=0.348597$ . The iv)  $u=0.3197375$  graph was chosen to coincide with a transmission minimum, and hence there is a large back reflected field.

In order to separate the spatial frequencies we can Fourier Transform the fields. We only include the wave inside the Coupled Cavity Waveguide, as we can characterise the external fields adequately.



**Figure 2.12 The FFT of the spatial fields across the transmission maxima of the 20 period CCW**

The result, as seen in Figure 2.12 reveals the folding of the field components explicitly. The pattern repeats up to the Nyquist limit of 2 samples per period - FFT sampling. The short (20 period sample) gives rise to low wavevector resolution.

The “carrier wave” is discerned by observing that the magnitudes of Fourier components with wavevectors in the range 1-1.5, are the largest. At the band edges the magnitudes of neighbouring folded bands balance out more evenly, and then cancel each other at the band edge. Each band has alternate slope corresponding to opposite group velocity. The slow group velocity of each band is a consequence of the sum of forwards and backwards waves of differing magnitudes.

As we saw from the IBZ bandstructure the lower frequencies have components with short wavevectors ( $k \sim 0$ ). At high frequencies it can be seen from the above graph that

there are forward and backward travelling waves which have very similar k vectors ( $k \sim 0.5$ ). These are excited by a CW input in a finite length device with reflective interfaces. It seems confusing to the observer that they are hinted at but do not appear on the band diagram. The best analogy one can draw on is that, were we to propagate two waves of different frequency ( $\omega_1 = ck_1$ ,  $\omega_2 = ck_2$ ) through each other in opposite directions, we would see a beating pattern in space, at a frequency equal to the difference,  $k_1 - k_2$ . Each wave is linearly independent of the other and adequately represented by its own Fourier spectrum.

## **2.9 Pulse Compression/Dilation**

Pulses created by modulated semiconductors lasers or transmitted through telecommunications networks become chirped. That is to say, their frequency content varies as a function of space/time along the length of the pulse. We have two simulation techniques available to us to simulate propagation in finite length structures, namely the FDTD – a direct time domain treatment, but also in linear systems we can always decompose the pulse into its Fourier components, which we have just obtained from our TMM calculation.

To see the effects of dispersion in a finite length structure we propagate a series of Gaussian pulses through the 20 period long CCW (case c) from 2.8. Centring the Bragg wavelength at  $\lambda_B=1.55\mu m$ , with  $n_1=1$  and  $n_2=3$ , gives a  $23.25\mu m$  long structure. A region (centred at  $\lambda_0=1.4914$ ) of high transmission of about 10nm in width with roughly linear Group Delay is evident (see Figure 2.13b), solid line). At  $\lambda_0$  the Delay is  $\sim 585fs$ , with a slope of approximately,  $-20ps/nm$ . Despite the apparent curvature of the band edge (see Figure 2.13b), dashed line, indicating third order dispersion), the finite length effects for this short device conspire to considerably linearise the Group Delay. The resulting Group Velocity Dispersion parameter is plotted in Figure 2.13c) and is about  $+1ps^2/mm$  ( $\pm 25\%$ ) over this range.

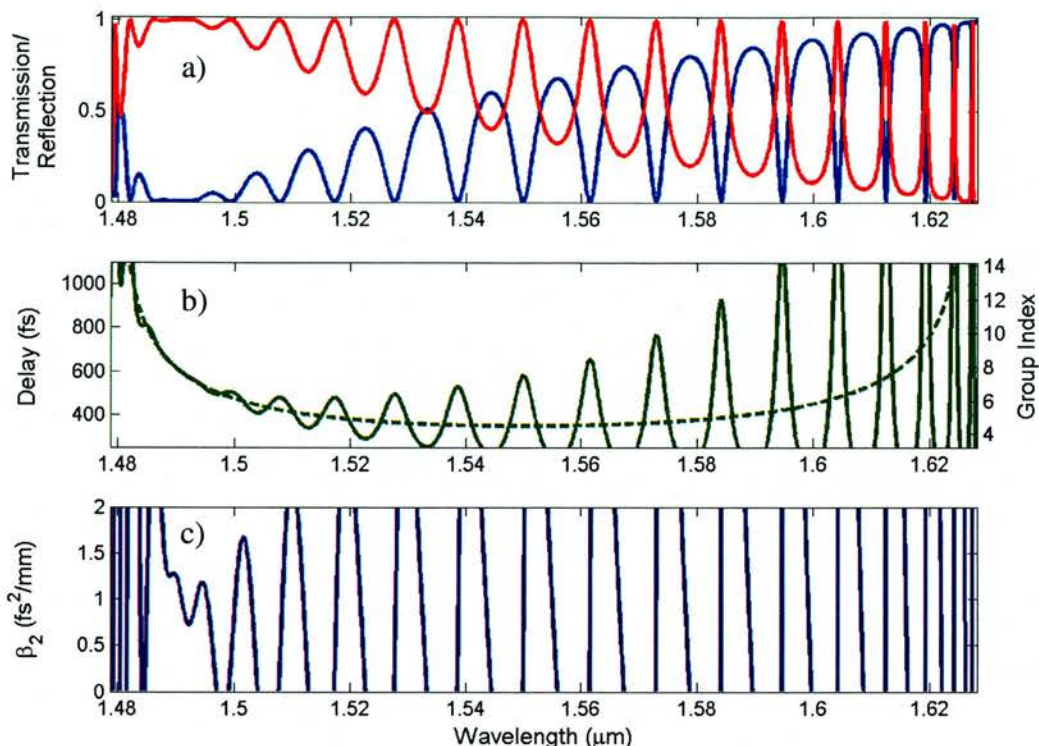


**Figure 2.13 a)** The Transmission (red) and Reflection (blue) spectra as in Figure 2.10.  
**b)** Corresponding Group Delay/Index for the finite (solid) and infinite (dashed) structures, for a device length 20a.  
**c)** The GVD parameter for the finite length structure.

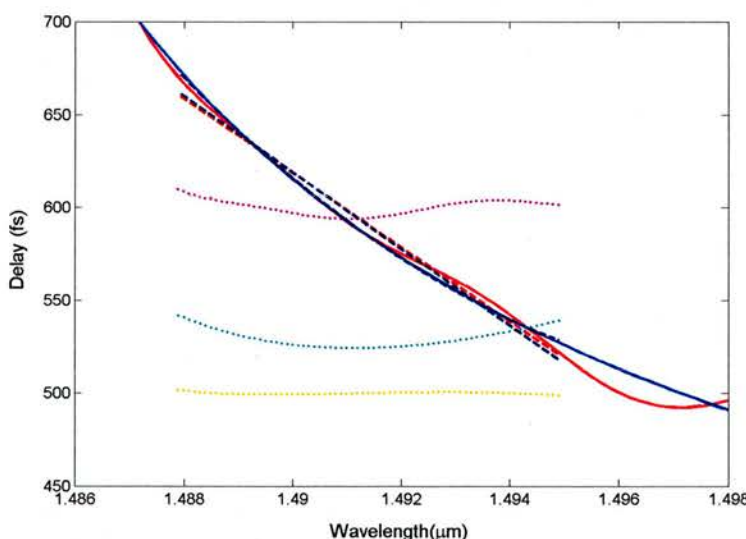


**Figure 2.14** Close up of Group Delay around pulse centre frequency. The dashed lines are linear/quadratic fits to the finite(red) and infinite (blue) dispersions. The pink dotted line shows a residual  $\pm 8\text{ fs}$  delay ripple, for the linear finite device. The cyan dotted line shows the residual ripple for the linear fit to the infinite band delay, and the yellow dotted line shows the residual ripple for the quadratic fit to the infinite band delay. Dotted lines are plotted at an arbitrary offset delay.

The effect of this positive GVD ( $\equiv$ negative D) on our input pulses will be markedly different for pulses with positive or negative chirp. Pulses transmitted through optical waveguides typically become more negatively chirped with distance, as the higher frequencies localise in the waveguide core, and thus travel more slowly. To simulate the effect of this chirp we simply apply a linear frequency chirp,  $b$ , to the optical carrier wave. The resulting phase shift is quadratic. The launched pulse has an electric field of the form,

$$E(t) = \exp(-at^2) \exp j(\omega_0 t + bt^2) \quad \{2.51\}$$

where  $a = \sqrt[4]{\tau^2}$ , and the temporal duration of the Electric field is related to the

intensity FWHM ( $\tau_p$ ) by  $\tau = \frac{\tau_p}{\sqrt{2 \ln 2}}$ .

A vital point to note is that in chirping the pulse in a linear dispersive system, we must maintain a constant optical bandwidth, to mimic linear propagation,

$$\Delta\omega = 2\sqrt{2 \ln 2} \sqrt{a \left(1 - \left(\frac{b}{a}\right)^2\right)} \quad \{2.52\}.$$

As the pulse dilates due to dispersion the chirp increases, and conversely as the pulse compresses the chirp decreases. Therefore if an initially transform limited pulse propagates through a dispersive medium, whether positive or negative, it becomes chirped. In a modulator or laser, the chirp associated with the refractive index modulation is responsible for adding bandwidth to the pulse.

The pulse duration of the launched pulses varies from ~710fs to 500fs (bandwidth limited duration), and the ratio of  $b/a$  varies from -1 to +1. The FDTD grid step is set at  $\Delta z = a/160$ , which converged to yield the same spectra as the TMM model.

The group index is calculated from the transit time delay of each pulse (centre of mass), and is plotted in Figure 2.15 b). These values correspond well with the group delay of 585fs, calculated for the pulse centre frequency. If we consider the length of the pulse in this structure,  $L = \frac{c\Delta t}{N_g} = 19.53\mu\text{m}$ , then we find that pulse (FWHM) is

shorter than the structure. It seems reasonable to use the FWHM to measure the

pulse duration, as the pulse rms duration (for a Gaussian  $\tau_{rms} = \tau_{FWHM} / \sqrt{2 \ln(2)}$ ) was found to be constant ( $\pm 2.5\%$ ) across the range of output pulses (see Figure 2.15c)). This indicates that there is no significant pulse reshaping, due to higher order dispersion.

Negatively chirped input pulses are compressed by the structure if their initial length is longer than approximately 520fs. After this point-of-inflection the dispersion is acts to dilate the pulse. The dispersion of this structure is of course limited to this short length of device. As the device becomes longer, the interfaces become less dominant in the spectrum and it is estimated that the higher order dispersion will become more significant.

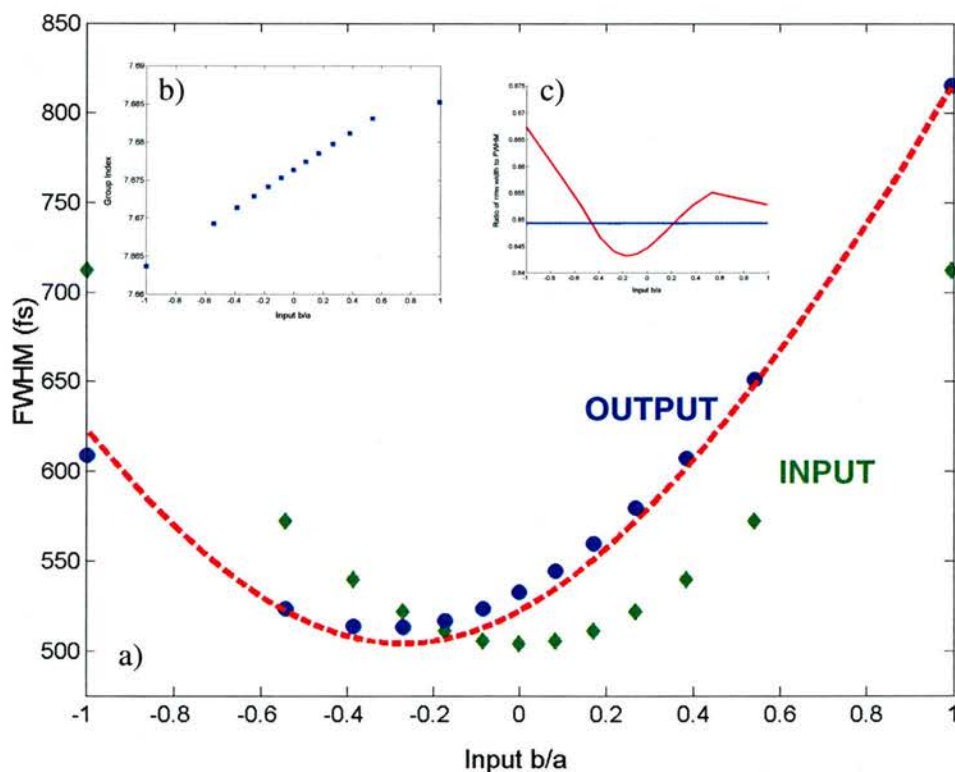


**Figure 2.15 Chirped pulse duration (blue dots, FWHM) after propagation through CCW, for chirps in range  $b/a = -1 \rightarrow +1$ . Transform limited pulse has 500fs duration. Theoretical transmitted pulse duration for constant  $\beta_2 = 1 \text{ ps}^2/\text{mm}$ , is shown by red dashed line. Input pulse durations shown as green diamonds. Pulse compression exhibited for negatively chirped pulse, pulse dilation exhibited for positively chirped pulse. Maximum 15% change in duration. b) Group index corresponding to anticipated 585fs time delay. c) Comparison between rms pulse width and FWHM, shows  $\pm 2.5\%$  ripple.**

## **2.10 Conclusion**

We have introduced the concept of a photonic bandgap and discussed the properties of a simple 1D periodic lattice. In order to efficiently compute the phase dispersion of complicated periodic multilayer structures we introduced the Transfer Matrix Method. We have then shown that the transmission of a finite length 1D Photonic Crystal is purely dependent upon the transmission through a single repeat period of the structure and the Bloch phase of this unit cell. To introduce the calculation techniques that we will use in the following chapters we then calculated the eigenfrequencies, the allowed states, of the Photonic Crystal using a Plane Wave Expansion of the dielectric function in reciprocal space. We will also make use of 2D and 3D FDTD in later chapters and so this real space, time domain technique was explained and contrasted with the two frequency domain techniques (TMM, PWE). The convergence of the PWE and FDTD were tested for a two layer structure. The TMM was then used to investigate a set of 1D Coupled Cavity Waveguides. The bandstructure and group velocities of the defect bands were calculated. Examining the spatial fields inside the structure then gave us more insight into the transmission characteristics of a finite length CCW. Modest pulse compression was then modelled for negatively chirped pulses close to the high frequency bandedge of a finite length CCW, for a defect band positive group velocity. The Group Velocity Dispersion was observed to be relatively linear due to the influence of the interfaces on the spectral amplitude and phase profile.

- 
- 1 Herman Haus, "Waves and Fields in Optoelectronics", Prentice Hall, 1984
- 2 J.D Joannopolous et al "Photonic Crystals: Molding the Flow of Light"
- 3 E. Yablonovitch, "Inhibited Spontaneous Emission in Solid State Physics and Electronics", PRL, **58**, pp2059-62, (1987)
- 4 S. John, "Strong localization of photons in certain disordered dielectric superlattices "Phys. Rev. Lett., **58**, 2486-9 (1987)
- 5 L. Chen, Y. Suzuki, G.E. Kohnke, "Integrated platform for silicon photonic crystal devices at near-infrared wavelengths", Appl. Phys. Lett., **80**, pp 1514-6, (2002)
- 6 T.F. Krauss, B. Vögele, C.R. Stanley, R.M. De La Rue, "Waveguide Microcavity Based on Photonic Microstructures", IEEE Photonics. Technol. Lett., **9**, pp 176-8, (1997)
- 7 E. Hecht, "Optics", 3<sup>rd</sup> ed., Addison Wesley, (1998)
- 8 H.A. McLeod, "Thin-Film Optical Filters", Adam Hilger, (1969)
- 9 B.E. Nelson, M. Gerken, D.A.B. Miller, R. Piestun, C-C. Iln, J.S.Harris Jr., "Use of a dielectric stack as a one-dimensional photonic crystal for wavelength demultiplexing by beam shifting", Opt. Lett. **25**, 1502-4, (2000)
- 10 A.V. Tikhonravov, P.W. Baumeister, K.V. Popov, "Phase properties of multilayers" App. Opt., **36**, 4382-92, (1997)
- 11 V.V. Lysak, I.A. Sukhoivanov, S.I. Petrov, "Group delay investigation of N-order chirping mirrors", Semiconductor Physics Quantum Electronics & Optoelectronics, **4**, 389-90, (2001)
- 12 D.-Y. Jeong, Y.H. Ye, Q.M. Zhang, "Effective optical properties associated with wave propagation in photonic crystals of finite length along the propagation direction", J. App. Phys., **92**, 4194-200,(2002)
- 13 J.B. Pendry, "Photonics Tutorial", (2000)
- 14 J.M. Bendickson, J.P. Dowling, M. Scalora, "Analytic expressions for the electromagnetic mode density in finite, one-dimensional, photonic band-gap structures", Phys. Rev. E, **53**, pp 4107-21, (1996)
- 15 D.W.L. Sprung, H. Wu, J. Martorell, "Scattering by a finite periodic potential", Am. J. Phys., **61**, pp1118-24, (1993)
- 16 D.J. Griffiths, C.A. Steinke, "Waves in locally periodic media", Am. J. Phys, **69**, pp137-54, (2001)
- 17 K. Sakoda, "Optical Properties of Photonic Crystals", Springer Verlag, (2001)  
available: [http://www.nims.go.jp/laser\\_sakoda/code/codej.html](http://www.nims.go.jp/laser_sakoda/code/codej.html)
- 18 J.B. Pendry, "Calculating Photonics Band Structure", J. Phys. [Condensed Matter], **8**, 1085-1108, (1996)
- 19 A. Reynolds website (seems to have been taken down)
- 20 I. El-Kady, S.-Y. Lin, Z.-Y. Li, K.-M. Ho, "Analytical Modal Expansion Method Applied to Highly Conducting 3D Metallic Layer-by-Layer Photonic Crystals", Progress In Electromagnetics Symposium, Honolulu, Hawaii, October 13-16 (2003)
- 21 S.G. Johnson, J.D. Joannopoulos, "Bloch iterative frequency domain methods for Maxwell's equations in a plane wave basis", Optics Express **8**, 173-90 (2001)  
MPB available <http://ab-initio.mit.edu/mpb>
- 22 S. Guo, "Plane Wave Expansion for Photonic Band Gap Calculation using MATLAB"; available <http://lions.odu.edu/~sguo002>
- S. Guo, S. Albin, "Simple plane wave implementation for photonic crystal calculations", Optics Express, **11**, 167-75, (2003)
- 23 J.D. Joannopoulos, R.D. Meade, J.N. Winn, "Photonic Crystals: Molding the Flow of Light", Princeton University Pres (1995)
- 24 P.R. Villeneuve, M. Piche', "Photonic band gaps –what is the best numerical representation of periodic structures", J. Mod. Opt., **41** pp241-256 (1994)
- 25 H.S. Soezuer, J.W. Haus, R. Inguva, "Photonic bands: Convergence problem with the plane wave method", Phys. Rev. B, **45**, 13962-72 (1992)
- 26 K.M. Ho, C.T. Chan, C.M. Soukoulis, "Existence of a photonic band gap in periodic dielectric structures", Phys. Rev. Lett., **65**, 3152-5, (1990)
- 27 L. Shen, S. He, "Analysis for the convergence problem of the plane-wave expansion method for photonic crystals", J. Opt. Soc. Am. A, **19**, 1021-4, (2002)
- 28 D.M. Sullivan, "Electromagnetic simulation using the FDTD method", IEEE Press, (2000)
- 29 A. Taflove, S.C. Hagness, "Computational Electrodynamics: The Finite Difference Time Domain Method", 2<sup>nd</sup> ed., Artech House, (2000)

- 
- 30 P. Harms, R. Mittra, W. Ko, "Implementation of the Periodic Boundary Condition in the Finite-Difference Time-Domain Algorithm for FSS Structures", IEEE Trans. On Antennas and Propagation, **42**, pp1317-23, (1994)
- 31 J.P. Berenger, "A perfectly matched layer for the absorption of electromagnetic waves". J. Comput. Phys., **114**, pp185-200, (1994)
- 32 R.P. Stanley, R. Houdré, U. Oesterle, M. Ilegems, C. Weisbuch, "Impurity modes in one-dimensional periodic systems: The transition from photonic band gaps to microcavities", Phys. Rev. A, **48**, pp 2246-50, (1993)
- 33 M. Bayindir, C. Kural, E. Ozbay, "Coupled optical microcavities in one-dimensional photonic crystal structures", J. Opt. A:Pure Appl. Opt. 3, 184-9, (2001);  
M. Bayindir, S. Tanriseven, E. Ozbay, "Propagation of light through localized coupled-cavity modes in one-dimensional photonic band gap structures", Appl. Phys. A, 72, 117-9, (2001)
- 34 J. Chilwell, I. Hodgkinson, "Thin-films field-transfer matrix theory of planar multilayer waveguides and reflection from prism-loaded waveguides", J. Opt. Soc. Am., **1**, 7, pp 742-53, (1984)
- 35 H.P. Uranus, M.O. Tjia, "Determination of Mode Field Profile and Its Evolution in Planar Waveguides with Arbitrary Refractive Index Profile using Characteristic Matrix Method", Proc. of the International Conf. On Electrical, Electronics, Communications, and Information (CECI), Jakarta-Indonesia, 2001

## Appendix A

### Bloch's Theorem

We stated in Chapter 2 that Bloch's Theorem allows us to expand the  $\mathbf{H}$  field in terms of periodic vector functions.

$$\mathbf{H}(\underline{\mathbf{r}}) = e^{i\underline{\mathbf{k}} \cdot \underline{\mathbf{r}}} h(\underline{\mathbf{r}}) \hat{\mathbf{e}}_k \quad \{2.32\}$$

where  $h(\underline{\mathbf{r}}) = h(\underline{\mathbf{r}} + \underline{\mathbf{R}})$ .

In order to prove that we need not take other functions into account we must show that the use of this restricted set is valid.

From Chapter 2 we remember that,

$$\nabla \times \frac{1}{\epsilon(\mathbf{r})} \nabla \times \mathbf{H}(\mathbf{r}) = \left( \frac{\omega}{c} \right)^2 \mathbf{H}(\mathbf{r}) \quad \{2.4\}$$

and the dielectric function expanded as a Fourier series.

$$\epsilon^{-1}(\mathbf{r}) = \frac{1}{\epsilon(\mathbf{r})} = \sum_{G_i} \epsilon(G_i) e^{iG_i \cdot \mathbf{r}} \quad \{2.33\}$$

If we express the eigenfunction of the magnetic field by a Fourier Integral

$$\mathbf{H}(\mathbf{r}) = \int d\mathbf{k} A(\mathbf{k}) e^{i\mathbf{k} \cdot \mathbf{r}} \quad \{A.1\}$$

and substitute {A.1} and {2.33} into {2.4}, we obtain,

$$\int d\mathbf{k} \mathbf{k} \times (\mathbf{k} \times A(\mathbf{k})) e^{i\mathbf{k} \cdot \mathbf{r}} + \left( \frac{\omega}{c} \right)^2 \sum_{G_i} \int d\mathbf{k} \epsilon(G_i) A(\mathbf{k} - G_i) e^{i\mathbf{k} \cdot \mathbf{r}} = 0 \quad \{A.2\}$$

The integrand vanishes as the equation holds for all  $\mathbf{r}$ .

$$\mathbf{k} \times (\mathbf{k} \times A(\mathbf{k})) + \left( \frac{\omega}{c} \right)^2 \sum_{G_i} \epsilon(G_i) A(\mathbf{k} - G_i) = 0 \quad \{A.3\}$$

The constituents of the eigenvalue problem are as equation {A.3} implies only Fourier components related by the reciprocal lattice vectors.

$$\mathbf{H}_k(\mathbf{r}) = \sum_{G_i} \epsilon(G_i) A(\mathbf{k} - G_i) e^{i(\mathbf{k}-G_i) \cdot \mathbf{r}} \quad \{A.4\}$$

---

$$v_k(\mathbf{r}) = \sum_{\mathbf{G}_i} \epsilon(\mathbf{G}_i) A(\mathbf{k} - \mathbf{G}_i) e^{j(\mathbf{k} - \mathbf{G}_i) \cdot \mathbf{r}} \quad \{A.5\}$$

is periodic satisfying

$$h(\mathbf{r}) = h(\mathbf{r} + \mathbf{R})$$

$$\mathbf{H}(\mathbf{r}) = h(\mathbf{r}) e^{j\mathbf{k} \cdot \mathbf{r}} \quad \{2.32\}$$

[A.1] K. Sakoda, Optical Properties of Photonic Crystals", Springer Verlag, (2001)

# Chapter 3

## 3.1 2D Coupled Cavity Waveguides

In this chapter we will apply the techniques outlined in Chapter 2 to the study of 2D periodic structures. Initially we examine the fields incident on the boundary between two dielectric materials at an angle and expand this to solve the modes of slab waveguides. This will allow us to attempt to treat the dispersion in the plane of the slab independently of the slab waveguide (an equivalent index approximation<sup>y</sup>)[1]. The concepts of dispersion diagrams are revised for 2D. We then update the TMM method to understand Eigenmode Expansion (EME) modelling and compare this with a 2D FDTD code. We will then present experimental transmission measurements of a large range of 2D CCWs. The dispersion of these devices is then modelled, including that of the heterostructure waveguide into which they are fabricated. The application of one of these structures to a pulse compression measurement is assessed. We then look at the full 3D picture and take into account the impact of the third dimension upon the device performance, to assess the validity of the 2D equivalent index approximation.

The work presented in the latter section of this Chapter is a summary of collaboration with the University of Cambridge. The experimental pulsed measurements were made by Chris Morgan and Yew-Jun Chai.

---

<sup>y</sup> There are many effective index approximations mentioned in the literature which correspond to various techniques used here. Instead of using the same name for different techniques, I have attempted to separate these into equivalent, effective and effectual indices. For clarity and convenience they are defined again here.

- Effective index is the total phase, accumulated as the frequency is increased from DC, divided by the length of the device, as used in Chapter 2,  $n_{eff} = \frac{\phi_{TOTAL}\lambda}{2\pi L}$ .
- Equivalent index is the phase or modal index of a waveguide,  $n_{equiv} = \frac{k_{equiv}\lambda}{2\pi}$ , the ratio of the waveguide wavevector to the free space wavevector.
- Effectual index is the group index of a waveguide as calculated for a multisection waveguide, where we cannot define a single equivalent index. For a constant input phase we observe the differential output phase.  $N_{group} = n_{equiv} - \lambda \frac{\partial n_{equiv}}{\partial \lambda} = -\frac{\Delta\phi}{2\pi L} \frac{\lambda^2}{\Delta\lambda}$

Each is effectively equal ( $=c/v=1$ ) in free space!

There are two reasons for wanting to work with two dimensional photonic crystals for the goals outlined in chapter 1;

1. They exhibit not only temporal dispersion, as did the PhCs of the previous chapter, but also spatial dispersion.
2. Integration of multiple components on a wafer scale will invariably involve narrow waveguides, photonic wires. These are directly compatible with PhC waveguides, which can provide extremely compact dispersion management.

The first point aims to maximise our control over the dispersion of a pulse by combining the *spatial prism* and *temporal waveguide* concepts from section 1.5. We could, for example, spatially separate the various spectral components of a pulse in our 2D plane and then disperse these components in time before recombining them. The *prism* (or alternatively *cavity*) demultiplexing element affords us much finer control of the dispersion, as we divide the light into individual temporal filter channels, ie. *spectrally slice* it. The temporal dispersion of the PhC *waveguide* then allows much more freedom to independently control the group velocity and GVD of the spectrally sliced pulse, used essentially as a point to point, or 1D PhC.

The second point recognises that high contrast integrated optics naturally includes very large wavevector components transverse to the direction of propagation. As we will see below the waveguide mode is simply formed by constructive interference between two Totally Internally Reflected waves. An easy way to include a phase delay is to allow these components to travel a longer transverse path before they re-interfere, for instance increasing the waveguide width (see Figure 3.1). Of course widening the waveguide may increase the number of modes. On the one hand these higher order modes are naturally more dispersive, but on the other hand we would like to couple 100% of the light into and back out of these modes. (We assume that we would prefer to begin (at A) and end (at B) in identical waveguides). The addition of scattering elements; interfaces and outer boundaries forms a resonant cavity, and assists with mode matching. This also provides a separate mechanism to adjust the temporal delay, by causing a fraction of the light to pass multiple times through the cavity. Corrugation of the boundaries of the cavity allows us to select only very specific modes, via Bragg diffraction, thus controlling their interaction. Combining these ideas to form a 2D periodic array of scattering elements, a 2D Photonic Crystal,

provides mode control to localise the field, maximising the mode coupling and simultaneously increasing the path length necessary for the wavelength dependent phase delay. This allows us to tailor the temporal dispersion of the diffracted light. The geometry that we will explore in Chapter 5 introduces much richer diffraction/refraction phenomena.

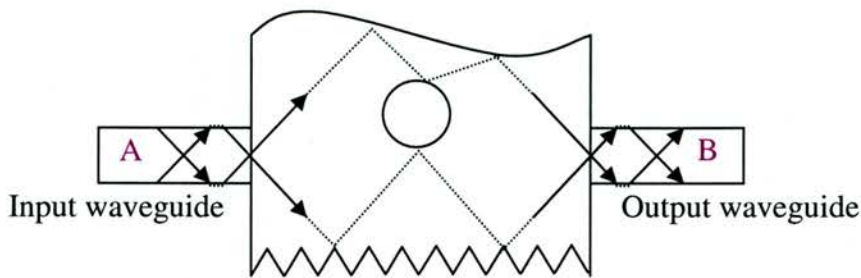


**Figure 3.1 High index contrast waveguide mode has large wavevector components.** To introduce a wavelength dependent phase delay between points A and B we can take advantage of the 2D space and harness the transverse component of the wavevector. Increasing the waveguide width, allows coupling to higher order modes which are more dispersive. Scattering from single features (a cylinder) or coherent scattering from corrugations (grating along bottom boundary) allows spectrally tunable phase delay.

We will investigate 2D PhCs in this chapter, both theoretically and experimentally. 1D devices are simple enough that we can design their interaction with free space light beams, modes radiating from Single Mode Fibres (SMF) (e.g. Thin Film Filters), or modes guided along the axis of single mode fibres (e.g. Fibre Bragg Gratings) using nothing more than paraxial ray optics. In order to deal with 2D PhCs we need to be in one of two regimes, either where the variation in the third dimension is negligible, or we must use a waveguide to confine the light in the third dimension to restrict the spread of wavevectors involved in the problem. In the former “semi-infinite” case the structure must be many wavelengths high [2] and in an effort to conserve energy in the presence of diffraction we must capture light over a larger aperture than that over which it is launched. In the latter “waveguide” approach we must take care that the dispersion of the complete system is slow enough not to impact adversely on the desired 2D dispersion. This can also entail minimising losses, which in a 2D (in plane) model are non-existent\*, but in a 3D system can attenuate the multiple reflections which give rise to the dispersion. Losses can be

---

\* Any loss would be due to absorption at a PML boundary, we must place boundaries far enough away from the guided modes. This can also be achieved by additional PhC cladding layers, minimising the field at the boundary.

either intrinsic to the design of the structure, i.e. diffraction, or extrinsic, i.e. due to roughness and fabrication tolerances.

### 3.2 2D Slab Waveguides – Out of plane dispersion

We adopt the waveguide approach in this work, and so must be able to calculate the modes of the waveguide and their dispersion. In the last chapter we very rapidly described the transfer matrix of a thin film without explicitly taking into account the fields. In the context of 2D structures a fuller description of the fields seems worthwhile to introduce the issue of polarisation. The components of the Electric, E, and Magnetic, H, fields tangential to the boundary must be continuous.

Having removed the 1D restriction from the previous chapter, light can now travel in a plane rather than just one direction. Say the light is confined to the plane of the paper, for our convenience. We now have to account for the polarisation in our calculations. Waves can be either Transverse Electric (TE) polarised, corresponding to a Electric field perpendicular to the plane circulated by Magnetic fields in the plane ( $E_y, H_x, H_z$ ) or Transverse Magnetic (TM) polarised corresponding to a Magnetic field perpendicular to the plane circulated by Electric fields in the plane ( $H_y, E_x, E_z$ ). We observe the naming convention from multilayer stacks and waveguide analysis in 2D because it is the Transverse field which observes the boundary condition.

These are sketched for the TE case in Figure 3.2.

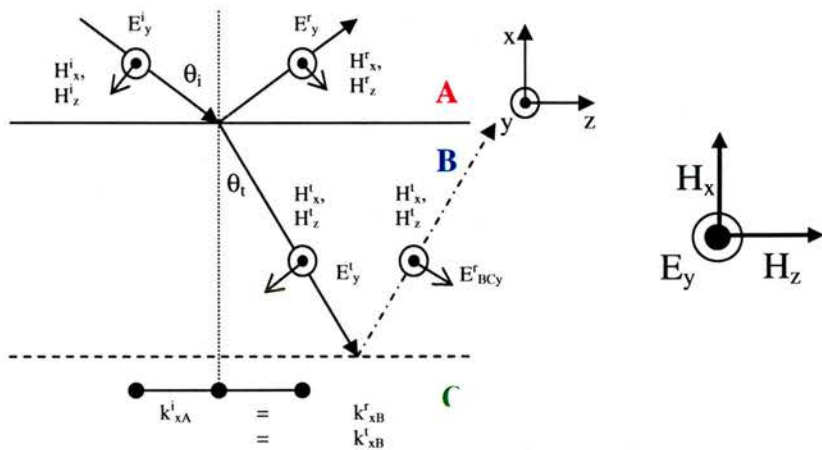


**Figure 3.2 Incident, reflected and transmitted fields at an interface between materials A and B. The wave has an electric field which is everywhere transverse to the boundary, i.e. TE polarised.**

The wavevector,  $k$ , in the  $z$  direction (along boundary) is conserved.  
Placing an additional material C creates a waveguide if  $n_B > n_A, n_C$

We can of course apply this analysis to Slab waveguides (i.e. where the above diagram is a side view of the waveguide) or to Ridge waveguides (where the diagram looks from the top down).

Be warned, in 3D we will swap the notation around, as the nomenclature follows the modes of the heterostructure waveguide. As conventional laser heterostructure waveguides are designed to have an Electric field which couples to the gain medium/quantum wells, the slab modes of interest to our integrated approach will be TE polarised. From another perspective, chronologically, the wafer is grown before the PhCs are etched, so we allow the Slab modes to dominate our naming convention. The Photonic Crystal community spent the best part of a year arguing this issue, as half had started etching PhCs into laser waveguide material and the others had turned their computers on and realised that the fields were best defined relative to the interfaces with the periodic scattering structures that they were studying. The common consensus to avoid ambiguity is to specify the field components and include a diagram if possible.

Introducing a second boundary beyond AB and between materials B and C causes a reflected wave,  $E_{BC}^r$  which contributes to the polarisation at the first boundary.

$$E_{AB} = E_{AB}^i + E_{AB}^r = E_{AB}^t + E_{BC}^r \quad (3.1)$$

$$H_I = \sqrt{\frac{\epsilon_0}{\mu_0}} (E_{AB}^i + E_{AB}^r) n_0 \cos \theta_{AB}^i = \sqrt{\frac{\epsilon_0}{\mu_0}} (E_{AB}^t + E_{BC}^r) n_1 \cos \theta_{BC}^i$$

On the far side of the second boundary there is only a transmitted field component.

$$E_{BC} = E_{BC}^i + E_{BC}^r = E_{BC}^t \quad (3.2)$$

$$H_{BC} = \sqrt{\frac{\epsilon_0}{\mu_0}} (E_{BC}^i + E_{BC}^r) n_1 \cos \theta_{AB}^i = \sqrt{\frac{\epsilon_0}{\mu_0}} E_{BC}^t n_2 \cos \theta_{BC}^t$$

The field transmitted across the layer undergoes a phase shift  $k_0 h = k_0 n_1 d \cos \theta_{BC}^i$

$$E_{BC}^i = E_{AB}^t e^{-ik_0 h} \text{ and } E_{BC}^r = E_{BC}^t e^{ik_0 h} \quad (3.3)$$

$$E_{BC} = E_{AB}^t e^{-ik_0 h} + E_{BC}^t e^{ik_0 h} = E_{BC}^t \quad (3.4)$$

$$H_{BC} = \sqrt{\frac{\epsilon_0}{\mu_0}} (E_{AB}^t e^{-ik_0 h} + E_{BC}^t e^{ik_0 h}) n_1 \cos \theta_{AB}^i$$

Rearranging these and substituting into the first pair of equations leaves us with,

$E_{AB} = E_{BC} \cos k_0 h + H_{BC} (i \sin k_0 h) / Y_{AB}$ , which is equation {2.1} when written in  $H_{AB} = E_{BC} Y_{AB} i \sin k_0 h + H_{BC} \cos k_0 h$

matrix form. It may seem strange to return to this derivation after we have made extensive use of the result, but what is important here is to reference the diagram (see Figure 3.2).

To guide light along the waveguide formed by the two interfaces we look for solutions of the field which decay exponentially with increasing spatial distance outwith the waveguide, in the cladding layers A and C, and oscillate in layer B, the waveguide core. Written in matrix form this is,

$$\begin{pmatrix} 1 \\ -Y_{AB} \end{pmatrix} \begin{bmatrix} E_{AB} \\ H_{AB} \end{bmatrix} = M \begin{pmatrix} 1 \\ Y_{BC} \end{pmatrix} \begin{bmatrix} E_{BC} \\ H_{BC} \end{bmatrix} \quad \{3.5\}$$

This can be solved to yield,

$$\chi = Y_0 m_{11} + Y_0 Y_s m_{12} + m_{21} + Y_s m_{22} = 0 \quad \{3.6\}$$

The zeros are the poles of the transmission and reflection coefficients. These correspond to total internal reflection and in the ideal case the wave is perfectly guided along the core (in the z-direction). In reality  $\chi$  will have a small complex component and this causes loss. This is typically a result of the substrate. By using the matrix formalism, complicated multilayer waveguides can be solved. The fields of the guided modes have cross sections  $\mathbf{E}=\mathbf{E}(x)$ ,  $\mathbf{H}=\mathbf{H}(x)$ , they are invariant along y and the z solution is obtained by multiplying the cross section by a phase factor,

$$\begin{aligned} E_y(z) &= E_{y0} e^{i(\alpha x - k_0 z)}, \\ H_x(z) &= H_{x0} e^{i(\alpha x - k_0 z)} . \end{aligned} \quad \{3.7\} \text{ for TE mode}$$

$$H_z(z) = H_{z0} e^{i(\alpha x - k_0 z + \pi)}$$

The  $E_y$  and  $H_x$  components are in phase but there is a phase difference between the  $H_x$  and  $H_z$  field components of  $\pi$ . The field lines for a symmetric waveguide fundamental TE mode are plotted in Figure 3.3. The antinodes of each component are marked.

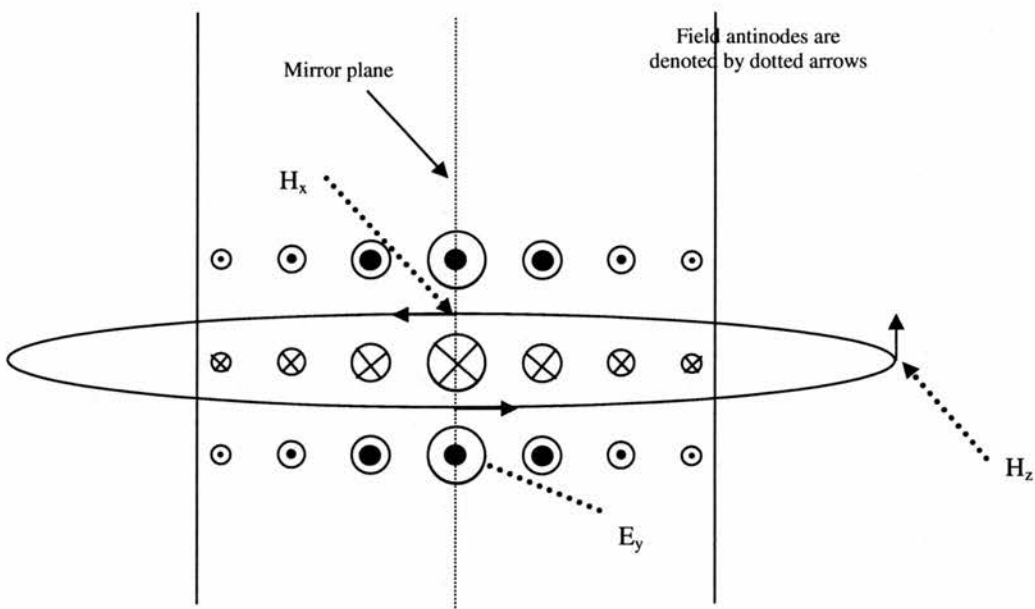


**Figure 3.3 Waveguide showing field lines in a symmetric waveguide for its fundamental TE mode.**

To summarise this technique, waveguide mode solving is introduced by equating the solutions for oscillating fields in the waveguide core with the exponentially decaying fields in the cladding. The equations are solved in a manner almost identical to the bound modes of a finite 1D quantum well, resulting in a set of transcendental equations which must be solved graphically or numerically. The reader can see that this step is taken care of in equation {2.4}. The angle of incidence is included in equations {2.1-2.6}. It can be appreciated that the waveguide modes occur for angles of incidence where the field, traversing the waveguide (AB-BC-AB) is returned with an integer  $2\pi$  phase shift, i.e. constructive interference. The waveguiding is essentially achieved by Total Internal Reflection (TIR).

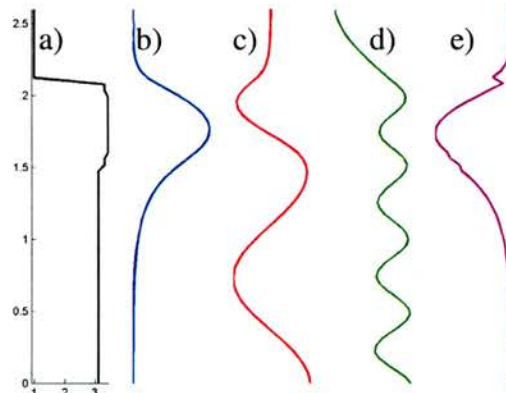
### 3.2.1 Symmetries

At this convenient juncture we will quickly introduce some basic concepts of symmetry, for later use. We have just dealt with structures with continuous translation symmetry, i.e. slab waveguides, for which  $X(x,y)=X(x+d,y)$ . And in the previous chapter the Bloch theorem introduced us to discrete translation symmetry,  $X(x,y)=X(x+\ell a,y)$ , where  $d=\ell a$  is now restricted to the case where  $\ell$  is an integer. We define a structure with even symmetry as that which is invariant under a mirror operation  $\sigma_x$  where  $X(x,y)=X(-x,y)$ . The mirror operation for odd symmetry,  $\tau_x$ , is likewise  $X(x,y)=-X(-x,y)$ . Rotational symmetries play a big role in the properties of PhCs, but we do not have cause to invoke them in the following.

### 3.3 Mode Solvers

There are many freely (and commercially) available 1D dielectric waveguide mode solvers [3,4,40], which are numerically optimised to find more or less the complete set of modes for a particular waveguide. For convenience we defer (subsequent to this point) to the computational power of these solvers. The fields of the modes are readily obtainable from the matrix technique above, or more quickly from the solvers. Conventionally, to aid the solver the decaying behaviour of the cladding fields is pre-empted by imposing a zero field value at a finite distance from the guide. This takes the form of a Dirichlet<sup>⊗</sup> boundary condition ( $E(x)=E(\text{boundary})=0$ , often known as a metallic/conducting wall – there are then no charges beyond the wall, the skin depth,  $\delta=0$ ). The problem is thus bound and is small enough to fit into a modern PC and be solved in short time. The Electric field profiles of the TE and TM modes for the “Scotland” structure (see Figure 3.16) waveguide are plotted in Figure 3.4. The  $E_y$  field is discontinuous at the dielectric interface for the TM mode. The solver returns the propagation constant of the mode,  $k_{\text{equiv}} = \frac{2\pi n_{\text{equiv}}}{\lambda}$ , corresponding to a equivalent refractive index,  $n_{\text{equiv}}$ . The real part defines the phase velocity,  $v_p = \frac{c}{\text{Re}(n_{\text{equiv}})}$ , at which the mode propagates along the waveguide. The imaginary part defines the rate of decay of the mode as it propagates along the waveguide  $n_{\text{equiv}}$ .

#### 3.3.1 Mode profiles for GaAs heterostructure




---

<sup>⊗</sup> The Dirichlet boundary condition in FDTD is as simple as setting a single Electric field component to  $E=0$  (a hard boundary).

**Figure 3.4 a)Refractive index profile of Slab waveguide, b) TE0 Ex mode profile, c) TE Ex leaky mode profile d) TE Ex radiation mode profile e) TM0 Ey mode profile**

The basic modes of the Slab waveguide used in this Chapter are displayed in Figure 3.4, calculated at  $1.55\mu\text{m}$ . The initial work with this waveguide was performed at  $1.31\mu\text{m}$ , where the light is better confined. The gentle vertical confinement produces mode profiles for the TE and TM which extend deep into the substrate ((a) and (d) have alpha factors,  $\alpha<10^{-6}\mu\text{m}^{-1}$ ). The alpha factor is defined as the  $1/e$  length, the length in which the field decays to a factor  $1/e$  of its initial value. The leaky modes (e.g. (c)  $\alpha=0.0714\mu\text{m}^{-1}$ ) have an oscillating component in the substrate and the radiation modes (e.g.(d)  $\alpha=0.8469\mu\text{m}^{-1}$ ) oscillate throughout the air and substrate regions, and form a continuum. Here the computational domain boundary artificially imposes a quantisation of these radiation modes.

The leaky mode region is exploited in prism coupling, where the prism forms a supplemental cladding layer for the short distance that it is in  $\sim$ contact with the waveguide. In this way light can be refracted into the waveguide core. In Chapter 4 we will also exploit this regime, but in order to examine the light leaking from a waveguide.

### 3.3.2 Mode dispersion

It can be seen from Figure 3.5 that for each mode - as the wavelength increases - the mode equivalent index decreases. The mode spreads out and is increasingly guided in the cladding.  $n_{\text{equiv}}$  is predominantly a real number ( $Re(n)>> Im(n)$ ). In an asymmetric guide the modes are cut off as the  $n_{\text{equiv}}$  drops below  $n_{\text{cladding}}$ , the index of the cladding. Presuming the top cladding for the heterostructures is air. as the mode index drops below 1, the mode  $n_{\text{equiv}}$  becomes complex. Beyond cutoff the behaviour of the mode is a numerical artefact, arising from the waveguiding facilitated by the Dirichlet boundary. We have not plotted this region here. The fields of cutoff modes retain their spatial symmetries and the complex mode index gradually tends to zero. This has consequences for scattering behaviour in these waveguides, as we will discuss later.

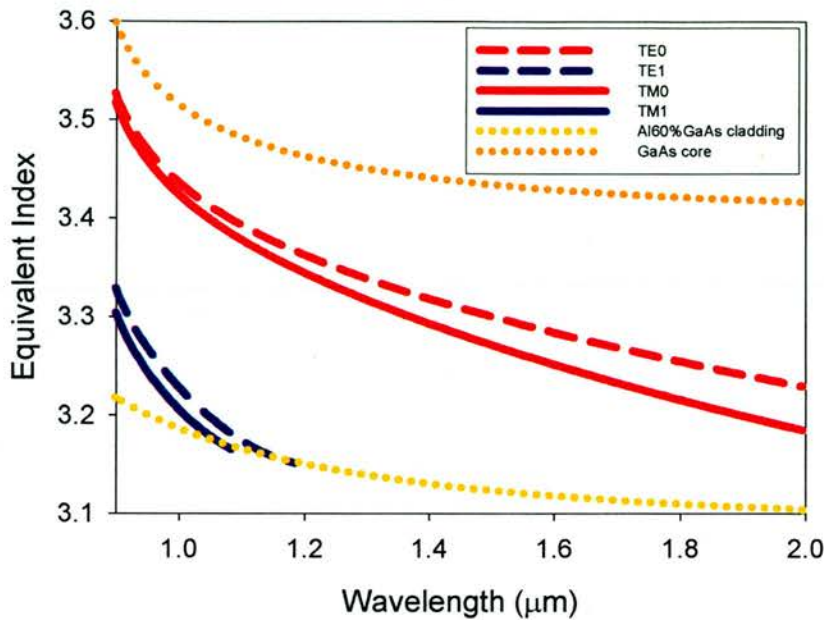


**Figure 3.5** Waveguide mode dispersion for “Scotland” structure 400nm GaAs core surrounding by 100nm of Al<sub>0.25</sub>GaAs cladding sitting on top of a 1.5μm Al<sub>0.6</sub>GaAs buffer

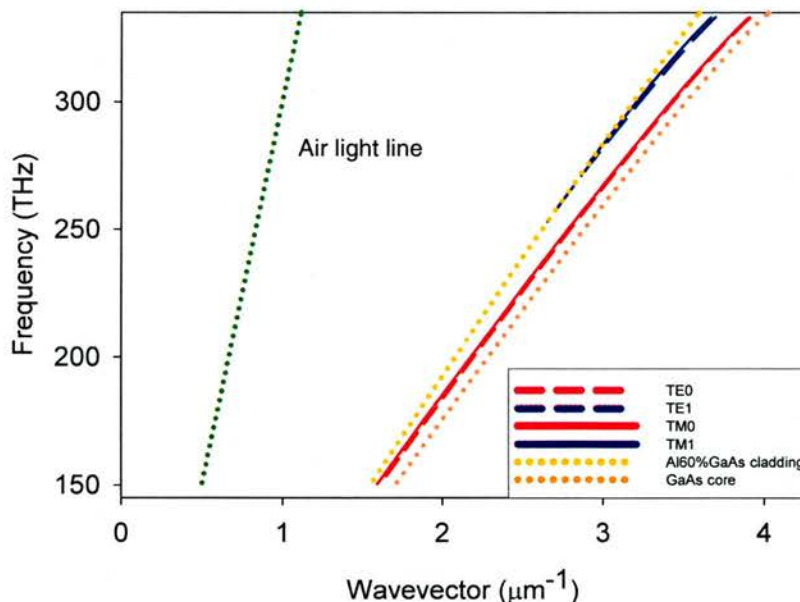


**Figure 3.6** Data from Figure 3.5 replotted in the form of a wavevector diagram. The boundaries defined by the core and cladding light lines are more distinct. TE and TM modes hardly differ over the entire telecommunications operating range.

In order to match to the photonic crystal waveguides we will employ tapered ridge waveguides. At the end of the taper, the width exactly matches the narrowest cross section of the PhC waveguide,  $width = \sqrt{3}a - 2R$ , where  $a$  is the lattice constant of the PhC and  $R$  is the radius of the holes. At this narrow width the equivalent index

depends strongly upon the wavelength. In the following we analyse the PhC behaviour, initially in 2D. At the end of the chapter when we get to 3D, be forewarned, that things are not quite all they seem for these narrow access ridges etched through heterostructure waveguides.

We plot this data as a wavevector diagram next (see Figure 3.6), remembering that the ordinates are in frequency and the abscissa is the inverse wavelength in the material. Here we have no preordained length scale, to which we can normalise the wavevector and frequency. The modes beyond the cladding cutoff are leaky, and are thus rapidly attenuated as the wave propagates. The wavevector plot allows us to distinguish the two bounds of the guided modes more readily. In the short wavelength (high frequency) limit the power in the wave sits in the core of the waveguide and has an equivalent index which approximates the refractive index of the core material. Towards longer wavelength the mode crosses the dispersion diagram and cuts off at an index equivalent to the lowest cladding refractive index (the cladding light line or the limit of TIR). The narrow spread of wavevectors involved in the heterostructure waveguide approach is emphasised in this plot.

### 3.3.3 Out-of-Plane confinement

As we stated at the beginning of the chapter we would ideally like to restrict the set of wavevectors in the problem. For this reason, to simplify the out of plane dispersion, we would like to use a single mode waveguide. There are many different types of slab waveguide where a single mode condition can be obtained. The waveguides treated in this report are of two types;

weak vertical confinement (Low Out-of-Plane contrast - LOP)

strong vertical confinement (High Out-of-Plane contrast- HOP)

The full 3D nomenclature was very neatly summarised by Baets[5]. The former constitute the conventional laser type heterostructures which have been successfully utilised in the GaAs/AlGaAs and InP/InGaAsP systems for many years. Their relevance to this project is that LOP provides a narrow spectrum of out-of-plane wavevectors. The dispersion of the heterostructure system is therefore very gentle. As we will deal with many scattering interfaces in the 2D systems, a mode which is spatially distributed (it has small out of plane wavevectors) will scatter only moderately and as such low loss is predicted by a heuristic approach [6]. LOP also

provides a good starting point for expanding the functionality of active devices providing a substrate with good thermal and electrical conductivity. The alternative latter approach, HOP, involves either membrane (air-semiconductor-air) or Silicon-On-Insulator (SOI) and AlGaAs/Al<sub>x</sub>O<sub>y</sub> structures. The stronger confinement here corresponds to very large out-of-plane wavevector components. A small change in waveguide structure or in wavelength causes a large change in equivalent index. The membranes are required to be very thin which causes a structural headache, in that they must be capable of supporting their own weight (thermal and electrical conductivity problems arise too). The asymmetry of the waveguides, as we will see later, strongly influences the behaviour of our full 3D system. The reader may have noticed from Figure 3.5 that it appears difficult to have a true single mode waveguide with only one mode of a single polarisation. A membrane, being vertically symmetric allows complete decoupling of TE and TM modes. In this system it is then possible to have a double-moded waveguide (one TE and one TM), but excite only a single polarisation. In the other, asymmetric waveguides, TE/TM mode coupling is a liability which we need to alleviate, or avoid. So far the higher contrast PhC systems have been more successful in terms of low loss and high dispersion. The dispersion is dependent upon low losses as slower waves naturally spend more time circulating around the system. We will concentrate on LOP contrast systems in this Chapter and HOP contrast systems in Chapter 4.

In [7, 8, 9] the losses due to a 1D grating etched into a slab waveguide are considered. The geometry is essentially a side view of our structure, for which the out of plane contrast is gradually increased (the core index is held constant). It is found in [7] that losses in a perforated slab waveguide are low for LOP, tolerating scattering defect cavities and bends. In the case of HOP an operating region is found where quasi-Bloch modes can exist, for perfectly periodic structures. As the index contrast is increased the losses peak, making it therefore advisable to work in the extremes of either of the two regimes. In [10] the scattering loss is examined for waveguides (LOP→HOP) with a constant V parameter. In short a HOP waveguide has a substantially higher Numerical Aperture (NA) than a LOP guide and consequently recaptures more of the scattered light.

### 3.3.4 Coupling Ridge Waveguides

As well as photonic crystal structures we will also etch ridge waveguides into our heterostructure. These allow us to establish a well defined input mode for both simulation and experiment. To analyse these in 2D (top view) we use an equivalent index approximation [1]. We solve the slab mode at the wavelength of interest and use this equivalent index as the refractive index of the ridge, with an air cladding. Over a narrow bandwidth, for convenience, the equivalent index was fitted with a polynomial. Solving the 2D modes of the ridge waveguide yields an “effectual index”,  $N_{\text{group}}$  which is plotted in Figure 3.7.

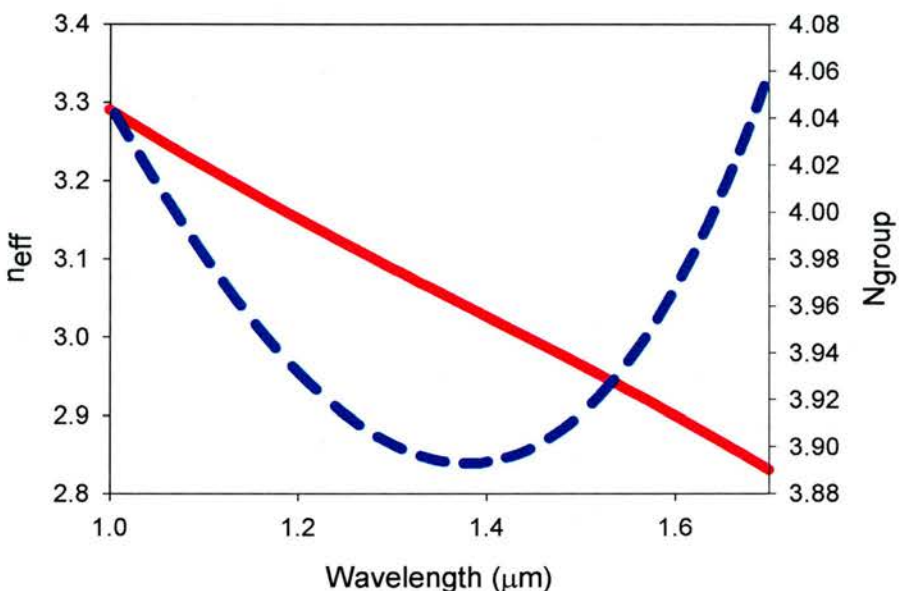


**Figure 3.7** The effectual index for the fundamental ridge waveguide mode across the telecommunications windows, the group index {see equation 3.16} is plotted indicating a zero dispersion point around  $1.39\mu\text{m}$

### 3.4 Bandstructure in 2D – In plane dispersion for a square of free space

We now need to acquaint ourselves with wavevector diagrams in 2D. How are the waves travelling in different directions represented? The bandstructure of a periodic square of free space is plotted in Figure 3.8a). The wavevector scale has been relabelled according to group theoretical considerations. The  $\Gamma$  point indicates a Bloch phase of  $k=0$  between neighbouring cells. Between  $\Gamma$  and  $X$  the phase in the  $x$  direction,  $k_x$ , evolves from 0 through  $\pi/a$  as in 1D. The band is folded back at  $k=0.5$  and as it has a group velocity,  $v_g = \frac{\partial u}{\partial k} = 1$  (in units of  $c$ ) intercepts the  $\Gamma$  point again at  $u=1$ .

In Figure 3.8b) the real-space  $z$  field components calculated at the points indicated are plotted. In each plot the real part of the complex field has been maximised.

- The first of these shows a wave travelling exclusively in the  $x$  direction, with a  $\frac{3}{4}\lambda$  (or  $3/2\pi$ ) wave fitting into the period. We can see that in the first figure the phase difference between  $y=0$  and  $y=a$  is zero and between  $x=0$  and  $x=a$  it is  $\frac{1}{2}\pi/a$ .
- Between  $M$  and  $\Gamma$  the phase of both  $k_x$  and  $k_y$  evolves equally in the opposite direction (this is simply for plotting convenience), from  $\pi/a$  to 0, resulting in a wave travelling diagonally across the space.
- The centre point is the most difficult to interpret. In the  $x$  direction, between  $X$  and  $M$ , the  $k_x$  phase is fixed at  $\pi/a$ . As the  $k_y$  phase rises from 0 to  $\pi/a$  the field starts to oscillate along  $y$ , with a quarter wave fitting at the point which has been plotted. This physically requires two waves. The waves are spectrally degenerate, and point in the two orthogonal directions of our grid.

It is now perhaps apparent that along  $XM$  we are also dealing with two waves, in our Cartesian representation. These remain, however, exactly in phase at each point between  $X$  and  $M$ . It is possible using a different set of lattice vectors to represent this as one wave.

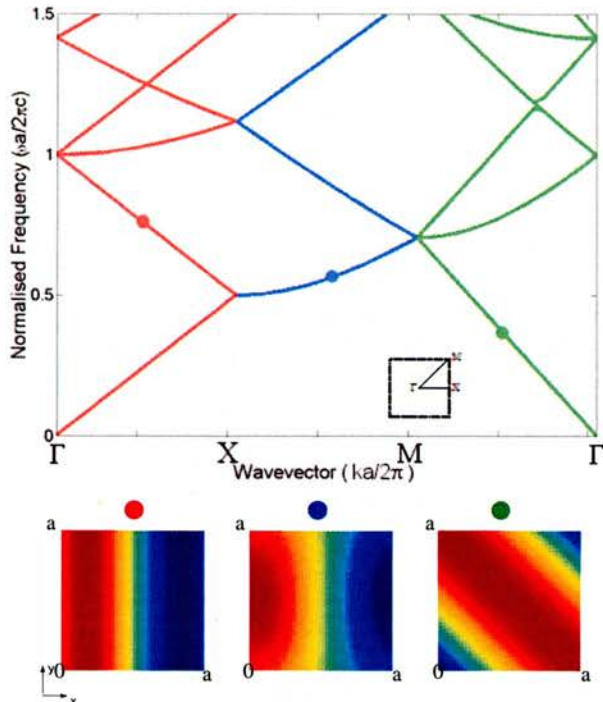


**Figure 3.8 a)** Free space wavevector diagram for the inset lattice structure ( $n=1$ )

**b) Fields plotted at marked points.**

The diagram that we have plotted traces along the edges of the IBZ (defined in Chapter 2). The reciprocal space representation of this k-space path is inset into Figure 3.8a). The eigenmodes that we will solve for more complex structures lie either on this path or just inside the edge of the IBZ.

It is worth noting the frequencies at which the  $\Gamma$  point intercepts occur; other than the trivial  $u=0$ , the lowest frequency crossings take place at  $u=1$  and  $u=\sqrt{2}$  as one might expect, given the square lattice. The first crossing points of X and M are  $u=0.5$  and  $u=\sqrt{2}/2$ . Introducing an infinitesimal index perturbation on this lattice will split open the bands at these points, as we observe in 1D. The stop band that this would create only has a partial effect on the optical transmission of this structure. Only when propagating directly along one of the corresponding real space lattice vectors would the field become evanescent. This is utilised successfully in many optical polymer gratings with weak 2D feedback provided by Distributed Bragg Reflection (DBR), using shallow embossed gratings [11]. Propagation is still allowed in all other directions, away from the lattice vectors. Ideally we would like a structure

which entirely forbids (or controls) wave propagation in the 2D plane, a 2D Photonic Band Gap (PBG).

There is one other factor, which we have ignored for several paragraphs - the polarisation, which obviously makes no difference in free space. We can see that the material interface reflectivity is modified for off axis angles of incidence, and that this is dependent upon the polarisation [12]. On the sub-wavelength scale of the Photonic Crystal lattices that we will investigate, the behaviour of the PhC becomes strongly polarisation dependent.

Due to the large ratio of the two lattice vectors  $a_2/a_1 = \sqrt{2}$ , obtaining a PBG might appear to be quite a tall order in a square lattice. Actually the answer is simply to increase the index perturbation further, to the point of creating a binary grating of air/semiconductor. Increasing the order of symmetry of the lattice also relaxes the ratio between the lattice vectors, e.g. for a hexagonal lattice this becomes  $a_2/a_1 = 2/\sqrt{3}$ .

The band gaps for two common lattices are plotted below (for a dielectric index of 3.31 corresponding to the equivalent index of the above waveguide at  $1.31\mu\text{m}$ ).

### 3.4.1 Pillars in Air – square lattice

In the first wavevector diagram we plot the eigenmodes for a square lattice of dielectric rods in an air background. The dielectric serves to couple the previously spatially degenerate waves. The dashed lines show that for the TM polarisation, only some of the spatial degeneracy has been lifted (along the  $\Gamma$ -M direction). For the TE modes shown by the solid lines, there are two frequency ranges where modes are entirely forbidden; i)  $u=0.223-0.246$  and ii)  $u=0.370-0.417$ . 225 plane waves were

used in this calculation, for a lattice with a fill factor of  $ff = \frac{\pi r^2}{A} = 0.454$ .

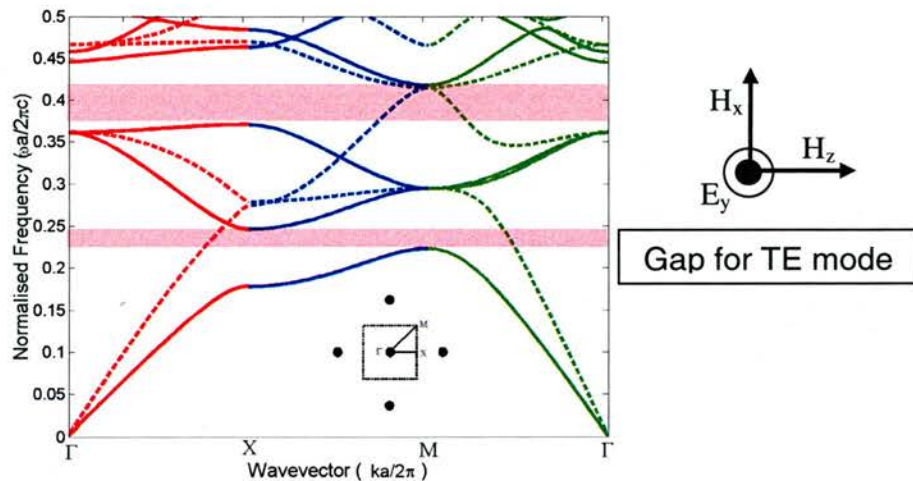


**Figure 3.9** Wavevector diagram for pillar of dielectric material in an air background, set in a square lattice ( $n=3.31$ ,  $R=0.38a$ ). Reciprocal lattice vectors are inset.

(TM modes dashed line, TE solid line)

### 3.4.2 Air Holes in Dielectric – triangular lattice

The higher symmetry of a triangular lattice allows a larger band gap, but for the opposite polarisation. For a triangular lattice of air holes etched into a dielectric background we have the reverse case. For the TM modes (indicated by the dashed line) there is a large photonic bandgap; between  $u=0.225-0.318$ , this has a width, relative to the gap centre frequency of  $\Delta u/u \sim 34\%$ . 225 plane waves were used in this calculation, for a lattice with a fill factor of  $ff = \frac{\pi r^2}{A} = 0.403$ .

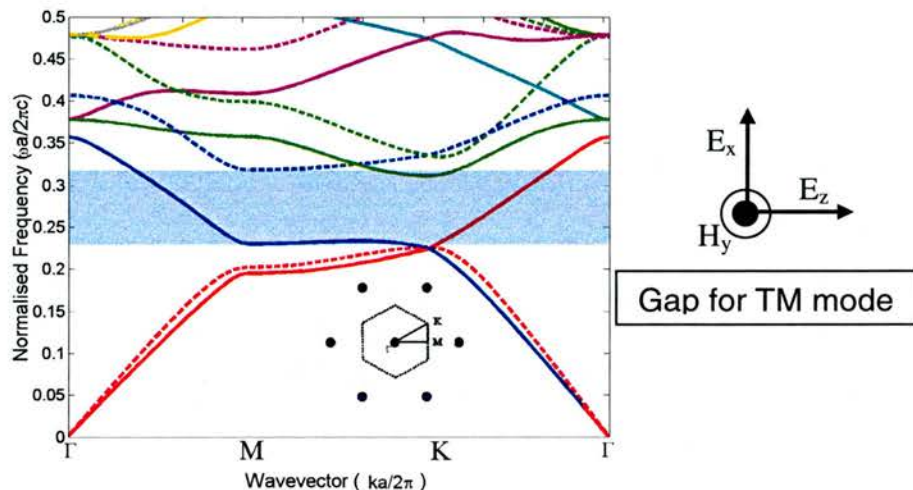


**Figure 3.10** Wavevector diagram for air hole in a dielectric background, set in a triangular lattice ( $n=3.31$ ,  $R=a/3$ ). Reciprocal lattice vectors are inset.

(TM modes dashed line, TE solid line)

For the TE modes (as shown by the solid lines) the degeneracy is now lifted in the  $\Gamma K$  direction and if we increased the hole radius beyond  $R=0.42$ , a small polarisation independent PBG would open. It is the large TM PBG that we will make use of in the remainder of this chapter. The ratio  $R=a/3$  provides a conveniently large bandgap, but is not the largest gap width. Small holes can be more difficult to etch deeply and as holes get bigger they encroach upon their neighbours and we can incur difficulties in patterning the PhCs due to electron beam dose proximity effects. We will tend to use this ratio as it is relatively easy to fabricate. We use this band gap with the assumption that the coupling between TE and TM modes can be avoided by careful design.

### 3.5 Coupled Cavity Waveguides

Coupled Cavity Waveguides (or alternatively Coupled Resonator Optical Waveguides - CROWs) were proposed by Stefano and Modinos [13] in 1999 and later by Yariv [17]. They constitute an entirely new class of waveguide, where the propagating field is localised to resonant cavities. The finite overlap between the evanescent fields in adjacent cavities permits tunnelling of the light along a chain of cavities. Two parameters are therefore available to us to control the speed at which the light hops between resonators, namely, the separation/evanescent field overlap between the cavities and the dispersion of the cavity mode itself. CCWs can be constructed from various elements such as ring resonators, microdisks, etalons, and in our case 2D PhC defect cavities. PhC defect cavities possess another useful parameter, which is the main motivation for our interest. PhCs are extremely functional in controlling evanescent fields and therefore we would anticipate further ability to manipulate the dispersion of these waveguides.

We have already examined some of the properties of CCWs in 1D, in Chapter 2. The addition of each successive cavity to the chain splits the cavity eigenfrequency,  $\Omega$ , and adds a further resonant peak to the spectrum. Each peak corresponds to a normal mode of the system. In the limit of very many cavities we form a band with an S shaped ( $\omega$ - $k$ ) dispersion given by the tight binding expression [14],

$$\omega(k) = \Omega[1 + \kappa \cos(k\Lambda)]. \quad \{3.8\}$$

The approach mirrors that of the Linear Combination of Atomic Orbitals (LCAO) from solid state physics.  $\kappa$  is the tight binding parameter given by the difference between the first order coupling coefficients and  $\Lambda$  the spacing between adjacent cavities.

Differentiation with respect to  $k$  yields the group velocity,

$$v_g(k) = -k\Lambda\Omega\sin(k\Lambda) \quad \{3.9\}$$

This presents a zero dispersion point at the band centre with high GVD of opposite slope on either band edge. Essentially we can operate in transmission and control the dispersion parameters in order to achieve pulse compression or dilation. In many cases the tight binding approach (as with coupled mode theory) has been applied by recovering the above parameters from experimental or calculation data.

The previous experimental work on PhC CCWs is now outlined. Using a microwave network analyser [14] the tight binding description of light propagating (by hopping) between cavities was experimentally verified in a square lattice of dielectric pillars in air with a lattice period,  $a=1.3\text{cm}$ , at a frequency of 11.5GHz ( $\lambda=2.6\text{cm}$ ). To impact upon the field of high contrast integrated optics the system was then dramatically scaled (by a factor  $\sim 10^5$ ) down to the optical regime. The study, using the highly successful internal source technique, by Olivier et al. [15] was limited to larger cavity types (orientated so that their hexagonal faces met -  $\Gamma\text{M}$ ), though showing remarkable agreement between PWE calculated bandstructures and experimental transmission spectra. The internal source was an InAs quantum dot layer embedded into a GaAs/AlGaAs heterostructure waveguide. The quantum dots were excited by focussing a visible diode laser near to the entrance to the PhC waveguides. The optical excitation was therefore point source-like. An objective lens was then used to capture the transmitted power, by focussing on the output side of the PhC, located behind the cleaved facet. The absorption of the quantum dots and dispersion of the heterostructure must be taken into account. Many PhC structures have been studied with this method, including lattices, and wide waveguides and large cavities [25].

Extending this work to smaller cavity systems proved to be difficult for the internal source technique. The mode mismatch between the point source excitation and the narrow waveguides appeared to constitute too great an insertion loss. Our own method, using an external laser source and tapered access waveguides, made it possible to couple light through these tiny cavities (orientated along  $\Gamma\text{K}$ ). Various access waveguide widths were investigated, including  $3\mu\text{m}$ ,  $1.5\mu\text{m}$  and  $\sqrt{3}a - 2r$ , as it was unclear how the cavity resonances would overlap with the guided mode [16]. In hindsight it appears obvious to match the widths of the input and coupled cavity waveguide exactly, keeping the width “piecewise continuous”, but the feedback and hence coupling mechanism to these cavities is aligned via the  $\Gamma\text{M}$  lattice direction. The cavities are more isolated when aligned along  $\Gamma\text{K}$  [24].

### 3.5.1 H1in1 CCWs

We now investigate this system starting from the properties of a single repeat unit of the cavity chain. We then look at how this system evolves with the relevant set of parameters, using a convenient time domain model. The fabrication of the structures is then discussed before presenting the results of transmission measurements. A short summary of the set of CCWs analysed in [24] is then presented.

To create a basic defect in a 2D lattice we can remove a single hole from the above triangular lattice. In order to compute the bandstructure for a waveguide consisting of a chain of defect states we again make use of a supercell, as we did in 1D. We will remove every second hole along the next nearest neighbour direction. In order to allow us to deal later with more exotic types of cavity we will alter the nomenclature (established in Yariv's paper[17]) to read "cavity type" in "spacer". So here we have a hexagonal cavity (one hole missing<sup>\*</sup>) "H1" and a single spacer "1", so this CCW is an H1in1. The extent of the supercell along the orthogonal direction needs to be wide enough in order to sufficiently decouple each defect waveguide from its neighbour. The supercell is now rectangular in both real and reciprocal space.

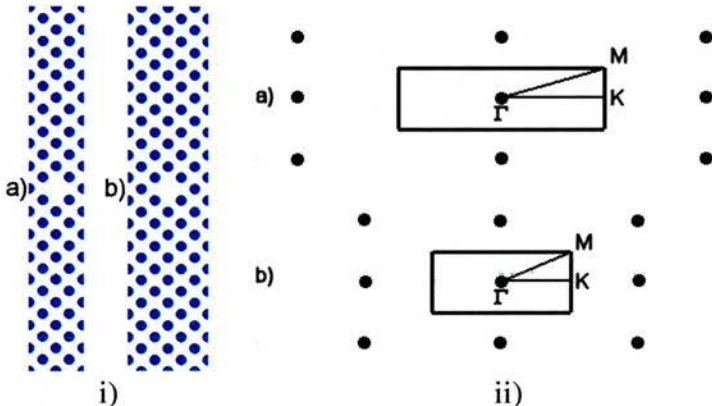


**Figure 3.11 i)** Supercells for a)H1in1 and b)H1in2 waveguides, ii) the respective rectangular reciprocal lattice vectors. As supercell becomes longer the IBZ contracts along the  $\Gamma K$  direction. The orthogonal direction is  $16\sqrt{3}a$  wide in this example.

The H1in1 bandstructure reveals two modes with opposite symmetries [18], see Figure 3.12 and Figure 3.13a) and b). Due to the high symmetry of the defect these two modes are degenerate at  $u \approx 0.27$ . This degeneracy has been noted to cause a dip

\* How a hole can go missing is a mystery to many of us. There is quite simply no easier way of saying that a single hole was omitted from the lattice. I personally prefer the tale of the nano-leprechauns.

in transmission at the frequencies where the modes cross. As an attempt to suppress the Fabry-Pérot “noise” evident in the transmission spectra, a set of waveguides were fabricated at an angle of 6° to the cleaved facets. This reduces the reflectivity for the fundamental waveguide mode, cleaning up the spectrum. In the case of the degenerate H1in1 modes, this allowed resolution of the transmission dip at the mode crossing.

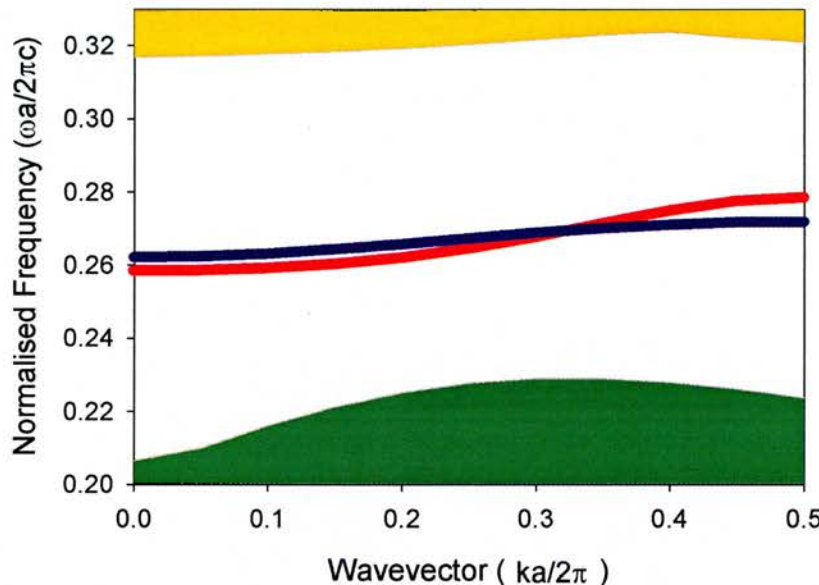


**Figure 3.12** Wavevector diagram for TM bands of H1in1 structure, along  $\Gamma$ K direction, calculated using MPB for  $R/a=0.3$ ,  $n=3.4$  (Blue narrow band Odd mode/Red broader band Even mode)

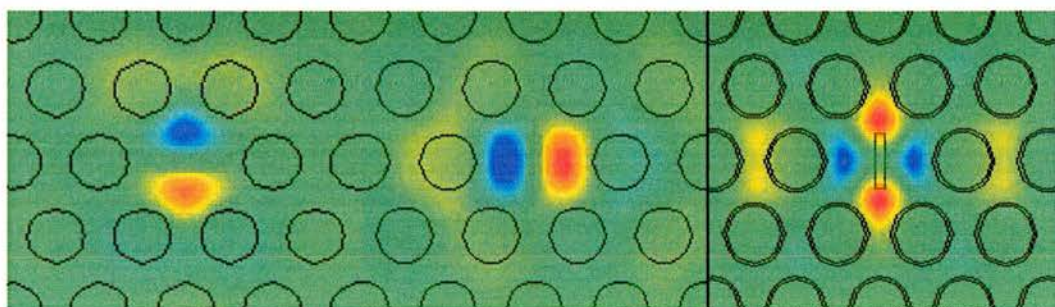


**Figure 3.13** The mid gap defect modes a) odd mode, b) even mode and c) the quadropole modes close to upper band edge even mode. These  $H_y$  field distributions are calculated for cavities surrounded by 7 layers of PhC and then PML.

The infinite bandstructures in this section are calculated using a freely available software package[19], MPB. This is a more sophisticated plane wave model, with excellent convergence performance, enhanced by preconditioning the matrices.

Fully-vectorial eigenmodes of Maxwell's equations with periodic boundary conditions were computed by preconditioned conjugate-gradient minimization of the block Rayleigh quotient in a planewave basis\*. The supercell optimisation and the bandstructure calculations were performed by Stefano Boscolo, at the Università degli Studi di Udine, Italy [20]. The supercell is Fourier Transformed from a real space representation.

In this section of the report we project the bandstructures. This assumes that once we have approximated the heterostructure waveguide behaviour (with an equivalent index) the structure is then 2D (it does not vary in the 3<sup>rd</sup> dimension). We can restrict the bandstructure to plot only the points of interest, for instance we may choose the maxima of the lower band and the minima of the upper band. This forms a very useful method for scanning various structural parameters, and thus comparing the strength of the bandgap. These so called "band maps" have been used to characterise the dependence on index configuration, hole shape and lattice types [21, 22]. Here we calculate a slightly different type of bandmap. We use 2D FDTD and excite a finite waveguide with a source (of even symmetry) and monitor the fields transmitted by the structure. We can determine the evolution of the defect state and the surrounding bands with respect to the parameters; hole radius and background index. Here we plot a "transmission bandmap"[23] which is the spectral transmission of the 7 cavity H1in1 CCW plotted versus hole radius, see Figure 3.14. The normalised parameters are considerably less relevant here as the absolute values of the transmission are determined by the FDTD source launch conditions, which are suited to a particular lattice constant. The centre wavelength was 1.31μm and the lattice constant,  $a=370\text{nm}$ . A PBG opens up at  $R/a=0.108$  and a defect state evolves from a centre wavelength of  $\lambda\sim1.55\mu\text{m}$  to  $\lambda\sim1.1\mu\text{m}$ . The PBG and the defect mode become indistinct beyond  $R/a=0.44$  as the holes then encroach upon one another and the narrow dielectric veins between the holes, require high spatial resolution, necessitating very rapid field variation. At longer wavelength the fields ignore this fine structure. Another symmetric mode can be seen on the upper band edge (at  $\lambda=1.1\mu\text{m}$ ,  $R=140\text{nm}$ ).

---

\* Rapidly becoming the most quoted phrase in the electromagnetics literature, on a par with "it has long been known"

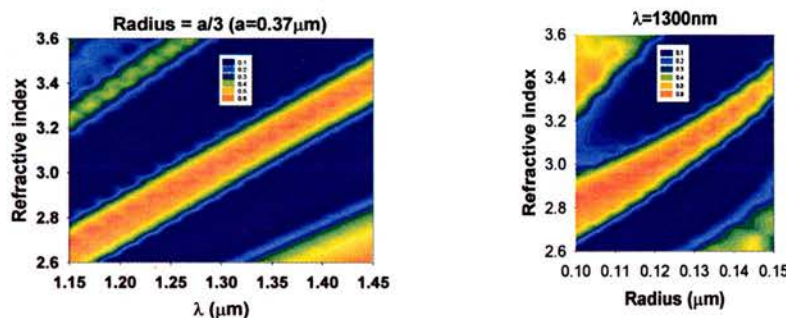
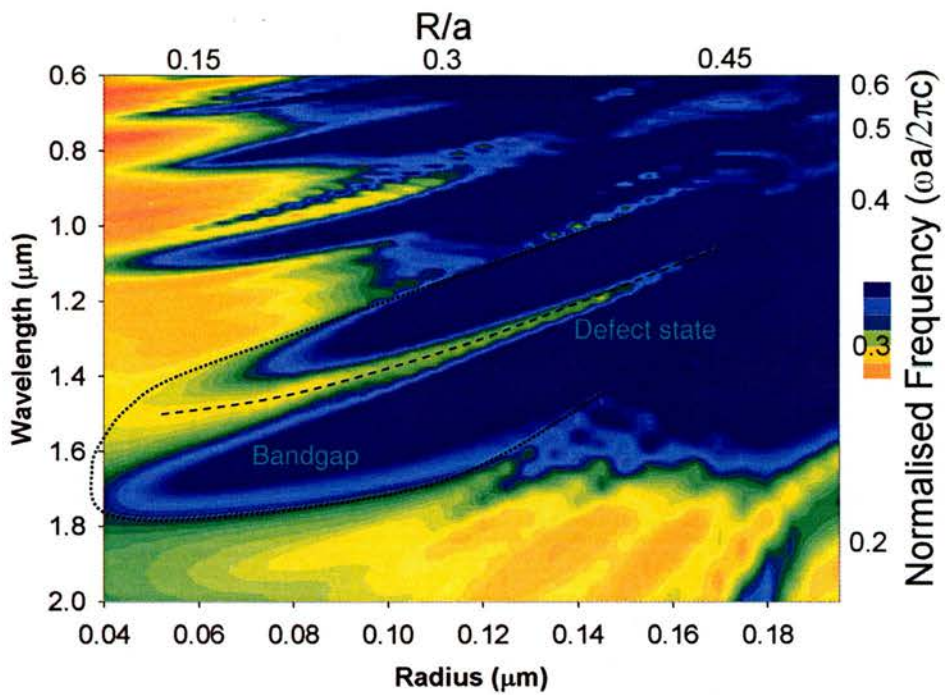


**Figure 3.14** Transmission bandmaps of CCW with  $a=370\text{nm}$ , for a) fixed refractive index ( $n=3$ ), b) fixed radius ( $R=a/3$ ), and c) fixed wavelength ( $\lambda=1.3\mu m$ )

### **3.6 Fabrication**

We now turn our attention to actually producing the waveguides. The heart of the technique is a two step dry etch process. This technique is fairly similar regardless of the material system. For the GaAs based PhCs in this report we have used a SiO<sub>2</sub> mask to transfer our desired pattern into the semiconductor. The SiO<sub>2</sub> mask is deposited by a PECVD (Plasma Enhanced Chemical Vapour Deposition) process (at the University of Glasgow), and was either 200nm or 300nm thick (in later work, for deeper etching). To define the pattern into this hard mask a 200nm PMMA (Poly(methyl methacrylate)) layer was spin coated onto the SiO<sub>2</sub> surface. The PMMA is an electron beam resist and is patterned using a Scanning Electron Microscope (SEM) by focussing a ~15nm spot onto the surface of the PMMA and exposing the resist. The desired design, having been corrected for proximity errors, is raster scanned with a Leica EPBG15 pattern generator[24]. The design files are generated with a combination of Matlab script files and Wavemaker to ensure minimal file size and low human error via efficient use of symmetry, scaling and replication. The smaller structures, which require a higher resolution, are placed on a separate mask layer to the larger features. The sequence in which these layers are written is discussed below. The exposed areas of resist are then removed in a development stage and the pattern checked under an optical microscope or SEM (at low current). We then choose a Fluorine based Reactive Ion Etch (RIE) process. The RIE comprises a large capacitor driven at an RF frequency of 13.56MHz, to accelerate ions of CHF<sub>3</sub> onto the cooled cathode upon which the sample rests. The capacitor plate separation, the RF power and the gas pressure are independently optimised to obtain roughly straight (80°) side walls. A mass flow controller determines the input gas flow rate and a butterfly valve controls the venting to a turbo pump to initially create the necessary pressure to enable a plasma to be struck, and thereafter maintains the plasma at lower working pressure to complete the etch. The basic outline of this process is schematically represented in Figure 3.6. The second stage of the etch process is critically dependent upon the quality of this etch mask.

We now use a Chlorine-based etch chemistry to transfer the mask pattern into the semiconductor. Earlier samples were entirely fabricated at Glasgow. The St Andrews system which came online in the latter half of 2001, is a Chemically Assisted Ion

Beam Etching (CAIBE) system. The core of the system is an  $\text{Ar}^+$  ion beam, accelerated by a pair of molybdenum grids, which have been pre-aligned to collimate the  $\sim 3\text{cm}$  wide beam. This positively charged beam is neutralised by the addition of hot electrons emitted by a tungsten filament (the otherwise purely positive charges repel and act so as to un-collimate the beam). The Chlorine is introduced into the vacuum chamber a small distance above the sample. The dissociation of the  $\text{Cl}_2$  adds a chemical component to the etch chemistry preventing the non-volatile compounds, which can form, from coating the sides of the high aspect ratio holes. The unique balance of the system is dependent upon base pressure, mediated by Ar and  $\text{Cl}_2$  flow rates, acceleration voltage, ion beam current, neutraliser current and  $\text{Cl}_2$  concentration and temperature at the sample. Where this process has been completed at the University of Glasgow  $\text{SiCl}_4$  has been used in a second RIE process.

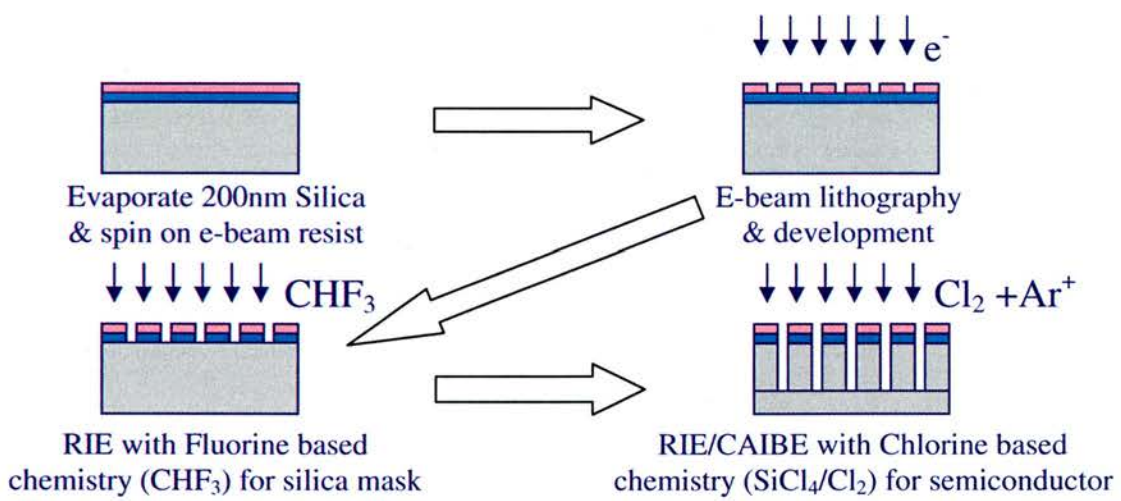


**Figure 3.15 The basic steps taken to fabricate deeply etched PhC waveguides on GaAs heterostructure (process flow is indicated by the arrows)**

The typical development cycle includes the etching of test patterns, usually comprising a set of bare photonic crystal lattices with  $a=210\text{-}410\text{nm}$ . These are cleaved to reveal the success of the etching. This cycle is iterated ( $\sim$ half a dozen times) with a fresh set of test patterns and eventually the optimised etching parameters are applied to the etching of the waveguide samples. On the waveguide samples the larger features (when defined at Glasgow) use a larger spot size ( $\sim 50\text{nm}$ ) and are simultaneously etched along with the PhCs. As the critical feature sizes are those of the PhCs the etching is tuned to provide the best features at this small scale. At the larger scale these conditions may not be ideal. In large open structures obtaining a

high local base pressure is more challenging. In practice the etching conditions have been relatively commensurate in the different regions, despite this difference. Following several production cycles, the decision was taken to extend the area patterned by the smaller spot size, to include the ridge waveguide tapers, which connect directly to the PhCs. Writing the various layers of the mask with different resolutions at separate times was causing a high rate of stitching errors. These errors cause much greater scattering loss if they occur at the intersections between smaller waveguides, due to the greater field densities. Figure 3.16 shows a cutaway schematic of the basic structures that we aim to fabricate.

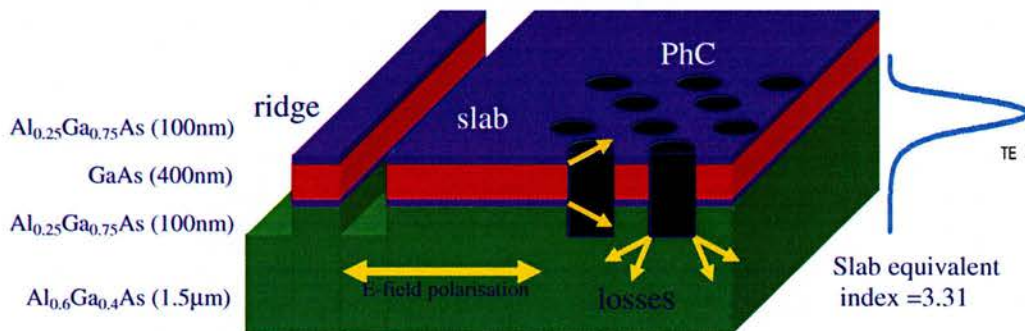


**Figure 3.16 Schematic of heterostructure waveguide with deeply etched PhC and ridge waveguides, the TE mode profile is inset. The E field polarisation is noted along with the sources of loss including intrinsic diffraction and scattering of components of the mode profile which extend beneath the etched features. On the right hand side is the layer structure of the waveguide, dubbed by Ron Hadley as the “Scotland” structure, this waveguide was designed and grown by M. Steer at the University of Sheffield.**

An example of the optimised etching is shown in Figure 3.17. Inset are images of the Silica mask showing the shape of the developed holes after the RIE stage. The CAIBE produces holes in GaAs of approximately  $2\mu\text{m}$  depth with vertical sidewalls and flat bottoms. Typical etch parameters to produce this quality of hole include; an acceleration voltage of  $V_{\text{acc}}=300\text{V}$ , temperature,  $T=105^\circ\text{C}$ , beam current of  $I_{\text{beam}}=17.5\text{A}$ , for a duration of 15 minutes. This amounts to an etch rate of approximately  $135\text{nm}/\text{minute}$ . The discharge voltage is set to  $40\text{V}$  and the acceleration ratio maintained at 0.15. The Chlorine flow rate is in the region of  $8\text{sccm}$  for an Argon flow rate of  $20\text{sccm}$ . The base pressure fluctuates around  $3\times 10^{-4}$  Torr.

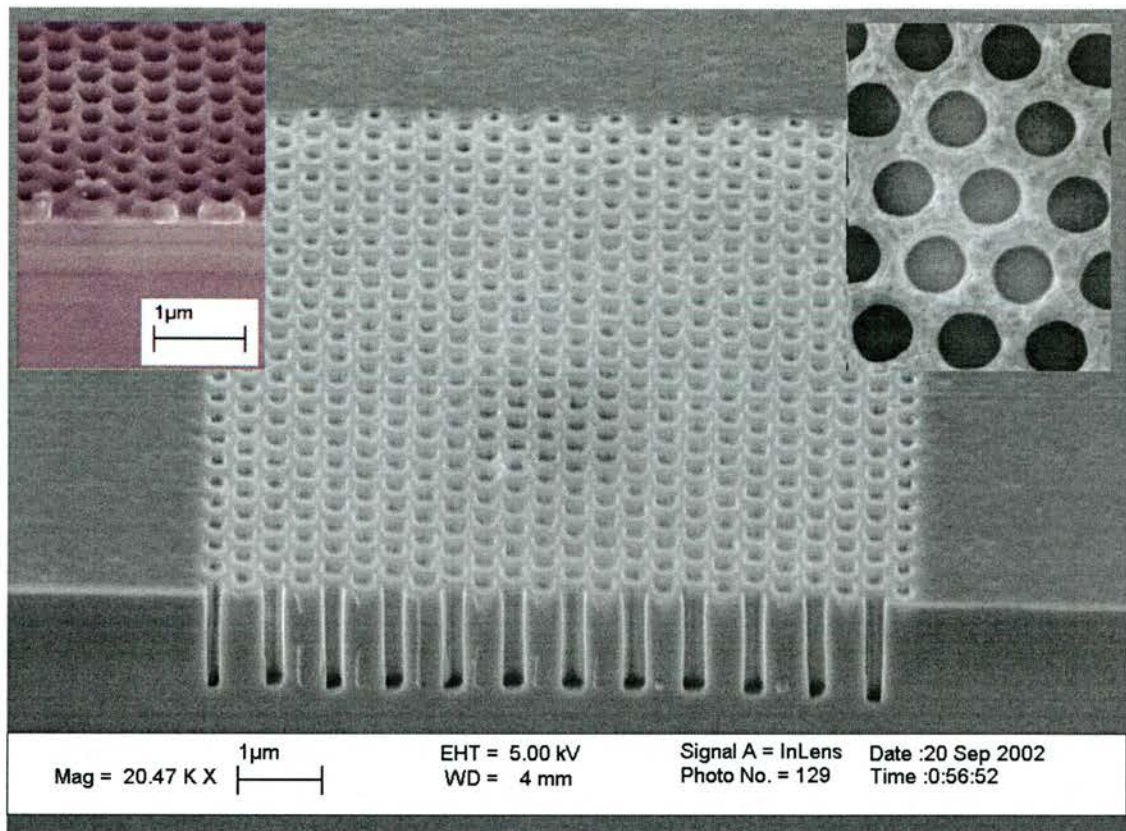


Figure 3.17 Having defined the pattern in PMMA the SiO<sub>2</sub> mask is Reactive Ion Etched to provide the etch mask for the GaAs etch. The results can be seen here from the top and from the side. The holes can be seen to be roughly circular, some hangover remains from the discretisation of the original design. SEM image of air holes etched 2μm into GaAs heterostructure using Chemically Assisted Ion Beam Etching (CAIBE) with Cl<sub>2</sub> chemistry, at St Andrews. Sample is tilted at 45 degree angle.

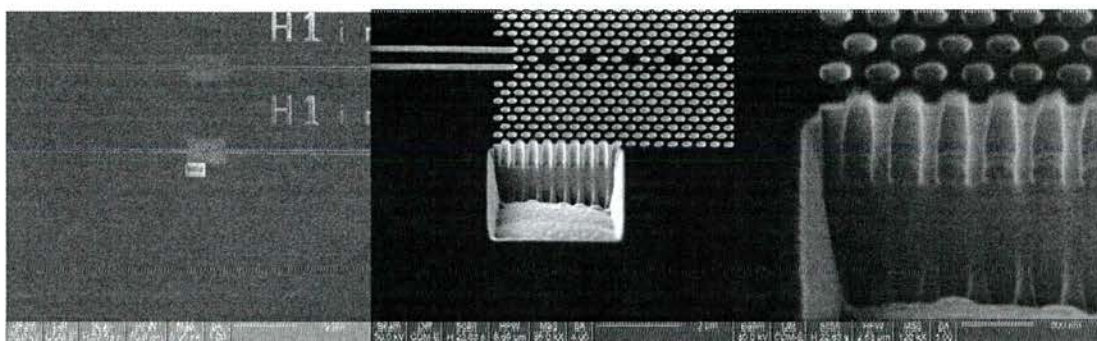
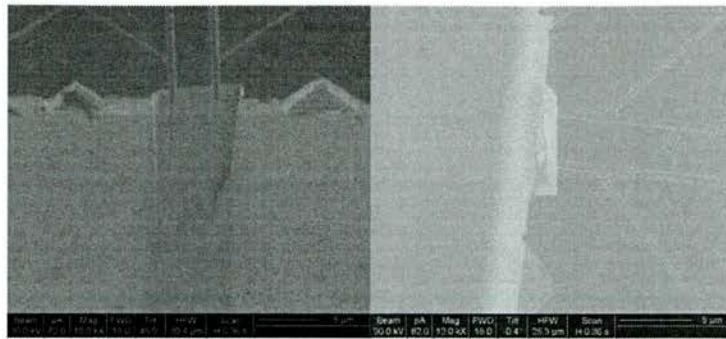


Figure 3.18 Focussed Ion Beam etching was used to inspect the etch profile without cleaving or destroying the sample. a) Overview showing the PhC. b) Trench cut for inspection c) Hole shape These PhC holes fabricated at Glasgow using RIE widen towards the bottom, perhaps explaining the spectral blue shifts observed in measurements. The lower structure on the RHS image is a shadow caused by the FIB milling. Images courtesy of Matthew Hill and Martin Cryan at University of Bristol



**Figure 3.19** FIB etching was also used to prepare the facets for initial pulse measurements. The waveguides were cut at an angle of  $\sim 7^\circ$ . This successfully suppressed the F-P effect in the input waveguide. Images courtesy of Chris Morgan at University of Cambridge

### 3.6.1 Results

Lithographic Tuning<sup>1</sup> is a well established method for mapping the transmission of 2D PhCs [25]. Mathematically similar structures are examined over the same wavelength range and the spectra are normalised to the length scale. In order to produce the graph below (Figure 3.20), we have fabricated structures with lattice constants in the range,  $a=310\text{-}450\text{nm}$ . This then corresponds to a normalised frequency range  $u=a/\lambda=0.23\text{-}0.36$  for a tunable laser with a bandwidth of  $\Delta\lambda=100\text{nm}$  around a centre wavelength of  $\lambda=1310\text{nm}$  (ie. 1255-1365nm). For our heterostructure waveguides the PhCs are similar in the 2D plane, but the waveguide prohibits true scaling of the structure. Thus we must examine the possible sources of error. Firstly, however, we take a brief look at other characterisation options.

The alternative and perhaps simpler technique is to characterise the waveguides with a wide band source (by wide we refer to  $\Delta\lambda=400\text{nm}$ ). Such sources typically offer very low spectral density e.g. halogen bulb ( $<50\text{dBm/nm}$ ) or multiple Light Emitting Diode source ( $>33\text{dBm/nm}$ ). Wide band multiple laser sources are available, which exhibit high spectral density ( $>1\text{dBm/nm}$ ), but are very expensive. Supercontinuum sources are only pseudo-CW (sub ns-pulsed) and provide a mid-range spectral density( $>20\text{dBm/nm}$ ). Erbium Doped Fibres are the basis for another type of

<sup>1</sup> Lithographic tuning takes advantage of the gentle dispersion of the waveguide into which we etch our PhCs. The linear scaling of the Helmholtz equation is again utilised to allow a tuneable light source to be utilised more effectively and essentially span a greater frequency bandwidth. Samples are fabricated with incremental scaling factors and characterised with the one source, the spectra are then plotted in Normalised Frequency units and overlapped (if the scaling is small enough). In this way a source with a 100nm tuning bandwidth can characterise a normalised frequency span far in excess of  $\Delta u=0.02$ . The dominant error is due to the finite difference in the heterostructure waveguide dispersion at the extremes of the bandwidth.

Amplified Spontaneous Emission source providing modest bandwidth with relatively high spectral bandwidth(>-13dBm/nm). Collimating and injecting such a wide bandwidth into the samples is non-trivial. The mode diameter of a Single Mode Optical fibre (6 $\mu$ m) is large compared to the waveguide dimensions, whilst a white light filament is ~500 $\mu$ m in diameter. Ideally achromatic optics are required to focus such a wide range of colours without aberration. Broadband antireflection coatings are crucial to maintain high throughput. The goal is to excite solely the fundamental waveguide mode over as wide a bandwidth as possible. In our case we use aspheric lenses and thus the spectral launched power decreases away from the focussing wavelength. This is more pronounced for higher magnification lenses. When working with short pulses, as pulse durations decrease and correspondingly their spectral bandwidth increases, achieving broadband coupling becomes important.

Wide band techniques also impose the material and dispersive properties of the waveguide upon the spectrum of the device. In essence we include absorption features and the long wavelength (lossy/dispersive) behaviour of the waveguides. In some cases this can mask interesting features.

Lithographic tuning is preferred in our case as we wish to use our devices in select wavelength regions. In particular to this chapter, obtaining the correct features at 1550nm was very important. By using a source with a modest bandwidth ( $\Delta\lambda=50$ -100nm), and many similar samples we can evaluate the device qualities of the photonic structure over a wide range of normalised frequency, without large variations in equivalent index or absorption. This is similar to the ideal non-dispersive case that the simple PWE or FDTD model assumes.

Etch depth is the final parameter to explore. This can depend on the fabrication technique, as reactively ion etched samples tend to suffer RIE lag, where smaller features etch to a shallower depth. If we consider etching into a uniform piece of semiconductor, the RIE etched sample would scale almost volumetrically, with feature size. Whereas a CAIBE etch can provide almost uniform etch depth over a wide range of feature sizes. In the presence of the heterostructure waveguide, where

the optical mode is bound in its vertical position the CAIBE seems more complimentary to our technique.

### 3.6.2 H1in1 Transmission and Reflection

Our characterisation setup is discussed in more detail in Chapter 4. The transmission of the H1in1 system, pictured in Figure 3.25b), is shown in detail in Figure 3.20. The light is injected and captured by identical tapered ridge waveguides. Two wide peaks in the spectrum correspond to the even CCW waveguide modes. The 3D FDTD bandstructure for the supercell etched into the GaAs heterostructure is plotted in Figure 3.21, displaying a pair of distinctive S shaped bands. The full experimental ridge-PhC-ridge system is modelled using 2D FDTD, predicting a ~52.3% maximum transmission into the fundamental ridge mode at  $u=0.275$ , with a reflection into the fundamental mode of ~7.6%, see Table 3-1. Firstly, why is there such a large (50%) discrepancy between the total power launched and that which is captured? And secondly why is there also disagreement between 2D model and 3D experiment?

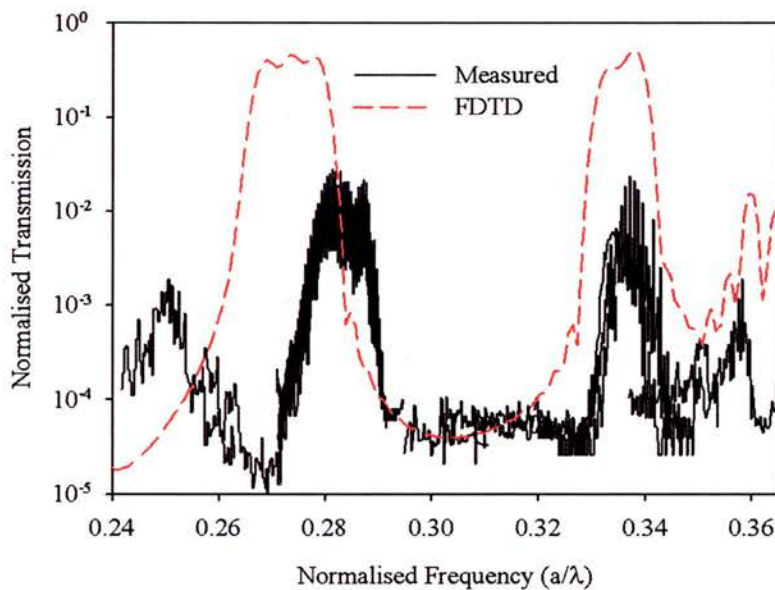


**Figure 3.20 Transmission spectrum of defect bands in the H1in1 waveguide. A 2D FDTD spectrum is shown for comparison. Defect bands are noted to have blue shifted in the smaller structures. There is a large discrepancy in transmitted magnitude. This indicates a high out of plane loss.**

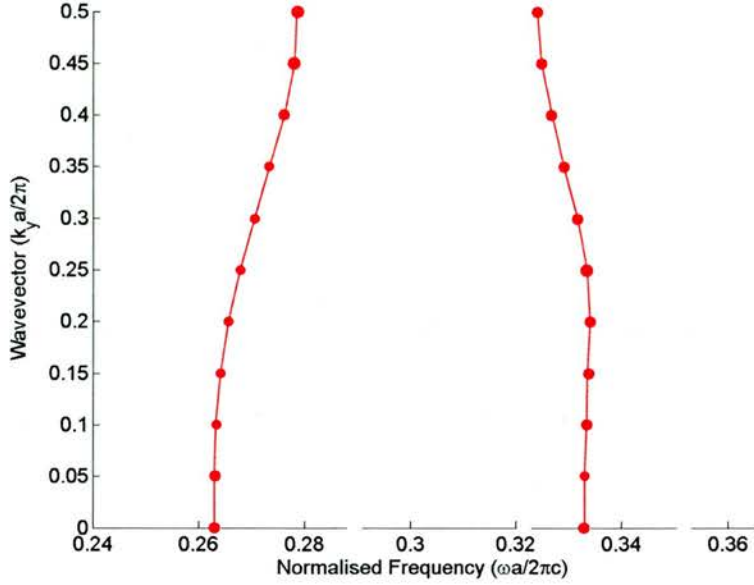


**Figure 3.21** 3D FDTD band diagram for the even modes of the H1in1 waveguide. The etched holes in this 3D model have vertical side walls and the band diagram agrees with the 2D FDTD transmission spectrum with its equivalent index approximation. The blue shift of the experimental data is very apparent.

In 2D the only possible leakage from the cavities occurs in the x-z plane. The isolated cavities have a Q factor  $Q=\omega/\Delta\omega \approx 300$  [26]. This tends to suggest that the leakage through the PhC is very low. Hence any substantial optical losses in our 2D model must occur at the ridge-PhC interfaces. The difference between the isolated cavities and the short CCWs, is that the cavities at the ends of the chain see far less feedback from the PhC than those in the centre of the chain [27]. This gives rise to surface states which localise at the interface to the CCW and channel power away from the ridge waveguides. To capture all the power exiting the 2D model we surround the computational domain with a set of power monitors and sum these to yield the total reflection from and transmission through the crystal. As expected the transmission through the sides of the PhC is negligible.

Reflection from the PhC occurs due to the high impedance mismatch between the ridge and PhC waveguide. There are several works which calculate the impedance [27, 28] or immitance [29] for PhC waveguides, we choose the scheme in [28], which defines the impedance,  $Z_{PhC}$ , of a Bloch mode in a PhC to be,

$$Z_{PhC} = \frac{E_x}{H_y} = \frac{|E_x|^2}{E_x^* H_y} \quad \{3.10\}$$

Where x is transverse, y is vertical (out-of-plane) and z is the propagation direction, valid for TM modes in 2D. On an x-y symmetry plane of a PhC supercell,  $Z_{PhC}$  is a purely real quantity. For the H1in1 we calculate this to be  $434\Omega$ , compared to around  $113\Omega$  for the ridge waveguide. The ridge waveguide has a lower impedance than free space,  $Z_0=377\Omega$ . The reflection anticipated from the interface between the two waveguides is then given by,  $\Gamma = \frac{Z_L - Z_B}{Z_L + Z_B}$ ,  $= 35.6\%$ . Summing the reflected power around the boundaries yields a 29% back reflection and repeating for the transmitted power, 70.9%. Implementing this scheme for the other waveguides summarised in the next section, demonstrates that the impedance is a very useful quantity for PhC waveguides. The spectral dependence of the impedance is plotted in Figure 3.26. The impedance, predicted reflection and calculated reflection into the ridge waveguides are summarised in Table 3-1. In Table 3-2 the total reflected and transmitted fields values are given. The field enhancement at the peak of transmission relative to the transmitted power is a consequence of the two reflective interfaces. We will make use of this reflectivity in the pulsed experiment at the end of this chapter. The field enhancement is calculated and displayed in Table 3-2, it is not dissimilar to the Standing Wave Ratio calculated by Boag [30].

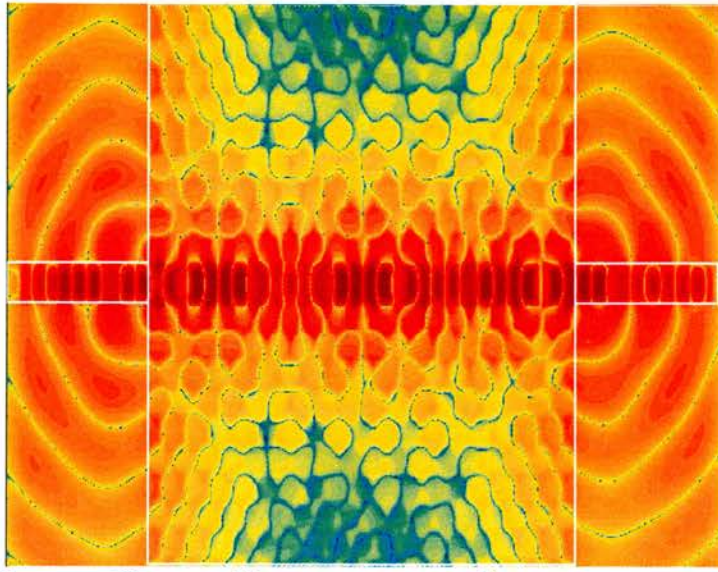


**Figure 3.22 Surface states at the boundaries to a L2in1 PhC CCW channel power away from the ridge waveguides and into the surrounding cladding. The white boundaries denote the ridge waveguides and PhC region ( $19a \times 10\sqrt{3}a$ ).**

We have not yet answered the second question - why does the 2D model not agree with the 3D measured transmission? The actual maximum measured transmission is ~3%. The additional discrepancy indicates the high confinement of these small cavities is causing a significant loss when considered in the 3D setting of a heterostructure waveguide. This loss impacts upon the bandwidths of the CCW modes as the coherent reflections from the PhC lattice are diminished, by the loss of field. The change in bandwidth affects the dispersion of the mode and hence the modes become flatter, lowering the group index at the centre of the band. This increases the reflectivity of the 3D ridge-PhC interface via the adjustment to the mode's impedance. We will show, at the end of the chapter, why the CCW patterning itself causes much of this additional loss.

The frequency offset (blue shift) of the spectra was attributed to a thin oxide skin on the inside of the holes in [24]. Applying an oxide skin to the 2D FDTD model allowed spectral agreement between measurement and model. The subsequent Focussed Ion Beam (FIB) characterisation [Figure 3.18] cast some doubt upon this analysis. The FIB uses Ga ions to etch/cut sections out of the structure, providing a fairly non-destructive analysis. The hole radius created by the Glasgow etching can

be seen to be slightly conical, increasing with depth, which could also account for the blue shifts. Despite this structural tuning dependence the lithographically tuned spectra stitch together admirably. This bodes well for the ability to tune these cavities by modifying the refractive index of the GaAs.

### 3.6.3 Coupled Cavity Waveguides – summary

This measurement technique favours the even modes of the system as the even cylindrical spatial mode emitted from a Single Mode Fibre is collimated and imaged onto the waveguide facet. Figure 3.23 summarises the strongest transmission peaks of the structures displayed in Figure 3.25. The 3D FDTD calculated dispersion curves for these modes is plotted in Figure 3.24. The variation between the transmission spectra for each PhC waveguide can be attributed to the factors discussed above in section 3.6.2, for the H1in1 CCW.

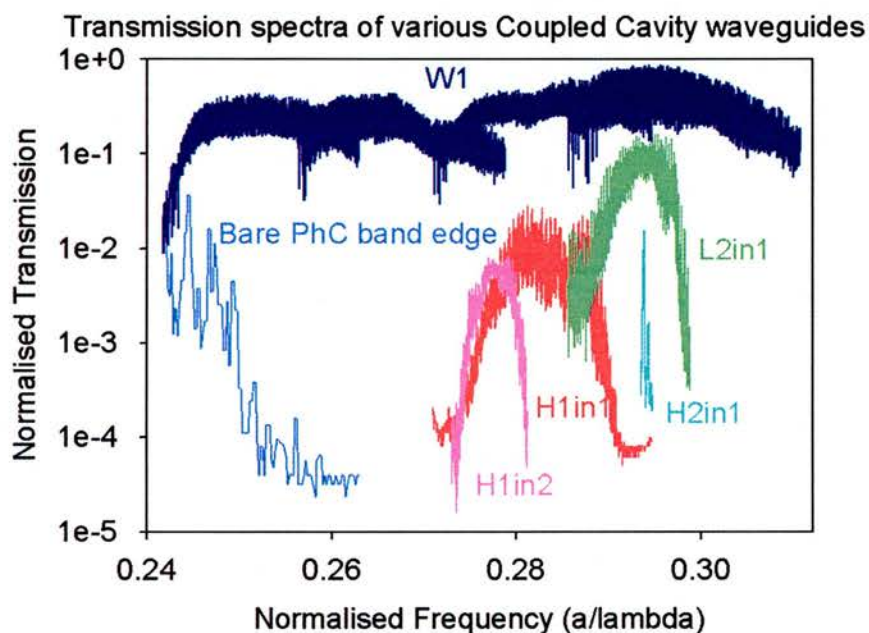


**Figure 3.23 A summary of measured transmission spectra of the various types of 2D CCW studied in the “Scotland” heterostructures**

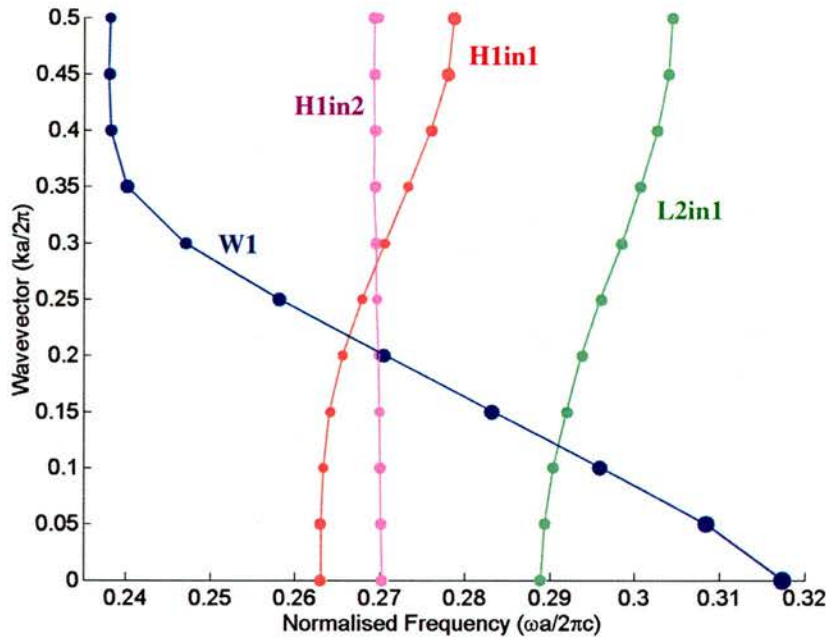


**Figure 3.24** 3D Bandstructure for the measured even bands for the **W1**, **H1in1**, **H1in2**, and **L2in1** waveguides. Note that other bands exist for these waveguides, but have either odd symmetry, are difficult to couple to because have vastly different group velocity from the input waveguide or are very lossy. The **H2in1** proved to be very difficult to model and is not included here. The period  $a$  of each waveguide, refers to the length of the CCW period.

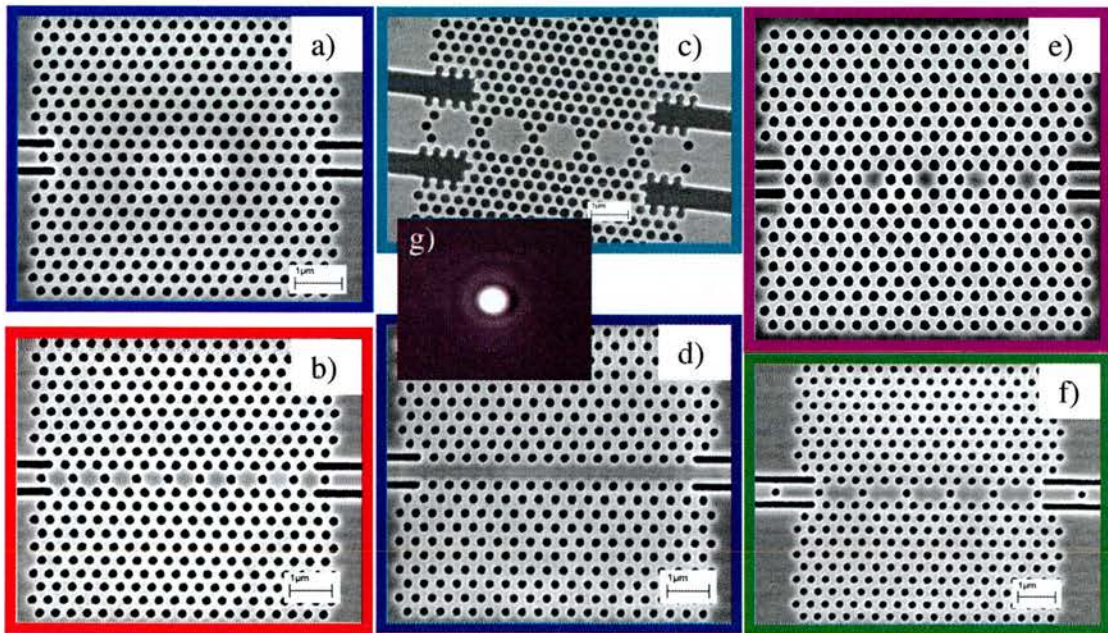


**Figure 3.25** SEM micrographs of CCWs measured in Figure 3.9 a) bare lattice, b) H1in1, c) H2in1, d) W1, e) H1in2, f) L2in1 g) Angled facet showing single mode launch into multimode tapered waveguide

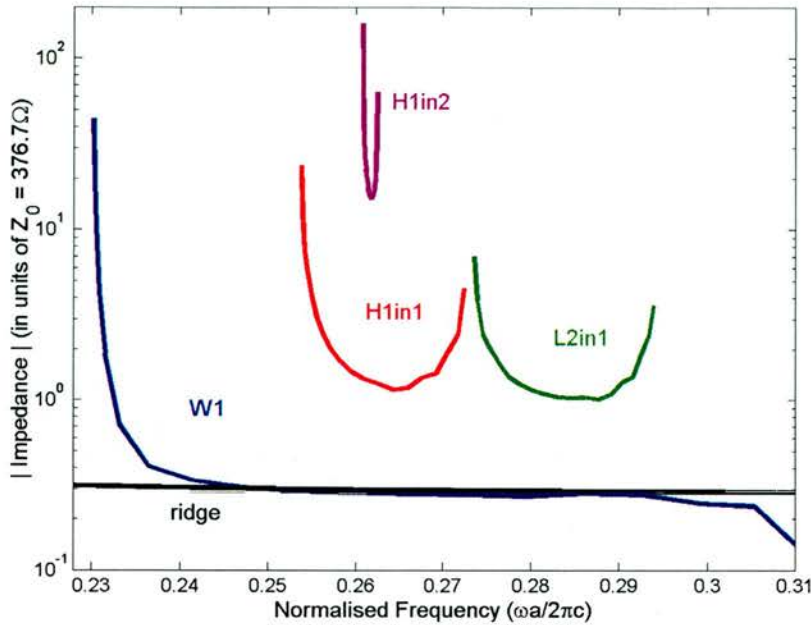


**Figure 3.26** 2D impedance calculated for the various waveguides, plotted in units of  $Z_0 = \sqrt{\frac{\mu_0}{\epsilon_0}}$ , the impedance of free space. Equivalent index approximation used, note the slight red shift with respect to the 3D bandstructure of Figure 3.24

Waveguide	Width of Band 2D / 3D	Group Index 2D / 3D	Impedance 2D ( $\Omega$ )	Predicted Reflection (%)	Transmission / Reflection (%)
H1in1	0.0192 / 0.0158	14.1 / 17.9	434	35.6	52.3 / 7.6
H1in2	0.00168 / 0.00089	222.2 / 378.8	5934	92.9	3.2 / 62.7
W1	0.0823 / 0.0792	3.7 / 3.9	110	~0	97.3 / 0.01
L2in1	0.0207 / 0.0157	16.4 / 21.0	377	30.2	62.4 / 4.1

**Table 3-1** Summary of the calculated PhC parameters, comparing the 2D and 3D calculated bandwidths and the effect this has on the slope of the bands. The impedance and the predicted reflection at the ridge-PhC interface. The calculated reflection and transmission into the coupling ridge waveguides.

Waveguide	Transmission / Reflection (%)	Field Enhancement
H1in1	70.9 / 29.0	5.10
H1in2	7.3 / 92.5	32.12
W1	97.3 / 2.7	1.08
L2in1	69.7 / 30.3	3.56

**Table 3-2** The total reflected and transmitted power calculated by summing around the 2D FDTD boundaries. The field enhancement inside the structure relative to the transmitted field.

The H2in1 waveguides here were deliberately written at a 6° angle to the normal to the chip facets. Earlier investigations showed that the tilt could suppress backreflections into particular waveguide modes and reduce the F-P fringes in the transmission spectra. The transmission spectra of the defect peaks for these waveguides were markedly “noise free”. The waveguide was cleaved at the narrow end of the taper to check the single moded behaviour. This is shown in Figure 3.25g. Two dimensional arrays of H1, H2, H3, and H4 cavities were also studied, in transmission, revealing broad defect peaks. The classification of these cavities follows Smith [31]. These superlattice devices are examined using a TMM in [32]. It is not clear how best to couple to these arrays in a linear waveguide geometry, the side coupling of larger cavities and waveguides is examined in [33] for a cavity excited by focussing a laser on 3 imbedded layers of InAs quantum dots. Much larger cavities (H6in1 along  $\Gamma M$ ) have been formed into a Coupled Cavity Waveguide Laser with chains of 40 cavities [34]. A recent out of plane study has indicated group velocities as low as 0.008c, in a 2D array of “S1” (single missing hole) square lattice defects [35]. Notably a slight x-y discrepancy in the SEM patterning lifted the degeneracy of the dipole-like modes. In the experiment some 3600 cavities are excited and hence coupled together. The resultant 7nm linewidths reported correspond to a Q of 220, confirming the high uniformity of the pattern definition.

The bands displayed here represent the even modes of the system, those which can be coupled to from an even mode, allowing us to couple efficiently from fibre. The bandwidth of each defect waveguide can be seen to be vary enormously. As we might expect, the H1in2 band narrows significantly compared to the H1in1, due to the

increased isolation. The H2in1, however, has a much narrower band as the mode is relatively well confined to the cavity. The L2in1, of all the CCW structures, appears to have large bandwidth and the highest transmission. The dispersion of these short PhC structures is now of interest, as we are aware of the large impedance at the interfaces of the device. Remembering for short 1D structures that the transmission band was characterised by one peak per cavity. It would appear that either the F-P “noise” or the losses are drowning out the normal modes.

There have been numerous analyses of CCW waveguide dispersion in the literature since these results were published [24]. The tunability of the 2D dispersion of the H1 cavity is demonstrated in [36] and its effect on the CCW dispersion. In [37] the authors solve the photonic bandstructure using a Finite Element analysis (FEM) and discuss results of FDTD pulse propagation through an H1in1 device. The work focuses on the bandstructure of an infinite crystal without taking into account the interfaces. A more sophisticated approach is adopted in [38] after originally calculating the H1in1 dispersion using PWE and fitting the parameters to a tight binding model, the authors match the otherwise highly reflective H1in1 interfaces using a 2D adiabatic taper, and show favourable transmission characteristics. The Tight Binding (TB) formalism, commonly known from solid state physics, is often treated in a similar manner to its cousin, Coupled Mode Theory, and the results of measurements or numerical simulations, fitted to yield the coupling and detuning coefficients. The work of Leuenberger [39] takes a different approach and constructs the behaviour of the CCW from its individual elements. The next nearest neighbour assumption of many TB models is surprisingly successful, given such close proximity between cavities the behaviour is totally dominated by adjacent cavities. This appears to hold even when propagating around bends, where the 2<sup>nd</sup> nearest neighbour distances varies with bend geometry[14].

We found in Chapter 2 that the dispersion was modified by the input wave impedance of the waveguides. We now require to calculate the transmission and dispersion of these finite length PhC devices. We will use two methods for this;

- i) a variation on the TMM, a 2D Eigenmode Expansion algorithm (FimmProp – Photon Design), which in order to describe the entire field, breaks the

problem into segments of varying cross section, solves the 1D modes in each segment and propagates them forwards and backwards to the neighbouring section.

- ii) The brute force approach in which we add a 2<sup>nd</sup> dimension to the FDTD algorithm. (FullWave – RSoft Inc)

## 3.7 EigenMode Expansion Modelling

### 3.7.1 Device dispersion using 2D EME

The TMM was found to provide an exact analysis in 1D. A slightly more sophisticated *scattering matrix* treatment is now outlined building on the foundations of the TMM and the waveguide mode solvers above. We wish to calculate the transmission properties of various complicated scattering elements. In 1D we multiplied the characteristic matrices of segments of constant refractive index and infinite extent. In 2D it is possible to discretise any complicated waveguide into a finite set of cross sections, which are each translation invariant (they possess continuous translation symmetry).

Each cross section has a unique set of eigenmodes. The field  $\Psi$  in any section is a linear sum of the eigenmodes in that section, i.e.

$$\Psi(x) = \sum_{i=1}^N (C_i^+ \Psi_i(x) e^{ik_i z} + C_i^- \Psi_i(x) e^{-ik_i z}). \quad \{3.11\}$$

These consist of guided modes, leaky and radiation modes. In order to handle the outgoing waves from leaky segments it is preferable to include a PML at the computational boundary. This necessitates a solver which can perform a search for complex eigenvalues. The imaginary part of the equivalent index,  $n_{equiv}(\omega) = n + i\kappa$ , is then responsible for attenuating a particular mode as it propagates, preventing it from reflecting back into the computational domain further along the simulation.

The spatial form of the propagating wave is,

$$e^{-ikz} = e^{-i\left(\frac{2\pi n_{equiv}(\omega)}{\lambda}\right)z} = e^{-i\left(\frac{2\pi(n+i\kappa)}{\lambda}\right)z} = e^{-i\left(\frac{2\pi n}{\lambda}\right)z} e^{\left(\frac{2\pi\kappa}{\lambda}\right)z} = e^{-i\left(\frac{2\pi n}{\lambda}\right)z} e^{\alpha z} \quad \{3.12\}$$

which can be seen to be attenuated for  $\kappa < 0$ . The exponential decay constant is given by,

$$\alpha = \frac{2\pi\kappa}{\lambda}. \quad \{3.13\}$$

Including an adequate number of modes, N, provides for an accurate representation of the complete field. The entire device is then modelled by calculating the overlap integrals for each of the modes ( $i=1:i=1,2,\dots,N$ ) from one segment to the next, at the boundary between segments. The scattering matrix for the entire device is then simply the product of each of the segment propagation matrices and each of the

overlap matrices. The method is bi-directional, as opposed to say the one way approach of a simple Beam Propagation Method (BPM). The overlap integrals between sections are typically the largest source of error. The size of the computation scales as  $O(N \log N)$ , rather than the  $O(N)$  of FDTD. Modes can be TE or TM polarised as discussed above, depending upon the solver used (in 2D). Any symmetry present along the waveguide can be exploited by placing a Metallic or Magnetic wall (TE or TM) in the centre of the waveguide. This halves the number of modes, reducing computation time. Each eigenmode is orthogonal to the others in the set.

At the start of Chapter 2 we discussed the dispersion in terms of the transmitted phase TMM. Rather than continue to calculate the equivalent index of a PhC structure we now look at the differential phase, to define an effectual or group index. This is important in examining the dispersion of finite length structures, which consist of multiple waveguide sections such as PhCs. The field inside the PhC will often combine many modes in each waveguide section, each with different equivalent indices. We first study a simple waveguide system to introduce and calibrate the algebra and computation.

A ridge waveguide, narrow enough to be considered a photonic wire, has a straightforward and strong dispersion. The TE or TM modes of the waveguide can be solved with a variety of index eigenmode solvers or the wave matching method [40,41,42,3]. As the frequency of the light decreases its fundamental mode becomes less confined within the dielectric and tends to a cutoff frequency. Numerically its

equivalent index decreases (phase velocity increases  $v_{phase} = \frac{c}{n_{equiv}} = \frac{\omega}{k}$ ), as we have

seen, and its group velocity decreases ( $v_{group} = \frac{\partial \omega}{\partial k}$ ,  $N_{group} = \frac{1}{c} \left( 1 / \frac{\partial \omega}{\partial k} \right)$ ). A wave of

frequency,  $\omega$ , travelling a finite distance,  $L$ , along the ridge waveguide undergoes a phase shift,  $\phi$ . The quantities are related by the simple relation phase shift,  $\phi = kL$ . We can recover this information in a number of ways, which are all trivial in this instance, but become increasingly relevant as we move to more complicated refractive index distributions. These include;

- i) The eigenmode solver can be asked to output the equivalent index if the structure possesses continuous translation symmetry (in the case of the ridge, it does).
- ii) The scattering matrix  $S_{12}$  gives the longitudinal transmission of the forward propagating field of the structure (the transmission,  $T=1$ , and phase,  $\phi = \frac{2\pi n_{equiv} L}{\lambda_0}$ , where  $\lambda_0$  is the free space wavelength).

From the phase we previously defined an effective optical length for the structure, having started from  $u=0$ , knowing that the absolute phase of the field is zero. Here we do not know the absolute phase, and so must make do with a relative or differential phase. The technique assumes that we can define the phase of the input wave in a particular mode  $j$  (with  $n_{equiv}=n_j$ ) and that the field exits the structure in a mode  $k$  (with  $n_{equiv}=n_j$ ). We would ideally prefer unity transmission from mode  $j$  to  $k$ , but nevertheless the dispersion calculated in this way is independent of the magnitude of transmission. In the majority of the work in this report identical ridge waveguides are used to launch the field at the entrance to the waveguide and collect the field at the output. These typically have the same width as the PhC waveguide on the inside of the first line of holes (for these H1in1, L2in1 CCWs and W1s  $width = \sqrt{3}a - 2r$ ).

To derive an expression for the group index in terms of the differential phase we consider the phase index. The group index,  $N_{group}$ , is determined by differentiation of

$$\text{the wavevector, } k = \frac{\omega n_{equiv}}{c}, \quad \{3.14\}$$

$$\frac{\partial k}{\partial \omega} = \frac{\partial}{\partial \omega} \left( \frac{\omega n}{c} \right) = \frac{n}{c} + \frac{\omega}{c} \frac{\partial n}{\partial \omega} = \frac{n}{c} + \frac{\omega}{c} \frac{\partial n}{\partial \lambda} \frac{\partial \lambda}{\partial \omega} \quad \{3.15\}$$

Since,  $\lambda = \frac{2\pi c}{\omega}$ ,  $\frac{\partial \lambda}{\partial \omega} = -\frac{2\pi c}{\omega^2}$ , we have

$$\beta_1 = \frac{\partial k}{\partial \omega} = \frac{n}{c} + \frac{2\pi c}{\lambda c} \frac{\partial n}{\partial \lambda} \left( -2\pi c \right) \left( \frac{\lambda}{2\pi c} \right)^2 = \frac{n}{c} - \frac{\lambda}{c} \frac{\partial n}{\partial \lambda} \quad \{3.16\}$$

$$N_{group} = n - \lambda \frac{\partial n}{\partial \lambda} \quad \{3.17\}$$

For two wavelengths  $\lambda_1$  and  $\lambda_2$ , the equivalent indices in the output waveguide are  $n_1$  and  $n_2$  respectively.

$$\Delta\phi = \phi_2 - \phi_1 = 2\pi L \left( \frac{n_2}{\lambda_2} - \frac{n_1}{\lambda_1} \right) = 2\pi L \left( \frac{\lambda_1 n_2 - \lambda_2 n_1}{\lambda_1 \lambda_2} \right) \quad \{3.18\}$$

From above, we define a set of convenient variables.

$$\begin{aligned} \Delta n &= n_2 - n_1 = N_{group} + \lambda_2 \frac{\Delta n}{\Delta \lambda} - N_{group} - \lambda_1 \frac{\Delta n}{\Delta \lambda} = \frac{\Delta n}{\Delta \lambda} (\lambda_2 - \lambda_1) = \frac{\Delta n}{\Delta \lambda} \Delta \lambda = \Delta n \\ n_1 + n_2 &= 2N_{group} + \frac{\Delta n}{\Delta \lambda} (\lambda_1 + \lambda_2) = 2N_{group} + \frac{\Delta n}{\Delta \lambda} 2\lambda_{centre} \\ \lambda_{centre} &= \frac{\lambda_2 + \lambda_1}{2}, \quad \Delta \lambda = \lambda_2 - \lambda_1 \quad \{3.19\} \\ \lambda_1 &= 2\lambda_{centre} - \lambda_2, \quad \lambda_2 = \Delta \lambda + \lambda_1 \\ \lambda_1 &= \frac{2\lambda_{centre} - \Delta \lambda}{2}, \quad \lambda_2 = \frac{2\lambda_{centre} + \Delta \lambda}{2} \end{aligned}$$

rearranging {3.18} gives, {3.20}

$$\begin{aligned} \frac{\Delta\phi}{2\pi L} &= \frac{\left( \frac{(2\lambda_{centre} - \Delta\lambda)n_2 - (2\lambda_{centre} + \Delta\lambda)n_1}{2} \right)}{\left( \frac{(2\lambda_{centre} - \Delta\lambda)}{2} \right) \left( \frac{(2\lambda_{centre} + \Delta\lambda)}{2} \right)} \\ &= 2 \left( \frac{(2\lambda_{centre} - \Delta\lambda)n_2 - (2\lambda_{centre} + \Delta\lambda)n_1}{(2\lambda_{centre} - \Delta\lambda)(2\lambda_{centre} + \Delta\lambda)} \right) = 2 \left( \frac{2\lambda_{centre}n_2 - \Delta\lambda n_2 - 2\lambda_{centre}n_1 - \Delta\lambda n_1}{(4\lambda_{centre}^2 - \Delta\lambda^2)} \right) \\ \frac{\Delta\phi}{2\pi L} &= 2 \left( \frac{2\lambda_{centre}(n_2 - n_1) - \Delta\lambda(n_2 + n_1)}{(4\lambda_{centre}^2 - \Delta\lambda^2)} \right) = 2 \left( \frac{2\lambda_{centre}\Delta n - \Delta\lambda \left( 2N_{group} + \frac{\Delta n}{\Delta \lambda} 2\lambda_{centre} \right)}{(4\lambda_{centre}^2 - \Delta\lambda^2)} \right) = \frac{-4N_{group}\Delta\lambda}{4\lambda_{centre}^2 - \Delta\lambda^2} \end{aligned}$$

$$N_{group} = -\frac{\Delta\phi}{2\pi L} \frac{(4\lambda_{centre}^2 - \Delta\lambda^2)}{4\Delta\lambda} = \xrightarrow{\Delta\lambda=0} -\frac{\Delta\phi}{2\pi L} \frac{\lambda_{centre}^2}{\Delta\lambda} \quad \{3.21\}$$

A group index,  $N_{group}$ , can be defined to represent the change in equivalent index with wavelength. We will dub this the effectual index approach. This is the first derivative of the frequency with respect to the wavevector,  $v_{group} = \frac{\partial\omega}{\partial k} = \frac{c}{N_{group}}$ . The second derivative gives the Group Velocity Dispersion, GVD. The relevance of the GVD to pulse compression will be discussed further in the following chapters. This has been calculated from CW phase values. Note from above that the scattering matrix term  $S_{12}$  recovers the propagated phase only to modulo  $2\pi$ . We need to unwrap the phase correctly, again requiring sufficiently high spectral resolution. We

can, however, begin unwrapping from the centre of a transmission band where the phase is well behaved as we only require relative values.

This has the consequence that we can define a group index for any structure, one that need not have a uniform index distribution, or one in which the power remains in a solitary mode. To calculate the dispersion of a finite length photonic crystal we merely treat the refractive index distribution as a black box.

To calculate the modes and their dispersion we used the 1D fully vectorial Eigen Mode Expansion solver FimmWave and 2D scattering matrix engine FimmProp [4]. To calibrate the technique we compare  $N_{\text{group}}$  (as calculated by equation{3.17}, directly from  $n_{\text{equiv}}$ ) to the  $N_{\text{group}}$  determined from the phase {3.21}. Additionally we plot the  $N_{\text{group}}$  values computed from an FDTD calculation. The EME result is plotted in Figure 3.7. Details of the phase recovery from the FDTD, follow in the next section.

The problem is then of solving the complicated scattering matrix of a photonic crystal. This presents a formidable task in that the PhC includes a huge number of interfaces. Not only do we require adequate discretisation of the transverse cross section, but we must also include many sections along the waveguide. We can make use of periodicity, though at the time of calculation this feature was surprising awkward to implement in the commercial package. As we perform each of the calculations at a single frequency it is simple enough to include the material dispersion and even the slab waveguide dispersion in this calculation. In the published work, the slab waveguide is introduced as a cubic fit to the slab waveguide dispersion data, which was deemed accurate enough for the wavelength range required.

We must be able to accurately discretise the circular structure of the air filled cylinders and the hexagonal lattice in such a way that we don't create too large a numerical problem whilst retaining sufficient detail. Too large a step between slices can cause a large reflection at each interface and dramatically affects the accuracy of the model. Power not reflected back into the segment or transmitted into a mode of the neighbouring segment is essentially entirely lost to the simulation. In the limit of sufficient modes this tends to the intrinsic losses of the particular structure.

Reflections from the boundaries are the largest source of error as this "radiated" loss can re-enter the simulation, akin to a reflection from the boundary conditions. Proper selection of the PML strength is essential to truncate the problem to a numerically soluble size, to alleviate these reflections as much as is possible and to take advantage of symmetries within the problem.

Although the PML can assist with the reduction of reflections from the computational boundaries, when used to model PhCs, the solver can struggle to find modes due to the high fields present at the very edges of the domain. These fields are present due to the large distributed feedback from the entire grating structure. Ideally we would include a large number of periods perpendicular to the waveguide, on the other hand this requires many more modes to be solved. We have to trade off the isolation that each layer provides against simulation run time. Therefore, despite the parasitic reflectivities of the Metal Walls these were chosen at each boundary for the TM polarisation ( $E_x$ ,  $H_y$ ,  $E_z$ ) in these 2D models. Checking for the presence of reflections from the boundaries is fairly trivial. The longitudinal boundaries play no role in the calculation, they do not reflect. Any standing wave in the output ridge waveguide, or a transmission greater than unity should be treated as highly suspicious and the model adjusted to minimise these effects. This would be the full story, if it were not for the PhC interfaces. Standing waves in the output waveguide can also be caused by the radiation of surface states at the PhC/ridge waveguide boundary. The role these surface states play in coupling has recently been investigated by [43]. Another occasional problem is that the entire simulation domain becomes resonant; the spurious points that this causes can usually be detected and eliminated and are only a nuisance if they delay or crash the solver engine. Narrow ridges have also been investigated to determine how the phase noise is affected by the resolution of the grid onto which the transverse profile is meshed. The requirement to combine many transverse periods of the PhC (i.e. a wide domain) with narrow access guides means that the narrow guides are in danger of being under resolved. Consequently the phase can be observed to glitch.

The discretisation was initially applied as a longitudinal angular segmentation of the circles, as this represents the part of the problem where the resolution is required. The overlapping nature of the hexagonal lattice then poses a problem to circles with radii

greater than  $\frac{1}{4}a$ , if the waveguide is aligned along  $\Gamma K$ . If ten segments are used for the circle, the unit cell for a single repetition of the lattice requires 21 segments. This can then be mirrored for the 2<sup>nd</sup> half of the period. An example of this approach is shown in Figure 3.27.

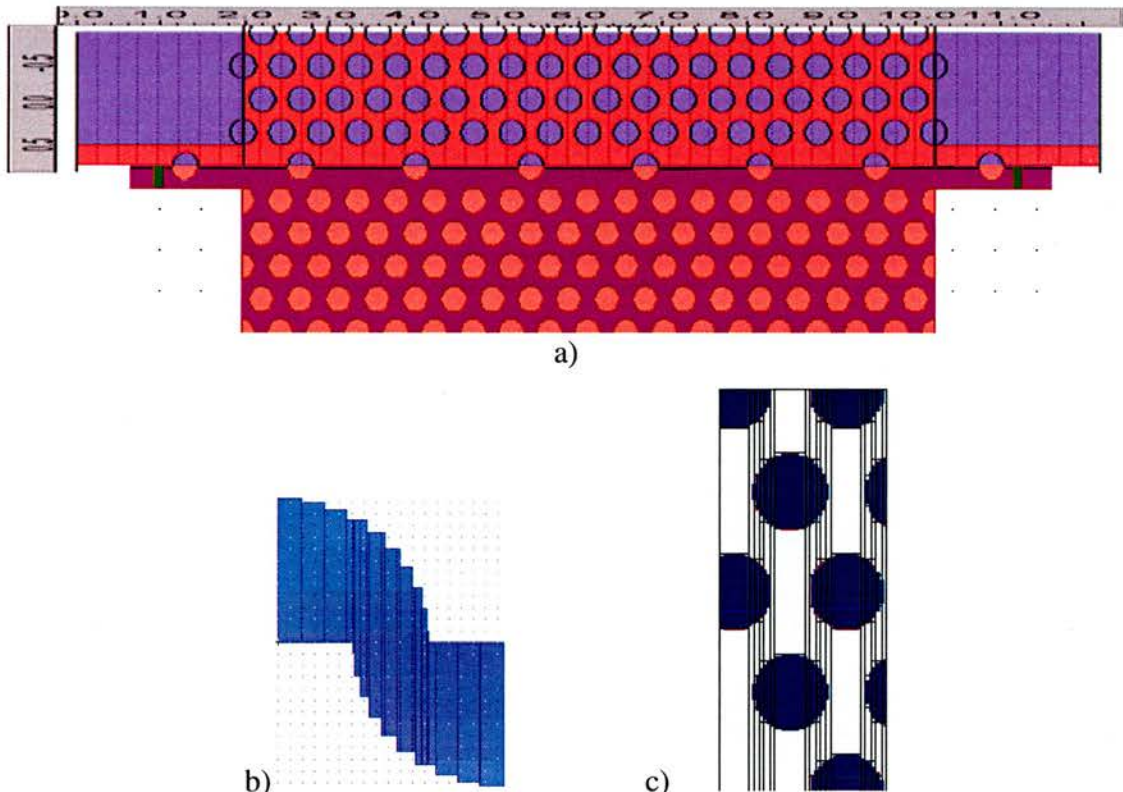


**Figure 3.27** a) L2in1 waveguides displayed from FimmProp 2D and Fullwave CAD packages respectively. b) A schematic of the gridding approach initially adopted to represent the circles as segments with intricate cross sections but invariant in the z direction. In a hexagonal lattice the shapes overlap and therefore affect each other. We have shown two half circles in order to appreciate the overlap. Here  $N=10$  units are used to discretise a circle, into angularly identical segments, overlapping them creates  $2N+1=21$  shapes. c) the automatic gridding algorithm in Fimmwave produces the overlapping sections and thus reconstructs the lattice from segments

The code was originally implemented in 3D including the vertical heterostructure, but proved to be difficult to debug. Errors in the various solvers conspired to thwart the implementation. To simplify the problem the newly available 2D layout editor was then used. This representation was not able to be ported as a periodic segment and so the entire structure was discretised, which is a rather inefficient use of the scattering

matrices. The reduction of the problem by one dimension decreases the calculation time significantly. The number of modes,  $N$ , required to adequately represent the structure was around 70, the majority of these having large imaginary  $n_{\text{equiv}}$ . An example of the automatically generated discretisation is shown in Figure 3.27. The EME technique is inherently faster than FDTD, though as the complexity of the structure increases and therefore the number of segments increases the method is slowed significantly. As the purveyors of the software have since been involved in developing many other solutions to modelling finite length PhCs, it suggests that this has been due to the lack of overwhelming success with EME for general PhC structures. Contrary to that, it is worth stressing the high accuracy of the results obtained over a wide bandwidth, something that FDTD cannot achieve easily.

In a periodic structure it would be very useful to make affective use of the periodicity. The freely available package CAMFR [3] has also been used in a similar manner to evaluate the dispersion of a periodic unit cell of the L2in1 CCW. The agreement with the MPB calculation is good (see Figure 3.31).

### 3.7.2 Phase Retrieval from 2D FDTD

To assure ourselves that the effectual index model is working accurately enough we require a 2<sup>nd</sup> calculation using exactly the same finite length crystal. We return to working in the time domain. In essence we use a time of flight approach to obtain the phase from a CW FDTD simulation[44]. The lattice is now discretised directly onto a 2D uniform Cartesian grid and in this instance all external boundaries are Perfectly Matched Layers. We can take advantage of the symmetry of the problem to model only half the simulation, with a Neumann type boundary condition ( $\frac{\partial E}{\partial x} = 0$ ) in the centre of the waveguide. The field in the access waveguides is stored to allow both reflected and transmitted field to be measured. The excitation was carefully set up to allow a built in mode solver to find and launch the exact waveguide mode at each consecutive frequency of interest. Unlike the EME model, the CW characteristic is not determined initially, but instead we must let the model propagate to a steady state to remove the transients, which is rather time consuming. The recovered data requires rather more processing than in the EME case. The field which we have probed

reaches the transmission monitor (situated on the downstream side of the PhC at a position L from the launch origin, z=0) after a time approximately corresponding to the  $c/n_{equiv}$  for the input ridge waveguide. The field then begins to ring around inside the structure until the transmitted field settles down to equilibrium.

The phase for the dispersion calculation is taken at the end of a fixed interval of time, T. The temporal field data file does not immediately yield the phase. The file is sinusoidal with a counterintuitive period  $\Delta t$  of lambda! ( $cT$  is in microns and frequency is constant). Calculation of the phase from the previous positive going crossing of the abscissa and the amplitude  $E(t)$  of the wave was found to introduce far too noisy a set of data, for the double differentiation which follows. Smoother data was obtained from a linear fit to the positive going crossing of the abscissa for the previous 100 cycles and an extrapolation to the time T. This provided sufficiently noise free data for the dispersion calculation.

The proof of the technique is fairly straightforward, ensuring that the values calculated are indeed the same group index as previously.

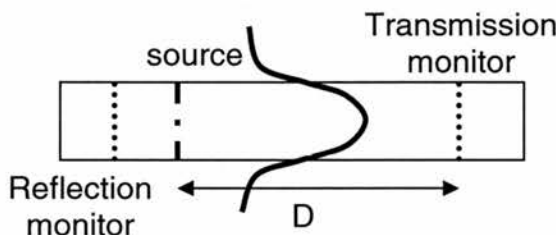


**Figure 3.28 Geometry involved in FDTD phase retrieval**

The phase expected at the time monitor after time T, is notionally,

$$\phi = 2\pi \left( \frac{cT - n_{equiv}D}{\lambda} \right) \quad \{3.22\}$$

We can process the FDTD time monitor data for the phase difference

$$\frac{\Delta\phi}{2\pi} = \left( \frac{cT - n_2 D}{\lambda_2} \right) - \left( \frac{cT - n_1 D}{\lambda_1} \right) \quad \{3.23\}$$

$$\frac{\Delta\phi}{2\pi} \lambda_1 \lambda_2 = cT(\lambda_1 - \lambda_2) - D(n_2 \lambda_1 - n_1 \lambda_2)$$

rearranging gives us,

$$-\frac{cT}{D} - \frac{\Delta\phi}{2\pi} \frac{\lambda_1 \lambda_2}{D(\lambda_2 - \lambda_1)} = -\frac{cT}{D} - \frac{\Delta\phi}{2\pi} \frac{\lambda^2}{D\Delta\lambda} = \frac{(n_2 \lambda_1 - n_1 \lambda_2)}{(\lambda_2 - \lambda_1)} \quad \{3.24\}$$

We use the LHS to determine a value for the RHS, which ...

...substituting from {3.19}

$$\begin{aligned} \frac{(n_2 \lambda_1 - n_1 \lambda_2)}{(\lambda_2 - \lambda_1)} &= \frac{1}{\Delta\lambda} \left( \frac{n_2}{2} (2\lambda_{\text{centre}} - \Delta\lambda) - \frac{n_1}{2} (2\lambda_{\text{centre}} + \Delta\lambda) \right) = \left( \frac{n_2 \lambda_{\text{centre}}}{\Delta\lambda} - \frac{n_2}{2} - \frac{n_1 \lambda_{\text{centre}}}{\Delta\lambda} - \frac{n_1}{2} \right) \\ &= \left( \frac{(n_2 - n_1) \lambda_{\text{centre}}}{\Delta\lambda} - \frac{(n_2 + n_1)}{2} \right) \\ &\left( \frac{\Delta n \lambda_{\text{centre}}}{\Delta\lambda} - n_{\text{centre}} \right) = -N_{\text{group}} \end{aligned}$$

where  $N_{\text{group}} = n - \lambda \frac{\partial n}{\partial \lambda}$  {3.17} and we have defined  $n_{\text{centre}} = \frac{(n_2 + n_1)}{2}$ ,

yields the negative group index. With this analysis we can use FDTD to verify the finite device Eigenmode Expansion dispersion data, which gives us greater confidence in our modelling. This is important because it allows us to check the convergence of the EME model, and we can then recycle the expansion of only a single period, to greatly reduce the computation time for longer waveguides.

### **3.8 Pulse Measurement on L2in1 waveguides**

#### **3.8.1 Introduction**

The preceding sections have established the techniques required to analyse the properties of both infinitely periodic and finite length 2D photonic crystal structures. We have examined the dispersion of the heterostructure waveguide into which the devices are etched. The photonic bandstructure for 2D square and triangular lattices was introduced. By creating defect cavities in the triangular lattice we form Coupled Cavity Waveguides. The coupling between cavities splits the eigenfrequency of the individual cavity mode and forms a band as more cavities are introduced. Light propagating along the waveguide is delayed in particular at the band edge where the light is strongly dispersed. The fabrication process, used to manufacture short chains of cavities in the heterostructure waveguide, was outlined. Light was coupled to these CCWs using ridge waveguides and thus their transmission properties were measured under CW excitation. The transmitted signal intensity and spectral bandwidth are found to be in good agreement with a 3D FDTD model. Two independent techniques were elucidated upon which calculate the 2D dispersion properties of these finite structures.

In the following sections we apply these techniques exclusively to the L2in1 CCW waveguide. Firstly we calculate the transmission spectrum and phase response of a chain of 7 coupled cavities. We then outline a pulse propagation measurement for picosecond pulses centred spectrally at the bandedge of the CCW. We show using a 3D FDTD model that we have fabricated a close-to-optimum structure for this heterostructure waveguide, taking into account the various loss mechanisms. Finally we combined the fibre and 3D FDTD dispersion data to explain the pulse compression observed in these waveguide.

### 3.8.2 Device properties

The L2in1 waveguide (see Figure 3.29) has an attractively high transmission for a CCW band which we have marked D in the bandstructure plotted below (see Figure 3.30).

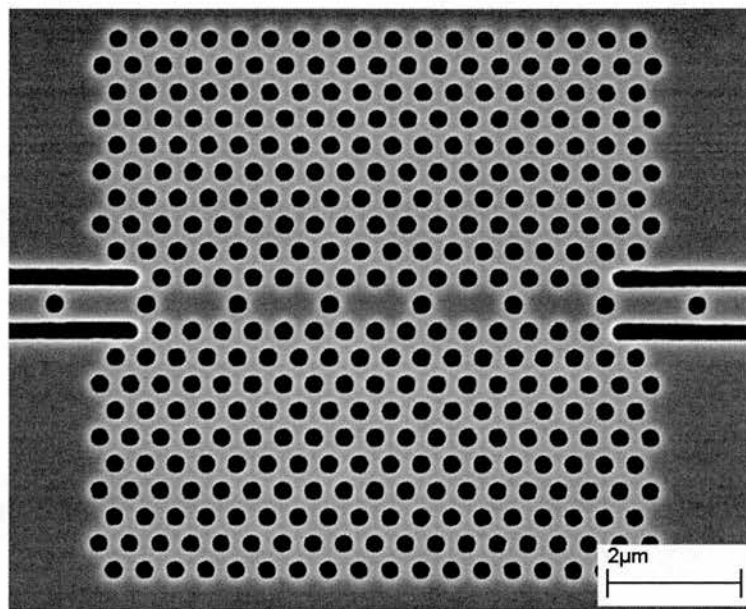
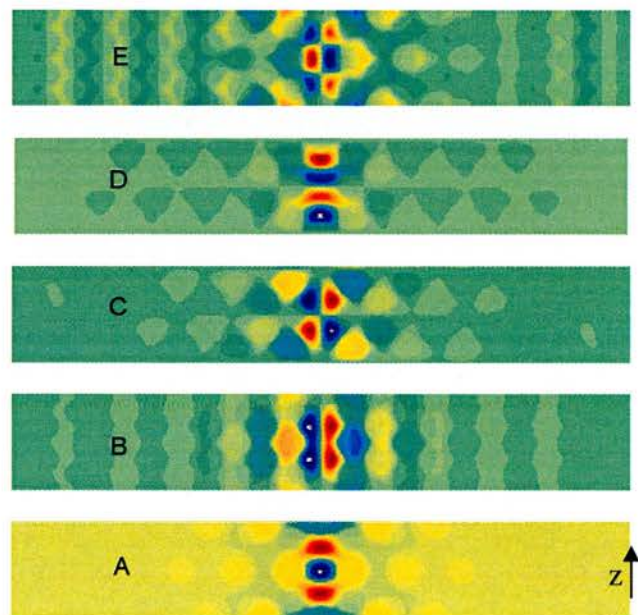
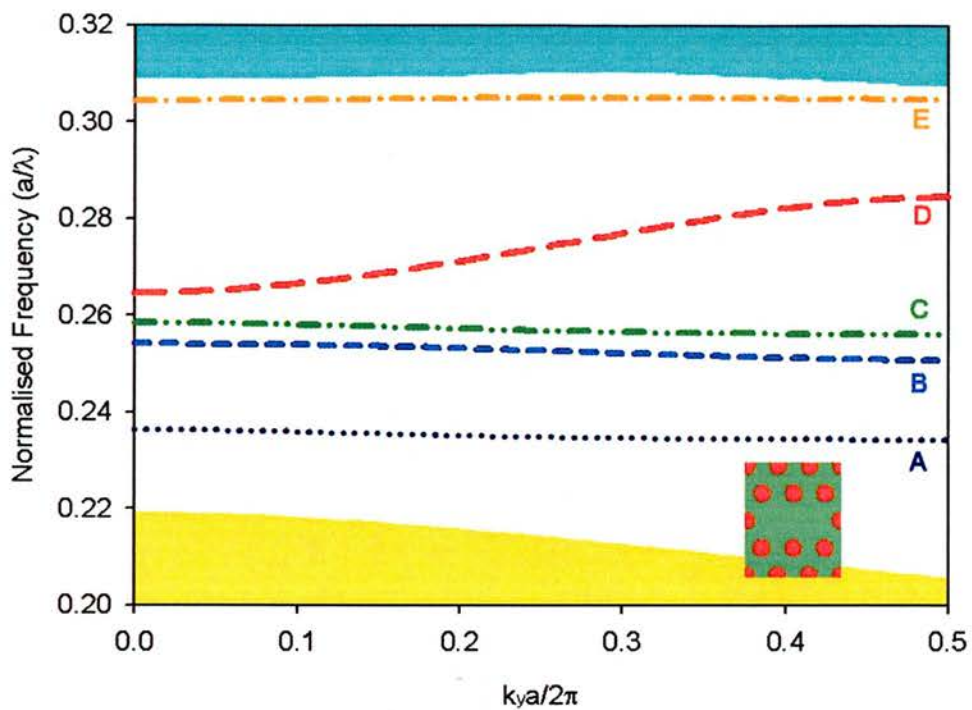


Figure 3.29 SEM micrograph of L2in1 CCW etched into “Scotland” structure

Firstly this mode has even symmetry which allows us to use end fire coupling. This is important so that our devices can be measured using standard fibre transmission equipment. The high transmission for this mode can be attributed to the large bandwidth of the mode and the relatively high group velocity of the mode. The other modes have very flat bands making coupling rather difficult.



**Figure 3.30 a)** The MPB calculated bandstructure of an L2in1 CCW, showing five modes spanning the bandgap ( $u=0.22-0.31$ ), **b)** The  $H_y$  field distributions at the  $\Gamma$  point for each mode. The propagation direction,  $z$ , is vertical here, and only modes A and D have even symmetry. They are all essentially Fabry-Pérot modes. In the propagation modelling modes B and C are observed to interact, even though their bands are distinct from one another, this has previously been noted as a split quadropole mode[45].

The results of the finite length EME and FDTD calculations reproduce the asymmetric-triangular shape of the measured transmission band (see Figure 3.37). In addition we observe one peak for each of the seven cavities (as seen in Figure 3.29). These are not as pronounced (they have lower visibility) than in 1D and could easily be obscured due to the F-P noise. At the high frequency (short wavelength) band edge it appears that we have not only high transmission but also strong dispersion. Indeed both positive and negative dispersion are present due to the short length of the structure which creates a situation akin to a Gires-Tournois interferometer. The slight input impedance creates a cavity between the front and rear facets of the PhC, a very short (G-T) etalon. In a conventional etalon the Q and delay are controlled by the mirror reflectivity and the cavity spacing respectively. In our device these change as we cross the transmission band, yielding a complicated set of peaks with varying Q. Where the cavity is well matched this Q is small and the associated field enhancement is small. In this manner the group index ripple occurs with sufficient bandwidth to consider using this dispersion to compress pulses. In practice we can only consider using the spectral regions with high transmission.

The agreement between the EME and FDTD models is very encouraging, considering the entirely different calculation techniques (frequency versus time domain) and the contrasting Boundary Conditions utilised (reflective versus PML). The longitudinal phase yields a close match. In the limit of shorter structures this time domain technique becomes very noisy indeed. The advantage of using the EME technique is simply the NlogN response when faced with longer structures. With increasing computing power and refined techniques the FDTD does have its own benefits, and is easily the most robust method for modelling these complicated structures.

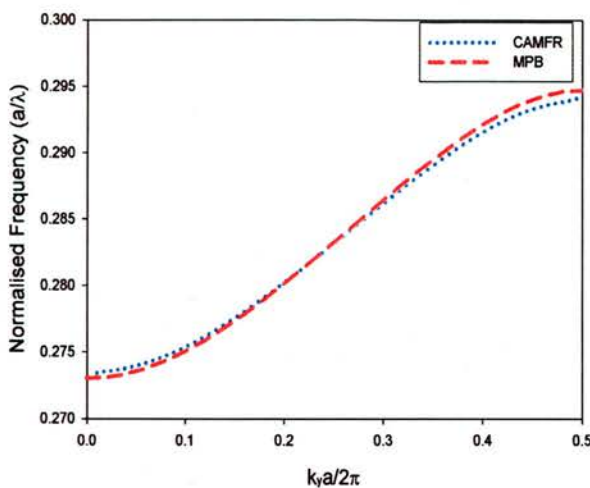


**Figure 3.31 Comparison of CAMFR EME bandstructure with MPB bandstructure,**

The 2D EME code CAMFR also allows solution of the  $\omega$ - $k$  diagram and therefore can be readily compared to the results of an MPB calculation (see Figure 3.31). This allows for rapid convergence testing of the structure before it is implemented in the propagation model, helping to alleviate phase errors.

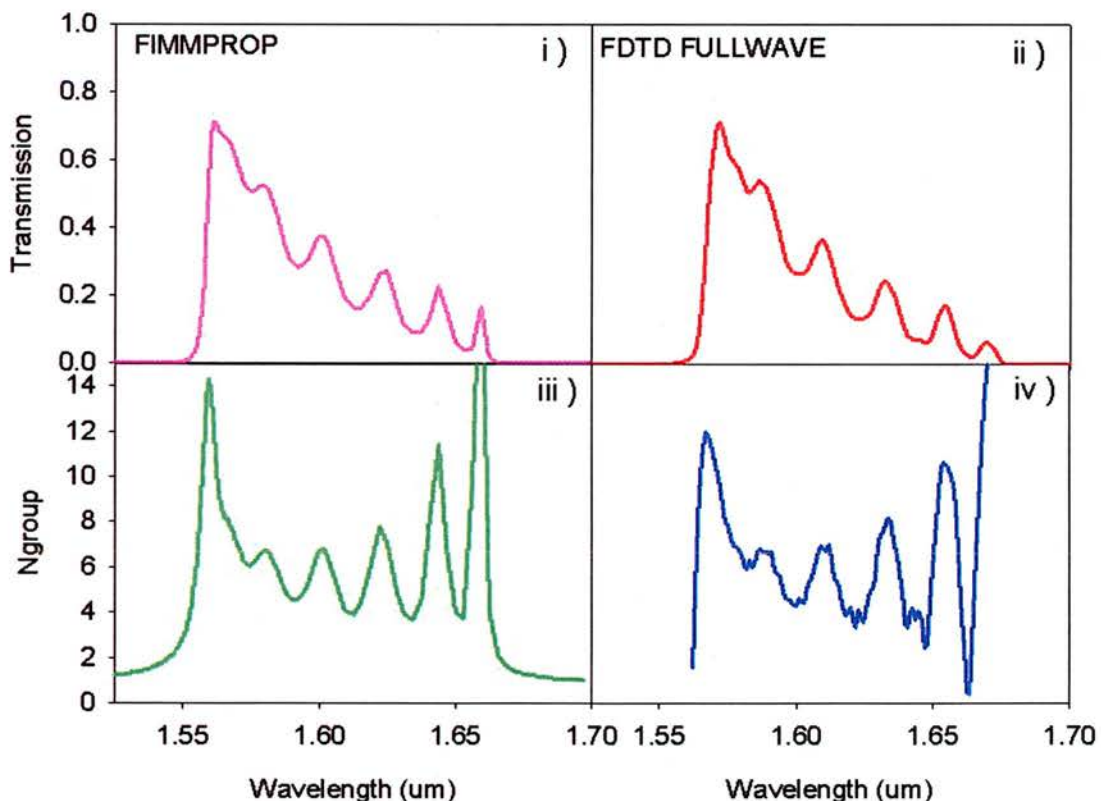


**Figure 3.32 Transmission and Group Index retrieved from EME and FDTD models. One peak can be seen for each of the cavities in the waveguide. Correspondingly we observe peaks in the**

**Group index which are largest at the edges of the transmission band and hence large GVD. The Group index is always larger than that of the coupling waveguide ( $N_g > 4$ ).**

### **3.8.3 Measurements**

Investigating the propagation of picosecond pulses through this structure[45] posed several challenges;

- i) The structure required tuning to the 1536nm fixed wavelength of the gain switched DFB laser source.
- ii) As the transmission spectrum shows (see Figure 3.24) the maximum transmission measured relative to a fibre to fibre connection was -25dB.
- iii) The high power EDFA used (as a result of ii) caused thermal overload on one of the devices. Avoiding non-linearities with such high power is critical.
- iv) In using pulses which are comparable to the length of the sample, the Fabry Pérot cavity, formed by the device facets, filters the spectrum
- v) Keeping the source and associated filters stable, the input/output coupling constant over a long enough time to allow the autocorrelator to scan.

To overlap the spectrum of the device with that of the source, a set of devices with lattice constants in the range  $a=412\text{-}460\text{nm}$  ( $\Delta a=8\text{ nm}$ ) was fabricated. This approaches the resolution limit of the e-beam system. Preliminary work was attempted with slightly longer pulses for which the facet reflectivities were deemed a problem and so the waveguide facets were angled by a FIB etch (see Figure 3.19). Moving to sub picosecond pulses eliminated this problem, as the pulse lengths are shorter than the facet-PhC distance.

The source operates in the C-band (1530 - 1565nm) so that we can take advantage of the availability of amplifiers at this wavelength range. These were Erbium Doped Fibre Amplifiers (EDFAs) and were used to boost the input and output power to enable a large enough signal to drive the non-linear crystal in the autocorrelator. Balancing the pre- and post-amplification was important to avoid overloading the device and exciting any non-linearities. Checking for a linear relationship between power-in versus power-out indicated that we did not encounter any nonlinear

behaviour. This was tested for both blank and PhC waveguides up to powers of 17dBm (50mW). The high, 10GHz, repetition rate of the source may be the key factor here in avoiding Two Photon Absorption in the GaAs core of the waveguide. This is prevalent at 1550nm as we are still above the half bandgap of GaAs. TPA would represent a loss of transmitted signal, and the resulting free carriers might affect the waveguide dispersion. The low average energy, ( $E=5\text{pJ}$ ) in the waveguide mitigates the onset on TPA that we observe at lower repetition rates (80MHz).

The second and critical reason for the restriction on the operation wavelength was to enable the compression of the 10GHz gain switched pulses. These are emitted from the laser with a temporal duration of approximately 12ps; they are significantly chirped. A series of dispersion compensating (DCF), dispersion shifted (DSF) and Single Mode (SMF) fibres are then required to produce a pulse width of 1ps. The 400m DCF ( $D=-80\text{ps/nm/km}$ ) is used for compensation of the modulation induced chirp and the DSF ( $D=-0.5\text{ps/nm/km}$ ) for Self Phase Modulation (SPM) induced spectral broadening. The bandwidths of the various dispersion shifted and compensating fibres are designed to operate at the centre wavelength of the gain switched laser. As the pulse is once again chirped by the SPM a 250m length of SMF ( $D=17\text{ps/nm/km}$ ) is required to provide a 1ps pulse.

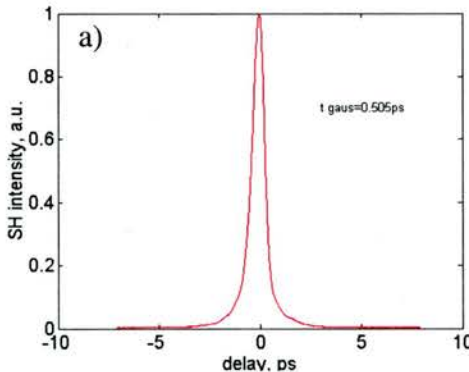


**Figure 3.33 a) 500fs Transform limited pulse at entrance to system**

These short pulses can be further compressed to 500fs by spectral broadening using a Dispersion Imbalanced Loop Mirror (DILM) [46]. This is a loop of DCF and Dispersion Flattened Fibre (DFF), where counter-propagating pulses see different dispersions according to their individual power levels. The pulses then gate

themselves, as only the high power components constructively interfere at the output coupler. In essence the DILM is a non-linear switch. The DILM also acts to suppress the noise in the high pulse pedestal.

The pulses are then transmitted along a length of  $\text{SMF}_1$ , amplified and then coupled to the PhC waveguides (see Figure 3.34). The set of PhC waveguides was augmented with blank waveguides with identical tapers and a straight section ( $\text{width} = \sqrt{3}a - 2r = 490\text{nm}$ ) to replace the PhC. The output from the chip is amplified and transmitted through a length of  $\text{SMF}_2$  to a non linear crystal based autocorrelator.

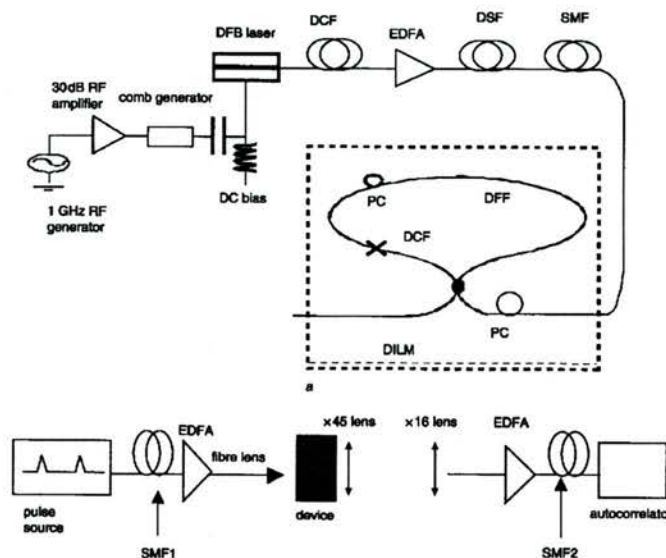


**Figure 3.34a)**Experimental configuration for generating, compressing, amplifying and transmitting short pulses through PhC waveguides

The output from the DILM varies as a function of the total length of  $\text{SMF}_{\text{total}} = \text{SMF}_1 + \text{SMF}_2$ . As the pulse has a  $\beta_2 C < 0$  its width decreases to a minimum values of 500fs and then increases monotonically thereafter. The pulses transmitted through the blank waveguides demonstrated this behaviour. For pulses transmitted by the  $a=460\text{nm}$  PhC waveguides, however, a strong positive dispersion, opposite to that of the SMF was observed. The pulse durations for an additional 20m length of SMF ( $\text{SMF}_{\text{total}}=140\text{m}$ ) are shown in Figure 3.26. The pulse width transmitted through the blank waveguide has a duration of 1.91ps and that transmitted through the PhC has duration 1.17ps. The  $8\mu\text{m}$  L2in1 CCW has compressed the pulse by 40%.

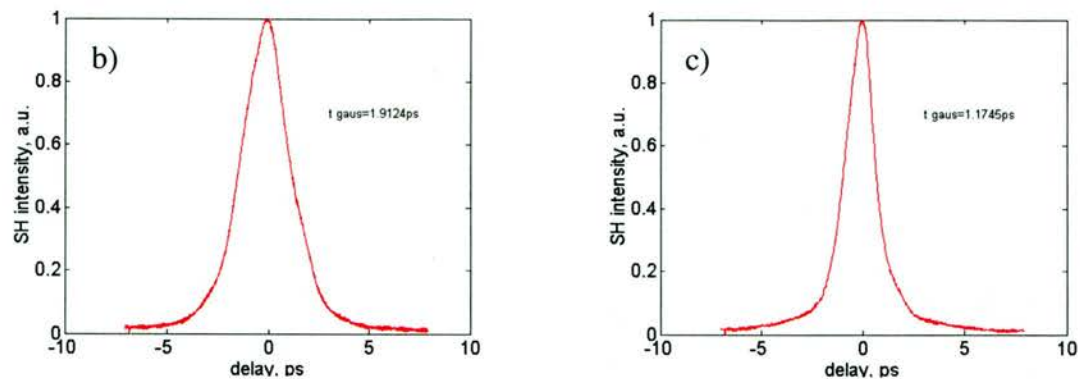


**Figure 3.35a)1.91ps transmitted through SMF and blank waveguide b) 1.17ps transmitted through SMF and PhC waveguide**

This is comparable to 17m of standard SMF. The dispersion induced by the PhC is  $>10^6$  times larger than SMF at this important telecommunications wavelength.

We can calculate the  $\beta_2$  (GVD parameter) by differentiating the infinite dispersion curve, using

$$\beta_2 = \frac{d^2 k}{d\omega^2}, \quad \{3.25\}$$

as plotted in Figure 3.36, or taking into account the finite length effects using

$$\beta_2 = \frac{d}{d\omega} \left( \frac{N_g}{c} \right) = \frac{1}{c} \frac{d\lambda}{d\omega} \frac{dN_g}{d\lambda} = -\frac{2\pi}{\omega^2} \frac{dN_g}{d\lambda}, \quad \{3.26\}$$

(both are 2D so ignore out of plane loss).

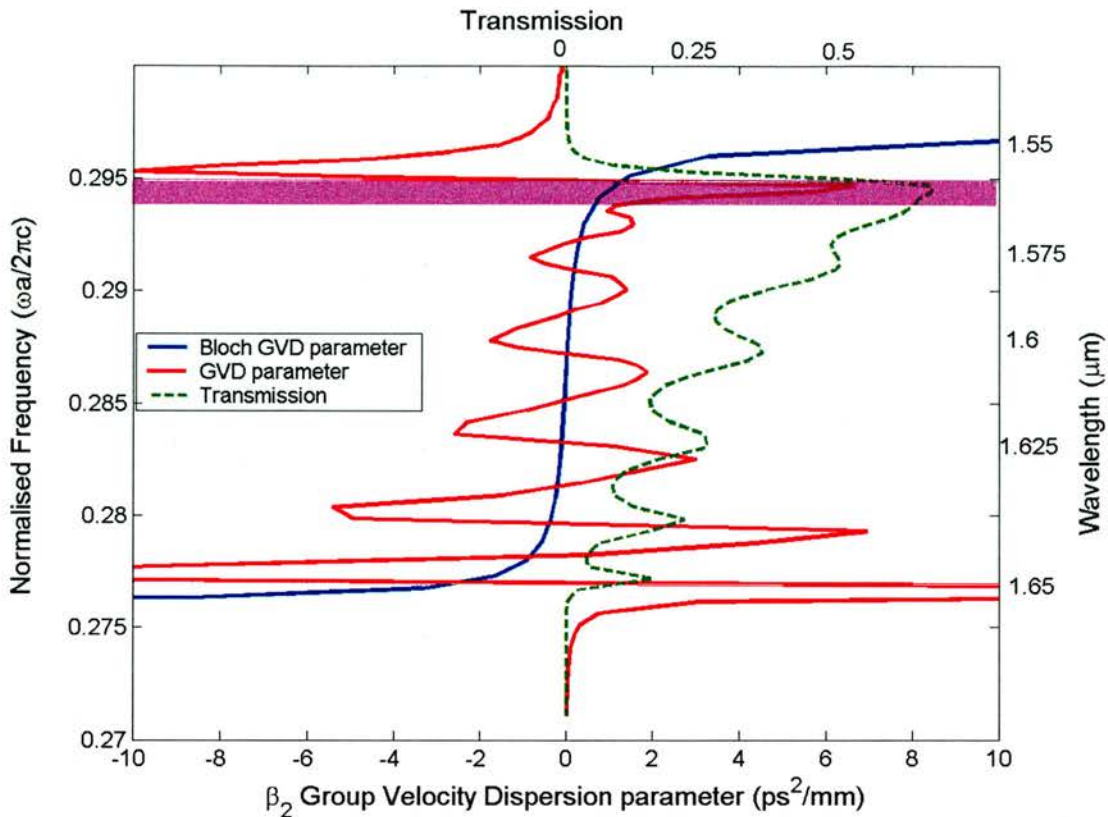


**Figure 3.36** Plot of the GVD parameter for the finite L2in1 waveguide {equation 3.1} and that calculated for an infinite waveguide. Note the two curves intercept at the transmission maxima and minima. The large GVD ripple creates a region with high positive GVD of several nms of bandwidth around the high transmission window (as indicated by the purple band).

The experiment holds a lot of promise for integrated dispersion compensation. We must, however, examine two points in order to improve upon this result. Firstly a CW characterisation of the phase dispersion of the actual sample would have enabled the optimum pulse parameters to be used. These include centre frequency, duration and pre-chirp.

Secondly the devices are very lossy. The low transmission exhibited in the CW spectrum in Figure 3.37 arises from a combination of factors. Firstly, the input coupling through the waveguide facets was found, on average, to give 10dB loss with free space lens coupling (*often referred to as end fire*). In the pulsed experiment lensed fibre was used which accounts for another  $\sim 1.5\text{dB}$  of loss. Recently HOP contrast waveguide devices have been designed with well matched interfaces, e.g. using polymer clad waveguides, removing the need for lensed coupling [47]. The devices can be butt-coupled directly to fibre. This is challenging to do with a heterostructure, but surely spot size converters are not impossible. This would

remove >10dB loss from the system, which is in general a headache for anyone dealing with III-V devices. The remainder of the loss (13.5dB) is due to reflection and scattering inside the waveguide device. The ideal 2D case gives a 70% maximum transmission. Is the 3D case so different that only 1/6th of the power makes it through? We examine the loss in greater detail in the final two sections of this chapter.

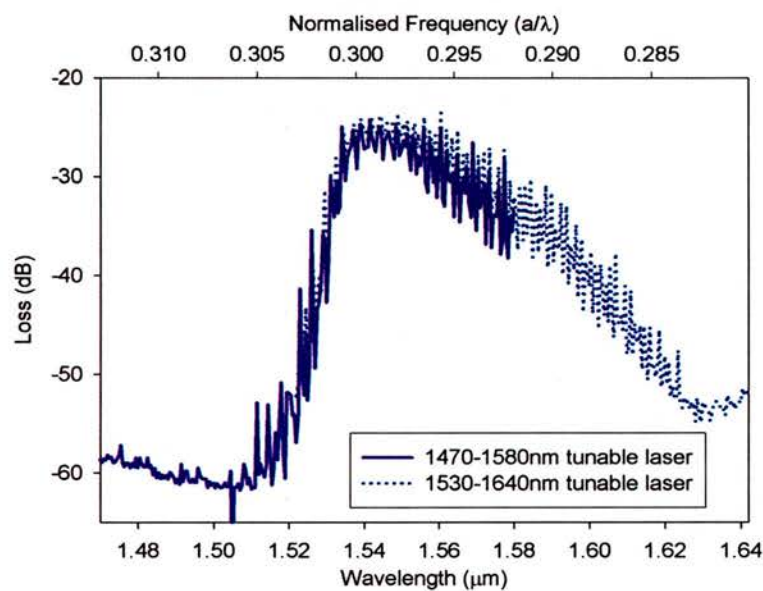


**Figure 3.37** The transmission spectrum of the L2in1 CCW, re-measured courtesy of Chris Morgan at University of Cambridge

### **3.9 3D Bandstructure Calculations Using FDTD**

It is very useful to be able to calculate the photonic bandstructure of rather arbitrary shapes or novel geometries. More useful still is to be able to calculate the response of structures which you are also able to then calculate transmission, reflection, CW or dynamic behaviour at exactly the same resolution. It quite simply minimises the errors prevalent in transferring designs between modelling tools. The FDTD is a real space technique and so the problems of representing the structure accurately in Fourier space are removed. We have discussed the relative merits of the PWE calculated bandstructure in previous chapters. The PWE technique is quick, but eventually breaks down in the limit of too great a number of plane waves, in that the problem cannot be handled in the memory of the computer. The FDTD is also naturally memory limited by the size of the computational domain and resolution, a larger supercell requires a greater number of grid points and a longer time response.

We used 2D FDTD in Figure 3.13 to calculate the cavity eigenmodes of several basic PhC cavities. A Dirac delta-like function is then used to excite the structure. This narrow temporal impulse supplies a huge bandwidth. Field monitors are positioned at random points within the calculation domain and sample the field. The response of multiple monitors can be summed together, or used individually to determine modal symmetries. The trick in their positioning is to avoid antinodal positions. In Fullwave care must also be taken with non-square lattices (e.g. triangular), to construct the unit cell on a square basis, and launch the impulse function in the upper right quadrant and replicate this in all other cells. Fourier Transformation of the temporal response after an elapsed time,  $T$ , returns a set of peaks, which correspond to the eigenmodes of the structure. The data are normalised to the spectrum of the pulse source.

For the cavity mode solving we surround the domain with a Perfectly Matched Layer (PML) Boundary Condition (BC). The off-resonant frequencies are then attenuated much more rapidly than those which are on-resonance. The same technique can be used to solve the eigenmodes of supercells of periodic material. In this last section we adopt periodic boundary conditions at the repeating interfaces of the computational domain. This was first introduced for 2D PhCs by Boroditsky [48] and is used

extensively in [49]. {The special variable FDTD\_complex =1 must be set in RSoft's Fullwave. RSoft will no longer support calculation of bandstructures with Fullwave if the add-on Bandsolve package is not purchased.} Post processing is however very simple and a short routine in Matlab can be used to threshold the peaks corresponding to eigenmodes and plot these versus normalised frequency. Note that in a PWE method supercell the eigenmode frequencies are scaled by the size of the supercell, here with FDTD we glean the information from the temporal response of the monitors and therefore this scaling does not occur.

For convenience we can half the simulation region by applying a Neumann, or Perfect Electric Conductor (PEC) BC. This allow us to concentrate on the even mode. In 3D FDTD the field components are represented on the Yee cell (shown in Figure 3.38). The PEC involves setting the tangential  $E_y$  and  $E_z$  components on the leftmost boundary to zero. Periodic Boundary Conditions (PBC) are implemented at the Hz interfaces. PML was applied at the vertical extrema, (the top Hy faces here). Following the advice of Ron Hadley [50], the external (rightmost) boundary was also included as PML. He observed surprising large fields at this boundary when modelling PhC waveguides with a Finite Difference Frequency Domain (FDFD) model and the PML was suggested to him by Philip Lalanne [51] to aid convergence, by removing outward travelling radiation.

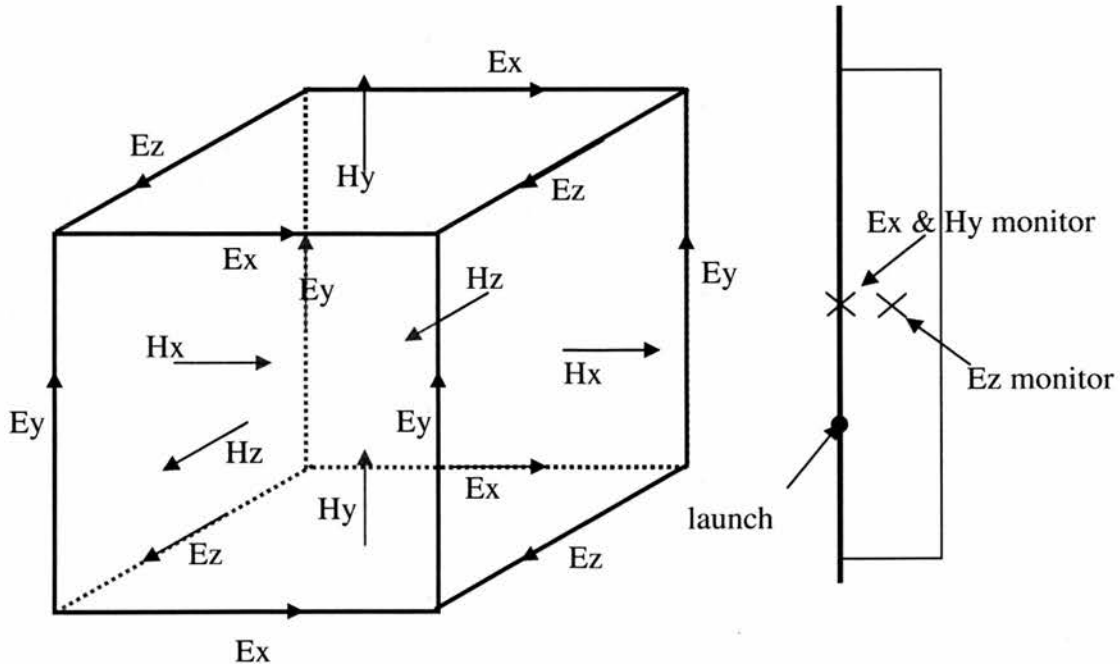


**Figure 3.38** The Yee cell, indicating the relative positions of the field for a 3D FDTD calculation. Take for instance the Hz component pointing out of the plane of the paper. It is calculated from the 2D face of the cube which surrounds it. The top view of the waveguide is shown on the right indicating the positions of field components and monitors.

We can vary the depth of the etched holes to investigate the effect of the mode confinement upon the intrinsic loss from the structure. Additional loss quickens the ring down of the cavity. At present this has only been calculated from the field decay. The correct manner in which to calculate this, is from the rate of decay of the Energy Density, and can also be verified by observing the Poynting vector travelling outwards from the structure (through vertical and right hand boundaries). As can be seen there is support for the argument that simply etching deeper holes can provide better confinement [6]. The fraction of the waveguide mode which is scattered by the bottom of the holes is lower, for greater etch depth. This method does appear to have reached its limit, however, beyond a depth of  $1.5\mu\text{m}$ , as the Q does not substantially increase by etching an extra 500nm to  $2\mu\text{m}$ . As we can see from Figure 3.4 at this depth there is very little remaining field in the mode tail.

We have to consider two additional points in determining the source of the loss. Firstly the fully vectorial solution of the ridge waveguide mode requires analysis in 3D. Secondly we must take into account the folding of the Bloch components of the wavevector. In the sense of the folding from the wavevector diagram (Figure 2.11) we have two states above the cladding light line ( $n_{\text{Al}60\% \text{GaAs}}=3.1$ ). In order to properly confine the light in a cavity, without any loss mechanisms, is it necessary to modify the operating position with respect to the light line.

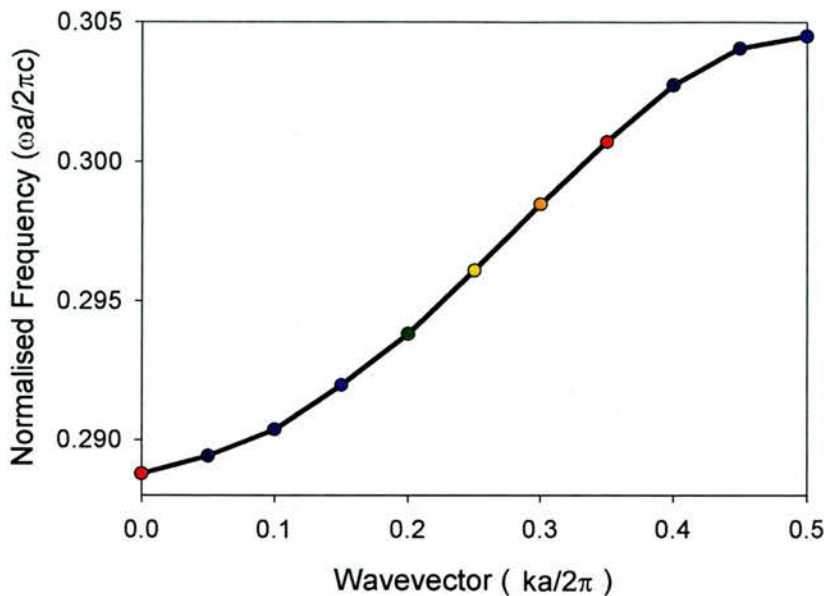


**Figure 3.39 Dispersion of mode D calculated using 3D FDTD, in superb agreement with the bandwidth of the transmission measurement shown in Figure 3.37.**

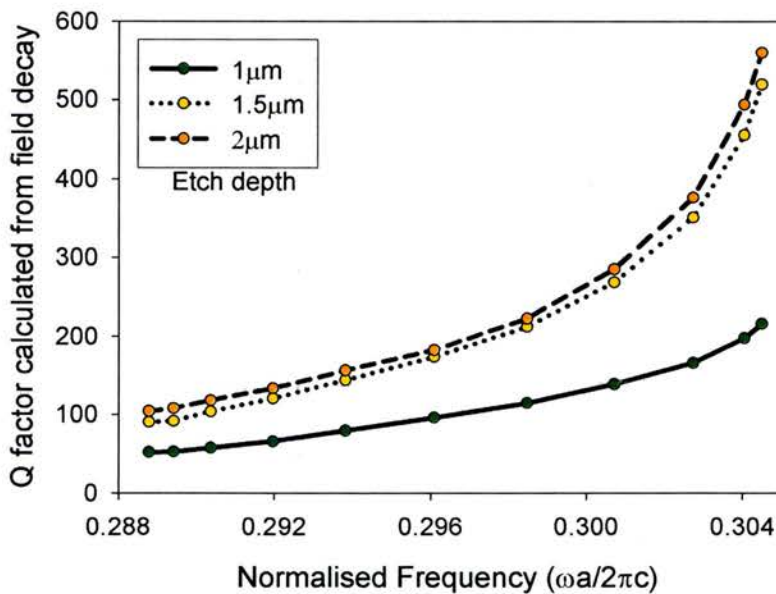


**Figure 3.40 The quality factor calculated from the field decay.** There is certainly a threshold etch depth at which the mode becomes better confined. This improvement has apparently reached a limit however, indicating that an alternative route to high Q, low loss cavities must be sought. The Q factor follows the trend from the triangular Transmission spectrum, in having higher Q where there is better Transmission. The high transmission states are we recall, resonances of the Bloch modes of the structure and as such have high field enhancement when well matched.

It was possible to fit half of the entire L2in1 structure into the memory of my Desktop computer. The calculation used 1.08Gb of memory and with a 1.5GHz processor took 30 hours. The grid was  $N_x=121$ , wide,  $N_y=43$ , high and  $N_z=394$  long for grid steps of  $\Delta x=23\text{nm}$ ,  $\Delta y=60\text{nm}$ ,  $\Delta z=23\text{nm}$ . At the current low memory prices our group now has several machines with this memory capacity. Computation of the transmission spectrum is then possible. The data in Figure 3.31 show a transmission maximum of 23%. This is almost identical to the original data which is plotted normalised to the blank waveguide transmission. This indicates that we have 6dB loss through our  $8\mu\text{m}$  long PhC waveguide.

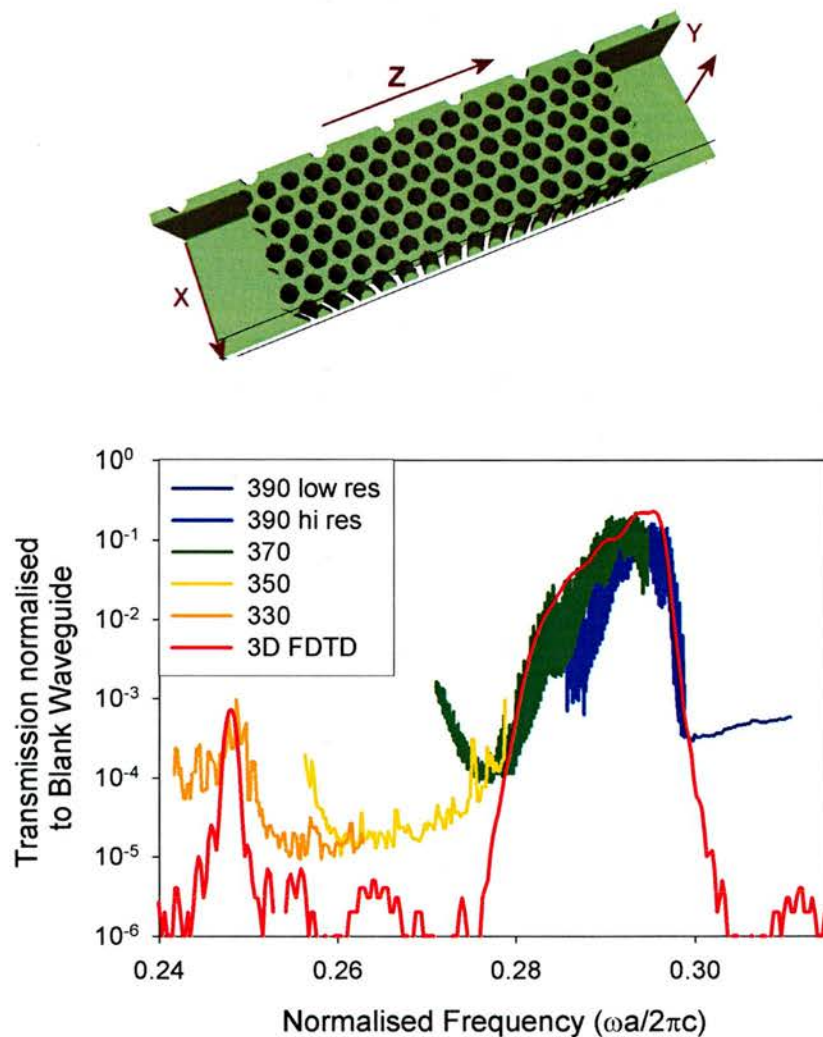


**Figure 3.41 Transmission spectrum for L2in1 waveguide measured using lens endfire and normalised to the transmission of a blank waveguide. 3D FDTD spectra calculated for 460nm structure and therefore requires frequency red shift of  $\Delta u=-0.008$  to account for the lower modal index at 1.55um. Note agreement with lower defect peak at  $u=0.25$ .**

The leaky nature [52] of the launch mode is dealt with by solving the 2D waveguide mode using a PBC, thereby allowing transients to radiate away. This is necessary as the built in mode solver could not deal with the large complex component of the mode index. Attempts to launch a mode solved with Fimmwave, discretised on to the FDTD grid were unsuccessful. The field cross section is captured after an elapsed time (as a BPM input file) and is launched into the L2in1 access waveguide.

The agreement between experiment and model is very good indeed. The high impedance and loss of the structure are well represented. If we take the fibre to fibre measurement of Figure 3.37, the total loss is 25dB.

The average coupling loss with lens end fire is 10dB

Difference between lens end fire and lensed fibre end fire 1.5dB

Subtracting these from 25dB gives 13.5dB

The transmission data normalised to the blank waveguide and the 3D FDTD both agree on ~6dB loss, which accounts for impedance mismatch and intrinsic loss.

Therefore we can put an upper limit on the roughness induced scattering loss and input waveguide loss of about 7.5dB.

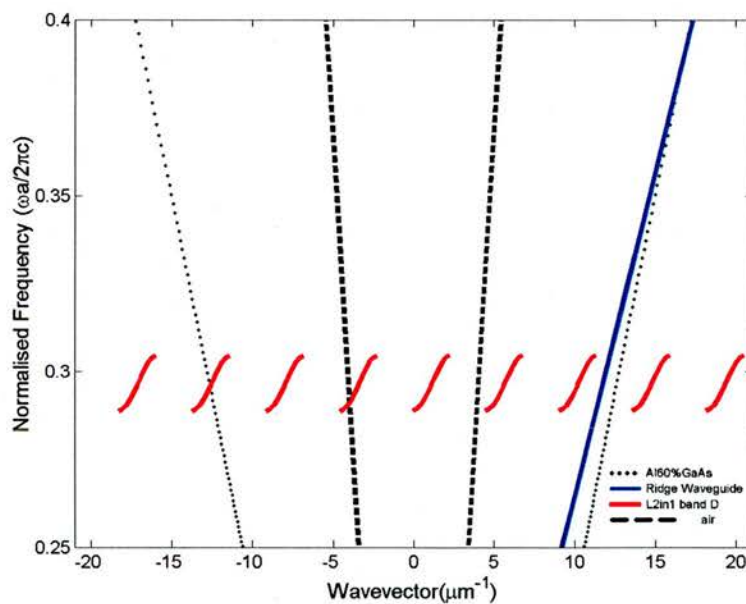


**Figure 3.42** The origin of the high loss in the GaAs waveguide. At  $1.55\mu\text{m}$  ( $\mu=0.29$ ) the coupling ridge waveguide mode (width= $\sqrt{3}a - 2R$ , solid blue) lies above the  $\text{Al}_{60\%}\text{GaAs}$  cladding line (dotted). The waveguide has become too narrow for this vertical heterostructure. The unfolded L2in1 mode has two components at this wavelength which lie above the air light line (dashed) and a total of six above the cladding light line. The light is lost due to radiation into the substrate and diffraction into both the air and substrate.

## 3.10 Pulse Compression

### 3.10.1 Fourier Transform propagation method

The two dispersive media (fibre and PhC) in the experiment act over considerably different length scales. If we treat the PhC as a linear filter (assuming that no nonlinear effects occur in the GaAs waveguide or fibre) we can model the pulse propagation through the entire experimental system. In doing so we can build upon Yew-Jun Chai's explanation (see Section 4 of Chai et al. [45]) of the pulse propagation experiment, but also including the dispersive effects of the PhC.

If we describe the electric field of the pulse as,

$$U(t, z) = \frac{1}{2\pi} \int_{-\infty}^{\infty} \tilde{U}(\omega, 0) e^{-j\omega t} d\omega \quad \{3.27\}$$

where the Fourier Transform of the input pulse ( $T=0$ ) is given as,

$$\tilde{U}(\omega, 0) = \int_{-\infty}^{\infty} U(t, 0) e^{j\omega t} dt \quad \{3.28\}$$

we can use the Fourier Transform method [53] to observe the pulse evolution in time. After obtaining the Fourier space ( $\omega$ -space) representation of the input pulse,  $\tilde{U}(\omega, 0)$ , we apply the dispersion by introducing the phase factor  $e^{j\beta(\omega)z}$ . Completing the inverse Fourier Transform returns us to temporal space.

We can also include the spectral filtering at the band edge as  $A(\omega)$ , the amplitude transmitted through the PhC. For the fibre we assume that this is,  $A=1 \neq A(\omega)$  as the fibre loss is as low as 0.2dB/km@1550nm with little spectral dependence in our pulse bandwidth. The band edge filtering of the Fourier components in the PhC has significant potential to cause pulse reshaping.

The resulting temporal pulse is given by,

$$U(t, z) = \frac{1}{2\pi} \int_{-\infty}^{\infty} \tilde{U}(\omega, 0) A(\omega) e^{-j(\omega t + \beta(\omega)z)} d\omega \quad \{3.29\}$$

where a change of variables  $\Delta\omega = (\omega - \omega_0)$ , shifts the frequency axis to the origin and allowing us to track the pulse in time  $T = t - \beta_1 z = 0$ ,

$$U(t, z) = \frac{1}{2\pi} e^{j(\omega t - \beta_0 z)} \int_{-\infty}^{\infty} \tilde{U}(\Delta\omega) A(\Delta\omega) e^{j(\Delta\omega(t - \beta_1 z) + \frac{1}{2}(\Delta\omega)^2 \beta_2 z)} d\Delta\omega$$

$$U(T, z) = \frac{1}{2\pi} e^{j(\omega T - \beta_0 z)} \int_{-\infty}^{\infty} \tilde{U}(\Delta\omega) A(\Delta\omega) e^{j(\Delta\omega T + \frac{1}{2}(\Delta\omega)^2 \beta_2 z)} d\Delta\omega \quad \{3.30\} \text{ c.f. } \{1.4\}$$

by moving our temporal window at approximately the same velocity as the pulse, i.e.

$v_g = \frac{1}{\beta_1}$ . The zero order coefficient  $\beta_0$  provides simply an overall phase, so can be

neglected until the end of the calculation. For the PhC we leave all the  $\phi = \beta_1 z$  terms in the phase factor, as it is so short that the offset caused by  $\beta_1 z$  does not exceed the  $N\Delta t$  window,

$$U(T, z) = \frac{1}{2\pi} e^{j\omega T} \int_{-\infty}^{\infty} \tilde{U}(\Delta\omega) A(\Delta\omega) e^{j\phi} d\Delta\omega \quad \{3.31\}$$

### 3.10.2 Fibre & CCW Dispersion

The fibre dispersion was calculated from the formula for SMF28e ‘photonic fiber’ from Corning [54], this is typical of fibre which meets ITU recommendation, ITU-T

G.652. The dispersion is given by,  $D(\lambda) = \frac{S_0}{4} \left( \frac{\lambda - \lambda_0^4}{\lambda^3} \right)$  ps/(nm·km) which is valid

over the spectral window 1200-1625nm. At the zero dispersion wavelength,  $\lambda_0 = 1313\text{nm}$  the zero dispersion slope is  $S_0 = 0.086 \text{ ps}/(\text{nm}^2 \cdot \text{km})$ . At 1310nm the group index is  $N_{g1310} = 1.4677$ , and at 1550nm,  $N_{g1550} = 1.4682$ . Using equation {1.9} we can convert this to  $\beta_2$ . Although the  $n_{\text{equiv}}$  in the fibre falls monotonically with wavelength, it is evident from the increase in  $N_g$ , beyond the zero dispersion wavelength, that the dispersion D is positive (negative  $\beta_2$ ), thus in this fibre red wavelengths are delayed more with respect to blue wavelengths (at  $\sim 1550\text{nm}$ ). This is an important point in the following.

The PhC dispersion is obtained from the 3D FDTD data as displayed in Figure 3.41.

The launched pulse has the form  $X(t) = e^{-\left(\frac{t-t_d}{\tau}\right)^2} \cdot \sin \omega t$ , where the  $\tau$  corresponds to the 1/e width of the pulse and the time delay,  $t_d$ , is equal to  $4\tau$ . At time  $T=0$  the centre of the pulse is located at  $z = -\frac{\omega_0 t_d}{\beta_1} = -\frac{4\omega_0 \tau}{\beta_1}$ . Filtering of the time domain

signal is required to remove the truncation ripple from the FFT. This was achieved using half of a cosinusoidal amplitude filter on the last half of the data. The temporal resolution for the pulse propagation was chosen to be approximately equal to  $\sim\Delta t=40$ as (attosecond), as typically required by the FDTD grid [55]. The total time window  $N\Delta t$  must be of order  $>2$  times the maximum pulse FWHM.

Using the pulsed, as opposed to the previous CW, technique to determine the dispersion, will eventually yield increasing errors if we attempt to recover the phase over too wide a spectral bandwidth. The technique launches all the power in the fundamental mode of the waveguide at the pulse centre frequency. Power at frequencies above and below the centre frequency is then either radiated from the waveguide or diffracts to excite higher order modes. In the CW simulation the resulting phase errors are avoided. To overcome this limitation to the pulse technique we would need to ‘bootstrap’ the incident pulse, running a simulation for a reasonable length of the input waveguide to allow the fields to settle down and save the resulting temporal file in the computer memory [56]. This feature is unavailable to us at present in the commercial software. For 3D simulation this would represent a major time penalty.

We compare the 3D L2in1 CCW to the small section of ridge waveguide (length $\sim 9.5\mu\text{m}$ ) as in the experiment and in this way do not include the effects due to the GaAs input and tapered waveguide sections. A fully vectorial mode solver (Fimmwave) was used to determine the lossy (below cutoff) dispersion of the  $\sqrt{3}a - 2R$  wide mode for this section, at  $\lambda=1550\text{nm}$ ,  $n_{\text{equi}}=2.9091$ . The ridge waveguide dispersion parameters,  $N_g$  and  $\beta_2$ , are plotted on the same scale as the L2in1 dispersion parameters in Figure 3.43. The ridge waveguide GVD parameter is negligible ( $10^{-3}\text{ps}^2/\text{mm}$ ) over this short distance when compared to the L2in1. Comparing c) and d) the effect of the high loss on the Group index is apparent. Those components which are delayed at  $1577\text{nm}$  in 2D ( $N_g=13.5$ ) do not show as pronounced a resonance (a flatter peak) in 3D ( $N_g=13$ ), although the magnitude of the delay is comparable. The net effect of this smoothed delay and this decreases the size of  $\beta_2$ . In both cases the peak delay occurs to shorter wavelength than the transmission maximum and thus the peak GVD parameter coincides with high transmission.

If we recall from Figure 1.2, that pulse compression was observed in a Gires Tournois Interferometer, where the GVD parameter displayed constant sign but whose magnitude varied across the pulse bandwidth (FWHM=13nm). The same argument can be made if we note that the regions of positive GVD parameter, in Figure 3.43 e) & f) are the same width as the pulse bandwidth (FWHM=8nm). Thus we chose to try to measure pulse compression experimentally in this structure. Ideally for true quadratic phase compression of these pulses we require a constant magnitude of GVD ( $0.02\text{ps}^2$  for 1m of SMF, the L2in1 GVD varies between  $0.02\text{-}0.05\text{ps}^2$  for  $10\mu\text{m}$ ). This would be more like the system of Figure 2.13. As in Chapter 2 we operate around a transmission maximum, created close to the band edge by the influence of the device interfaces. At the band edge the L2in1 dispersion behaves in a similar manner to the cascaded GTIs of Figure 1.3. In this case the dispersive PhC replaces the air filled Fabry-Pérot cavity. The PhC band edge dramatically decreases the local FSR of the cavity. This close proximity of the two peaks at the band edge generates a wider bandwidth of positive GVD.

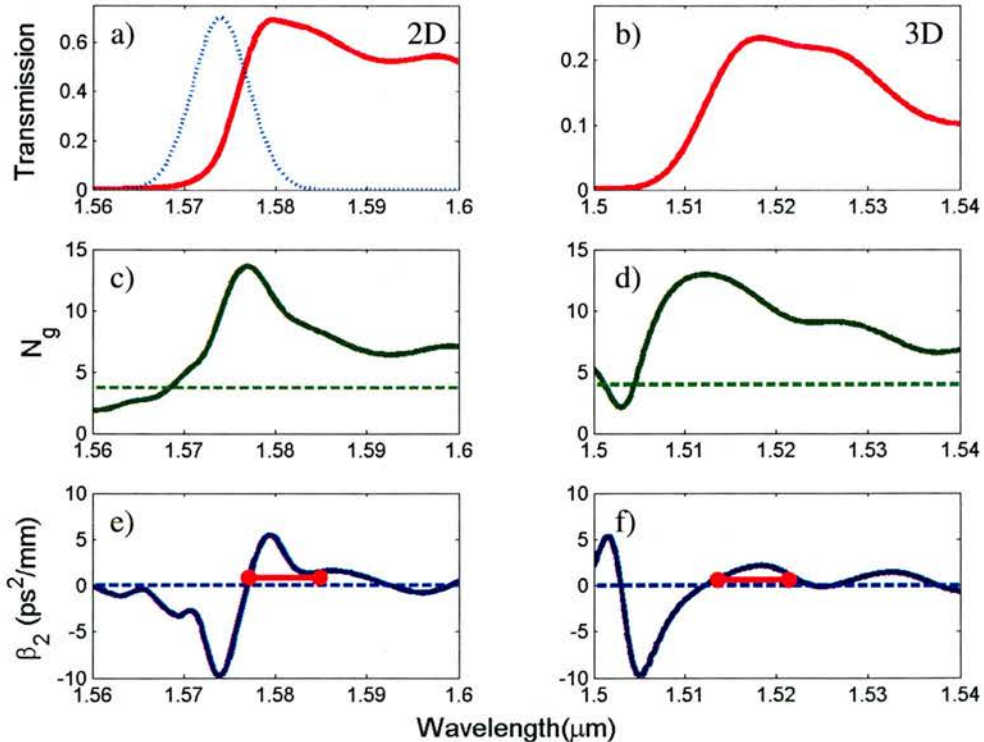


**Figure 3.43 a)** The Transmission spectra from the a) 2D and b) 3D FDTD models. The outline of the pulse spectrum is indicated by the light blue dotted line in a).  
**c) & d)** Corresponding Group Index (dark green) with the ridge waveguide (light green dashed) .

e) & f) GVD parameter (dark blue) with ridge waveguide data (light blue dashed), in 2D  
 $\beta_2 \sim 0.5 \times 10^{-3} \text{ ps}^2/\text{mm}$ , for the 3D waveguide  $\beta_2 \sim 1.5 \times 10^{-3} \text{ ps}^2/\text{mm}$ .

### 3.10.3 Comparison between Experiment and Model

Experimentally the pulses are seen to compress to around 500fs (bandwidth limited), indicating no residual higher order dispersion. The photonic crystal ‘filter’ can be positioned so that the high repetition rate pulses pass through it after they have been dilated by the pulse source (FWHM=14ps). The system is then less prone to non-linear effects. The delay at the band edge of the CCW is of order 350fs, which may conversely increase the likelihood of non-linear effects.

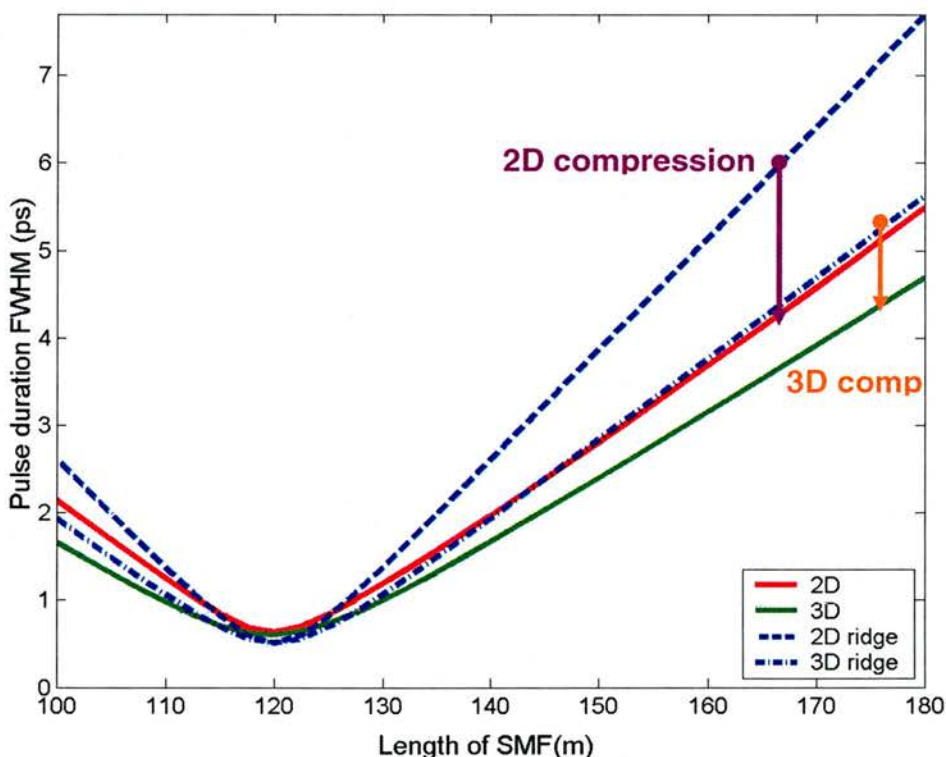
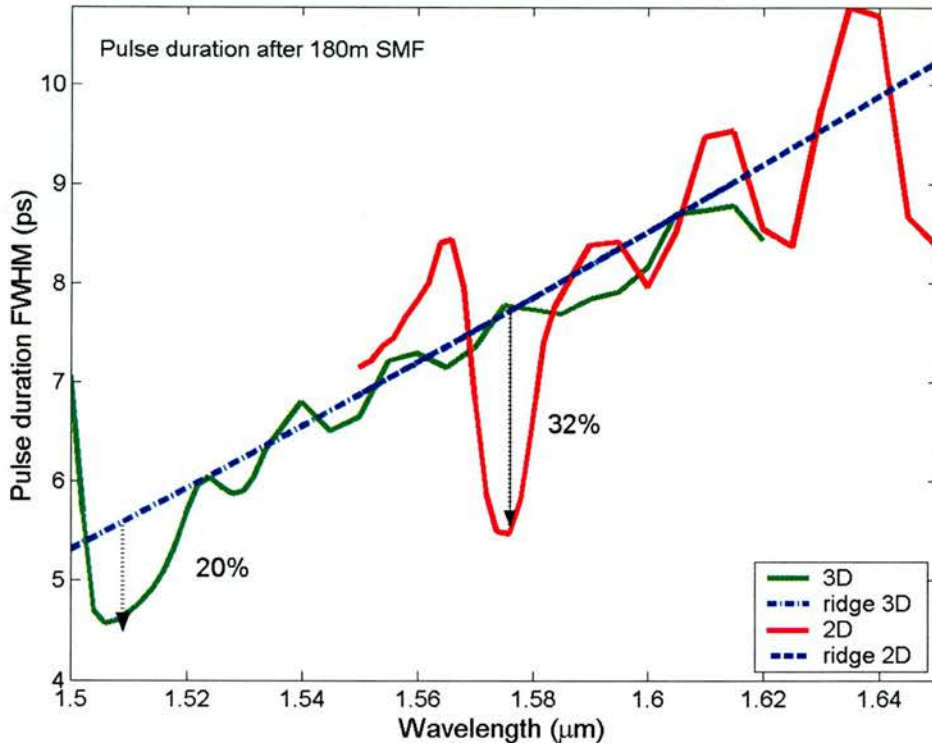


Figure 3.44 Propagating the Fourier components of the pulse through the PhC and SMF, yields a compression of the pulses with respect to pulses propagating through the ridge waveguide and SMF (blue dashed lines). Here the 3D data is plotted for  $\lambda=1510\text{nm}$  and the 2D data for  $\lambda=1576\text{nm}$ . The loss of bandwidth via spectral filtering in the PhC is apparent from the increase in the pulse width at the minimum. The difference in ridge dispersion between the two centre wavelengths is explained in the next graph, Figure 3.45

In the experiment the positive dispersion of the device counters the negative dispersion of the fibre and shifts the minimum (pulse waist) by several metres to longer lengths of fibre. Hence for shorter lengths of fibre, (ie. before the waist) the

pulse which has propagated through the PhC is observed to be longer than that which has propagated through the ridge waveguide. If the pulse waist is shifted (in the direction of longer lengths of fibre) then the pulse appears to have been further compressed, increasing the apparent pulse compression.



**Figure 3.45** Pulse durations plotted for a total length of SMF = 180m. At the band edge the pulses are compressed relative to pulses propagating through the ridge waveguides (dashed blue lines). This is more pronounced for the 2D data (red line), than for the 3D (green line). The background trend indicates that we have taken into account the variation of  $\beta_2$  with centre frequency for the SMF. The transmitted power obviously falls off as we drop lower down the band edge and also in 3D as we move to longer wavelength in the pass band.

The largest pulse compression which was observed from the model was for pulse centre frequencies centred (as shown in Figure 3.43 a)), relatively far down the band edge. In the experiment the pulse centre frequency was closer to the transmission maximum. The pair of EDFA s allow us to operate in this low transmission region of the spectrum. The low transmission is caused by impedance mismatch as we have shown above. The 2D model predicts a maximum compression of 32%, and the 3D model gives 20%, which are both less than the experimentally observed 40% pulse compression. The exact shape of the phase dispersion around the transmission maxima is unknown, which may account for the underestimation. The origin of the high dispersion appears to lie in a complicated interplay between the spectral amplitude filtering of the band edge and the phase dispersion of the Fabry-Pérot peaks

from the finite length device. The Photonic Crystal coupled cavity system is unfortunately overly prone to diffraction loss and this precludes extending the length of the device, in order to obtain more Group Velocity Dispersion.

### **3.11 Conclusions**

It has been possible to analyse many of the properties of 2D PhC Coupled Cavity Waveguides using 2D Plane Wave Expansion and 2D FDTD. In 2D FDTD and EME an equivalent index approximation is made to account for the dispersion of the heterostructure waveguide, into which a triangular lattice of air holes is etched. A range of CCWs were fabricated and their transmission characteristics measured. The spectral position of these peaks was found to be in good agreement with the 2D models.

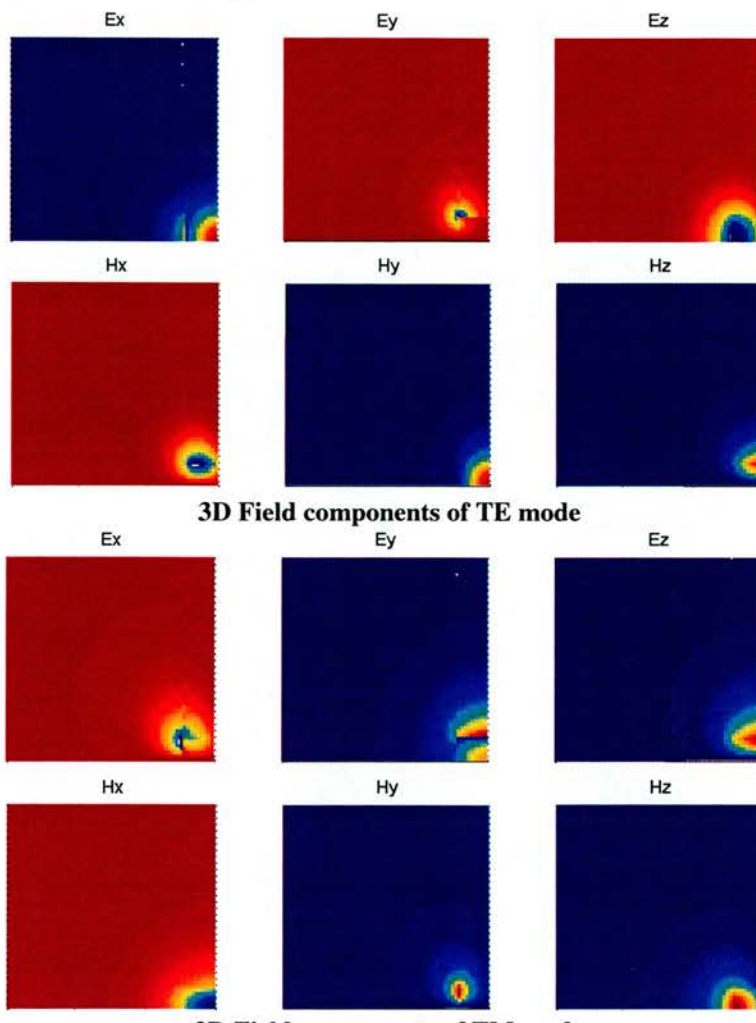
Improvements to etching at St Andrews using CAIBE for the second generation of samples allowed us to achieve a deep  $2\mu\text{m}$  etch depth. This permitted a high enough transmittance to warrant an attempt to measure the propagation of picosecond pulses through these waveguides. With the help of a pair of Erbium Doped Fibre Amplifiers a non-linear characterisation of the pulses was made possible.

The measurement comprehensively showed a large negative dispersion of the L2in1 CCW at the higher band edge. This is replicated in the large group index observed in both 2D EME and 2D FDTD at the upper bandedge.

The loss of the L2in1 waveguide was studied using 3D FDTD, remarkable agreement was found with experiment. Taking the fibre to fibre loss and the data normalised to the blank waveguide into account a maximum fabrication tolerance and waveguide loss is in the region of 7.5dB, which could be distributed across the entire 1mm long sample.

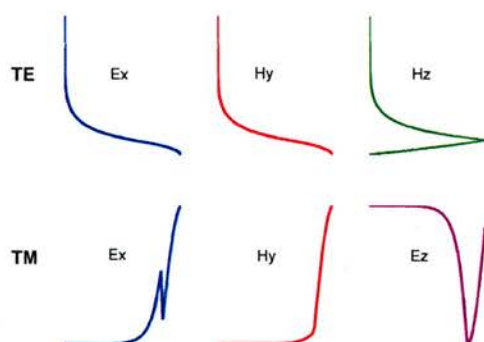
We can design our 2D waveguide to have high dispersion, but what is most critical for practical application of these devices is minimising the high loss.

## Appendix B – Field Components



Whilst writing this report the, very kind, proof readers pointed out that the polarisation was still an issue. The compatible components for the equivalent index approximation were not very clear. I have therefore plotted the 6 cartesian field components for a symmetric  $\text{Si}_3\text{N}_4$  ridge waveguide just for clarity.

On the next graph we consider the mode flattened to 2D, first from the side and then the top. The Ex and Hy components remain but the z component swaps from  $\mathbf{H}$  to  $\mathbf{E}$ .



**From the side a TE mode → TE mode. But viewed from above a TE mode → TM mode**

- 
- 1 Min Qui, "Effective index method for heterostructure-slab-waveguide-based two-dimensional photonic crystals", *Appl. Phy. Lett.*, 81 pp 1163-5, (2002)
- 2 Albert Birner, Ralf B. Wehrspohn, Ulrich M. Gösele, and Kurt Busch, "Silicon-Based Photonic Crystals", *Adv. Mater.* **13**, pp 377-88, (2001)
- 3 CAMFR, and P. Bienstmann, "Rigorous and efficient modelling of wavelength scale photonic components", doctoral thesis. Universitet Ghent, Vakgroep Informatietechnologie, (2000-1) Available <http://camfr.sourceforge.net/>
- 4 Fimmwave and Fimmprop, Photon Design Available <http://www.photond.com/>
- 5 R. Baets University of Ghent, INTEC, Belgium, "Managing out-of-plane coupling in 2D photonic crystals", Two Dimensional Photonic Crystals, Monte Verita, Ascona, Switzerland (2002)
- 6 T.F. Krauss and R. M. De La Rue, "Photonic crystals in the optical regime — past, present and future", *Progress in Quantum Electronics*, 23, pp 51-96, (1999)
- 7 W. Bogaerts, P. Bienstmann, D. Taillaert, R. Baets, D. de Zutter, "Out of Plane Scattering in 1-D Photonic Crystal Slabs", *Opt. & Quantum Electronics*, **34**, pp 195-203, (2002)
- 8 R. de Ridder, R. Stoffer, "Applicability of the finite difference time-domain method to photonic crystal structures", Tutorial presented at "Nanoscale linear and nonlinear optics" at the International School of Quantum Electronics", Erice, Sicily, Italy, (2000)
- 9 M. Kafesaki, M. Agio, C.M Soukoulis, "Waveguides in finite-height two dimensional photonic crystals", *J. Opt. Soc. Am. B*, **19**, pp2232-40,2002
- 10 W. Bogaerts, P. Bienstman, R. Baets, "Scattering at sidewall roughness in photonic crystal slabs", *Opt. Lett.*, **28**, pp689-91,(2003)
- 11 J. R. Lawrence, P. Andrew, W. L. Barnes, M. Buck, G. A. Turnbull and I. D. W. Samuel, "Optical properties of a light-emitting polymer directly patterned by soft lithography", *Appl. Phys. Lett.*, **81**, pp. 1955-1957 (2002)
- 12 M. Born and E.Wolf, "Principles of Optics: Electromagnetic Theory of Propagation, Interference and Diffraction of Light", 7th ed. , Cambridge University Press, (1999)
- 13 N. Stefanou, A. Modinos, "Impurity bands in photonic insulators" *Phys. Rev. B* **57**, pp 12127–133 (1998)
- 14 M. Bayindir, B. Temelkuran, and E. Ozbay, "Propagation of photons by hopping: A waveguiding mechanism through localized coupled cavities in three-dimensional photonic crystals", *Phys. Rev. B*, **61**, 11855-8, (2000) ; M. Bayindir, B. Temelkuran, and E. Ozbay, "Tight-binding description of the coupled defect modes in three-dimensional photonic crystals", *Phys. Rev. Lett.*, **84**, 2140-43, (2000) ; M. Bayindir, B. Temelkuran, and E. Ozbay, "Heavy photons at coupled-cavity waveguide band edges in a three-dimensional photonic crystal", *Phys. Rev. B*, **62**, 2247-50, (2000) ; E. Ozbay, M. Bayindir, I. Bulu, and E. Cubukcu, "Investigation of Localized Coupled-Cavity Modes in Two - Dimensional Photonic Bandgap Structures" *J. Quantum Electron.*, **38**, pp 837-43, (2002)
- 15 S. Olivier, C. Smith, M. Rattier, H. Benisty, C. Weisbuch, T. Krauss, R. Houdré, and U. Oesterlé "Miniband transmission in a photonic crystal coupled-resonator optical waveguide," *Opt. Lett.* **26**,1019-21 (2001).
- 16 T. J. Karle, D. H. Brown, R. Wilson, M. Steer and T. F. Krauss "Transmission through Photonic Crystal Coupled Cavity Waveguides with varying degrees of isolation" [Post deadline Conference Paper], QEP 15, Glasgow
- 17 A. Yariv, Y. Xu, R. K. Lee, A. Scherer, "Coupled-resonator optical waveguide: a proposal and analysis", *Opt. Lett.* **24**, pp 711-3 (1999); Y. Xu, R. K. Lee A. Yariv, "Propagation and second-harmonic generation of electromagnetic waves in a coupled-resonator optical waveguide", *J. Opt. Soc. Am. B*, **17**, pp387-400, (2000)
- 18 O.J. Painter, A. Husain, A. Scherer, J.D. O'Brien, I. Kim, P.D. Dapkus, "Room Temperature Photonic Crystal Defect Laser at Near-Infrared Wavelengths in InGaAsP", *J. Lightwave. Technol.*, **17**, pp2082-8, (1999); J. Vučković, M. Lončar, A. Scherer, "Design of Photonic Crystal Microcavities", preprint; O.J. Painter, J. Vučković, A. Scherer, "Defect modes of a two-dimensional crystal in a optically thin dielectric slab, ",*J. Opt Soc. Am. B*, **16**, pp275-85, (1999);
- 19 S. G. Johnson and J. D. Joannopoulos, "Block-iterative frequency-domain methods for Maxwell's equations in a planewave basis," *Optics Express* 8, 173-90 (2001), available <http://ab-initio.mit.edu/mpb/>
- 20 This supercell size and resolution necessary for PWE convergence has been independently verified at St Andrews.

- 
- 21 J.D. Joannopoulos, R.D. Meade, J.N. Winn, "Photonic Crystals: Molding the Flow of Light", Princeton University Pres (1995)
- 22 R. Padjen, J.M. Gerard, J.Y. Marzin "Analysis of the Filling Pattern Dependence of the Photonic Bandgap for Two-dimensional Systems", *J. Mod. Opt.*, **41**, pp 295-310 (1994)
- 23 E. Centeno, D. Felbacq, "Characterization of defect modes in finite bidimensional photonic crystals", *J. Opt Soc. Am A*, **16**, pp2705-12, (1999)
- 24 T. J. Karle, D. H. Brown, R. Wilson, M. Steer, T. F. Krauss, "Planar Photonic Crystal Cavity Waveguides," *J. Sel. Top. Quantum Electron.* **8**, pp909 (2002).
- 25 D. Labilloy, H. Benisty, C. Weisbuch, T.F. Krauss, R.M. De La Rue, V. Bardinal, R. Houdré, U. Oesterlé, D. Cassagne, C. Jouanin, "Quantitative measurement of transmission, reflection and diffraction of two dimensional photonic bandgap structures at near infrared wavelengths", *Phys. Rev. Lett.*, **79**, pp 4147-50, (1997)
- 26 T. J. Karle, D. H. Brown, R. Wilson, M. Steer and T. F. Krauss, [Invited Conference Paper], *Progress In Electromagnetics Research Symposium*, Cambridge, Mass, USA, July 2002.
- 27 S. Boscolo, C. Conti, M. Midrio, C.G. Someda, "Numerical Analysis of Propagation and Impedance Matching in 2-D Photonic Crystal Waveguides With Finite Length", *J. Lightwave Technol.*, **20**, pp304-10, (2002)
- 28 R. Biswas, Z.Y. Li, K.M. Ho, "Impedance of photonic crystals and photonics crystal waveguides", *Appl. Phys. Lett.*, **84**, pp1254-6,(2004)
- 29 J. Uschida, M. Tokushima, M. Shirane, A. Gomyo, H. Yamada, " Immitance Matching for Multi-dimensional Open-system Photonics Crystals", arXiv; cond-mat/0306260 v2 7 Aug 2003
- 30 A. Boag, "Design of Coupling Structures for Photonic Crystal Devices", Session 1P2: EBG/PBG Structures – II, *Progress In Electromagnetics Symposium* 2003, Hawaii, October 2003
- 31 C.J.M. Smith, T.F. Krauss, H. Benisty, M. Rattier, C. Weisbuch, U. Oesterle, R. Houdré, "Directionally dependent confinement in photonic-crystal microcavities", *J. Opt. Soc. Am. B*, **17**, pp2043-51, (2000)
- 32 A.L. Reynolds, U. Peschel, F. Lederer, P.J. Roberts, T.F. Krauss, P.J.I. de Maagt, "Coupled Defects in Photonic Crystals", *IEEE Trans. Microwave Theory and Techniques*, **49**, pp1860-7, (2001)
- 33 C.J.M. Smith, R.M. De La Rue, M. Rattier, S. Olivier, H. Benisty, C. Weisbuch, T.F. Krauss, R. Houdré, U. Oesterle, "Coupled guide and cavity in a two dimensional photonic crystal", *Appl. Phys. Lett.* **78**, pp1487-9, (2001)
- 34 T. D. Happ, M. Kamp, A. Forchel, J. L. Gentner, and L. Goldstein, "Two-dimensional photonic crystal coupled-defect laser diode," *Appl. Phys. Lett.* **82**, 4-6 (2003).
- 35 H. Altug and J. Vučković, "Two-dimensional coupled photonic crystal resonator arrays", *Appl. Phys Lett.* **84** , pp161-3, (2004); H. Altug and J. Vučković, "Experimental demonstration of the slow group velocity of light in two-dimensional coupled photonic crystal microcavity arrays", submitted, (2004) (arXiv, physics/0406109)
- 36 M. Soltani, A. Adibi, Y. Xu., R.K. Lee, "Systematic design of single-mode coupled-resonator optical waveguides in photonic crystals", *Opt. Lett.*, **28**,pp 1978-80, (2003)
- 37 W.J. Kim, W. Kuang, J.D. O'Brien, "Dispersion characteristics of photonic crystal coupled resonator optical waveguides", *Optics Express*, **11**, pp3431-7, (2003)
- 38 P. Sanchis, J. Garcia, A. Martinez, F. Cuesta, A. Griol, J. Martí, "Analysis of adiabatic coupling between photonic crystal single line-defect and coupled-resonator optical waveguides", *Opt. Lett.*, **28**, pp1903-5, (2003); A. Martinez, A Garcia, P. Sanchis, J. Martí "Group velocity and dispersion model of coupled-cavity waveguide in photonic crystal", *J. Opt. Soc. Am. A.*, **20**, pp147-150, (2003)
- 39 D. Leuenberger, R. Ferrini and R. Houdré, "Ab initio tight-binding approach to photonic crystal waveguides", *J. App. Phys.*, **95**, pp 806-9, (2004)
- 40 M. Hammer , 1D, 2D WWM mode solvers <http://wwwhome.math.utwente.nl/~hammer/>
- 41 Fimmwave and FimmProp 3D, Photon Design, [www.photond.com](http://www.photond.com)
- 42 BeamProp built in solver for modes which are then meshed to FDTD grid (Iterative or Correlative)
- 43 P. Kramper, M. Agio, C.M. Soukoulis, A. Birner, F. Müller, R.B. Wehrsporn, U. Gösele, V. Sandoghdar, "Highly directional emission from Photonic Crystal Waveguides of Subwavelength Width", *Phys. Rev. Lett.* **92**, 113903, (2004)
- 44 Fullwave, RSoft Inc, Ossining, N.Y, USA
- 45 T.J. Karle, Y.J. Chai, C.N. Morgan, I.H. White, T.F. Krauss, "Observation of Pulse Compression in Photonic Crystal Coupled Cavity Waveguides", *J. Lightwave. Technol.*, **22**, pp 514-9, (2004); Y.J. Chai, C.N. Morgan, R.V. Penty, I.H. White, T.J. Karle, T.F. Krauss, "Propagation of optical pulses in photonic crystal waveguides", *IEE Proc.-Optoelectronics*, **151**, pp109-13, (2004)

- 
- 46 I.Y. Krushchev, I.H. White, R.V. Penty, "High-quality laser diode pulse compression in dispersion-imbalanced loop mirror", Electron. Lett., **34**, pp1009-10, (1998)
- 47 T. Shoji, T. Tsuchizawa, T. Watanabe, K. Yamada and H. Morita, "Low loss mode size converter from  $0.3\mu\text{m}$  square Si wire waveguides to single mode fibers," Electron. Lett. **38**, 1669-1670 (2002).
- 48 M. Boroditsky, R. Cocciali, E. Yablonovitch, "Analysis of photonic crystals for light emitting diodes using the finite difference time domain technique", Proc. SPIE, 3283, 184-90, (1998)
- 49 T. Ochiai, K. Sakoda, "Dispersion relation and optical transmittance of a hexagonal photonic crystal slab", Phys. Rev. B, **63**, 125107, (2001); K. Sakoda, "Optical Properties of Photonic Crystals", Chpt 8, Springer Verlag (2001)
- 50 G.R. Hadley, private communication; G.R. Hadley, "Out of Plane Losses of line defect photonic crystal waveguides", IEEE Photon. Technol. Lett., **14**, pp642-4, (2002)
- 51 Ph. Lalanne, "Electromagnetic Analysis of Photonic Crystal Waveguides operating above the light cone", IEEE J. Quant. Electron., **38**, pp800, 2002; Ph. Lalanne, H. Benisty, "Out of plane losses of two dimensional photonic crystals waveguides: Electromagnetic analysis", J. Appl. Phys., **89**, pp1512-4 (2001) ; M. Palamaru, Ph. Lalanne, "Photonic crystal waveguides, Out-of-plane losses and adiabatic modal conversion", Appl. Phys. Lett., **78**, pp1466-8 (2001)
- 52 D. Marcuse, "Theory of Dielectric Optical Waveguides", Academic Press, (1974)
- 53 G.P. Agrawal, "Nonlinear Fibre Optics", 3<sup>rd</sup> edition, Academic Press, (2001)
- 54 Corning® SMF-28e® Photonic Fiber, PI14456, April 2005, Corning Inc
- 55 B. Khubchandani, "Nonlinear Pulse Propagation Through An Optical Fiber: theory and Experiment", Thesis (2004)
- 56 S. Hagness, PhD dissertation, "FDTD Computational Electromagnetics Modeling of Microcavity Lasers and Resonant Optical Structures", Northwestern University, 1998

# Chapter 4

## 4.1 Line defect waveguides

We looked at the response of point defects, where individual holes had been removed to form cavities within the lattice, in Chapter 3. In this chapter we will remove entire rows of holes along the  $\Gamma$ K lattice direction, forming line defects in the PhC lattice. From another perspective, we could also consider these to be ridge waveguides with a 2D corrugated cladding. The dispersion of the corresponding PhC waveguide modes then falls into two categories; they are either index guided or gap guided. The index guided modes follow roughly the same dispersion as the waveguide modes of a ridge waveguide of similar width. The gap guided modes in 2D are supported above the light line and originate from the  $\Gamma$  point, at non-zero frequency.

The intersections that this gives rise to between index guided and gap guided modes, give the waveguides interesting dispersion properties. In the CCWs of the previous chapter the group velocity approached zero only at values of  $k=0$  and  $\pi/a$  (the  $\Gamma$  and K points). In this chapter we will study partial band gaps (Mini Stop Bands - MSBs) which allow the group velocity to tend to zero at other points, designated by the crossing point between the modes. This allows us more freedom to tailor the waveguide dispersion. Practical considerations, pertaining to the suitability of the waveguide heterostructure for guiding whilst dispersing the light provide a sobering limit to the applicability of some of these 2D effects.

There has been a noticeable divide between the various groups working on 2D PhC waveguides around the globe. The major European collaborations have concentrated their efforts [1] on etching photonic crystals into heterostructure waveguides with Low-Out-of-Plane (LOP) contrast. The main motivation for this is to provide a substrate for thermal and electrical conduction. The inherent compatibility with heterostructure laser sources and modulators has been seen as a strong motivation to pursue this approach. In many cases, very successful demonstrations of PhC phenomena have ensued. This is certainly the main impetus for our own approach.

The Japanese and American groups have on the whole pursued the “membrane” approach with High-Out-of-Plane contrast (HOP). That is to say, they have wet etched away the substrate underneath their waveguides to form a free standing structure. The major attraction has been the ability to strongly confine the light and being able to retain folded states beneath the steep cladding (air) light line. The distinction is by no means absolute and may reflect the technologies that were the focus of attention at the time when optical PhC waveguiding became a serious research topic. This divergent approach has benefited everyone as many more varied fabrication, modelling and measurement techniques have been adopted. On balance the most significant results have come recently from the strong and healthy competition between IBM, NTT and FESTA where low losses in a W1 waveguide have reached the 0.6dB/mm mark [2,3,4]. W1 follows the classification from the previous chapter and represents a “Waveguide” consisting of a single (1) missing row of holes.

Low loss is essential to the practical implementation of PhC waveguides. In the context of this chapter, low loss is essential because we desire to probe the photonic bandstructure of the waveguides. This requires longer lengths of waveguide, in order to minimise the finite length effects which were prevalent in the previous chapter, and to demonstrate the net benefit of the PhC waveguide. This chapter is divided between W1 and the wider W3 waveguides. As we calculated in Section 3.6.3 the impedance mismatch, between ridge and line defect PhC waveguide, is very small away from the band edges. The wider guides are anticipated to demonstrate lower loss values due to their reduced lateral confinement. Increasing the width of the guide does tend to produce an increasingly multimode waveguide however.

To investigate the properties of these waveguides in their 3D settings, we will experimentally measure their transmission spectra, as in the previous chapter. Additionally we will make use of near and far field imaging techniques to directly probe the fields of the guided and radiating modes. From this information we can plot the dispersion relation of the waveguides and using 3D FDTD we can compare theory to experiment. Firstly in 4.2.1 we calibrate our 3D model against a benchmark structure. We then detail the results of a near field probe measurement (in 4.2.2), of a similar structure, and compare the dispersion to our 3D model. We then outline the

development of wide band transmission techniques for the characterisation of PhC waveguides. These are then applied (in Section 4.2.3), firstly to a selection of Low-Out-of-Plane contrast (LOP) AlGaAs W1 heterostructure waveguides (those that were available to us) and then (in Section 4.2.4) to a High-Out-of-Plane contrast (HOP) Silicon on Insulator W1 waveguide. This sequence is then repeated for the wider W3 waveguides, firstly studying the transmission properties of AlGaAs W3 waveguides (in Section 4.3.14.3) and then looking in detail at the measured and simulated dispersion of an SOI W3 waveguide (in Section 4.4). Finally we attempt to shed some light on the mechanisms behind the interesting dispersion characteristics of these waveguides.

## 4.2 Line defect waveguides –W1

To begin we consider the 2D dimensional structure of the W1 waveguide and the impact that the triangular lattice states have on the bandstructure.

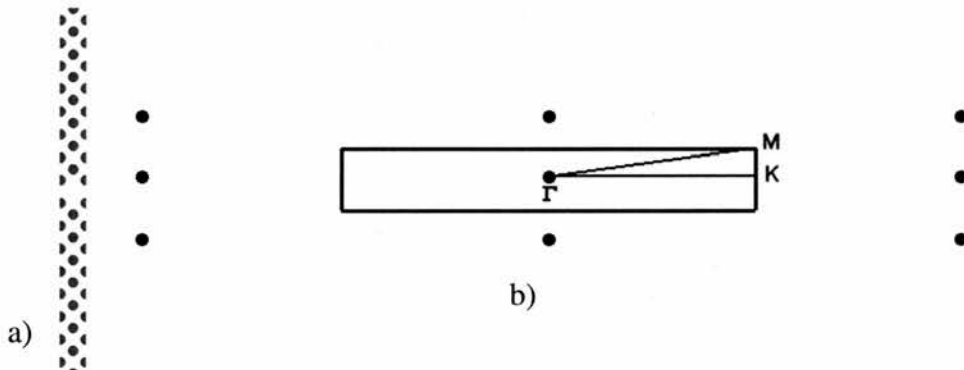


**Figure 4.1 Supercell and reciprocal lattice vectors for W1 waveguide, (scale equal to Figure 3.11)**

The supercell for a W1 waveguide is depicted in Figure 4.1a), along with its reciprocal space representation, b). The lattice vector along the waveguide direction is now equal to the unit cell lattice vector,  $a$ . The CCW lattice vectors ( $2a$ ,  $3a$ ,...) were always longer than the unit cell lattice vector, as we have seen in previous chapters. That the vectors are equal simplifies the explanation of why, for the CCWs, the lower band edge has a frequency maximum in the centre of the wavevector diagram, and not at the  $K$  point (see for example Figure 3.12). To elucidate we plot the reciprocal space representations of both the W1 (from above) and the unit cell on the same axes (see Figure 4.2). It is apparent that the set of accessible wavevectors in the Irreducible Brillouin Zone (IBZ) is restricted to the range  $\Gamma \rightarrow K'$  rather than

$\Gamma \rightarrow K$ . If we look along this axis (the purple dotted line) outside the W1 IBZ we intersect first K and then the M point of the next BZ. The former point, K, is folded inside the IBZ to point  $k = 2K' - K$  and the latter point, M, is folded back to the origin, or  $\Gamma$  point [5]. This is a consequence of the rectangular supercell and so applies to the W1, W3 and to each of the 2D CCW supercells from the previous chapter.

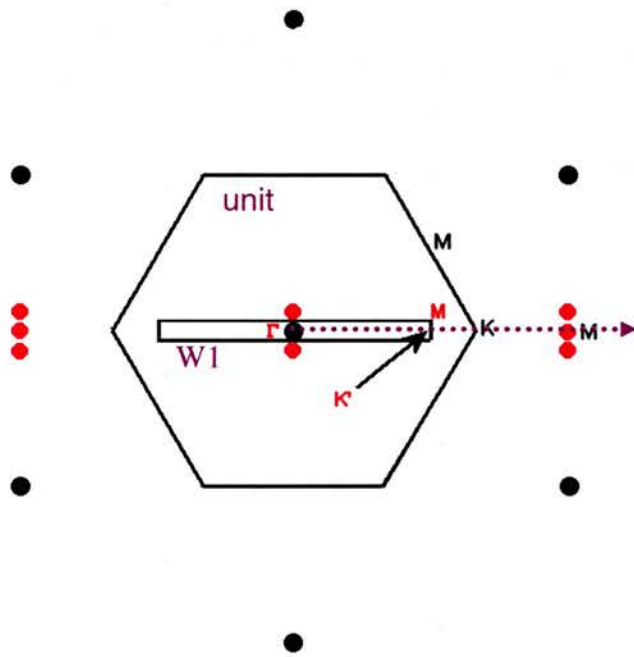
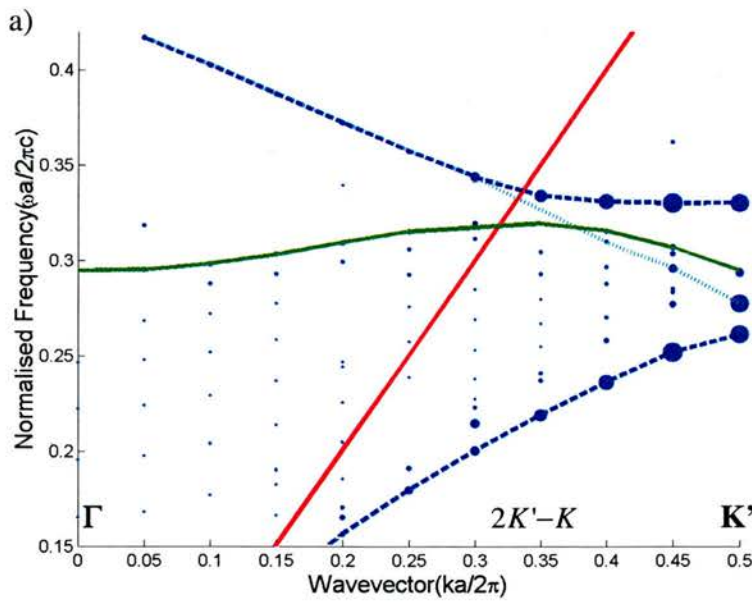


**Figure 4.2 Reciprocal space representation of W1 waveguide (red dots) plotted with the single unit cell (black dots) of the triangular lattice. The rectangular supercell causes the IBZ to restrict the set of wavevectors along the  $\Gamma K$  direction that we can access to  $\Gamma \rightarrow K'$ . This causes additional folding at  $k = 2K' - K$ . Smaller scale than in Figure 4.1**

#### 4.2.1 W1 Silicon Membrane – modelling benchmark

This additional folding has important ramifications for the dispersion of the W1 waveguide. To illustrate this we consider a photonic crystal etched into a thin membrane of semiconductor ( $n=3.4$ , thickness,  $d=0.258\mu\text{m}$ ). The slab waveguide is vertically single mode and only horizontally even waveguide modes are considered in Figure 4.3, in order to simplify matters. The blue dots are the eigenmodes solved by a 3D FDTD simulation, the waveguide mode is highlighted by the dashed blue line. Larger dots indicate a longer lifetime, i.e. a higher Q mode. The plot depicts the lower band edge with a maximum at  $k=0.35$ ,  $u=0.32$ , this is caused, as explained above, by

the folding of the K point back in to the IBZ. The index guided mode of the W1 waveguide (marked by the dashed blue line) folds strongly at the K point. The mode actually folds beneath the band edge (the two large dots at  $k=0.5$ ,  $u=0.26$  and 0.28) and then appears to repeat again above the band edge, in the bandgap ( $k=0.5$ ,  $u=0.34$ ). The ‘almost’-flat dispersion inside the bandgap actually belongs to a gap guided lattice mode (the green line) which is highly localised around the defect row, and has the same symmetry and polarisation as the fundamental. The interaction between these modes results in a Mini Stop Band (MSB, see later in this Chapter). This high curvature at the band edge is of interest with regard to PhC delay lines and dispersion compensators. For researchers who wish to transmit data pulses along this waveguide the high dispersion is an inconvenience. Typically data transmission would require an index guided waveguide mode with a steep, linear slope. This is the case for frequencies above the light line, but in this region the mode is not guided by TIR and suffers diffraction loss, as is indicated by the smaller dots (lower Q states).



b)

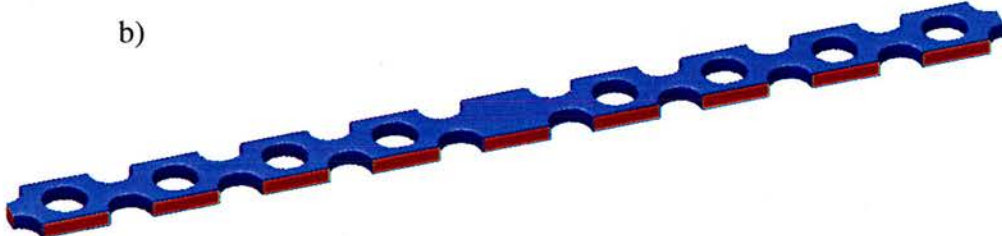


**Figure 4.3** 3D FDTD bandstructure diagram for the even modes of a W1 waveguide, consisting of a triangular lattice of holes perforating a thin membrane of semiconductor ( $n=3.4$ ,  $a=0.43055$ ,  $r/a=0.3$ , thickness,  $d=0.6a$ ). The fundamental waveguide mode is seen to fold strongly at the K

point. The red solid line denotes the air light line. Many researchers wish to be able utilise the high dispersion at this point, but it creates a headache for those seeking low loss guiding. Ideally for low loss a fast mode (one with a steep slope,  $v_g = d\omega/dk$ ) is required with significant bandwidth beneath the light line. Larger dots indicate a longer lifetime ( $Q$ ) of the state, and indicate that the longer lifetime states indeed occur beneath the lightline. This structure is now a benchmark for loss analysis. b) Calculated for 9 transverse rows of holes, with a symmetry boundary at the centre.

On the above plot (see Figure 4.3) the size of the dot indicates the  $Q$  of the mode. The sharp increase in  $Q$  below the air light line (TIR boundary) illustrates, very visually, the preferred operating regime of many researchers. The diffractive losses occurring above the light line are detrimental to the propagation, as we saw in previous chapters. Researchers would like, however, to find a steep mode confined by the photonic band gap, as this would be theoretically lossless. The first, and very challenging, task is to position a steep mode inside the bandgap, but beneath the light line. It can be seen that the only part of the mode beneath the light line, and hence having no intrinsic loss, is highly curved. The flatness of the band also denotes a high group index. The extrinsic loss, the loss due to roughness and disorder, has been calculated to increase linearly with the group index,  $N_g$  [6].

This benchmark structure provided a particularly good calibration structure for the 3D FDTD simulations in this chapter. Very good agreement between the spectral position and diffractive losses was obtained. Indeed the agreement with 3D PWE band structure calculations was within 1% across the entire waveguide mode [7].

#### 4.2.2 W1 Silicon Nitride Membrane – model and experiment

We can retain a TE bandgap even at substantially lower index contrast. Using a Scanning Near Field Optical Microscope (NSOM), measurements were made of the optical fields propagating inside a W1 waveguide fabricated on a Si rich  $\text{Si}_3\text{N}_4$  film. The experimental work was carried out by Rob Engelen at the University of Twente in the Netherlands [42]. The details of the measurement technique will be discussed at the end of the chapter. We gain direct access to the fields in the waveguide by coupling part of the evanescent mode tail from the waveguide mode. As the structure is a membrane, it is vertically symmetric and therefore theoretically the TE and TM

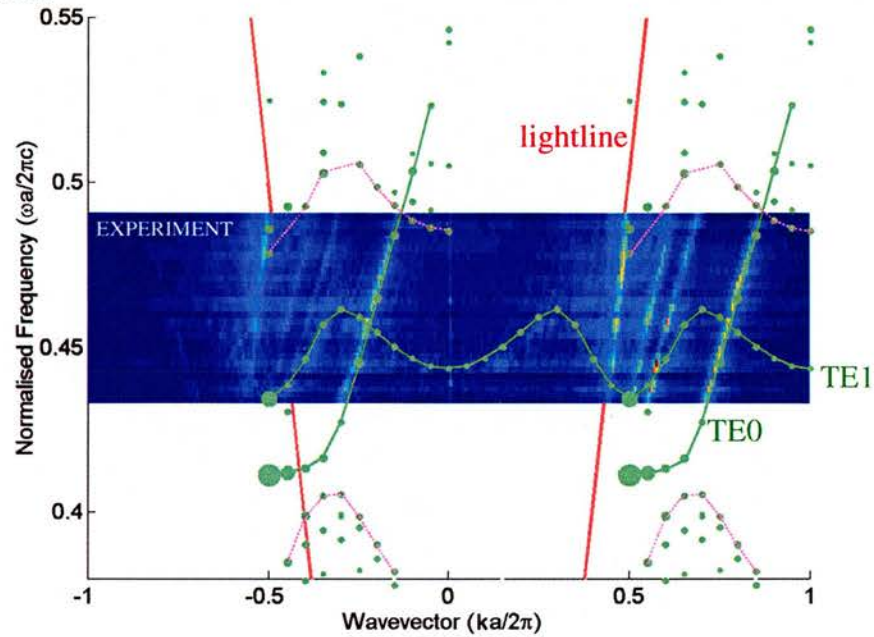
modes cannot mix. One drawback of this measurement technique is that the apparatus appears unable to discriminate between orthogonal polarisation states. The fields are mixed in the cylindrically tapered NSOM tip [see Figure 4.15] and we require a numerical model to assist in categorising the modes of the waveguide under test. The resolution of the tip is in this case enhanced by metallization, which creates a narrower aperture at the apex of the tip. We can consider the tip as an antenna which must be excited correctly in order to obtain a travelling wave in the single mode fibre (which has been drawn down to form the tip). As such this may create a bias when measuring particular field distributions and care needs to be taken in assessing the response of this near field probe. Again a model is useful here for purposes of calibration.

The index of refraction of the  $\text{Si}_3\text{N}_4$  is taken as 2.16. The membrane is  $0.16\mu\text{m}$  thick. The W1 waveguide was patterned by Laser Interference Lithography (LIL) [8]. The waveguides were characterised using a tunable source of visible laser light. The detection setup measures both the phase and amplitude of the propagating field. This complex data is then summed across the waveguide to yield a single row of data. This row is then Spatially Fourier Transformed along the waveguide axis. Plotting the real part of the Fourier Transform as a function of the centre wavelength of the laser yields the eigenstates presented in Figure 4.4. When plotted for the entire measurement range the bands become apparent and from their slope ( $v_g = \partial u / \partial k$ ) we can ascertain that the pulses are forward travelling. The waves which make up this pulse travelling in a periodic waveguide are both forward and backward travelling. We will return to this point later in the chapter.

A 3D FDTD simulation was performed for this membrane PhC, with  $a=0.293\mu\text{m}$ ,  $d=0.16\mu\text{m}$ ,  $r/a=0.34$ . Two separate calculations were necessary, one for TE and one for TM polarisation. These are plotted as two separate data sets overlaid on top of the one set of measurements (the blue background regions are identical). A band gap exists for TE polarisation between  $u=0.41-0.49$ . In the upper Figure 4.4 a) the green lines denote the TE modes, and as in Figure 4.3 we have a strong contribution from the folded even fundamental mode TE0. The faint outline of the gap guided TE1 mode can be seen in the +1BZ, this mode has horizontal odd symmetry with respect

to the waveguide axis. In the lower Figure 4.4b) the pink dots denote the TM eigenmodes. With inspection of the Q factor and the trend of the line the TM0 and TM1 modes can be seen, corresponding to the two closely spaced lines between the TE0 and the lightline. The lightline is prevalent in both FDTD and measurement due to the excitation of modes which cutoff at higher frequency but which localise in the vicinity of the waveguide. The other pink dots extend throughout the region as there is no bandgap for TM modes, and they have relatively low Q.

a) TE modes



b) TM modes

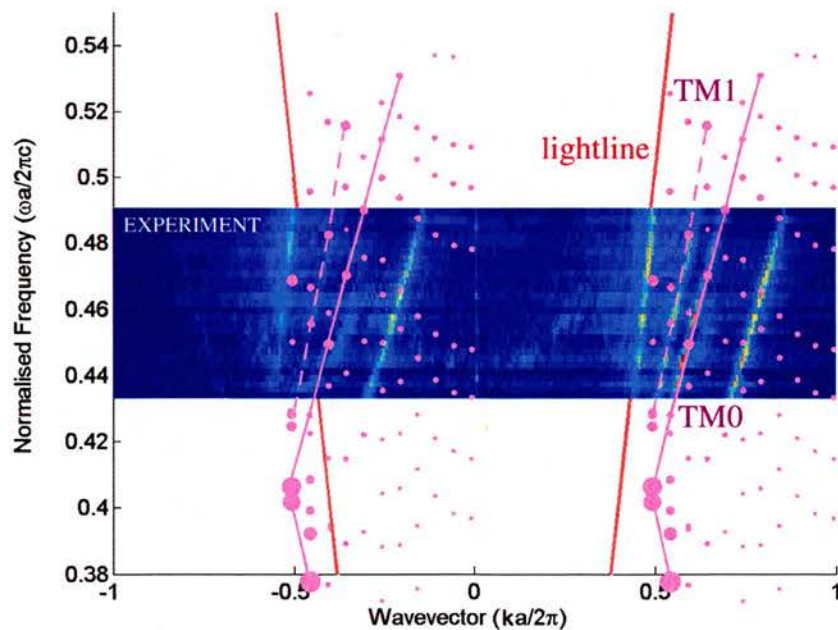


**Figure 4.4** The a) TE and b) TM band structures calculated for a W1 Si<sub>3</sub>N<sub>4</sub> waveguide using 3D FDTD,  $a=0.293$ ,  $r/a=0.34$ . These are overlaid upon the complex measured Fourier Transformed data. A band gap exists for TE polarisation between  $u=0.41-0.49$ . The W1 waveguide mode was coupled directly by lens end fire and it would appear that this excites both the fundamental TE and TM modes. The TE data is scaled by 4% to fit the measurement ( $a=0.274$  and  $0.280$ ), the TM data fits perfectly. Larger dot indicates higher Q. Some FDTD data points are distributed along the light line in agreement with its experimental observation. The gap guided TE1 (odd mode) appears as a faint outline its presence in the +1BZ would indicate that it was travelling forwards.

The 3D FDTD bandstructure is obtained by exciting the periodic supercell with a broadband pulse. The bandgap in this case occurs, naturally, at much higher frequency due to the lower index contrast. By exciting each eigenfrequency with a narrow band excitation the loss can be determined by the rate of decay of the temporal data. We have included this information as a Q factor, in Figure 4.3 and Figure 4.4, larger Q is denoted by larger dots. As with the higher contrast grating (4.2.1 W1 Silicon Membrane) the Q of the mode increases drastically as we cross the lightline boundary. The sample's lattice constant and the frequency-doubled laser's tuning range (590-675nm) limit the measurement to the spectral region above the lightline. The NSOM apparatus is able to resolve the separate spatial components of the waves which travel in this periodic waveguide. The fundamental waveguide modes are detected in both the -1BZ and the +2BZ. In the 3D FDTD data there are TM states throughout the experimental region i.e. there is no band gap for TM polarisation. The TE field is strongly folded back by the periodicity of the grating. Examining the ratios of the longitudinal component of the Poynting vector,  $S_z = E \times H$ , associated with the forward and backward travelling waves we find 10% of the energy is folded into the -1BZ [agreeing well with 32]. Here we have been able to directly measure the sign of the wavevector, in contrast to [32]. The TM resonance is only represented as a small fraction in the -1BZ in the measured data. The light cone appears to fold incorrectly in the -2BZ, it has positive slope in each BZ, its slope should be negative for negative k.

#### **4.2.3 W1 AlGaAs heterostructures – Transmission measurements**

W1 waveguides were fabricated on 3 separate heterostructure waveguides. These were

- A. a 220nm GaAs surface waveguide atop 2 $\mu$ m Al<sub>90%</sub>GaAs cladding
- B. an Al<sub>20%</sub>GaAs core structure (details in section 4.3.3 below)
- C. the “Scotland” GaAs heterostructure (details in Chapter 3)

Devices of varying length were fabricated for waveguides A and B and so we present an analysis of the loss mechanisms below. Firstly we discuss the optical characterisation techniques that were employed.

These W1s were all characterised in transmission at St Andrews using a 1300nm tunable diode laser (Agilent 8167B). The typical measurement setup is illustrated in Figure 4.3. Lock-in detection is used to remove background signals. The laser’s collimated free space output is 99.5% polarised and a half-waveplate is used to obtain the required input polarisation state, a Glan Thompson prism is used as an analyser. Aspheric lenses with broadband IR coatings are used to launch and capture the waveguided light. Cleaved Single Mode Fibre (SMF) has also been used to launch light (see Chapter 5). This does not however provide a suitable match to the spot size and numerical aperture of the waveguide. Spherical and cylindrical lensed fibres have been investigated to solve this mismatch - they were found to be about half as efficient as lens end fire. Transmission through these short lengths of fibre leads to a polarisation scrambling of ~5%.

In its current configuration the laser scanning speed is relatively slow. Several schemes were devised to increase the scan speed or improve the reliability of the data. The laser is computer controlled by GPIB using a Labview script. The main problem is caused by the lack of internal hardware status information. When the laser receives a command to change the wavelength, it operates on each command sequentially until the command list is clear. The grating, which forms the tuning mechanism in this external cavity DFB laser, is then actuated to tune the laser to each successive wavelength. There is unfortunately no built in hardware “flag” to indicate that the laser has tuned to the required wavelength, rather the operation complete bit is set as soon as the firmware has processed the command. In short, the status information

indicates the status of the firmware rather than the hardware. An additional complexity arises as between wavelengths the laser output is shut off (possibly to allow the correct output power to be set) as is the modulation signal and so the lock-in must reacquire the signal and reference. The most satisfying and stable solution to this problem was to loop the data capture from the lock-in until a stable signal ( $>0$ ) was recovered, ensuring that the laser had successfully reached the desired wavelength and was providing the desired power level.

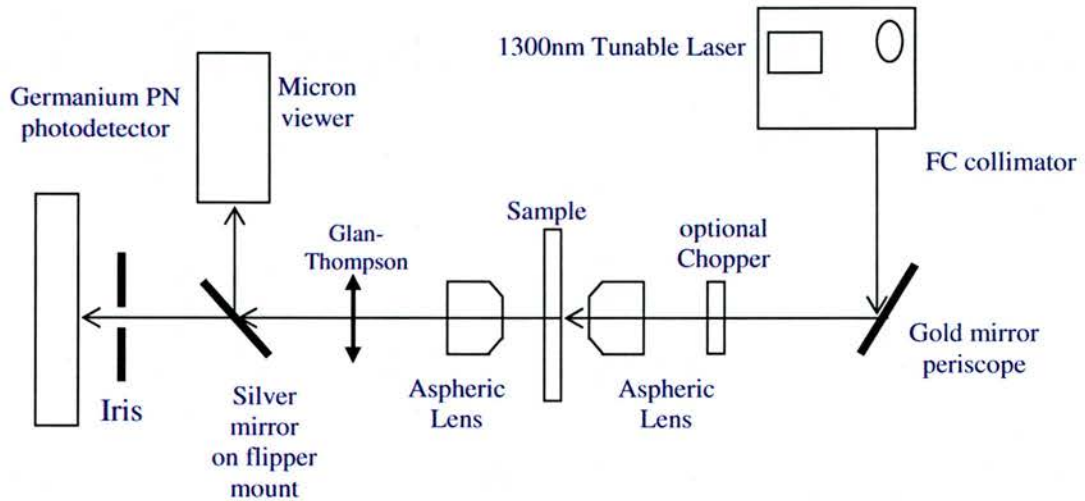


**Figure 4.5 Standard transmission measurement setup.** The Ge PN detector signal is fed to a lock in amplifier. The incident beam is chopped using either the internal modulation of the laser or an external wheel. The laser scan and the lock-in data is fed to a Labview program via GPIB. Cameras are used to monitor back reflections, to provide a plan view of the sample or to image the transmitted signal.

Due to this heavy time constraint an alternative technique was gradually developed. White light from a halogen source (Ocean Optics) was waveguided along the blank GaAs ridge waveguides early on in the project. The visible component of this light is strongly absorbed. This is very broadband light but has low spectral density in the IR( $>-53\text{dBm/nm}$  @ 1300nm). The low pointing stability and achromatic focussing also conspire to make halogen bulb waveguide measurements difficult. Judith Hankey and Amr Helmy at Agilent supplied us with  $1.3\mu\text{m}$  Edge Emitting LEDs to provide increased spectral density over a  $\sim 50\text{nm}$  wide spectral range. L2in1 transmission spectra were measured using these. Niara Elejade was kind enough to lend us her fibre pigtailed  $1.55\mu\text{m}$  Super Luminescent LED for testing. Agilent Semiconductor Optical Amplifiers (SOAs) were a compatible source at  $1.4\mu\text{m}$ , these consisted of just the bare dies, and used to measure W3 devices (see below). The secret to success with these measurements was a broadband fibre splitter (JDS Fitel

AC1100-A4). This allowed optimisation using a photodetector to integrate the transmitted spectrum without having to disconnect the fibre from the Optical Spectrum Analyser (OSA - Advantest Q8384). Cameron Rae was very helpful in allowing us to use the Ando OSA for testing and with advice on both SMF and MMF fibre coupling schemes. Chris Morgan at Cambridge was also able to lend his invaluable experience. Eventually we acquired two turnkey sources; a triple ELED source 1350-1600nm (>-33dBm/nm @1550nm - Agilent 83437A) and an Erbium Doped Fibre source (1520-1570nm – Agilent 83438A) which offered not only ease of use, but higher spectral density (>-13dBm/nm @1550nm).

As a suggestion for future development of the broadband source characterisation techniques a promising solution from Southampton University addresses the problems of achromatic focussing and the need for a broadband source by developing a supercontinuum PCF based source (>-23dBm/nm @1300nm). This is a quasi CW (ns pulsed) source almost as spectrally dense as the EDF source.

#### **A. GaAs surface waveguide**

For the first waveguide the losses were obtained from the peak transmission across W1 samples with period,  $a$ , ranging from 320-400nm in 20nm steps and  $r/a=1/3$ . The transmission spectra are plotted in Figure 4.6. The transmission spectra have been stitched together and averaged. The lower edge of the W1 even fundamental mode is seen at  $u=0.255$ , but it is rapidly eroded with increasing device length. The odd mode crosses the even mode at about  $u=0.285$  in experiment and slightly higher in the FDTD. The transmission is then slightly higher (~10dB) above this point, for the longest length of waveguide.

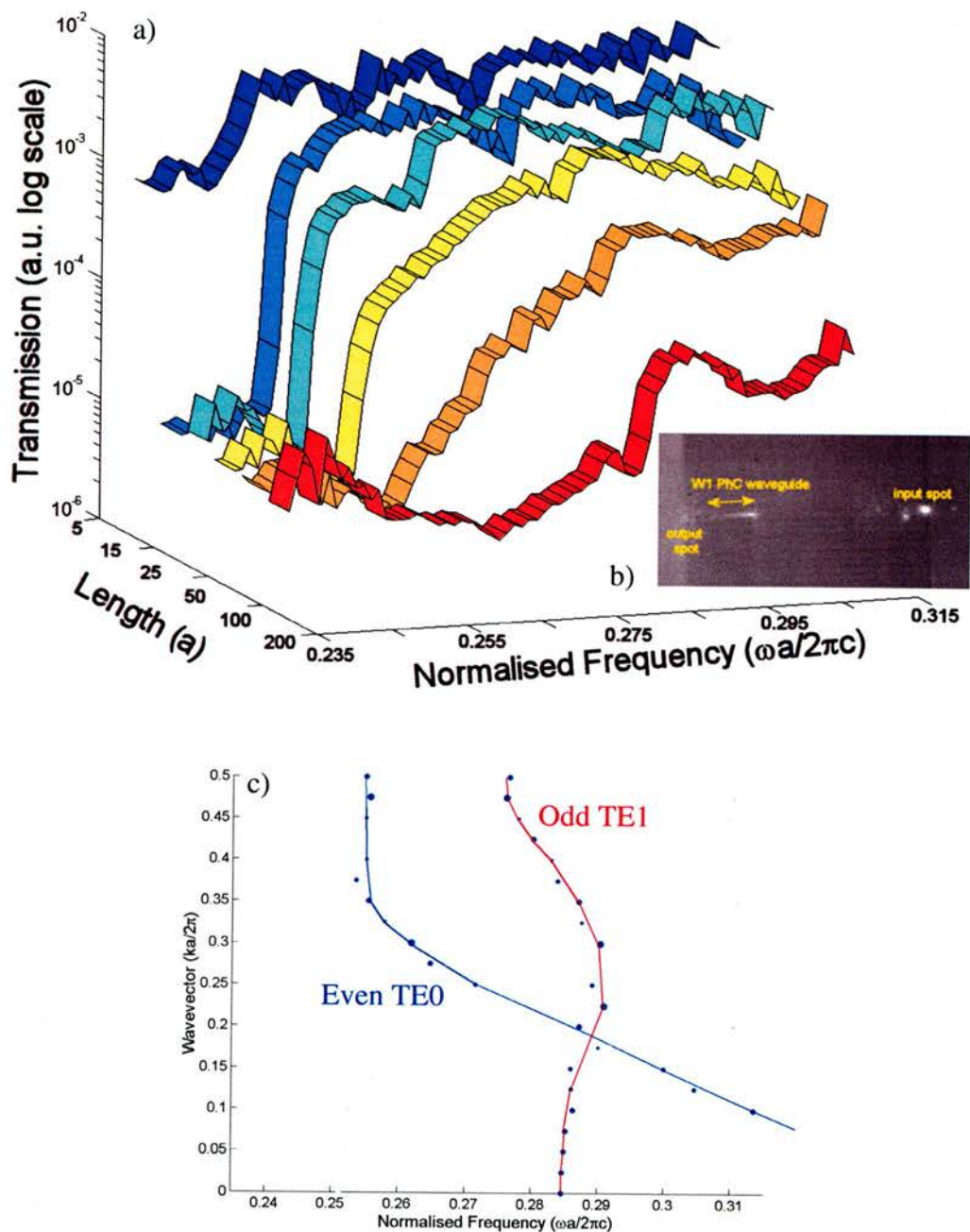


**Figure 4.6** a) Transmission of W1 waveguide fabricated on surface waveguide for 6 different device lengths. Overlapping spectra have been stitched together. For shorter lengths relatively high transmission is observed with a strong bandedge evident at  $u=0.255$ , this feature is eroded with increasing device length. At the longest length sample a sharp feature is present at  $u=0.29$ . b) The scattered light captured at  $u=0.315$  on the  $a=400\text{nm}$ , 200 period long W1 PhC waveguide. c) 3D FDTD bandstructure showing the even and odd modes of the W1 waveguide.

For this waveguide the transmission losses were estimated to be of the order  $130\text{dBmm}^{-1}$ , or  $\alpha=321\text{cm}^{-1}$ , by fitting an exponential curve to the peak transmission. These data agree with the calculations of Kuang et al. [9] who compare membrane, oxide clad and deeply etched structures. Although the deeply etched waveguide performs worst, they find lower loss for a deeply etched structure above the odd mode crossing. Finding this odd mode is difficult in transmission as the end fire excites predominantly the even modes.

A more comprehensive loss measurement technique is sought. The noise in the above measurement is mainly F-P fringes from the facet-device-facet cavities in the system. With a typical refractive index of  $n=3.5$  and cavity length of 1mm, a fringe spacing of  $\sim 0.35\text{nm}$  can be expected. If this were a blank waveguide the losses could be derived directly from the F-P fringe visibility, this is often referred to as the Hakki-Paoli method [10]. The visibility  $= \frac{I_{\max} - I_{\min}}{I_{\max} + I_{\min}}$  is a parameter naturally independent of the coupled optical power. This is useful as there is a strong variation in mean transmitted power between blank waveguides. This was observed in the CCW work in Chapter 3. The reason for this variation is that the facet quality (angle/tilt/roughness) varies between waveguides and hence the coupled power (in and out) is slightly different each time. This naturally affects the facet reflectivity which gives rise to a variation in the standing waves within the waveguide and hence the visibility. For a high reflectivity ( $R=0.3$ ) the fringes are not simple sinusoids but an exponentially weighted sum of harmonic sinusoids or in other words an Airy function. In [11] by Fourier Transformation of the sub-lasing threshold spectra of diode lasers it is possible to recover the propagation loss or gain of the system. In a passive measurement the slope of a line fitted through the peaks of the FFT of the spectral data (Hz) recovers the loss per unit time (dB/s) [12]. Each peak represents a round trip in one of the cavities in the system. The first of these peaks has been used in [13] to examine the performance of tapers between ridge and PhC waveguides. In [13] the peaks due to reflections at the interfaces are diminished in matched devices. The strength of other peaks, however, is not enhanced and so a question remains whether the matching is just scattering the light.

The technique has been investigated in order to determine its suitability for PhC loss measurements. We have combined this with the EDF and ELED source, which both have coherence lengths on the order of 80 $\mu$ m.

### **B. Al<sub>20%</sub>GaAs core structure**

With the 50nm wide spectrum of the EDF source it is only possible to stitch the spectra together continuously if we reduce the lithographic tuning step to 10nm. In doing so we obtain insight into the loss characteristics of W1 waveguides fabricated on the Al<sub>20%</sub>GaAs core heterostructures. The fundamental mode is everywhere beyond cut off. Over the measurement range we fortuitously track the entire folded band. The lithographic tuning means that for each sample of smaller lattice constant the W1 waveguide becomes narrower and the mode tail is squeezed further and further into the substrate, and hence the losses increase. The dip at the centre of the band has either of two origins. Either it marks (i) the odd mode (TE1) crossing the folded fundamental (TE0) or (ii) the TE0 mode crossing the TM0 mode.

- i) In the first case the coupling between these modes of opposite parity could be attributed to the integration over the transmitted parts of the 50nm spectrum on the photodetector. Optimising for maximum signal appears to preferentially weight the launch into the higher order mode. This mode crossing was observed in the Si<sub>3</sub>N<sub>4</sub> results above. The 2<sup>nd</sup> mode is naturally leakier than the fundamental. In this CW measurement the facets and interfaces can generate forward and backward travelling waves and help couple power between folded and unfolded modes.

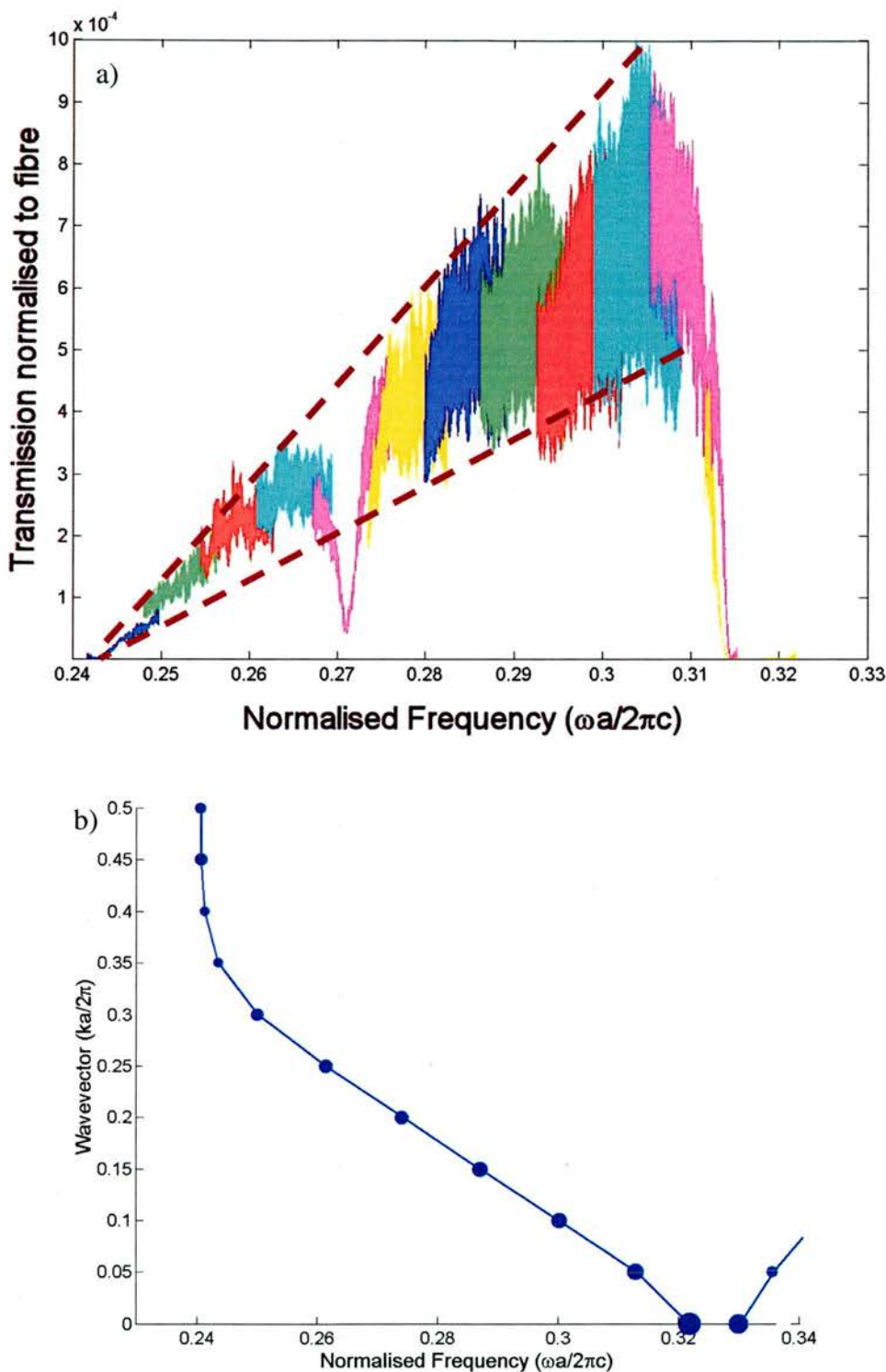


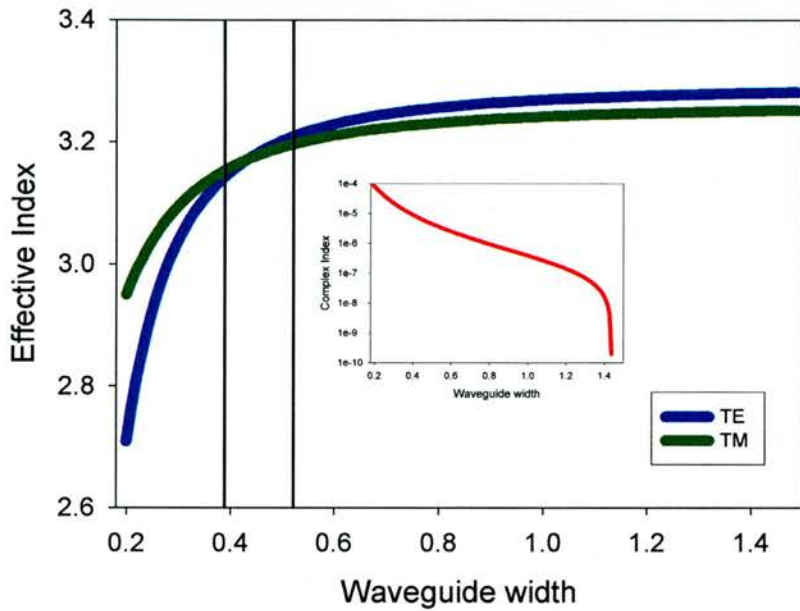
**Figure 4.7** 90 period W1 waveguide with  $r=0.3a$ . 12 lithographically tuned sample spectra are stitched together between  $a=380-490\text{nm}$ . The characteristic triangular spectrum tells the simple tale that the waveguide mode is beyond cut off. Not only does the average transmission fall with normalised frequency but the visibility of the fringes diminishes at the same rate. The same behaviour is observed for samples with different lengths and  $r/a$  ratios. Another mode crosses the fundamental at  $u=0.27$ , giving rise to a dip in the transmitted power. b) The even fundamental mode as calculated by 3D FDTD simulation.

ii) Alternatively the asymmetry of the heterostructure waveguide allows the TE0 and TM0 fundamental modes (opposite polarisations) to cross when the waveguide width becomes small enough. To illustrate the ambiguity in slightly more detail, we plot the real part of the effective index in Figure 4.8, as we vary the width of a ridge waveguide (continuous translation symmetry) at constant etch depth (of  $2\mu\text{m}$ ). The important factor here is the use of a fully vectorial mode solver. At these narrower widths the modes are no longer strictly TE or TM. Below a width of  $0.43\mu\text{m}$  the TM mode becomes the dominant mode in this waveguide. The TE and TM modes cross in the middle of this range. We initially expected that the gap was due to a higher order TE mode present in this region. Looking at the full set of measurement data (not presented here) it becomes more evident that the gap occurs at a similar (constant) waveguide width. We note the position of the gap in a set of W1 waveguides with a different  $r/a$  ratio. The equivalent mode crossing width appears to be  $\sim 0.47\mu\text{m}$ . In case (i), the spectral position of the higher order mode would change with the ratio  $r/a$ .

In both cases (i & ii) we require roughness to couple power from even to odd modes or TE to TM modes. In (i) a forward travelling wave is coupled to a backward travelling wave. In (ii) both waves propagate forwards. The difficulty in determining the origin of the gap is in collecting power coupled to higher order modes, as these may not couple to the input/output waveguides as efficiently as the fundamental waveguide mode.

The triangular appearance of the stitched spectrum (see Figure 4.7), as apparent in the visibility and mean transmission can be explained by plotting the imaginary part of the effective index (for the fundamental TE mode). The increasing complex index accounts neatly for the increasing loss into the substrate as the width of the waveguide decreases.

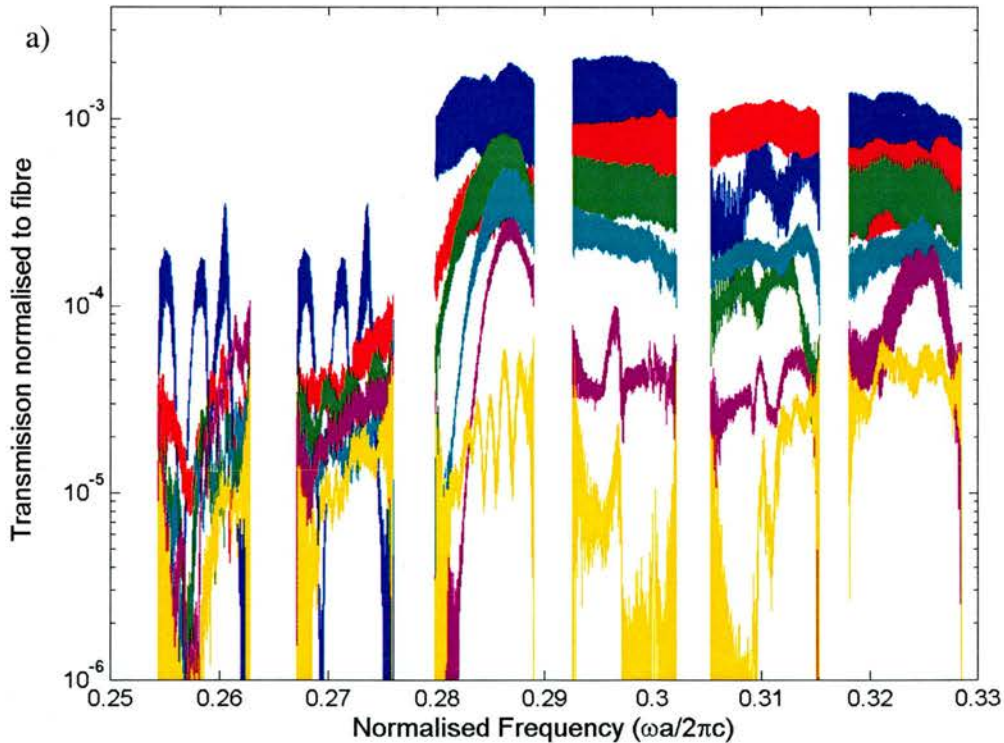
To date the even TE modes have been investigated using a 3D FDTD model. This needs to be expanded to include the odd and TM modes in this structure.



**Figure 4.8** The real and imaginary (inset) parts of the effective index, for a ridge waveguide etched  $2\mu\text{m}$  deep. The TE mode loss increases for decreasing ridge width. The lithographically tuned range (width=0.39–0.52 $\mu\text{m}$ ) is denoted by the vertical bars. For narrower ridge widths the TM mode becomes the dominant mode (highest effective index) in the waveguide. Below a width=0.5 $\mu\text{m}$  the fundamental waveguide mode is no longer strictly TE or TM.

#### 4.2.4 W1 SOI

Many more interesting mode crossings and couplings crop up in the spectrum of a W1 waveguide etched into a Silicon on Insulator (SOI) waveguide. In this case the steps in the lithographic tuning are 20nm and so the spectra do not stitch together continuously. As the samples become longer the seemingly wide passband ( $u=0.28\text{-}0.33$ ) is rapidly eroded to reveal several narrower peaks. The two obvious peaks at  $u=0.295$  and  $u=0.31$  appear to have a sharp edge features at their high frequency and low frequency edges respectively. It would appear that these belong the TE1 mode which lies under the light line at around  $k=0.5$ ,  $u=0.3$  and crosses the TE0 mode at around  $k=0.2$ ,  $u=0.31$ . As the sharp edge reverse side we infer that these two modes have opposite slope. These modes are weakly coupled to from the fundamental mode along the length of the guide, and suffer only extrinsic loss where it lies beneath the light line. These points appear to dominate the spectra at lengths of 220 $\mu\text{m}$  and beyond. An estimate of the loss for both these higher order modes is <30dB/mm. This assumes that the roughness induced coupling is constant with device length, which seems reasonable.



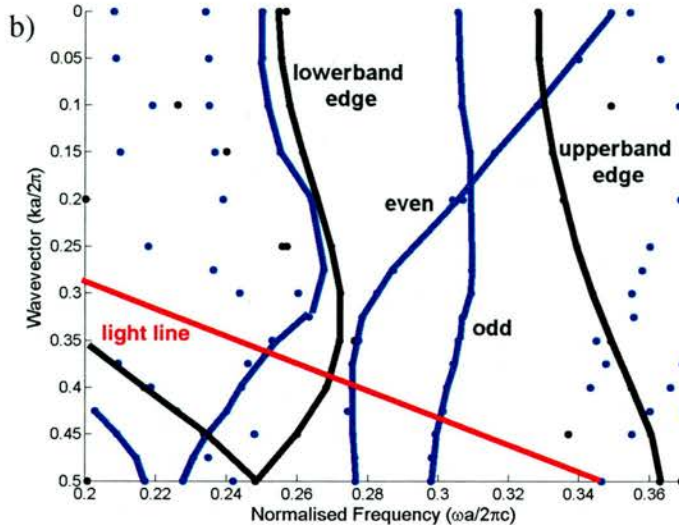


**Figure 4.9** a) Transmission of a set of W1 waveguides (+6 dose). The lowest loss is observed for a normalised frequency of  $u=0.28$ . Several additional features remain in the spectra for the longest length samples (Blue=16a, Red=32a, Green=64a, Cyan=128, Magenta=265a, Yellow =512a) b) The 3D FDTD bandstructure for the W1 waveguide (blue lines) and a unit cell of the lattice (black lines),  $a=415\text{nm}$ . Good agreement is observed between the lower limit of the band at  $u=0.28$ . Hardly any bandwidth exist below the  $\text{SiO}_2$  light line. The upper limit at  $u=0.33$  is denoted by the upper band edge. The two interesting features coincide with the TE1 mode under the light line and the even-odd mode crossing.

#### 4.2.5 W1 Summary

The most interesting dispersive region in each of the above W1 waveguides, is the lower band edge (see Figure 4.10). The Group Index and GVD parameter are plotted for this region of the spectrum, for an ideal 2D W1. Unfortunately due to various limits and loss mechanisms (wavelength range, structural tuning, roughness, mode cutoff, diffraction) it was not possible to directly measure the variation in waveguide dispersion. In the Silicon Nitride experiment of Section 4.2.2, this feature fell outside of the maximum wavelength accessible by the laser. In the surface waveguide of Section 4.2.3A, the spectrum erodes quickly with increasing device length around this feature. Loss caused by the AlGaAs ridge waveguide mode cutoff also yields the very low transmission at the lower band edge in Section 4.2.3B (the same mechanism is also believed to affect the GaAs waveguide of Section 4.2.3C). The narrow bandwidth of the mode lying beneath the air light line in the SOI W1 of Section 4.2.4 also frustrates access to the lower band edge. The band edge shift was measured to shift about  $\Delta u \sim 4.3\%$  across the dose range (-6 to +6) available from the 8" SOI wafer (for the 1550nm EDF source). The Deep UV exposure dose is deliberately varied across the wafer to create a range of devices, mainly by changing the hole radius.

Proximity effects across the wafer can also vary the relative sizes of holes neighbouring the defect waveguide. It is believed that a larger scan of the waveguide parameters (period, radius) might allow measurement of this dispersive feature. Note that the GVD is monotonously increasing indicating higher order dispersion.

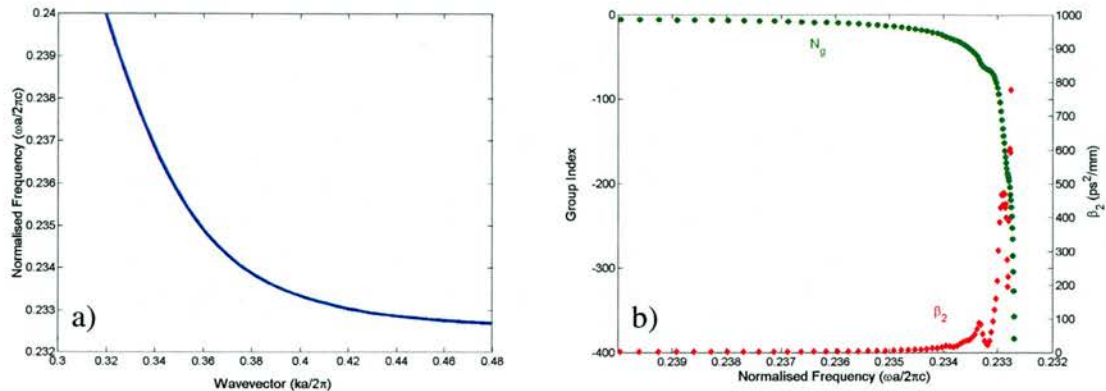


**Figure 4.10 The dispersion of an ideal 2D W1 waveguide at the lower band edge. a) Bandstructure (solid blue), b) Group Index (green dots) and GVD parameter (red diamonds) note axis is reversed for b)**

### **4.3 Line defect waveguides –W3**

The remainder of this chapter focuses on two collaborations, the first internal to the UPC, with the Semiconductor Physics group at St Andrews. Firstly we discuss the design of line defect waveguide components to disperse short pulses in AlGaAs heterostructures. Secondly we report on an external collaboration with the University of Twente in the Netherlands, using an SOI slab waveguide. In both experiments we have aimed to take advantage of the high quality of pulses generated by an Optical Parametric Oscillator (OPO). Streams of pulses are produced by a mode-locked Ti:Sapphire at an 80MHz repetition rate and are incident upon a non-linear crystal of Periodically Poled Lithium Niobate (PPLN). Using different sets of PP gratings and thermal control of the PPLN crystals creates a pulsed tunable wavelength source. At St Andrews a pair of OPOs are “dual” pumped allowing us to investigate the waveguides in two spectral ranges (1310 and 1550nm), with pulses of >750fs duration. At Twente the commercial OPO (Spectra Physics OPAL) is dispersion compensated by a prism pair to yield ~100fs pulses which are tunable around 1310nm.

The approach taken by each group is distinct but complimentary. At St Andrews the system is treated as a black box, and we aim to measure the spectrum of and autocorrelate the transmitted pulses. These measurements are then compared with the incident pulses. Both auto and cross-correlation geometries have been studied. At Twente the fields propagating inside the waveguides are probed directly in space and tracked in time.

Previous PhC measurements of Planar PhCs have been restricted to spectral analysis, due to nonlinear behaviour [14].

### **4.3.1 St Andrews W3 AlGaAs heterostructure**

We will begin with the St Andrews sample design.

At a repetition rate of 80MHz the peak pulse energies that we inject into the waveguides are high enough to excite non-linearities in the waveguides. Both red (~655nm) and blue (~522nm) Second Harmonic Generated (SHG) light have been observed in GaAs waveguides at 1310nm and 1045nm respectively. The narrow bandwidth of this light has been confirmed using spectral filters. This SHG is non-phase matched and the emission is restricted to the surface of the material as the GaAs is strongly absorbing at these wavelengths. More importantly we observe a non-linear transmitted Power Out versus Power In characteristic indicating the presence of Two Photon Absorption (TPA) (see Figure 4.11). TPA is an instantaneous non-linear effect in which two photons are absorbed simultaneously to generate a single electron-hole pair. The photons we consider here have energies below the bandgap of the semiconductor.

### **4.3.2 Non-linearities**

TPA is the mechanism by which the Semiconductor group non-linearly characterise the pulses transmitted by both passive waveguides and Semiconductor Optical Amplifiers (SOAs). The materials they use to achieve this in the telecommunications region of the IR are Si and GaP, amongst others. Having enough power to drive the detection process implies being in a non-linear regime inside the device, where the fields are more strongly confined. In the GaAs waveguide that we used in the previous chapter the energy density of the fundamental TE mode is increased as it tapers from  $3\mu\text{m}$  down to 490nm, by a factor ~6 [15]. The dispersive effects that we wish to observe are also capable of enhancing these nonlinearities [16].

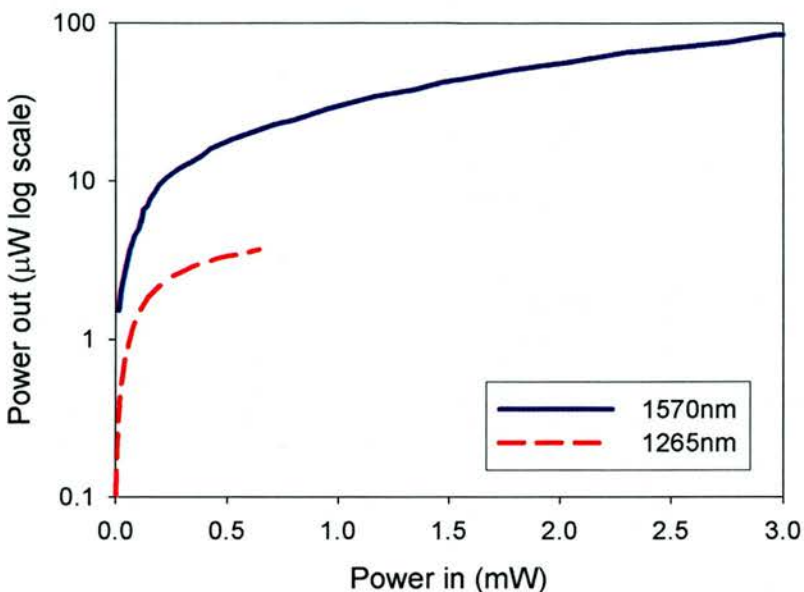


**Figure 4.11 Power out vs Power in for AlGaAs waveguide, exhibiting TPA at 1265nm which is above half bandgap, at 1570nm the response is almost linear**

Careful choice of material is therefore necessary to avoid the loss that the TPA causes whilst simultaneously enabling a signal large enough to allow autocorrelation with a TPA detector. TPA detection is simply more convenient, allowing high sensitivity, polarisation insensitivity, easier alignment and freeing bench space. Conventionally autocorrelation techniques have been based around a SHG crystal and use a Photo Multiplier Tube (PMT) to detect the weak signal.

### 4.3.3 Wafer design

We choose semiconductors with high TPA for detecting the light, but for our devices we require to minimise the non-linear effects. By operating at 1550nm which is below the half bandgap of Al<sub>20%</sub>GaAs we can work without TPA. The Aluminium content also serves to dilute the alloy somewhat and hence the refractive index contrast is decreased. This then requires a slightly different design of heterostructure waveguide and the opportunity arose to design this from scratch. A waveguide was therefore designed using Fimmwave and optimised using a python script to confine the light in a narrow ridge waveguide (width =500nm) etched into an AlGaAs heterostructures to a depth of 1.5μm.

Material	Layer thickness
Al <sub>25%</sub> GaAs	250nm
Al <sub>20%</sub> GaAs	488nm
Al <sub>30%</sub> GaAs	55nm

**Table 4-1** Layer composition of AlGaAs wafer

A semivectorial solver was used to determine the layer structure which minimised the amount of field in a 100nm layer placed at the bottom of the structure. The waveguide was not found to perform as well as expected for this narrow width at 1550nm as seen above (in section 4.2.3) [17]. This waveguide has found however found successful use where novel tapers have been used to inject light into PhC bends and Y-splitters [18].

#### 4.3.4 W3 Dispersion

W3 waveguides are formed by missing three rows of holes along the  $\Gamma$ -K direction. These wider width waveguides are transversely multimode and it is possible for the index and gap guided modes to intersect one another (see Figure 4.12 a)). Modes with the same symmetry (with respect to the waveguide axis) anticross and form Mini Stop Bands. The bandstructure, Group Index and GVD parameter are plotted for this region of the spectrum, for an ideal 2D W3.

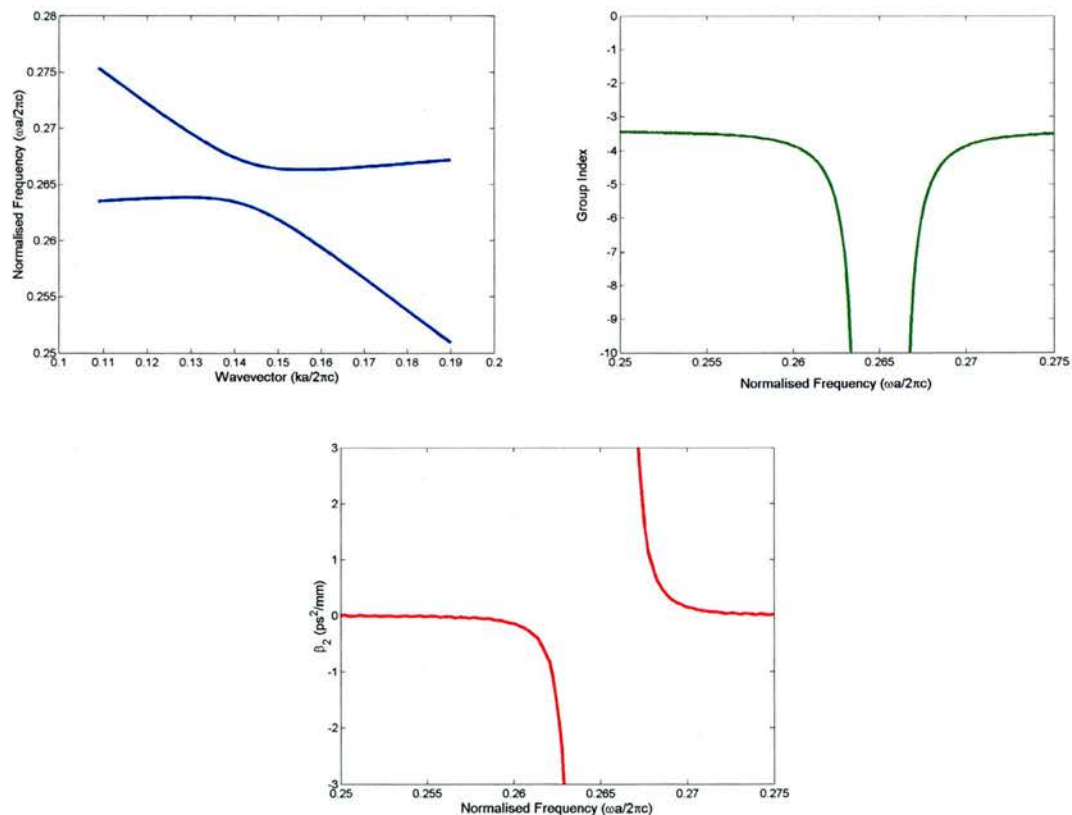


**Figure 4.12** The dispersion of an ideal 2D W3 waveguide at the Mini Stop Band for the fundamental mode, the steeper line. a) Bandstructure (blue), b) Group Index (green) and c) GVD parameter (red)

### 4.3.5 W3 AlGaAs transmission spectra

It was decided, in order to minimise losses, to pursue waveguides with a wider width (see Figure 4.8). These W3 waveguides with three missing rows of holes, have an average loss in the passband of 5.2dB/mm. The spectrum (plotted in Figure 4.13) is fairly monotonous across the band gap when compared to that of the W1 waveguides. Apart from, that is, where modes with the same symmetry and polarisation cross one another and cause the formation of mini stop bands (MSBs see Figure 4.13). The wider width of these W3 waveguides naturally supports many more modes than the narrow W1s. These MSBs are partial band gaps where two modes interact and cancel. Other propagating modes are unaffected by this interaction. In the case illustrated in Figure 4.13 the TE0 fundamental is launched into the coupling waveguide and this interferes with the TE4 mode creating an MSB. The origin of this stop band will be explained in more detail in the next section (4.4.4). The small peaks at the bottom of the MSB are due to the field tunnelling through the guide in the other higher order modes.

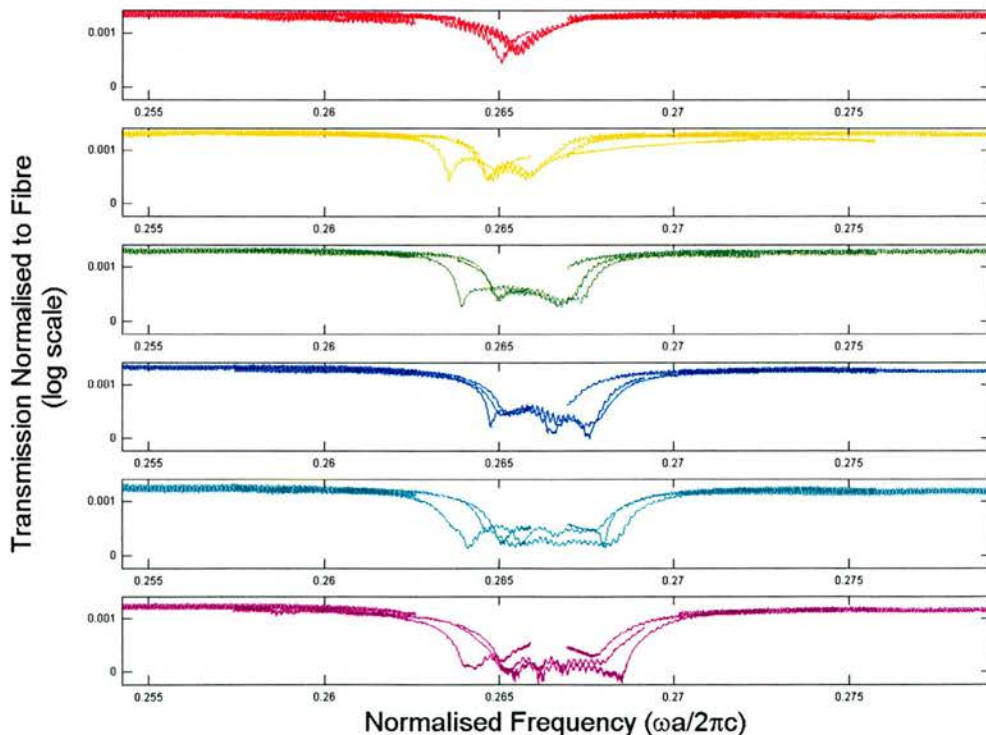


**Figure 4.13** The spectra of W3 waveguide around the Mini Stop Band for different lengths fabricated on the AlGaAs waveguide. The small stitching errors are now apparent as the

**differences in lattice constant are equal to the resolution of the e-beam. (Red=16a, Yellow=32a, Green=64a, Blue=128a, Cyan=265a, Magenta=512a. Log scale Y axis ticks at 1e-6, 1e-3**

To achieve overlap with the 1550nm range the lithographic tuning step was reduced to 5nm, equal to the resolution of the Glasgow e-beamwriter. The stitching errors this incurs are at worst  $\Delta u = 0.5\%$  in normalised frequency (or  $\Delta \lambda \sim 9\text{nm}$ ). The gap deepens and widens with increasing device length, to a width of  $\Delta u = 0.05$  at length=512a. The widening of the band denotes losses at the band edge, which are higher than in the transmission band. The devices are currently undergoing pulsed characterisation at St Andrews (a maximum transmission of 16% has been achieved).

We now compare these transmission data with FDTD simulation, but first of all we discuss some of the difficulties that we face in doing so. In order to locate the eigenfrequencies in the 3D FDTD data we no longer Fourier Transform the temporal data. The data may be sinusoidal in nature, but may also be rapidly decaying with time (especially above the light line). This exponential loss creates a real headache to locate those modes, which cause strong spectral features in transmission, but are strongly damped by diffractive loss. The sines and cosines which form the basis set of the FT are limited by the uncertainty principle and do not assume a specific form for the signal. The technique adopted in this chapter to successfully produce the 3D FDTD bandstructures is based on the “filter diagonalization method” [19], and more specifically takes the form of a free software package Harminv written by Steven G. Johnston [20]. The method was initially applied to the demanding problem of signal analysis for Nuclear Magnetic Resonance spectroscopy data. It is ideal for our electromagnetic simulations, where we expect a limited number of resonances in a given frequency bandwidth, which either decay or oscillate. The software provides the eigenfrequencies for a given temporal data set. With appropriate filtering to reject spurious modes or states with very low Q, this has become a highly useful tool in our group. Indeed most of the 3D FDTD banddiagrams in this report were created using Harminv.

Given the simple transmission spectrum for this W3 waveguide, we might expect that the bandstructure would be relatively straightforward. For this multimode waveguide in 2D for the TM polarisation apart from being a little overcrowded, things are relatively simple (as we will see in Figure 4.19). There is a set of 3~4 steep index

guided modes (with negative group velocity) and a set of 2~3 flat gap guided modes (with positive group velocity). The modes occur in sequence with the lowest order mode at lowest frequency, for both the folded index guided modes ( $-v_g$ ) and also for the gap guided modes ( $+v_g$ ). The reader is referred forward to the simpler bandstructure figure in Section 4.4.1, so as not to continually repeat the same information. Modes with the same symmetry can be seen to anticross and those with opposite symmetries cross each other unaffected.

For a W3 etched into a 3D AlGaAs heterostructure we have a particularly confusing situation, however, and the banddiagram is certainly more than a little difficult to interpret (see Figure 4.14). In this graph we choose to only plot the even TE polarised modes, by choosing even symmetry in the simulation. (Remember we have chosen to rename the modes 2D-TM = 3D-quasiTE). The full 3D diagram indicating even/odd modes and including both polarisations is very bewildering. All of these modes within the TE bandgap exist above the cladding lightline, making many of the higher order modes relatively lossy. The modes are perturbed by the presence of all these leaky components (see Figure 4.14 c)). The waveguide is not only transversely multimode (for TE and TM polarisations), but also vertically multimode. The fact that the experimentally observed interaction between the TE4 and TE0 modes is so strong, is in fact quite surprising. The transmission spectrum is optimised by integrating across the wide spectrum of the source, and if we consider the vertical asymmetry of the mode, it is very difficult to conceive that we could directly excite these modes. They are also particularly lossy. All of these higher order modes represent a sink for power scattered by the waveguide.

These higher order modes can be suppressed, to an extent, by filtering the modes and accepting only those whose spectral position is intolerant to varied sampling of the temporal data. The 3D FDTD mode solver is seeded with the mode profiles for a translation invariant waveguide of the same width (as solved by a 2D vector mode solver).

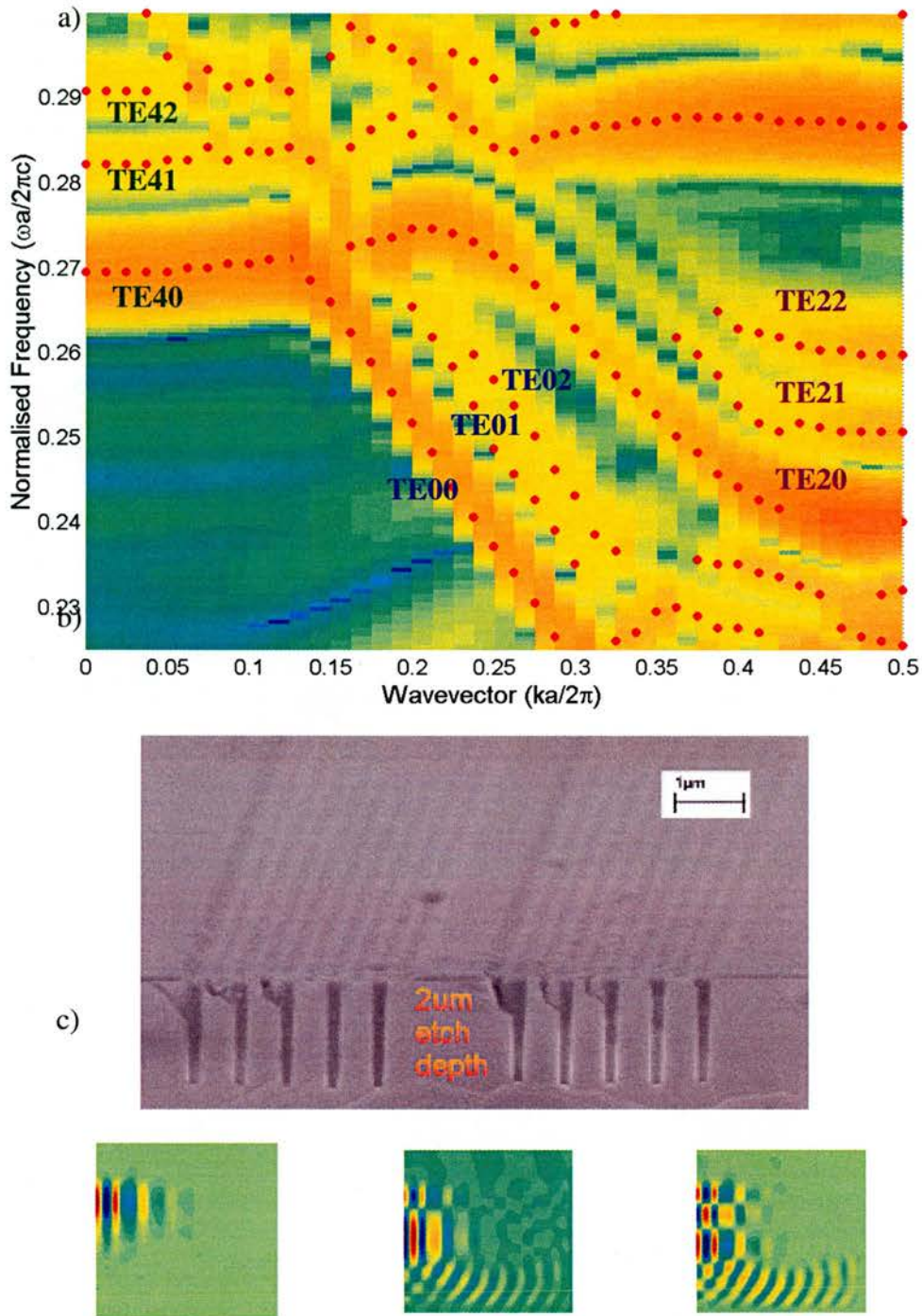


**Figure 4.14** a)The 3D FDTD banddiagram for the W3 AlGaAs waveguide, for even TE modes. Operating with such a wide ( $>1.1\mu\text{m}$ ) waveguide in a large heterostructure above the light line causes many medium Q modes to interact with low Q modes (leaky, TE or TM) creating a very confusing system. At roughly  $k=0.125$ ,  $u=0.27$  the TE4 intersects the TE0 mode giving rise to the experimentally observed MSB. b) SEM image of cleaved W3 waveguide in AlGaAs heterostructures, angled at  $45^\circ$ . c) The deep etching draws in vertically higher order modes, which the weakly guiding nature of the heterostructure cannot suppress. Here the TE4 mode acquires two replica modes, so we have TE40, TE41 and TE42, at frequencies  $u=0.2695$ ,  $u=0.2822$  and  $u=0.2908$  respectively.

In the next section we aim to simplify the experimental waveguide, by reducing the mode volume significantly and removing many of these awkward modes. As in other studies in order to study the local behaviour around the MSB we will have to resort back to 2D modelling.

#### **4.4 Time resolved heterodyne interference Scanning Near Field Microscopy**

Silicon-On-Insulator (SOI) is seen as one of the most promising material systems for the high volume integration of photonic components [21]. Realising planar photonic crystal (PhC) waveguides in this material system provides exceptional spatial and temporal control over the propagation of light [22]. The thin high index silicon film provides strong confinement in the vertical direction allowing low loss PhC waveguides to be demonstrated [23, 2]. The strongly dispersive nature of PhCs offers spectral and modal control over the optical propagation velocity, allowing one to envisage compact delay lines and pulse shaping devices. Furthermore, understanding and controlling the dispersive properties of a waveguide in general allows for the compensation or enhancement of material/gain dispersion in active materials e.g. for phase-matching and non-linear applications.

At Twente the aim is to directly measure the fields propagating in the waveguide. The technique which we use to accomplish this, Scanning Near-Field Optical Microscopy (NSOM), immerses a tapered fibre tip in the near field of the sample. This tip is formed by stretching a CO<sub>2</sub> laser heated length of SMF, coating it with aluminium, and then using a Focussed Ion Beam to create an ~80um aperture at the point of the fibre (such a fibre is shown in Figure 4.15). This probe is then sensitive to the evanescent tails of the fields propagating in the waveguides. The SOI proved to be the best platform to achieve both high field confinement and large evanescent mode tails. A piezo-electric bimorph is then used to raster scan the tip at a height of ~10nm across the sample.

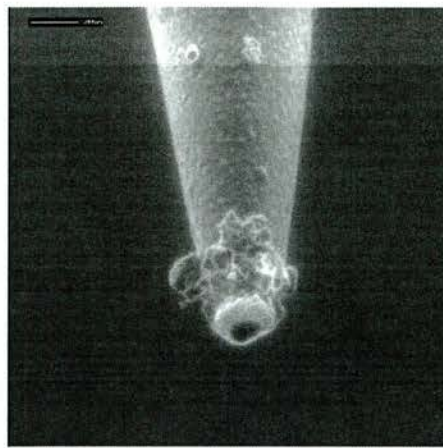


**Figure 4.15 Tapered fibre probe tip, metallized to reduce stray light, enhancing spatial resolution. This was the actual tip used over 3 weeks of continuous scanning. Scale bar shows 500nm.** SEM micrograph courtesy of Henkjan Gersen

Uniquely at Twente, the sensitivity of the near field technique is increased by locating the sample and scanning tip in one arm of a Mach-Zehnder interferometer[24]. The setup is thus illustrated in Figure 4.16.

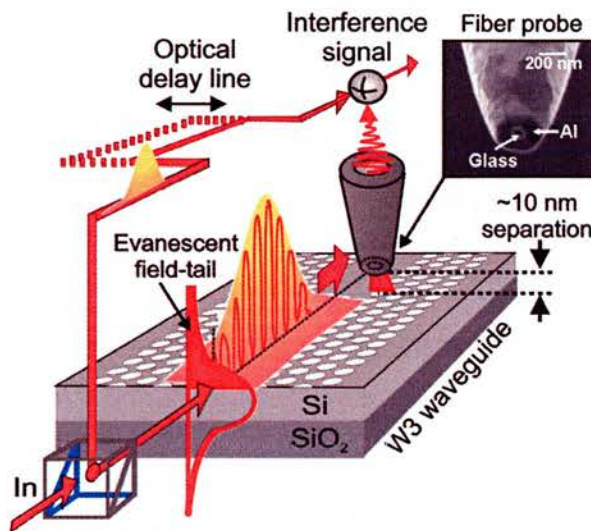


**Figure 4.16 Sample location in arm of Mach Zehnder interferometer. Other arm contains optical delay. Courtesy of Henkjan Gersen**

We first of all discuss the fabrication of our waveguide samples and then their transmission characteristics. We compare these with a 2D FDTD model and highlight the interesting features. Using this 2D model we examine the modes of a ridge waveguide and then our periodic PhC W3 waveguides, using a Spatial Fourier Transform technique, comparing and contrasting their dispersion. We then present our experimental results;

- i) imaging the scattered light from a CW source in the far field

- ii) measurements performed in the near field directly detecting the waveguide modes excited by a pulsed source.

We will discuss the limitations of this former technique. The numerical results lead us to analyse the Mini Stop Band behaviour in greater detail and by examining the field profiles of the anti-crossing modes we can better understand their high dispersion.

#### **4.4.1 Sample preparation - W3 SOI**

The waveguide samples were defined on an 8" SOI wafer by Deep UV 248nm lithography at IMEC Leuven. The wafer comprises a 220nm thick core layer of Si with a 1um  $\text{SiO}_2$  cladding on top of a Si substrate. The pattern was transferred into the Si core layer by reactive ion etching in a  $\text{Cl}_2/\text{O}_2/\text{He}/\text{HBr}$  plasma [25]. A selection of PhC waveguides of differing lengths and lattice constants were fabricated, and with the high capacity of this manufacturing technique many replica samples are created. A die covering an area of  $\sim 1\text{cm}^2$ , is stepped across the wafer and each successive column of dies receives a higher exposure dose. The resolution of the DUV process, specifically the impact of optical proximity correction, limits the minimum available feature size, resulting in the smallest lattice period of  $a=400\text{nm}$  being available. Using the highest dose die, i.e. the samples with the highest fill factor, centred the most interesting spectral features in the 1550nm wavelength window. The pulse characterisation setup was centred at 1310nm and so this required that the index contrast be reduced. By reducing the index, as explained in the next paragraph, the features are shifted to higher frequency.

The PhC waveguides studied in this section are W3 waveguides, i.e. they consist of three rows of holes removed from a uniform hexagonal lattice along the  $\Gamma\text{K}$  direction [26]. The initial spectral measurements of the waveguides were carried out at 1522-1572nm with a CW Erbium Doped Fibre source and used lithographic tuning (varying the lattice period in 20nm steps between  $a=400\text{-}500\text{nm}$ , with radius,  $R=1/3a$ ) to cover a normalised frequency range from  $u\sim 0.26\text{-}0.33$  (see lower half of Figure 2b). In all our measurements the injected light is TE polarised ( $\mathbf{E} \parallel$  to the crystal plane). The multimode dispersion of the W3 waveguides allows higher order modes to cross or

anti-cross, the anti-crossing causing Mini Stop Bands (MSBs) in the transmission spectrum of the waveguide [26]. The mid band gap MSB is located at around  $u=0.31$ . To align this interesting spectral region with the tuneable wavelength range of our CW laser (1255-1365nm see upper half of Figure 4.19b) and Optical Parametric Oscillator (OPAL Spectra Physics) pulse source (1180-1350nm), it was necessary to decrease the dielectric constant of the waveguides by approximately  $\frac{u_{\lambda_1}}{u_{\lambda_2}} = \left( \frac{500/1550}{400/1310} \right) = 6\%$ . This was accomplished by dry oxidising a single die from the wafer in an oxygen flow rate of 500 sccm at 1000°C for 30 minutes. An ellipsometric analysis of the neighbouring slab waveguide before and after oxidation showed that a 21nm layer of thermal SiO<sub>2</sub> had formed.

Material	Thickness (nm)
Air	$\infty$
SiO <sub>2</sub> (thermal)	20.92
Si	210.12
SiO <sub>2</sub> (clad)	998.37

**Table 4-2 Elipsometric fitted data for the composition of the oxidised reference waveguide**

The SOI wafer was supplied with total thickness of 750μm. The mismatch between the crystalline Si waveguide, the 1μm layer of SiO<sub>2</sub> and the Si substrate makes cleaving the samples particularly difficult. In order to achieve a reasonable quality facet, the samples are thinned to around ~250um, by an arduous process involving 3μm particles of Alumina suspended in water, a glass platen and a lot of elbow grease. The samples are then very fragile, but require cleaning. Dirt on the fibre tip can be seen in Figure 4.1. The close proximity of the tip to the sample and the 220nm steps (up and down) that the tip must negotiate across the complicated sample topography, necessitates a thoroughly clean surface. Multiple wash cycles in acetone, rinsing in IPA and drying were required to remove the wax and grit which accumulates around the sample during the thinning process. The samples were then scribed across the top Si waveguide surface. Note that this does not apply strain to the underlying substrate unless considerable force is used. The sample is then carefully lowered onto a razor blade and cleaved to produce a chip with optical quality facets. At this smaller size the sample becomes slightly easier to manage, and we apply our final cleaning step. The chip is then stuck to a layer of static film which

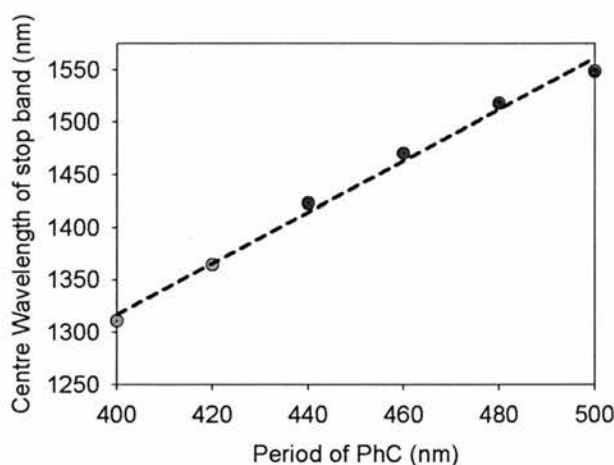
collects the remaining degreased, dust particles. Peeling this away then seems to successfully remove the vast majority of the dirt.

Figure 4.3 shows a full length (=256a) waveguide from the neighbouring die on the SOI wafer. This waveguide was not oxidised, which made it easier to image without the sample charging.



**Figure 4.17 W3 wavelength of length=256a**

With multiple copies of the waveguides available, a neighbouring die was first thinned, cleaved and measured, in this case with a broadband multiple ELED source. The centre of the MSB shifts by approximately 50nm for a 20nm step in lattice period (see Figure 3).



**Figure 4.18 . The centre wavelength of the Mini Stop Band tunes almost linearly with lattice constant, measured using multi-ELED source.**

With this information and taking account of the SOI TE slab mode dispersion [27], suitable tuning parameters were chosen. We suspect that the dry etched PhC features are affected more strongly by the oxidation process than the reference slab, due to the diffusion of O<sub>2</sub> through the porous SiO<sub>2</sub> cladding. Therefore the 2D equivalent index approximation in our model has a lower  $n_{\text{equiv}}$  (=2.89@ 1310nm) than that of the fundamental TE slab waveguide mode for the oxidised slab, to take account of this additional shift.

To identify the features in the transmission spectra a 253 period long waveguide was modelled using 2D FDTD (Fullwave-Rsoft Inc). A 2fs Gaussian modulated pulse with a centre wavelength of 1310nm, was launched in the fundamental mode of an input ridge waveguide, (width  $2\sqrt{3}a - 2R$ ,  $a=460\text{nm}$ ,  $n_{\text{equiv}}=2.89$ ), and the resulting transmission spectrum is plotted in Figure 4.19a. This is overlaid with the 2D photonic bandstructure of the waveguides, calculated using the MIT-Photonic Bands package [28] which compares admirably. The experimental CW transmission data of the oxidised sample (see Fig 2b) is displayed to the right. The transmission mirrors that of the fundamental mode from the FDTD. MSBs are observed as dips in the spectrum at i)  $u=0.27$ , ii) 0.305, iii) 0.36 and iv) 0.37, corresponding to the fundamental mode's interaction with the lower band edge i)  $k=0.3$ , the fifth mode [29] ii)  $k=0.15$ , itself as it folds at the band edge iii)  $k=0$  and the third mode inside the upper band edge iv)  $k=0.05$ , respectively. The shift between the upper and lower spectra in Figure 2b, is due to the lower vertical modal index at 1.55um.

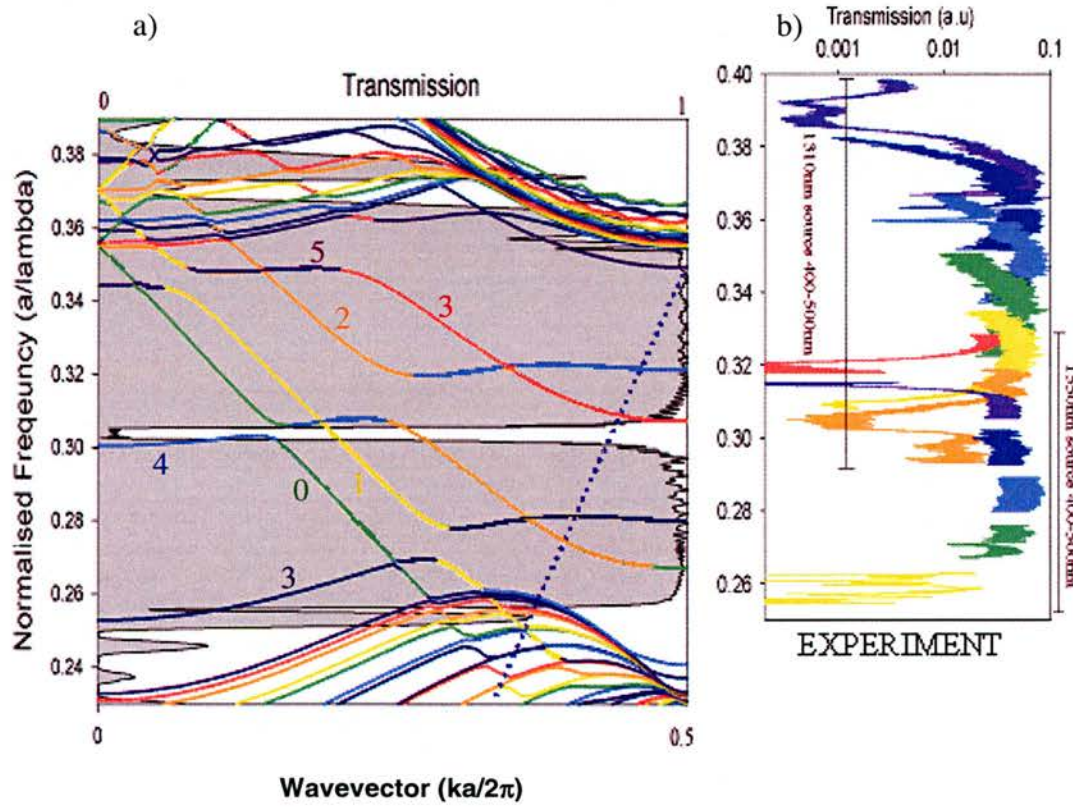


**Figure 4.19 a)** 2D bandstructure calculated using MPB overlaid upon 2D transmission spectrum of 2fs pulse launched into the fundamental TE0 mode of a 253a W3 waveguide. The transmission is plotted as a grey area against the LHS axis, the scale is at the top of the graph, this makes the gaps in the spectrum stand out. As can been seen the transmission follows the fundamental mode

and MSBs occur at  $u=0.305$ ,  $0.36$  and  $0.37$  where the fundamental anticrosses with the fifth, itself and then third modes respectively.  $\text{SiO}_2$  light line is marked as a dotted line.

b) The CW transmission of a set of lithographically tuned PhC waveguides. The upper six plots are measured with a  $1310\text{nm}$  source, lower six with a  $1550\text{nm}$  source. This means the largest gaps at  $0.305$  and  $0.32$  are identical, the larger modal index at the shorter wavelength red shifts the  $1310\text{nm}$  spectrum. The lattice constant,  $a$ , is varied in  $20\text{nm}$  steps, keeping the fill factor constant. Dips in transmission can be seen at corresponding points in the two spectra. The gaps at  $0.31$ ,  $0.29$ , and  $0.275$  are due to incomplete spectral coverage at  $1550\text{nm}$ . There are also stitching errors evident in the repetition of the feature at  $u\sim 0.32$  and  $u\sim 0.36$ . These are attributed due to the incorrect lithographic tuning (not writing constant  $r/a$  with change of  $a$ ).

The transmission spectrum of PhC waveguides yields practical information about the position of defect bands and allows characterisation of their losses. It does not however give information about their temporal qualities. Many of the diverse integrated optics applications of these structures rely strongly on their dispersion relation. This is most common plotted as a  $\omega$ - $k$  diagram. Measuring this diagram experimentally is highly desirable, but requires a very wide band technique to appreciate the scale of the structures. There are now several accounts in the literature of measurements of the dispersion of periodic nanoscale structures matching the theoretical accounts very well [30,31,32]. Here we are able to directly measure the dispersion of the PhC waveguide modes, firstly at low spatial frequency in the far field and then at much higher spatial frequency in the near field. Firstly, in order to appreciate the physics of the problem, it is necessary to examine the dispersion of a ridge waveguide with an air cladding, and then show how this dispersion evolves when we apply a periodic cladding.

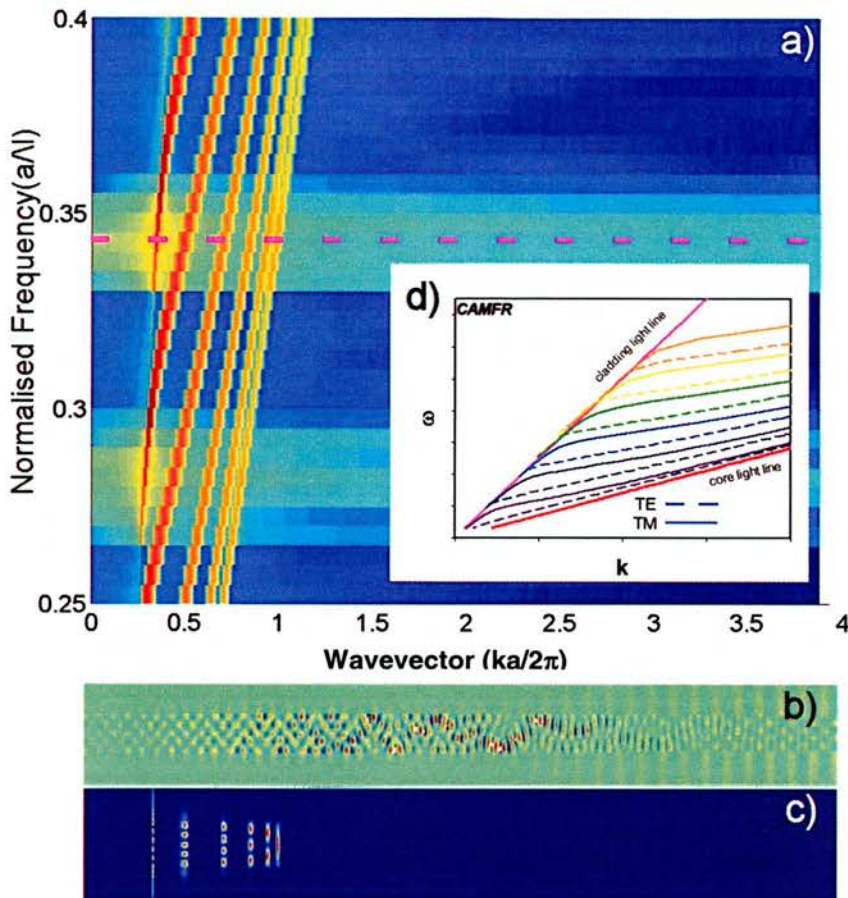


**Figure 4.20 Pulse excites TE modes of a ridge waveguide**

b) Field pattern for  $Hy$  after time  $T$  is superposition of individual modes ( $\omega=0.34$ , normalised frequency). c) Spatial Fourier Transform along propagation direction reveals spatial frequencies ( $k$ ) of individual modes and their field distributions. d) 1D mode solver shows modes bound by core light line and cut-off at cladding light line. a) Repeating FT for many pulse centre frequencies reveals mode dispersion, faster modes have steeper slope in  $\omega$ - $k$  diagram.

A 2D ridge waveguide supports guided modes with purely real wavevectors in the range  $\omega n_{\text{cladding}}/c < k_{\text{real}} < \omega n_{\text{core}}/c$ .  $n_{\text{core}}$  and  $n_{\text{cladding}}$  are the refractive indices of the waveguide core and cladding, respectively. These limits are represented on a  $\omega$ - $k$  (bandstructure) diagram as light lines, see Figure 4.20d). Propagation is forbidden in the region below the core light line, and modes are only truly guided in the wavevector space between the core and cladding lines (see Figure 4.20). Above the light line guided resonances can exist which have only a finite lifetime, due to allowed coupling to the continuum of radiation modes. In Figure 4.20b), the first six TE and TM modes of the input ridge waveguide are displayed, bounded by the

cladding and core light lines as calculated by a 1D mode solver (CAMFR width=2 $\sqrt{3}a$ -2r=1.29 $\mu\text{m}$ , a=460, neff=2.89). If in 2D FDTD we model a ridge waveguide with the same parameters and launch a pulse of 123fs duration simultaneously in the first 6 TE modes of the waveguide, after a time T the spatial Hy field distribution appears as in Figure 4.20c). Spatial Fourier Transformation (SFT) [11, 33, 13] of the field along the z-propagation direction yields sets of peaks denoting the spatial frequency of the various guided modes. Repeating this over a range of frequencies u=0.25-0.4 (summing the field along x - transverse to the guide) reveals the  $\omega$ -k diagram, as shown in Figure 4.20a). Note the agreement with the 1D mode solver (for this translation invariant waveguide). The higher order modes cut-off as they intersect the cladding light line. The blur of spatial frequencies (see Figure 4.20) excited as the mode cuts-off correspond to the multiple wavevectors subtended by the radiation modes.

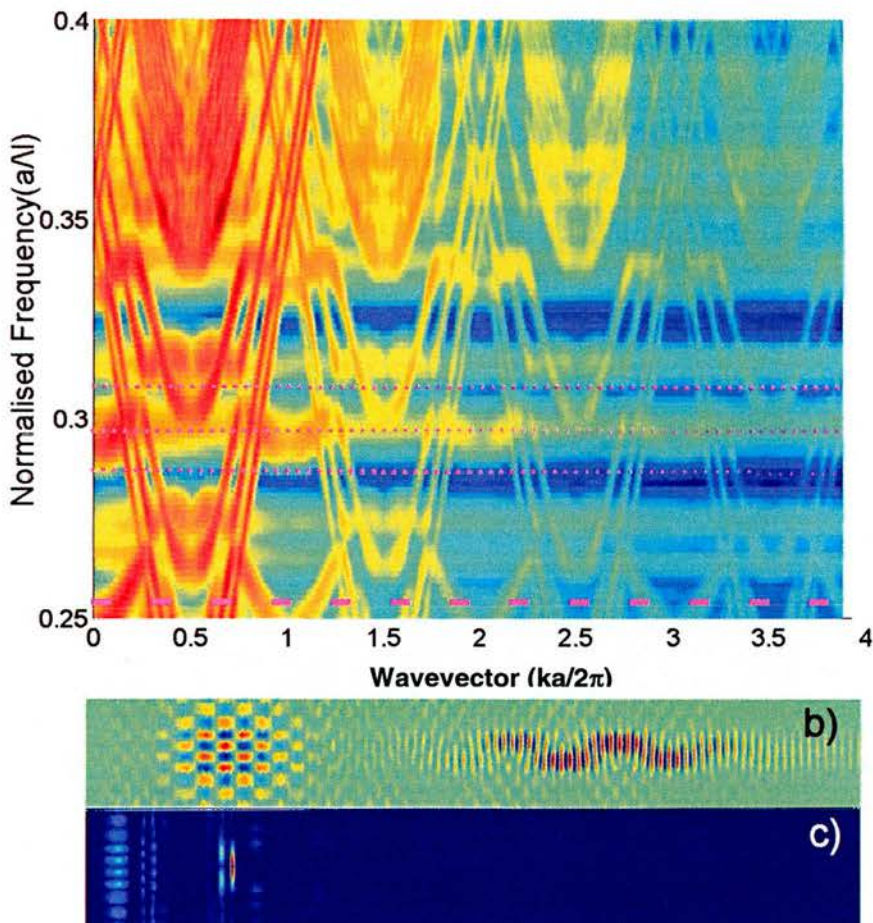


Figure 4.21 Pulse excites TE modes of a PhC waveguide

b) Field pattern for Hy after time T is superposition of individual modes (u=0.26, normalised frequency). c) Spatial Fourier Transform along propagation direction reveals spatial frequencies (k) of individual modes and their field distributions. a) Repeating FT for many pulse centre frequencies reveals mode dispersion, modes are folded at Brillouin Zone boundaries. Modes can now cross and anticross one another, creating gaps in the w-k diagram. Modes exist above the cladding light line.

For the modes of a PhC defect waveguide, the periodic modulation of the refractive index causes modes propagating from the ridge waveguide into the PhC waveguide to obtain additional wavevector components,  $k_{\text{secondary}} = 2\pi N/a \pm k_{\text{principal}}$ , where N is a integer ( $-\infty < N < +\infty$ ). Repeating the above calculation for the W3 PhC waveguide (width= $2\sqrt{3}a - 2r$ , length=253a, a=460nm, neff=2.89), we recover the PhC  $\omega$ -k diagram (see Figure 4.21). For a wide defect waveguide such as the W3, the principal component of the field follows roughly the same dispersion as a waveguide of identical proportions exhibiting continuous translation symmetry along its axis. These photonic states are coupled and thus folded by the periodic grating and the secondary components can exist above the air light line and below the core light line. Modes are no longer cut-off at the air-light line, but emanate with low group velocity from  $k=0$ .

#### 4.4.2 Far field imaging

Etching a 2D PhC in SOI combines the 2D periodic bandstructure with an asymmetric slab waveguide bandstructure. This 3D combination provides strong optical confinement for guided Bloch modes [34], but guided resonances [35,36] existing above the SiO<sub>2</sub> cladding light line are able to couple to the continuum. This has its advantages for characterising the dispersion. To this end, Loncar et al. utilised the light scattered from the surface of the sample which exists due to coupling of guided resonances to the radiation continuum above the Silica cladding line,  $\omega = ck/n_{\text{SiO}_2}$ . Imaging the light scattered from one of our oxidised waveguides (length=509a, a=480nm,  $\lambda=1314\text{nm}$ ) with a 100x long working distance objective, reveals a periodic intensity modulation, as can be seen in Figure 4.22b. The resulting intensity data recorded by a vidicon camera corresponds to a carrier signal, which is the standing wave formed along the entire length of the in/out-coupling waveguides (from cleaved facet to facet, i.e. the Fabry-Perot cavity) and an envelope modulation with a long period, see figure 6c. The ratio of the wavelength of this modulation relative to the

principal wavevector field is simply  $L_{\text{secondary}}/L_{\text{principal}} = n_{\text{principal}}/n_{\text{secondary}} = (1 - k_{\text{principal}})/k_{\text{principal}}$ , for a state with its principal wavevector in the 2<sup>nd</sup> Brillouin Zone. The resolution is eventually limited by diffraction and the chromatic focussing of the coupling and imaging objectives (to roughly 500nm or  $k=2 \times 10^6 \text{ m}$ , IR light imaged with visible optimised lens). Taking the SFT of these standing wave patterns along the waveguide again reveals sets of peaks. These peaks essentially correspond to the modulus of the field component that has been folded back into the 1st Brillouin Zone, by the periodicity of the waveguide, and therefore have twice the frequency of the field components. Repeating this at discrete wavelengths across the tuneable bandwidth of the narrow linewidth laser, and taking care of the factor 2 (because intensities are recorded by the camera, not fields), yields the far-field  $\omega$ - $k$  diagram for small values of  $k$ . Here the fundamental mode can be seen to fold at approximately  $k=0$ ,  $u=0.37$  (compared with  $u=0.36$  in the 2D bandstructure). As it folds it anticrosses with itself and a dip can be seen in the spectrum (see Fig 2). The low transmission is also recorded in the lack of Fabry-Perót (F-P) oscillation (the near vertical line at  $k=0.07$ ). The second mode is also detected occasionally with a stronger efficiency than the fundamental, highlighting the chromatic behaviour of the lenses. This out of plane scattered light evolves very strongly with the vertical focus

of the imaging lens corresponding to the angular spread of k-vectors.

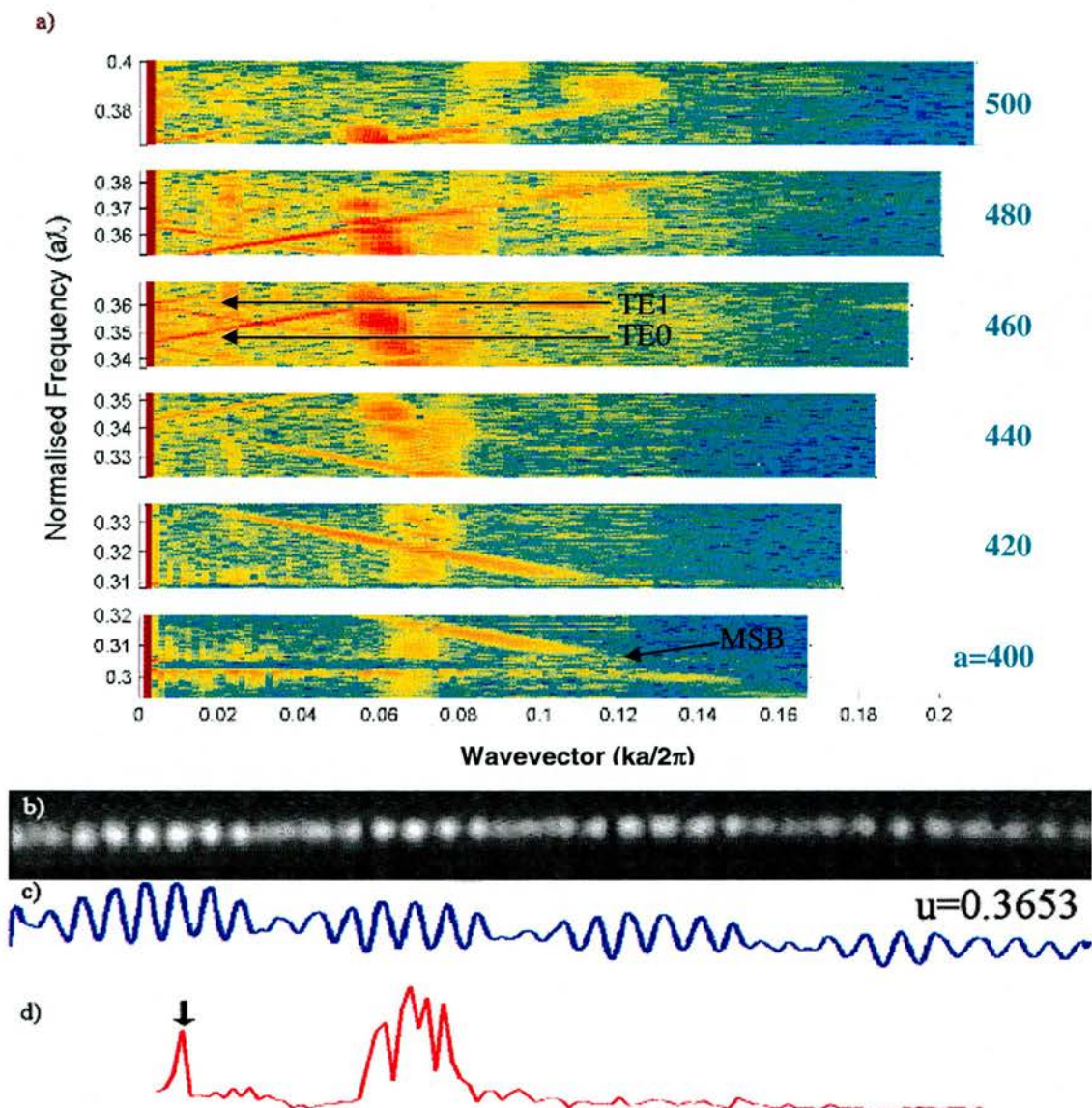


**Figure 4.22 CW Tunable laser excites TE modes of a PhC waveguide**

- b) Intensity distribution along W3 PhC waveguide (length=509a) imaged with 100x long working distance objective. c) Periodic modulation in intensity which changes with frequency (wavelength), Resolution limited by diffraction limit, only slow spatial frequencies are observable. d) Spatial Fourier Transform along propagation direction reveals spatial frequencies ( $k$ ) of individual modes and their field distributions. The  $k$ -axis is identical to (a) a) Repeating FT for many frequencies reveals mode dispersion, plotted as  $\omega$ - $k$  diagram. Lithographically tuned samples reveal the folded fundamental and 2<sup>nd</sup> order mode.



**Figure 4.23 b) Light scattered from W3 waveguide of length 253a, at 1364 nm for a= 420nm, (u=0.308). Mini Stop Band seen as bright standing wave at entrance to waveguide.**

Examining the field around the MSB using the same technique is not quite so simple. Indeed unlike the folding point at  $k=0$ , at the MSB anticrossing at  $k=0.15$ ,  $u=0.31$ , the longer secondary component of the spatial field is oscillating too often to resolve. The absence of propagation in the waveguide is apparent at the MSB (see Figure 4.23), as the wavelength approaches the MSB the field is scattered strongly at the waveguide entrance. Resolving the field at this spatial frequency requires the much higher resolution, provided by near field imaging techniques.

#### **4.4.3 Near field imaging**

Such a high resolution is achievable, for modes both above and below the silica light line, with a Near Field Scanning Optical Microscope (NSOM). As described previously a metallised optical fibre probe, with a narrow diameter aperture etched at its apex is used as a detector [37,38]. The evanescent tail of the optical mode is captured at the air-Si interface and when the tip is scanned over the surface, the field distribution in the waveguide can be mapped. By including the NSOM apparatus in one arm of a Mach-Zehnder interferometer, the detected signal can be mixed with a frequency shifted reference beam in a heterodyne technique to recover both amplitude and phase information [39]. Using a pulsed source with a temporal duration of  $\Delta t \sim 123\text{fs}$  removes the spatial noise of the Fabry-Perot oscillations which plague the CW measurements [40]. Repeating the above out-of-plane experiment with the NSOM probe and the OPO pulse source, the dispersion of the W3 can be mapped over a very large bandwidth. Two devices, with periods, 400nm and 460nm, were measured in the pulsed NSOM experiment, both  $N=253a$  long. The centre wavelength of the pulse is scanned in 5nm steps across the full tuning range (1180-1350nm, the full normalised frequency range covering the majority of the TE band gap of the PhC). The resulting field data (as amplitude and phase information is now available) corresponds to the fields excited in the periodic waveguide by the input pulses. Varying the delay in the reference arm of the Mach Zehnder allows us to visualise the pulse propagating through the PhC Waveguide (see Figure 4.24) [41].

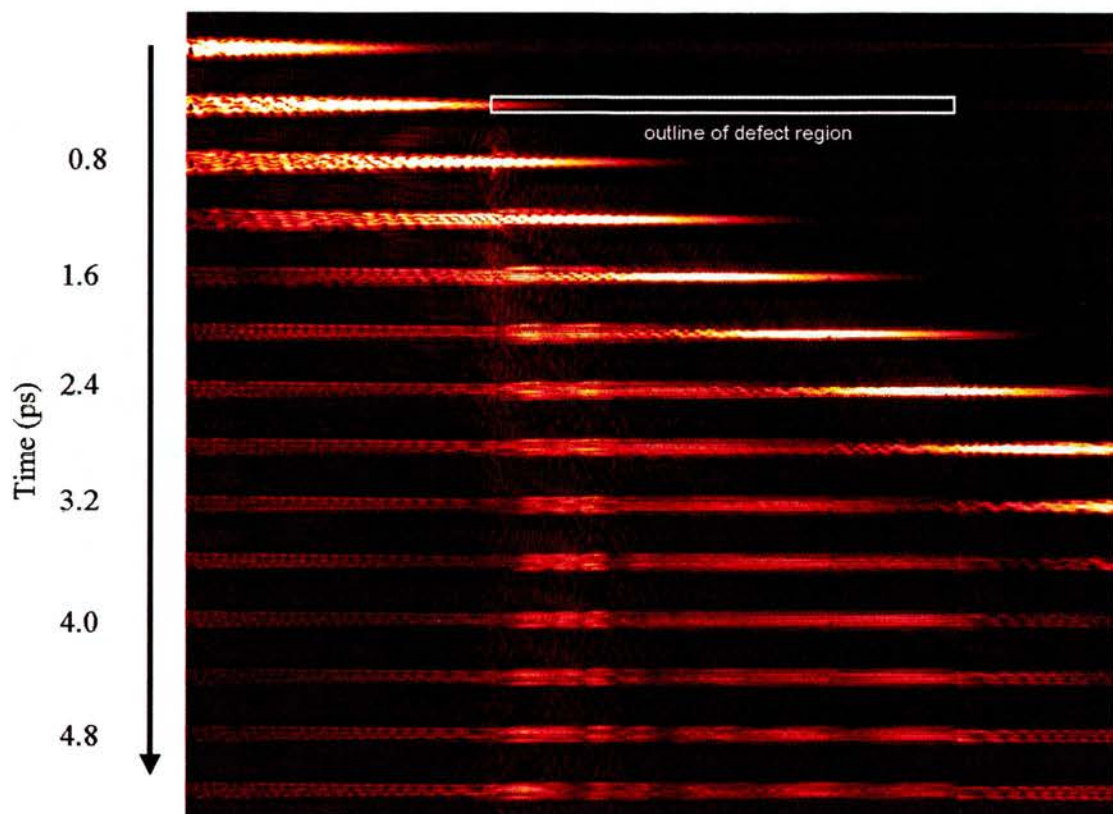


**Figure 4.24** Pulse propagation visualised in (length=253a) W3 photonic crystal waveguide at  $u=0.305$  ( $\lambda=1310\text{nm}$ ) for  $a=400\text{nm}$ . The delay between each frame is 400fs, introduced via the reference arm. At the entrance to the PhC a standing wave pattern is excited. We observe this evolve over >5ps time scale, and only a small shift in mean position is evident.

The standing wave pattern shifts after a duration of 3.5ps. A tentative estimate of the group velocity of this mode is of the order  $c/1000$ . At this wavelength the folded 4<sup>th</sup> mode and the MSB exist with significant curvature. The SFT of the latter image only contains components in the range  $k=0.4-0.6$  this indicates that it this likely to be the 4<sup>th</sup> mode. The beating in the tail of the main pulse indicates the presence of more than one spatial mode inside the PhC [39].

It is very evident that the launch mode consists of many spatial modes. The field appeared much smoother in the wider access waveguide. Several measurements utilising the temporal delay have been repeated where interesting pulse effects were observed. By Fourier filtering the amplitude and phase information the Centre of Mass (COM) of the individual pulses can be tracked in various waveguide modes. A range of group velocities are observed for the 460nm sample at  $\lambda=1245\text{nm}$ , ranging between 0.121c and 0.243c. The input pulse very quickly breaks up into a sequence of four distinct pulses. The COM of each is tracked along the waveguide and plotted versus the time delay. The intercepts of the propagation distance versus time plots are

not all coincident, indicating that the multiple modes are excited at different points [41]. This may be the effect of roughness or perhaps a non-linear effect in the tapered waveguide. At this repetition rate, short pulse length (123fs) and high optical confinement either of these effects is possible. A more systematic study would be required to determine this however.

The OPO was then tuned across the wavelength range 1180-1350 in 5nm steps. The data across the waveguide (in the x-direction) was summed together, so as to include all even and odd waveguide modes, and then Spatial Fourier Transformed (along the waveguide z-direction). We take the Discrete Fourier Transform of the data set. The measurement uses samples 400 and 460nm and therefore covers a range of approximately,  $u=0.3-0.39$ . The data is displayed in Figure 4.25

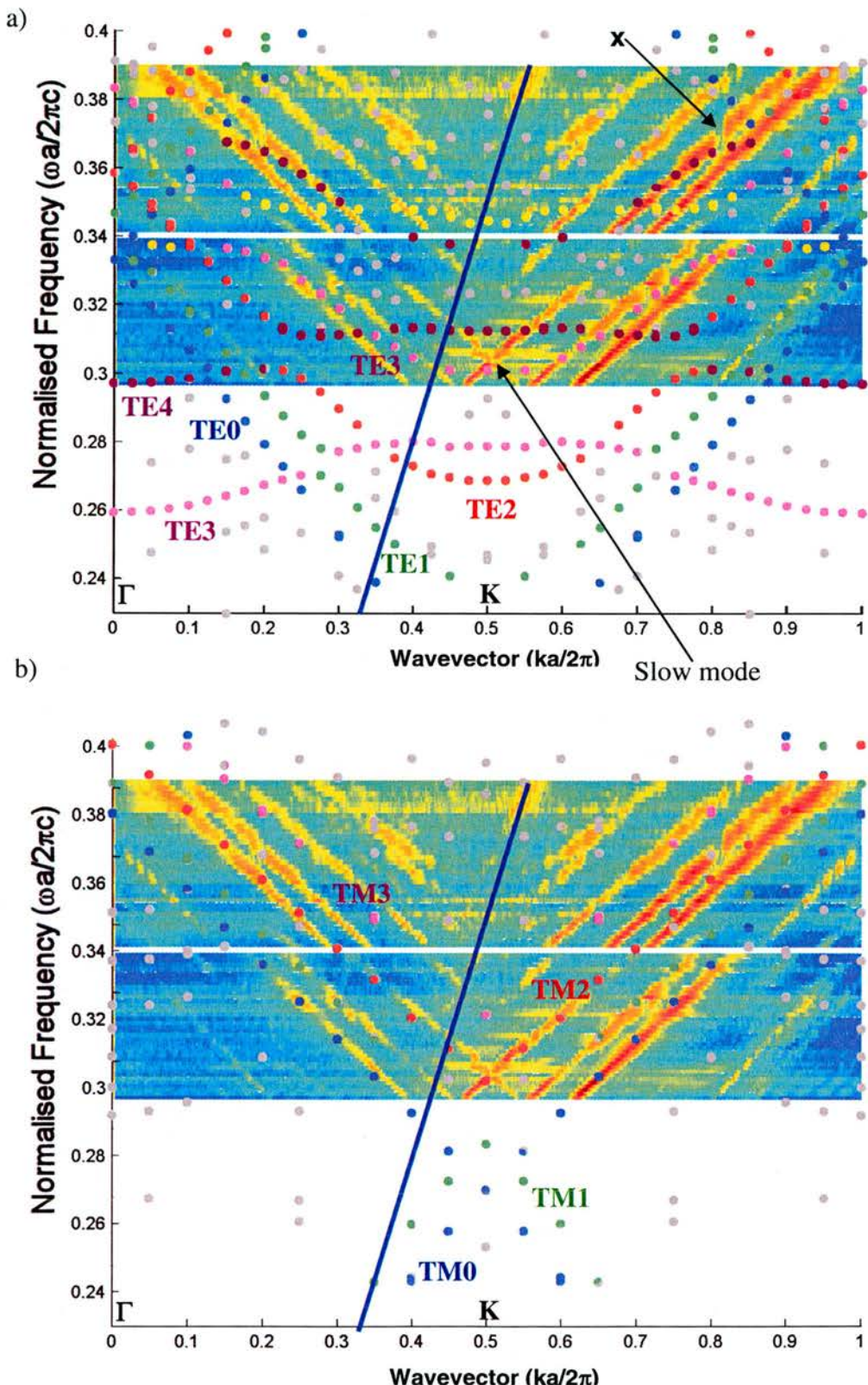


Figure 4.25 a) Spatially Fourier Transform of field for each wavelength. The individual waveguide mode dispersions immediately become apparent. The modes fold at the K point as we saw in the FDTD data. The  $\text{SiO}_2$  light line is marked on the diagram as the blue line. Modes are observed both above and below the light line. The 4<sup>th</sup> mode (the U shaped curve marked with 'Slow mode') is evident, but notably only underneath the light line (blue un-broken line). It is at

this point that the long lived standing wave was observed. b) The 3D FDTD data is plotted to overlay the TE modes and the TM modes on the left and on the right hand sides respectively.

The main modes that have been excited are predominantly TM. Though the 4<sup>th</sup> TE mode is observed at  $k=0.5$ ,  $u=0.3$ . At this point the band is extremely flat. The bands are coloured blue fundamental (0), green second (1), red third (2), pink fourth (3), and purple fifth (4).

This is the first investigation which has directed imaged the Bloch harmonics above and below the light line. These are folded at the edges of the Brillouin zone at  $k=0.5$ . Similar folding was observed in Si<sub>4</sub>N<sub>4</sub> waveguides with the same experimental setup [42]. The large quasi-continuum of Gap edge states is evident on the upper diagram of Figure 4.25 .

Small gaps are evident in the bands, as vertical lines, near the x in Figure 4.25. These would appear to be anticrossings, but only one of the band is observed on the diagram. The lines appear vertically rather than horizontally as we have been used to k as our independent variable. Here we use the normalised frequency, u, as our independent variable.

#### 4.4.4 Fourier mode profiles

The lock-in amplifier used in the heterodyne detection system yields a cosinusoidal and a sinusoidal term. Initially we made the mistake of neglecting this complex data set ( $\cos\theta+i \sin\theta$ ) and treated only the real part. More recently we have made use of the full complex data (see section 4.2.2), which provides us with information about the sign of the wavevector components. The phase properties of the Bloch harmonics at a single frequency, but in different Brillouin zones (at  $k=0.393$  and  $k=0.607$ ) have been compared and contrasted in detail [41]. In the 2nd Brillouin Zone (2BZ) the sine component is leading, whereas in the 1<sup>st</sup> Brillouin Zone (1BZ) it lags. This corresponds to waves travelling in different directions, i.e. different phase velocities.

Using this complex data set we can replot the previous graph, see Figure 4.26. The phase velocities of the different Bloch harmonics are now correctly represented, by either negative or positive wavevectors. From our pulse tracking experiment we know that advancing our delay line, increases the length of the reference branch in our interferometer and shifts the position of the pulse forwards in waveguide. From the slope of each of the Bloch harmonics, we can tell that the group velocity of our modes is reassuringly positive.

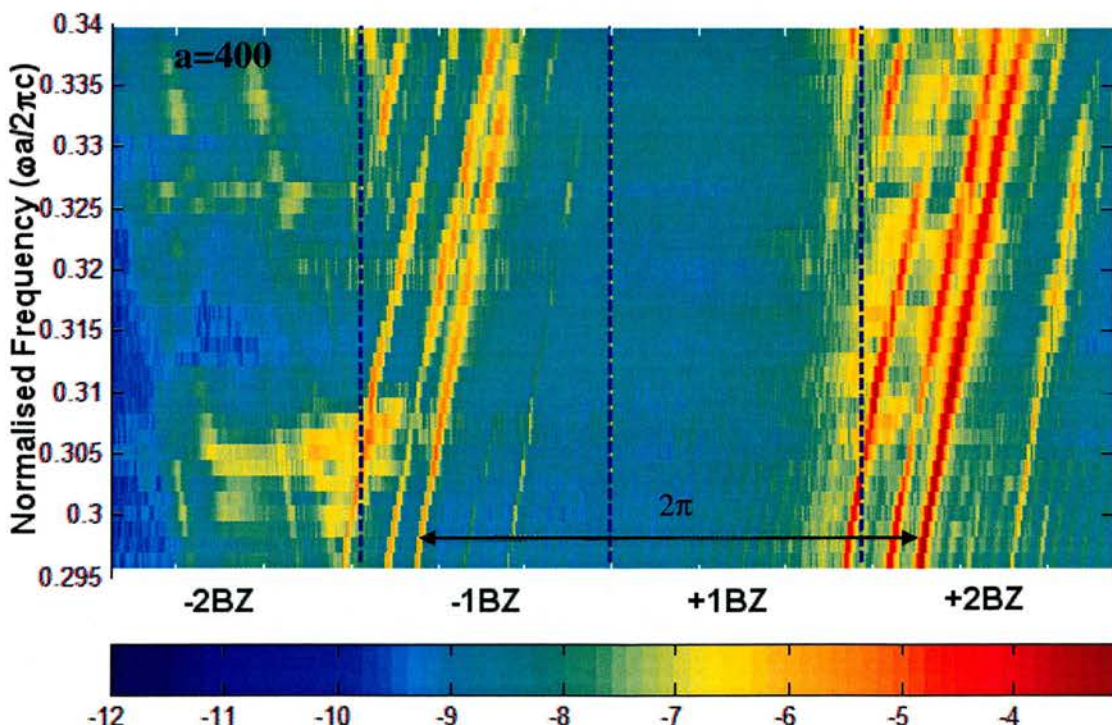
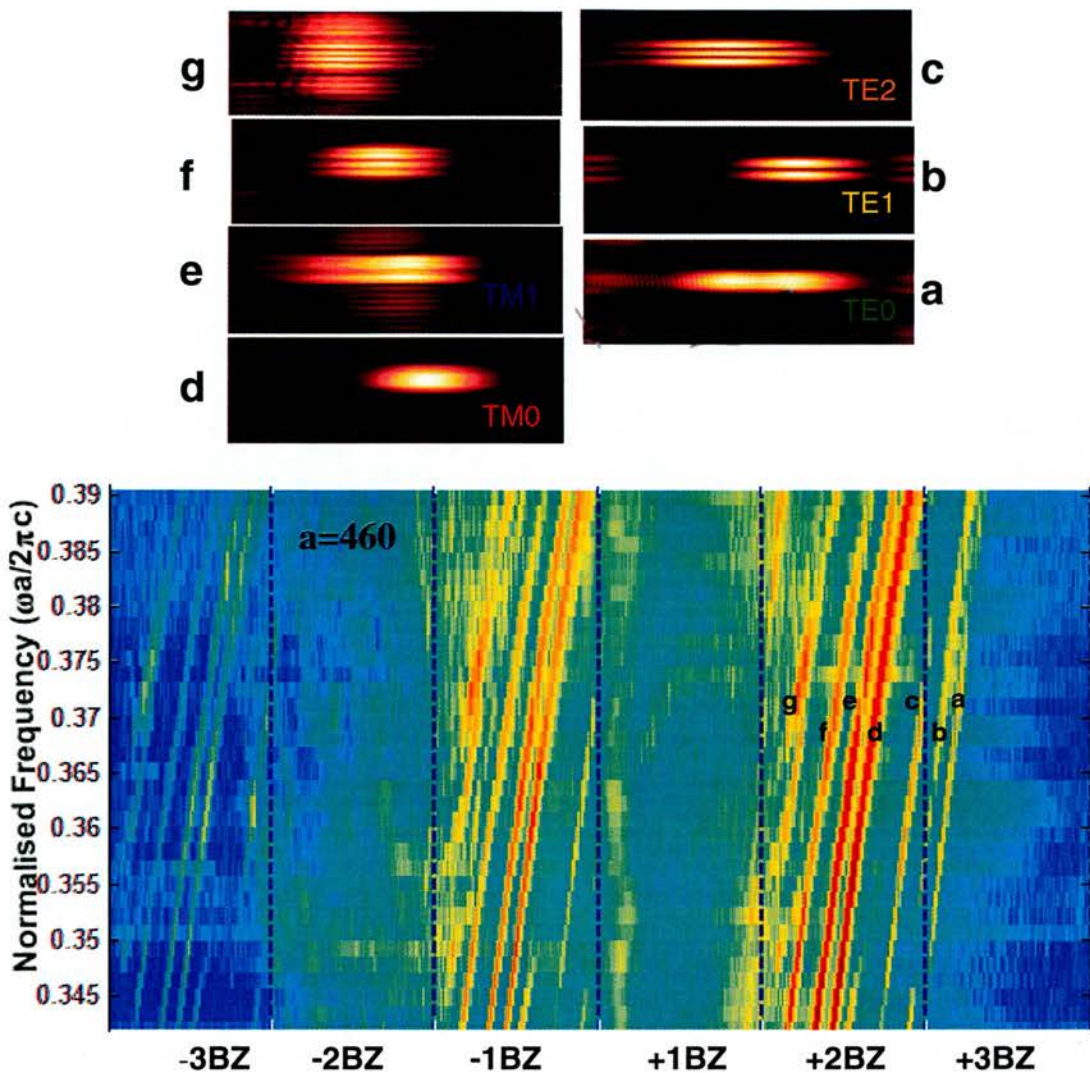


Figure 4.26 The SFT of the complex data set for the  $a=400$  sample.



**Figure 4.27** Mode identification for the 460nm sample at a normalised frequency of  $u=0.37$ , the Fourier Transformed data is windowed to only include components at a narrow range of Spatial Frequencies and inverse Fourier Transformed to real space. a,b,c) TE modes, d,e,f,g) TM modes (courtesy of Henkjan Gersen)

It is possible to identify the modes by windowing the SFT data to include just a single mode and inverse Fourier Transforming. In this case the field profiles in the +2BZ and +3BZ have been plotted for the 460nm sample. Looking at an individual SFT of the field along the waveguide, it is immediately apparent that the fields at the principal and secondary Bloch wavevectors have very different spatial profiles (see Figure 4.28) . A pulse with centre frequency  $\omega$ , exciting a individual Bloch mode [30] travels at a single group velocity but each harmonic component of the mode travels with a distinct phase velocity,  $v_{\text{phase}} = c/n_{\text{phase}} = \omega/(2\pi N/a \pm k_{\text{principal}})$ . In this

experiment the pulse excites many Bloch modes, which tends to confuse the eye a little.

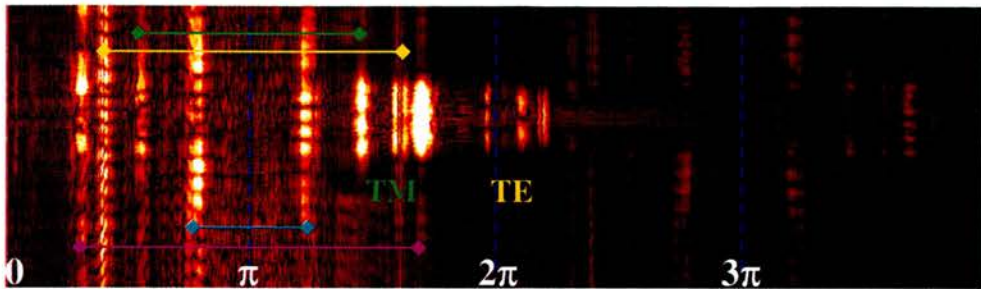


**Figure 4.28** Experimental SFT data for the 460nm sample at a wavelength of 1245nm. Only the real part of the data has been FFTed, artificially folding the -1BZ into the +1BZ. The plot displays the first 4 +BZs. The difference between the mode profiles of Bloch harmonic components in different Brillouin Zones is obvious (courtesy of Henkjan Gersen).

The TM modes dominate the measured data, whereas we were initially interested in the behaviour of only the TE modes. The intensities of the folded Bloch harmonics for the TE modes are fairly weak. In order to investigate the mode profiles in more detail we resort to our 2D FDTD model. The presence of the Photonic Band Gap for these TE modes serves to clean up the picture a little.

To illustrate the point we will look at the region around the ministop bands for the 2D TM (equivalent to TE in 3D) modes. In Figure 4.29 we plot the absolute field for the excited mode and restrict ourselves to the first two Brillouin Zones for the W3 waveguide. A central symmetry boundary limits the set of modes to those which are even about the waveguide axis. The centre frequency of the Gaussian excitation pulse is  $\omega \sim 0.325$ . The vertical axis is a linear scale.

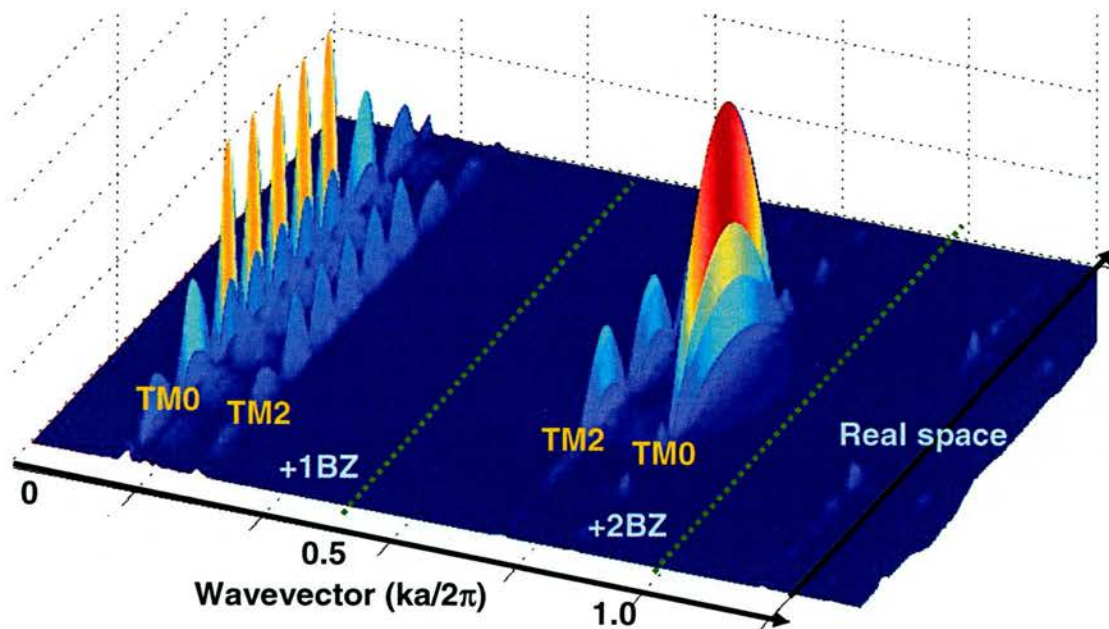


**Figure 4.29 First 2 Brillouin zones for W3 waveguide at  $u \sim 0.325$ ,  $a = 400\text{nm}$ , even modes only.**  
Only two of the three lobes are visible behind the fundamental mode! At this frequency the TM4 is cut off

The principal Bloch harmonics for the TM0 and TM2 have their expected form in the 2BZ, whereas in the 1BZ they appear identical. If we trace the behaviour of these two modes up through the region of the mini stop band (caused by the TM0/TM4 mode crossing) at three different centre frequencies,

- i)  $u=0.289$ , below the MSB
- ii)  $u=0.298$ , at the edge of the MSB
- and iii)  $u=0.3085$  above the MSB,

we gain a new insight into the cancellation mechanism which forms the stop band. These frequencies are denoted on Figure 4.21 by the three dotted lines. In this case we include both odd and even modes. We will denote the main Bloch harmonic as the principal component.

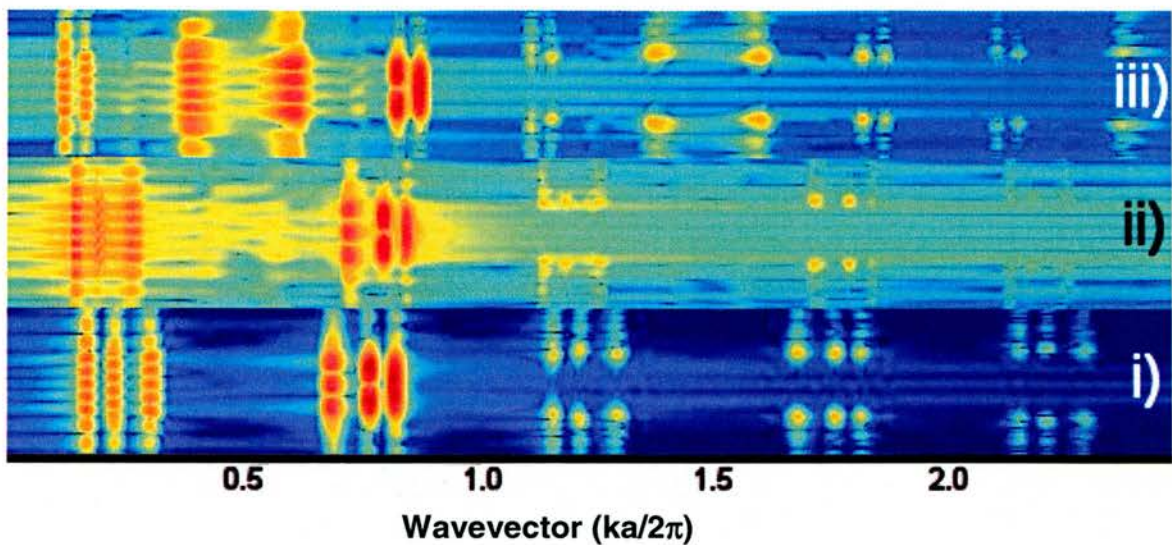


**Figure 4.30** The SFT along the waveguide axis at three different centre frequencies for a W3 waveguide with  $a=400\text{nm}$ ,  $r=a/3$ . i)  $u=0.289$ , ii) 0.298, and iii) 0.3085

In i) the gap guided principal TM4 mode is just appearing at the  $\Gamma$  point, the profiles of the other (TM0, TM2) even, index guided modes in the 1BZ resemble those in Figure 4.29 above. The field profile of these modes in the 1BZ is very similar to the TM4 mode.

In ii) the TM0 mode is slightly cut-off at the edge of the MSB.

In iii) The TM2 mode has been cut-off by the TM2/TM4 MSB. The index guided TM3 appears similar in both 1BZ and 2BZ. The advent of the TM4 mode appears to have changed the profile of the TM1 mode in the 1BZ.

In each case the principal Bloch harmonics appear to take the same profile as the equivalent ridge waveguide mode. Whereas the composite Bloch modes are by definition orthogonal (the operator in our original eigenvalue problem was a Hermitian operator), it appears as if their folded components can be degenerate with other principal components. This degeneracy leads to the very strong interaction where the modes intersect one another, and anticross. As principal components become guided the folded profiles of other modes with the same parity changes. Also at wavevectors longer than the principal component no strong field components exist in the waveguide core.

The investigation of this effect is by no means complete, but the initial work has raised some interesting questions. The same behaviour has been modelled in the

narrower W1 and W2 waveguides. We have also observed MSBs close to the K point in 1D integrated grating structures. Their location so far above the light line, however, is not entirely unique to 2D PhC structures. Such MSBs can be observed in novel metallic and Omniduide waveguides. What is unique to PhCs is that the two interacting bands can have opposite dispersion slope.

These highly dispersive PhC waveguides exhibit many consequences of the 2D periodicity. The gap guided states (a consequence of the folding of the transverse components onto the  $\Gamma$  point) impact upon both W1 and W3 dispersion performance. In seeking to mitigate the practical limits imposed by propagation losses, one can remove as many modes as possible to yield single mode states which are intrinsically low loss or alternatively choose larger multimode waveguides which may less sensitive to extrinsic loss. The application of these structures will eventually determine which route is more successful.

## **4.5 Conclusions**

The high contrast of these Planar Photonic Crystals makes them very effective at coupling together many modes, those of similar parity and polarisation. This occurs when the periodicity of the grating creates degeneracy when states are folded back across each other. Theoretically the modes either interact or do not; i.e. they anticross or cross. The anticrossings give rise to small partial band gaps known as Mini Stop Bands. In seeking to use these mode crossings to take advantage of their high dispersion we must be very wary of the other modes. We have shown that an asymmetrically confined waveguide can accentuate the coupling of modes which cross one another. We have observed power coupled to higher order modes and other polarisation states. All of these has some noticeable effect on the transmission, but its effect on the phase is so far less well understood.

We have demonstrated a beautiful technique for mapping out the bandstructure of PhC waveguides experimentally, and shown excellent agreement with theory. Using a detailed modal analysis employing Spatial Fourier Transforms (SFTs) we have shown how the index guided modes of a ridge waveguide develop, in the presence of a photonic crystal cladding, into both index guided and also bragg-guided modes. These modes are folded by the periodicity, accruing additional wavevectors, spaced by multiples of  $2\pi/a$ . Each wavevector component has an orthogonal spatial field profile that is affected strongly by the existence of other guided states (resonances and modes). At the intersections (anticrossings) between folded modes of identical polarisation and parity these modes become degenerate leading to strong splitting of the bands.

- 1 Photonic Crystal Integrated Circuits PCIC IST-1999-11239, the substrate approach was written into the “innovation section” accessed [http://esperia.iesl.forth.gr/~cond-mat/photonics/PCIC/PCICannex1\\_public.html](http://esperia.iesl.forth.gr/~cond-mat/photonics/PCIC/PCICannex1_public.html)
- Photonic Integrated Circuits using photonic Crystal Optics PICCO, admittedly did adopt a SOI (HOP) based approach as well as their GaAs work
- COST 268 modelled both types of structure
- 2 S. J. McNab, N. Moll, and Y. A. Vlasov, "Ultra-low loss photonic integrated circuit with membrane-type photonic crystal waveguides," *Opt. Express* **11**, pp2927-39 (2003)
- 3 M. Notomi, A. Shinya, S. Mitsugi, E. Kuramochi, and H. - Ryu, "Waveguides, resonators and their coupled elements in photonic crystal slabs," *Opt. Express* **12**, 1551-1561 (2004)
- 4 Y. Sugimoto, Y. Tanaka, N. Ikeda, Y. Nakamura, K. Asakawa, and K. Inoue, "Low propagation loss of 0.76 dB/mm in GaAs-based single-line-defect two-dimensional photonic crystal slab waveguides up to 1 cm in length," *Opt. Express* **12**, 1090-6 (2004)
- 5 A.Y. Petrov, M. Eich, Zero dispersion at small group velocities in photonic crystal waveguides”, *Appl. Phys. Lett.*, **85**, pp4866-8, (2004)
- 6 S. Hughes, L. Ramunno, J.F. Young, J.E. Sipe, “Extrinsic optical scattering loss in photonic crystal waveguides: Role of fabrication disorder and photon group velocity”, *Phys. Rev. Lett.*, **94**, pp033903 (2005)
- 7 Many thanks to Melanie Ayre for the 3D MPB calculations. Above the lightline there is no provision in MPB to deal with radiating fields. A new commercial code Photon Design’s “Crystalwave” and Dennis Prather’s group at Delaware have included absorbing boundaries in plane wave simulations, to deal with these effects. The work of Sauvan and Lalanne on the Fourier Modal method adopts a similar approach.
- 8 L. Prodan, T.G. Euser, H.A.G.M. van Wolferen, C. Bostan, R.M. de Ridder, R. Beigang, K-J. Boller, L. Kuipers, “Large-area two-dimensional silicon photonic crystals for infrared light fabricated with laser interference lithography”, *Nanotechnology*, **15**, pp 639-42, (2004)
- 9 W. Kuang, C. Kim, A. Stapleton, W.J. Kim, J.D. O’Brien, “Calculated out-of-plane transmission loss for photonic crystal waveguides”, **28**, pp1781-3, (2003)
- 10 B.W. Hakki, T.L. Paoli,, *J. Appl. Phys.*, **44**, pp 4113, (1973)
- 11 D. Hofstetter, R.L. Thornton, “Loss measurements on semiconductor lasers by Fourier Analysis of the emission spectra”, *Appl. Phys. Lett.*, **72**, pp404-6, (1998)
- 12 Many thanks to Michael Mazilu who was instrumental in establishing the correct way to generate and process the data using the FFT. The simple FFT may not be the optimum tool to use for a stable method for obtaining the loss figures. My thanks also to Amr Helmy for suggesting the technique to us in the first instance.
- 13 A. Talneau, M. Mulot, S. Anand, P. Lalanne, “Compound cavity measurement of transmission and reflection of a tapered single-line photonic-crystal waveguide”, *Appl. Phys. Lett.*, **82**, pp2577-9 (2003). A. Talneau,, presentation at “Two Dimensional Photonic Crystals” workshop, Monte Verita Ascona, Switzerland, (2002)
- 14 M.D. Rahn, A.M. Fox, M.S. Skolnick, T.F. Krauss, *J. Opt. Soc. Am. B*, **19**, pp716-721, (2002)
- 15 Calculated using Fimmwave, comparing the three waveguides 3μm width tapered to 490nm

Wafer	Ratio of energy density at narrow end of taper to broad end
GaAs (Scotland structure)	5.88
AlGaAs	6.15
SOI (220nm thick)	5.75

16 In an AlGaAs W3 waveguide using 100fs pulses at a rep. rate of 3GHz the pulse transmission spectrum around the MSB was markedly different at higher power than at low.

17 M. Settle, T.J. Karle, T.F. Krauss “Fourier Analysis of Photonic Crystal Waveguide Losses”, [Poster Presentation], Tu-P36, PECSV Kyoto, Japan, 2004,

- 
- 18 M. Ayre, T.J. Karle, L. Wu, T. Davies, T.F. Krauss, "Experimental Verification of Numerically Optimised Photonic Crystal Y-Splitter and Bend", IEEE Selected Areas in Communications, accepted for publication
- 19 V.A. Mandelshtam, H.S. Taylor, "Harmonic inversion of time signals", J. Chem. Phys. **107**, 6756-69, (1997), Erratum, *ibid*, **109**, 4128 (1998)
- 20 Harminv version 1.2.1 written by S.G. Johnston, available at <http://ab-initio.mit.edu/harminv/>
- 21 B. Jalali, S. Yegnanarayanan, T. Yoon, T. Yoshimoto, I. Rendina, and F. Coppinger, "Advances in Silicon-on-Insulator Optoelectronics", IEEE J. Sel. Top. Quant. Elect., **4**, p.938, (1998)
- 22 M. Lončar, T. Doll, J. Vučković, A. Scherer, "Design and Fabrication of Silicon Photonic Crystal Optical Waveguides", J. Lightwave Technol., **18**, pp 1402-11, (2000)
- 23 M. Notomi, A. Shinya, K. Yamada, J. Takahashi, C. Takahashi, and I. Yokohama  
"Structural Tuning of Guiding Modes of Line-Defect Waveguides of Silicon-on-Insulator Photonic Crystal Slabs", **38**, IEEE J. Quant. Elect., (2002), p. 736
- 24 H. Gersen, J.P. Korterik, N.F. van Hulst, L. Kuipers, "Tracking ultrashort pulses through dispersive media: experiment and theory", Phys. Rev. E, **68**, 026604, (2003)
- 25 W. Bogaerts, V. Wiaux, D. Taillaert, S. Beckx, B. Luyssaert, P. Bienstman, and R. Baets,  
"Fabrication of Photonic Crystals in Silicon-on-Insulator Using 248-nm Deep UV Lithography", IEEE J. Select. Topics Quant. Elect., **8**, pp928 (2002)
- 26 S. Olivier, M. Rattier, H. Benisty, C. Weisbuch, C.J.M Smith, R.M. De La Rue, T.F. Krauss, U. Oesterle, R. Houdré , "Mini-stopbands of a one dimensional system: The channel waveguide in a two-dimensional photonic crystal", Phys. Rev. B, **63**, 113311, (2001)
- 27 The TE slab waveguide mode and indeed each of the observed principal ridge waveguide modes can be fitted with good agreement with a 2D mode solver (Fimwave - Photon Design, Oxford UK)
- 28 S.G. Johnson, J. D. Joannopoulos, "Block-iterative frequency-domain methods for Maxwell's equations in a planewave basis," Optics Express **8**, (2001), p.173
- 29 S. Olivier, H. Benisty, C. Weisbuch, C. J. M. Smith, T. F. Krauss, R. Houdré, "Coupled-mode theory and propagation losses in photonic crystal waveguides", **11**, Optics Express, (2003) p. 1490
- 30 P.St.J. Russell and R. Ulrich, "Elementary and coupled waves in periodic planar waveguides", 2nd European Conference on Integrated Optics, Florence IEE Conf. Publication **227**, pp88 (1983)
- 31 V.N. Astratov, D.M. Whittaker, I.S. Culshaw, R.M Stevenson, M.S. Skolnick, T.F. Krauss and R.M. De La Rue, "Photonic band-structure effects in the reflectivity of periodically patterned waveguides", Phys Rev B, **60**, (1999)
- 32 M. Lončar, D. Nedeljković, T.P. Pearsall, J. Vučković, A. Scherer, S. Kuchinsky, D.C. Allan, "Experimental and theoretical confirmation of Bloch-mode light propagation in planar photonic crystal waveguides" App. Phys Lett , **80**, (2002), p.1689
- 33 A. Jafarpour, A. Adibi, Y. Xu and R.K. Lee, "Mode dispersion in biperiodic photonic crystal waveguides", Phys. Rev. B **68**, 233102 (2003)
- 34 S.G. Johnson, S. Fan, P.R. Villeneuve, J. D. Joannopoulos and L. A. Kolodziejski , "Guided modes in photonic crystal slabs", Phys Rev B **60** (1999), p.5751
- 35 S. Fan, J. D. Joannopoulos , "Analysis of guided resonances in photonic crystal slabs", Phys. Rev. B, Vol. 65, 235112, (2002)
- 36 T. Ochiai, K. Sakoda, "Dispersion relation and optical transmittance of a hexagonal photonic crystal slab", Phys Rev B **63**, 125107, (2001)
- 37 E. Flück, M. Hammer, A. M. Otter, J. P. Korterik, L. Kuipers, and N. F. van Hulst, "Amplitude and Phase Evolution of Optical Fields Inside Periodic Photonic Structures", J. Lightwave. Technol. **21**, (2003) p.1384
- 38 S. Fan, I. Appelbaum, and J. D. Joannopoulos , "Near-field scanning optical microscopy as a simultaneous probe of fields and band structure of photonic crystals: A computational study", Appl. Phys. Lett., **75** (1999)
- 39 M. L. M. Balistreri, J. P. Korterik, L. Kuipers, and N. F. van Hulst , "Phase Mapping of Optical Fields in Integrated Optical Waveguide Structures" J. Lightwave. Technol. **19**, (2001) p. 1169
- 40 M. L. M. Balistreri, H. Gersen, J. P. Korterik, L. Kuipers, and N. F. van Hulst  
"Tracking Femtosecond Laser Pulses in Space and Time", Science **294** (2001) p. 1080
- 41 H. Gersen, T.J. Karle, R.J.P. Engelen, W. Bogaerts, J.P. Korterik, N.F. van Hulst, T.F. Krauss, and L. Kuipers, "Real space observation of ultraslow light in photonic crystal waveguides", Accepted for publication PRL (2004)
- 42 R.J.P. Engelen, H. Gersen, J.P. Korterik, T.J. Karle, T.F. Krauss, L. Kuipers and N.F. van Hulst  
"Direct probing of Bloch mode dispersion in photonic crystal waveguides", to be submitted.

## **Chapter 5**

### **5.1 Spatial dispersion and Routing in Planar Photonic Crystals**

This chapter briefly looks at some of the complementary work that my colleagues, Lijun Wu, Rab Wilson, Michael Mazilu, Thomas Krauss and myself investigated in 2002. We have tended in this report to look at pseudo-1D effects in 2D PhCs. We now look at the possibilities of using the 2D nature of the crystals for spatially separating one beam into two. It is envisaged that such components could then form the basis of minuscule Wavelength Division Multiplexing devices or switches based on Mach-Zehnder interferometers.

### **5.2 Superprism**

We will start by introducing the superprism effect. At the bandedge of a photonic crystal the curvature of the bands allows for a very large spatial angular deviation with either change in incident wavelength or incident wavevector. The first experimental demonstration of this effect (in 1996) used a millimetre wave source [1] in the 100GHz range. The effect was maximised as the source centre frequency approached the band edge of a triangular lattice of dielectric pillars in air. This effect utilised the phase velocities of the waves to generate the strong dispersion. In 1998 Kosaka et al. [2] choose to construct a very elaborate 3D autocloned structure in order to demonstrate a similar effect, based on the dispersion of the group velocity. They were able to demonstrate a huge angular tuning range, for a beam incident within an angular range of  $\pm 12^\circ$  the beam inside the Photonic Crystal was deflected by  $\pm 90^\circ$ . This dispersion is two orders of magnitude stronger than that observed from conventional prisms and gratings. The work sparked a huge interest in the spatial dispersion characteristics of periodic structures, as researchers strove to realise and simplify the effect. A 2D Transfer Matrix approach was used to study this in [3]. A comprehensive overview of the work is given in [4].

In Chapter 3 we looked at the bandstructure of point defects and in Chapter 4 looked at the bandstructure of line defect waveguides. For each of these cases we were interested only in states on or close to the edges of the IBZ boundary. We will now

calculate and examine the dispersion surface, across the entire IBZ, for a hexagonal lattice of air holes in a dielectric background. This is plotted in Figure 5.1, for the first 4 TM bands ( $H_y$ ,  $E_x$ ,  $E_z$ ). The reader may wish to refer back to Figure 3.10 for the corresponding IBZ edge plot. The conical lower band can be seen to curve gently at the edges of the bandgap at  $u=0.214$ . The hexagonal lattice can be recognised from the near ~six fold symmetry of the higher bands.

This is an attractive albeit rather awkward format in which to display the data. We can get an idea of the appealing dispersion regions by producing a histogram plot (binning the number of states in narrow frequency ranges). This reveals a density of states plot, as shown in Figure 5.2. The frequency regions with a high density of states indicate where there is substantial wavevector degeneracy i.e. where it may be possible to have a large change in propagation direction for a small frequency change.

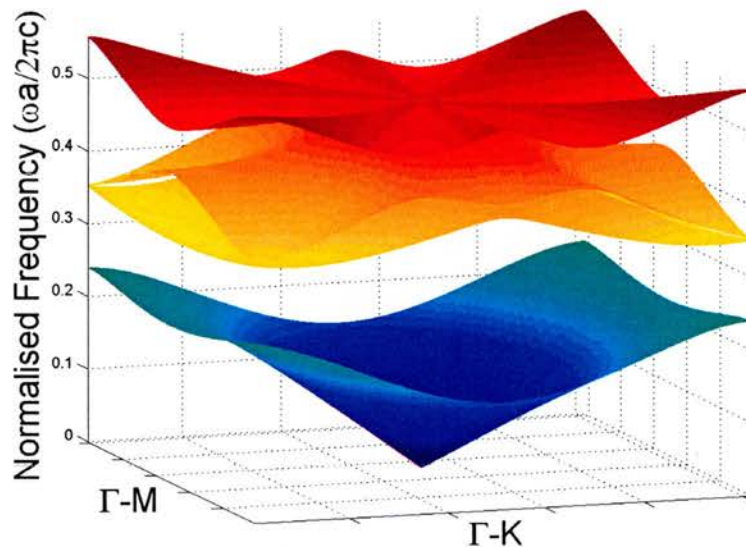


**Figure 5.1 Wavevector diagram plotted for IBZ, tiled to fill space**

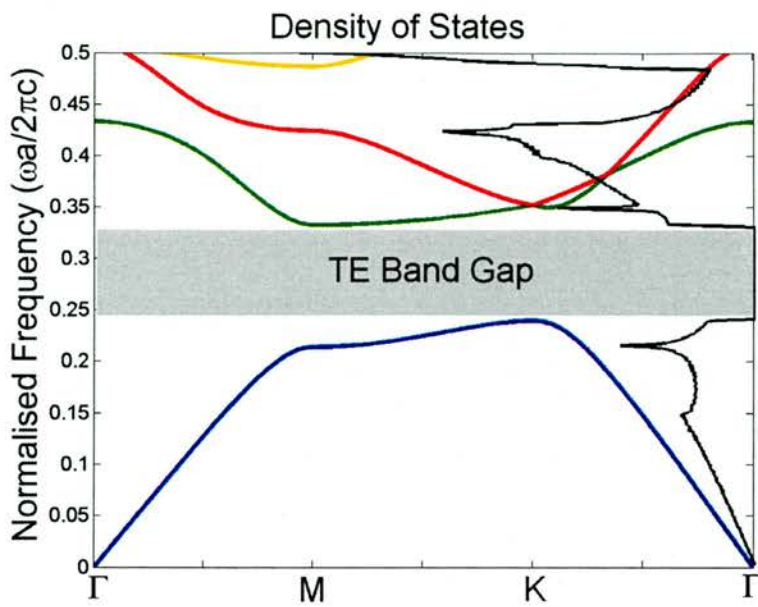


**Figure 5.2 The density of states for the triangular lattice overlaid upon the original IBZ edge plot.**

The experimental heterostructures into which the PhCs were etched had a 240nm GaAs core and a  $2\mu\text{m}$   $\text{Al}_{0.9}\text{Ga}_{0.1}\text{As}$  cladding. Including the  $\text{SiO}_2$  etch mask in the layer structure, at  $1.31\mu\text{m}$  this has an equivalent index of  $n_{\text{equiv}}=3.1$ . This index value is then used in the 2D model. The folded states within the IBZ lie inside the light cone of the cladding material ( $\text{Al}_{0.9}\text{Ga}_{0.1}\text{As}$ ,  $n\sim 2.98$ ). The consequence of the air localising in the holes is that losses are increased due to the inability of the perforated waveguide to guide the radiation. The high aluminium content allows the cladding to be steam oxidised, thus giving a cladding index of  $\text{Al}_x\text{O}_y$ ,  $n\sim 1.6$ . The waveguide would then have an equivalent index of  $n_{\text{equiv}}=2.95$ . It was found that any benefit of the increased confinement, which this configuration provides, is traded against an increased scattering due to roughness in the oxidised cladding layer; the losses remained high.

The density of TE states of the bands also peaks close to the lower band edge. As we move to higher frequency it then tends to zero. While a complete PBG does not exist for this ratio of  $R/a$ , the low number of TE states will inhibit mode conversion. The TE states were examined by first solving for the equivalent index of the slab ( for  $E_y$ ,  $H_x$ , Hz in the plane).

To examine the curvature of the lower bandedge in more detail we flatten this plot. Plotting the equifrequency<sup>\*</sup> contours of the wavevector diagram, reveals an interesting regime of operation (see Figure 5.3). For telecommunications applications (coarse WDM in particular), we are interested in devices which can demultiplex two wavelengths with spacings of 10s of nm. As in the previous chapter the dispersion of the input ridge waveguide (width 10 $\mu\text{m}$ ) lies outside of the IBZ (denoted by the dotted hexagon), its dispersion here is marked by the two concentric dashed rings, relating to wavelengths of 1.31 $\mu\text{m}$  and 1.29 $\mu\text{m}$  (or  $u=0.214$  and  $u=0.217$ , respectively). At the interface between the waveguide and PhC we determine the propagation direction from a construction line. The construction line is a graphical representation of our momentum conservation rule (from the start of Chapter 3,  $k_{xA}^i = k_{xB}^r = k_{xB}^t$ ) that the tangential components of the wavevector be conserved. It lies normal to those equifrequency contours which meet the incident wavevector. Note, that these lie significantly further from the IBZ boundary than in previous diagrams.

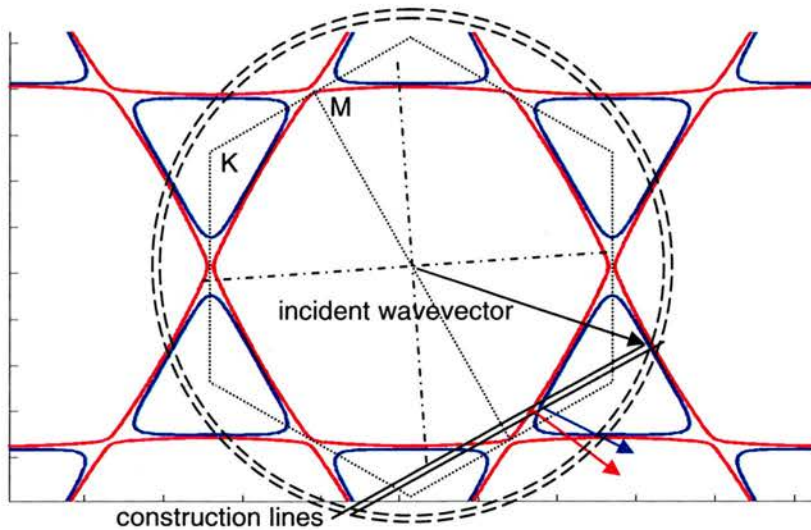


**Figure 5.3 Equifrequency contours for  $u=0.214$  and  $u=0.217$ . Original calculations by Michael Mazilu/Lijun Wu**

The wavevectors are folded back inside the IBZ and the propagation direction of the light beyond the boundary, in the PhC points along a direction normal to the equifrequency contour. In this frequency range the contours inflect from a hexagonal

---

\* Equifrequency contours: lines connecting wavevectors with equal eigenfrequencies.

to a triangular shape. The curvature of the equifrequency contours are opposite resulting in a  $\sim 10^\circ$  deviation for a 20nm shift in frequency.

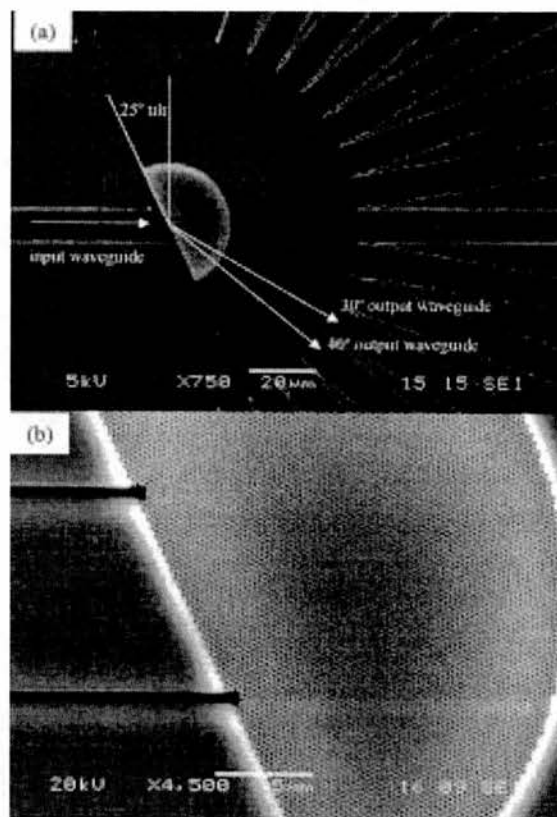


**Figure 5.4Experimental layout of superprism**

In the experiment by Wu [5], in order to access the interesting regions of the wavevector diagram the waveguide/PhC interface was tilted by  $25^\circ$  to the  $\Gamma M$  direction. To some extent this has the added benefit of reducing F-P noise in the input waveguide. The experiment has recently been repeated and thus verified in a SOI waveguide [6]. As in our original experiment this newer work places an array of output waveguides at the exit of a semicircular PhC region. From an experimental point of view this would successfully capture a diffracted beam, from a grating, for example waveguides in a AWG are placed on the circumference of a Rowland circle. This was not an ideal case for the diffracting/refracting behaviour of the superprism. It can be appreciated from the many field plots in the literature of superprism behaviour [7], that the finite extent of the input beam affects the resolution of the device. The variation in beam shape at the output interface with wavelength is a problem particular to the superprism.

Several schemes have since been reported in the literature for better matching at the interface of a PhC superprism. Baba et al. have been the most active researchers in developing matching interfaces, initially cutting the prism at particular planes normal to the excited wavevectors [7]. Wu et al. have demonstrated a cascaded PhC collimator operating near the flat dispersion region [8,9]. External diffracting structures have been suggested which calculations show to enhance the coupling to Bloch modes 10 fold, to ~86% [10].

The resolution of the basic superprism is denoted highly efficient in [11], but calculates that the device size for sub-nm resolution would be several cms in size (comparable with existing technologies). Building upon this work Baba [12] has utilised the refraction of the  $k$  vector at the interface to the PhC in order to achieve much greater shifts. This does not entirely preclude the need to match the interfaces, but can, as predicted by FDTD simulation, match or better the above superprism effects.

### **5.3 Waveguide junctions and bends**

One of the highly publicised features of 2D PhC circuits was the ability to bend light through very sharp angles and achieve 100% Transmission. This was first computed by Mekis [13] for a 2D square array of dielectric pillars in air. The microwave experiment by Ozbay et al [14] hints at the possibilities offered by realising 2D/3D routing, though they achieve ~100% transmission through a defect waveguide, only 35% is guided around a bend. After studying the 2D CCWs they were able to achieve much higher efficiencies. A similarly successful demonstration of a similar effect at optical frequencies has been notably absent. [15,16]

### **5.4 Conclusions**

The superprism offers many opportunities for dispersion compensation, perhaps most simply in a prism/grating pair configuration. The problems of interfacing to the periodic structure from access waveguides to cleanly excite the mode of interest and designing the output interfaces to distribute the spectral data are the two greatest challenges in developing this concept, outwith the need to reduce the losses further.

- 
- 1 S.Y. Lin, V.M Hietala, L. Wang, E.D. Jones, "Highly dispersive photonic band-gap prism," Opt. Lett. **21**, 1771- 1773, (1996).
- 2 H. Kosaka, T. Kawashima, A. Tomita, M. Notomi, T. Tamamura, T. Sato, S. Kawakami, "Superprism phenomena in photonic crystals: Toward microscale lightwave circuits," J. Lightwave Technol., **17**, pp.2032–8, (1999).; H. Kosaka, T. Kawashima, A. Tomita, M. Notomi, T. Tamamura, T. Sato, S. Kawakami, "Superprism phenomena in photonic crystals", Phys Rev B, R10096, (1998)
- 3 B. Gralak, S. Enoch, G. Tayeb, "Anomalous refractive properties of photonic crystals", J. Opt. Soc. Am. A, **17**, 1012-20 (2000)
- 4 M. Notomi, "Theory of light propagation in strongly modulated photonic crystals: Refractionlike behaviour in the vicinity of the photonic band gap", phys. Rev. B, **62**, pp10696, (2000)
- 5 L. Wu, M. Mazilu, T. Karle, T.F.Krauss, "Superprism Phenomena in Planar Photonic Crystals", IEEE J. Quantum Elect., **38**, pp915-8 (2002)
- 6 A. Lupu, E. Cassan, S. Laval, L. El Melhaoui, P.Lyan, J.M. Fedeli, "Experimental evidence for superprism phenomena in SOI photonic crystals", Opt. Express., **12**, pp5690-96 (2004)
- 7 T. Baba, M. Nakamura, "Photonic Crystal Light Deflection Devices using the Superprism Effect", IEEE J. Quantum Elect., **38**, pp909-14 (2002)
- 8 L. Wu, M. Mazilu, T.F.Krauss, "Beam Steering in Planar-Photonic Crystals: From Superprism to Supercollimator", J. Lightwave. Technol., **21**, (2003)
- 9 L. Wu, M. Mazilu, J-F. Gallet, T.F.Krauss, "Square Lattice Photonic Crystal Collimator", Photonic and Nanostructures, **1**, pp31-6 (2003)
- 10 J. Witzens, M. Hochberg, T. Baehr-Jones, A. Scherer, "Mode matching interface for efficient coupling of light into planar photonic crystals", Phys. Rev. E **69**, 046609 (2004)
- 11 T. Baba, T. Matsumoto, "Resolution of Photonic Crystal Superprism", Appl. Phys. Lett, **81**, pp2325-27, (2002)
- 12 T. Matsumoto, T. Baba, "Design and FDTD simulation of Photonic Crystal k-vector Superprism", IEICE Trans. Electron. E87-C, 393-7 (2004)
- 13 A. Mekis, J.C.Chen, I. Kurland, S. Fan., P.R.Villeneuve, J.D.Joannopoulos, "High transmission through sharp bends in Photonic Crystal waveguides", Phys. Rev. Lett., **77**, pp3787-90, (1996)
- 14 B. Temelkuran and E. Ozbay, "Experimental demonstration of photonic crystal based waveguides", Appl. Phys. Lett., **74**, pp. 486-8 (1999); Mehmet Bayindir, B. Temelkuran, and E. Ozbay, "Photonic-crystal-based beam splitters", Appl. Phys. Lett.,**77**, pp3902-4 (2000)
- 15 R. Wilson, T.J. Karle, I. Moerman, T.F.Krauss "Efficient photonic crystal-Y junctions", J. Opt. A.: Pure Appl. Opt. **5** pp76-80, (2003)
- 16 S. Boscolo M. Midrio, T. F. Krauss , "Y junctions in photonic crystal channel waveguides: high transmission and impedance matching", Optics Lett. **27**, pp 1001-1003, (2002)

# **Chapter 6**

## **Conclusion**

Planar Photonic Crystals appear to be able to provide both temporal delay and compression of optical pulses. This has been demonstrated in this report at the telecommunications relevant wavelengths of 1.3 and 1.5 $\mu$ m and over pulse bandwidths of tens of nanometers. The materials used, Si and AlGaAs/GaAs are transparent over this wavelength range and exhibit only slight material dispersion ( $\Delta n_{Si}=0.5\%$ ). Careful choice of laser pulse duration and also repetition rate are vital in avoiding non-linear contribution to the dispersion and loss. In seeking to use the well defined pulses from an 80MHz OPO to characterise these devices the inherent non-linear absorption (TPA) has been a significant problem.

*At 1550nm 500fs pulses with a 10GHz rep rate were transmitted through GaAs waveguides with an absence of non-linearity. To allow use of the 1ps, 80MHz OPO pulses, we designed a heterostructures waveguide with an Al<sub>20%</sub>GaAs. This has been highly successful at relieving TPA beyond the half bandgap of 1500nm.*

The 2D nature of the PhCs lends itself to the goal of high density optical integration. The compact scale of the devices is part of their potential, but creates many of the headaches in dealing with them. Their small scale is permitted by the high index contrast, and resultant strong coupling between the grating and the incident waves. In seeking to delay the various spectral constituents of an optical pulse, with a passive waveguide, we require a finite distance over which the pulse must travel. Using e-beam lithography (at a prescribed resolution) limits the dimensions of the structures that can be readily fabricated without introducing stitching errors. Optimisation of etching parameters has led to increased hole uniformity, etch depth and verticality of side wall features, rivalling the best small feature size GaAs etching. The hole profile obtained using CAIBE etching as opposed to our initial RIE etching has dramatically improved device performance over several “production” cycles.

*During the project we moved the lithographic tuning step ever closer to the quoted 5nm resolution limit of the LEICA EBPG-15. This appears to be a well defined limit,*

*as at this limit the stitched spectra exhibit irregular glitches of  $\Delta u=0.5\%$ . The field stitching using a laser-interferometrically controlled stage appears to give us the opportunity of working with several mm of access waveguide, and up to  $160\mu\text{m}$  long PhCs. The most significant development in this process was writing the narrowest taper sections at the same high resolution as the PhC. Heterostructure waveguide PhC patterns with lattice constants ranging from 210-410nm have been fabricated successfully with near vertical sidewalls and depths of  $2\mu\text{m}$  in GaAs. For the L2in1 devices we were then able to show a limiting behaviour in the device performance for an increase in etch depth.*

The field stitching allows us to create high contrast, periodic waveguides, that are several hundred lattice constants long. This appears to suggest that we can utilise a combination of high dispersion and relatively long path lengths to disperse pulses. In reality we have struggled against the intrinsic losses from these structures. We have sought to accurately measure these losses from a Fourier analysis of the transmission spectrum, interrogating the multiple round trip information present in the facet/facet Fabry-Perot fringes. At the time of writing this work is incomplete, exhibiting unusually non-linear behaviour (independently verified) and heavily dependent on facet quality. The results of the mathematical analysis are keenly (critically) dependent upon the sampling window.

*The losses above the light line for WI waveguides are prohibitively high for transmitting pulses ( $>100\text{dB/mm}$ ). This is essentially where the device acts as a highly efficient grating coupler. We should attempt to take advantage of this to couple waveguides. The loss is too great to consider compensating by inserting a gain element into the circuit. The light line argument appears to have great validity as witnessed in Chapters 3 and 4. The restriction it imposes, to some extent rains on the parade of 2D PhCs, creating an engineering challenge to achieve modes with interesting dispersion under the light line in the reality of 3D. Modes underneath the cladding light-line have been shown numerically and experimentally to have much longer lifetimes ( $Q_s$ ) than those above. Aligning modes beneath the cladding light-line is not possible using a Low Out-Of-Plane contrast approach. These modes are*

*uniquely lossy, but the loss is in the range which may be compensated by a gain element (>20dB/mm).*

Modelling these finite length devices poses some real challenges. A great deal of effort has been expended to improve our confidence in results, by benchmarking and cross checking of models in 2D and 3D. A single supercell can be modelled and very effectively transformed into a propagation model, to calculate both the allowed states and the transmission/reflection coefficients. The robust FDTD algorithm has been our main workhorse in this task, demonstrating remarkable stability and intuitive behaviour. The ability to seamlessly and simultaneously deal with advanced absorbing and periodic boundary conditions. There is a clear path to expanding the capabilities of the code to deal with non-linear and dispersive materials. The issue of bootstrapping remains very critical in dealing with pulsed excitations and evaluating the dispersive nature of devices. To this end CW simulations were preferred when analysing the dispersion of short finite length devices. To complement this Eigenmode expansion modelling has also performed. Agreement is very good given the differences in nature of the two techniques and the complicated geometry. This seems less readily expandable to fulfil the NlogN efficiency which this technique promises. The difficulty is in dealing with the radiation at the boundary in a stable manner and ensuring conservation of energy between modes. Using a fourier basis for the expansion appears to be a very successful method of dealing with 2D periodic structures.

The excitation of single modes in waveguide has been a significant challenge. The multimode input waveguides have introduced a modal uncertainty into experiments. A single mode approach has been successfully demonstrated on SOI, elsewhere. The dispersion of our wider ridges, tapered down to the narrow PhCs provides an effective modal match to the waveguides and to some extent alleviates some of the optical loss and overloading that may be present in narrower guides. The tapers do allow short phase matched interactions between many modes, which is certainly not desired.

*Our end-fire coupling techniques have demonstrated an average 10% coupling efficiency. This is very dependent on facet quality and often represents half of the total loss. To make the devices more accessible to further pulsed measurement it*

*would be wise to attempt to increase this percentage substantially. Mode matching at the external and internal interfaces is critical to providing high transmission. It is worth noting that the high dispersion of the L2in1 devices is apparently due to the lack of a sufficient match at the coupling ridge/PhC interface. In the presence of moderate optical gain in discrete devices, this mismatch could be exploited. In a passive device the need to match the dispersion at the interfaces to ensure high transmission, creates a question about how to couple to very slow states (i.e. the rate of Energy flow must be constant across the boundary).*

We have reviewed the existing methods used to compensate the dispersion of optical pulses which have been either chirped in transmission through a telecommunications system or a modulated laser source. Dispersion Compensating Fibre (DCF) has been deployed in networks successfully and engineered to adapt to faster bit rates. Newer fibres based on Higher Order Mode (HOM) dispersion and Fibre Bragg Gratings (FBG) offer low non linear response, and low loss and even tunable dispersion control. Although electronic techniques are able to adaptively configure (pre-compensate) pulses, possibly up to 10Gb/s and beyond, they eventually will be unable to provide Digital Signal Processing at higher bit rates. Solutions involving discrete MEMS etalon components and HOM waveguide devices appear to be able to provide significant dispersion control.

*Comparison of recent research results involving ultra dispersive elements, Photonic Crystals, reveals great promise for the integration of compact compensating systems. Light has been observed to be significantly dispersed in devices which can be fabricated in lengths which make the magnitude of the dispersion practically relevant. The support of those working on Silicon integrated optics is making a significant difference to this work. The lithographic challenges that this has posed have been addressed and this has improved the fabrication of other high contrast waveguide solutions. Group velocities in the region of  $v_g=c/100-c/1000$  are being routinely reported. The ability to vary the group velocity over a small spectral region has allowed pulse compression and dilation to be demonstrated.*

The high dispersion available from high contrast waveguide devices is probed using fibre optics systems equipment. Despite the high losses (insertion and propagation) a non-linear pulse characterisation is achievable using external amplifiers. The experiment was performed at a single wavelength, but using multiple lengths of fibre a rigorous assessment of the Group Velocity Dispersion is possible.

*The dispersion of short L2in1 Coupled cavity Waveguides has been assessed using a 3D FDTD model and 2D mode solver. Only this 3D approach realistically includes the intrinsic device loss. Accurate normalisation of the transmission spectrum allows comparison with the full 8 $\mu$ m device transmission, studied using 3D FDTD. These are found to be in excellent agreement. The highest transmitting structure an L2in1 waveguide was found to be suitable for temporal measurements using ps pulses at 1550nm. The first demonstration of pulse compression in Planar Photonic Crystals was achieved with a 40% reduction in pulse length for a device which is only 8 $\mu$ m long. An estimate of the Group Velocity Dispersion of 10<sup>7</sup>ps/nm/km was made, by introducing successive lengths of fibre in to the system to disperse the pulses which had been transmitted by the device.*

Direct access to the optical fields propagating inside a Photonic Crystal is sought using a near field technique. The far field analysis of scattered light is limited by diffraction whereas the near field probe is capable of imaging the many higher order harmonics in the waveguide. This can be compared to the transmission spectrum in order to understand which modes have been excited in the waveguide. The technique was finally successfully applied to PhCs, as the large evanescent mode tail of the fundamental mode of the SOI wafer provides a high enough signal level for detection. The tunability of the laser source and lithographic tuning extends the measurement across a range equal to 10% of the centre frequency.

*The direct visualisation of 100fs pulses propagating in a Photonic Crystal waveguide was achieved by time resolved heterodyne interference NSOM measurement. The Fourier analysis of the spatial data allows us to map the photonic bandstructure of the waveguides. We resolve the Bloch harmonics of the Planar Photonic Crystals*

*both above and below the light line as a result of this phase sensitive technique. Analysis of the data reveals waves travelling with positive and negative phase velocities (both forwards and backwards) whilst the pulse can seen to move with positive group velocity. Pulse breakup is observed due to the high dispersion; as is a standing wave, in an open structure which does not diminish over a timescale of >5ps.*

These results show great promise for dispersion management of ultrafast pulses. In particular increasing the length of our low loss devices to the mm lengths achieved by Japanese researchers would allow dispersion compensation of telecommunications pulses.